NASA CR-137843
MDC E1415 VOL. II

NASA CONTRACTOR
REPORT

NASA CR-137843
MDC E1415 VOL. II

(NASA-CR-137843) PLANETARY/DOD ENTRY TECHNOLOGY FLIGHT EXPERIMENTS. VOLUME 2: PLANETARY ENTRY FLIGHT EXPERIMENTS Final Report, 1 Apr. 1975 - 29 Feb. 1976 (McDonnell-Douglas Astronautics Co.) 227 p HC $8.00 CSCL 03/13

N76-28244
Unclas
47941

PLANETARY/DoD ENTRY TECHNOLOGY FLIGHT EXPERIMENTS

Planetary Entry Flight Experiments

By H.E. Christensen, R.J. Krieger, W.R. McNeilly and H.C. Vetter

Prepared by

MCDONNELL DOUGLAS ASTRONAUTICS COMPANY — EAST
St. Louis, Missouri 63166 (314) 232-0232

for Ames Research Center

NATIONAL AERONAUTICS AND SPACE ADMINISTRATION • WASHINGTON, D.C. • FEBRUARY 1976

NASA CR-137843
MDC E1415 VOL. II
29 FEBRUARY 1976

PLANETARY/DoD ENTRY TECHNOLOGY FLIGHT EXPERIMENTS

COPY NO. 30

Planetary Entry Flight Experiments

By H.E. Christensen, R.J.Krieger,
W.R. McNeilly and H.C. Vetter

Prepared Under Contract No. NAS 2–8678 by

MCDONNELL DOUGLAS ASTRONAUTICS COMPANY – EAST

Saint Louis, Missouri

for

NATIONAL AERONAUTICS AND SPACE ADMINISTRATION

FOREWORD

This final report was prepared by McDonnell Douglas Astronautics Company-East (MDAC-E) for NASA Ames Research Center Contract NAS2-8678, Planetary/DoD Entry Technology Flight Experiments. It covers the period 1 April 1975 to 29 February 1976. This effort was performed for the National Aeronautics and Space Administration, Ames Research Center, under the direction of the Thermal Protection Branch with Dr. Phillip R. Nachtsheim as Contract Technical Monitor and with the cooperation of Capt. R. J. Callahan of SAMSO and R. C. Loesch of Aerospace Corporation as advisors for the DoD portion of the study.

The report consists of four volumes:

Volume I - Executive Summary
Volume II - Planetary Entry Flight Experiments
Volume III - Planetary Entry Flight Experiments Handbook
Volume IV - DoD Entry Flight Experiments

TABLE OF CONTENTS

TABLE OF CONTENTS (CONT)

GLOSSARY

Booster	Upper stage that provides initial thrust on the PDS deployed from Shuttle, e.g., Transtage, Delta, Centaur, Agena, and may include TE 364-4 auxiliary stage.
ETR	Eastern Test Range
HL	High Level Signal
IUS	Interim Upper Stage
LL	Low Level Signal
KBPS	Kilo Bits Per Second
MUX	Multiplexer
PCM	Pulse Coded Moduled Signal
PDS	Payload Deployment System is the Shuttle deployed payload. The assembly of a booster, spin separation system plus entry vehicle and associated avionics.
RCS	Reaction Control System
K_a	Apa Apsis Radius
R_N	Nose Radius
SIP	Strain Isolation Pad
Shuttle	Space Shuttle
SPS	Samples Per Second
SW	Switch
T/C	Thermocouple
T_S	Shock Temperature
V	Velocity
Y	Distance through shock layer measured from vehicle surface
β	Ballistic coefficient
γ	Entry angle
γ_R	Relative entry angle
ΔV	Velocity increment
δ	Shock standoff distance or Shock layer thickness
ρ	Density

1.0 INTRODUCTION

Unmanned exploration of the outer planets of our solar system is a major goal of NASA. Startling new discoveries have been made by the Pioneer and Mariner programs. Another step in this exploration process is the entry into the atmosphere of an outer planet. It is expected that a great number of atmospheric probe flights will be made in the future. As the results of early missions are analyzed, new and more comprehensive measurements will be planned. Progressively more severe environments will be explored. To these ends advances in planetary entry technology, particularly in the thermal protection system, will be necessary.

Due to the high approach velocity caused by the gravitational pull of a large planet, intense radiative and convective heating is predicted for entry into the hydrogen-helium atmosphere of these planets. Entry probe designs have evolved (References 1 and 2) which employ a blunt cone configuration to reduce atmospheric penetration rate, loads and heating. Even so, high heating (30 to 50 kW/cm^2) is predicted. Ground testing and flight testing of a probe-like vehicle will establish probe integrity under extreme conditions.

A timely and cost-effective approach to the advancement of planetary entry technology is to simulate the desired entry environment in earth flight test experiments, using the Space Shuttle as a launch platform. Heretofore, such experimentation has been expensive, and higher speeds required of planetary entry simulation will be even more demanding than on previous experiments. Large sophisticated space equipment will be required. Such equipment will be available at reasonable cost with the advent of the Space Shuttle and its upper stages. Thus, the purpose of the present study is to determine the feasibility of using the Shuttle to perform planetary entry technology flight experiments.

The results of a system design study for such a flight is contained herein. The specific objectives for such a flight are outlined in Figure 1. An entry vehicle configuration similar to the outer probe was selected for the study. Size and mass were adjusted to meet the entry simulation needs. The physical characteristics of the baseline entry vehicle designed in this study are:

- o blunt 60° half angle cone
- o 88.9 cm outer diameter
- o 22.2 cm nose radius
- o hemispherical aft cover

PLANETARY ENTRY EXPERIMENTS

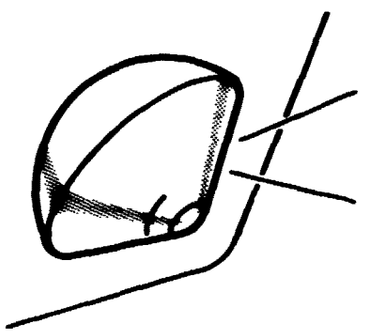

PRIMARY OBJECTIVES

HEATING ENVIRONMENT PREDICTION
- SHOCK LAYER RADIATION
- RADIATION BLOCKAGE BY ABLATION

HEAT SHIELD DESIGN
- CARBON PHENOLIC MECHANICAL EROSION
- SILICA PERFORMANCE AND STRUCTURAL INTEGRITY

OTHER OBJECTIVES

- BOUNDARY LAYER TRANSITION
- TURBULENT HEATING INFORMATION
- DECELERATION LOADS
- AFTERBODY HEATING
- HEAT SHIELD THERMAL STRESS
- VEHICLE AERODYNAMICS AND STABILITY

FIGURE 1

- o 120 kg/m^2 ballistic coefficient
- o instrument and system complement
- o air recovery system

Critical to the success of the entry phase of the mission is the prediction of the spectral radiation caused by the compression of the hydrogen-helium atmosphere between the shock wave and the vehicle. Computation of shock layer radiation depends on gas composition, temperature distribution and surface temperature of the entry vehicle surface. The gas injected by the ablating heat shield also influences the radiative heating. Consequently the primary objective of the earth entry experiment is to match the heating and other environments expected during outer planet entry. Of great importance during any test is the measurement of environments, so the earth entry flight experiments was designed to measure the radiative heating and other environments. These measurements will be used to validate the prediction techniques and to update predictions for the hydrogen-helium environment. The heat shield of the outer planet probe constitutes approximately 40% of its mass. Consequently the selection of the material for the heat shield and its sizing greatly affects the launch weight and the amount of instrumentation that can be carried. Candidate heat shield materials fall into two categories: (1) a carbonaceous ablator which accommodates the intense heating by ablation resulting in large mass injection and (2) a highly reflective material such as hyperpure silica which reflects a large portion of the radiative heating. Carbon phenolic is subject to mechanical erosion and silica is subject to significant thermal stress. Validation of the structural integrity of both materials can be made in an earth entry test. Instrumentation was designed to measure the performance of the heat shield materials. Experiments were also devised to measure the parameters necessary to increase the technology base for designing outer planet probe.

The scenario of a planetary entry flight experiment launched from Shuttle is depicted in Figure 2. After the Shuttle has established a circular orbit (160 nmi, nominally), the Payload Deployment System (PDS) consisting of an assembly of a booster (two or three stage propulsion system), a spin system and the entry vehicle is deployed from the Shuttle cargo bay. The first stage of the booster is fired to accomplish the Hohmann transfer to a high orbit (up to synchronous altitude) where a deorbit burn is accomplished. The spent stage is jettisoned and the vehicle accelerates towards earth converting potential energy into kinetic energy. Just prior to the sensible atmosphere the final burn is accomplished increasing the entry

PLANETARY ENTRY SIMULATION MISSION

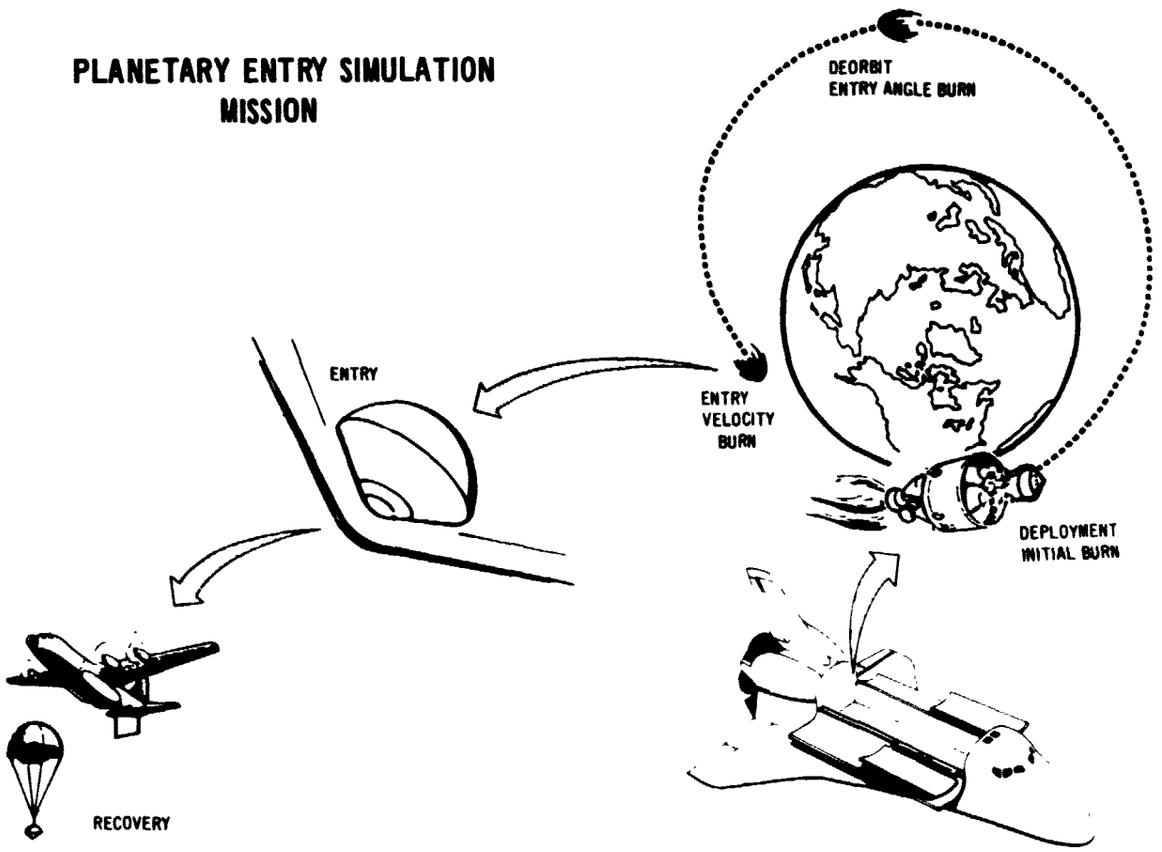

FIGURE 2

velocity. The final stage and the entry vehicle are spin stabilized. During entry the flight measurements are made documenting environments and vehicle performance. At the conclusion of the entry which occurs near the NASA test range at Ascension Island, the entry vehicle is air recovered so the heat shield and other components can be examined. The complete analysis of such a mission including environments, experiment design, vehicle design, booster interfaces, heat shield performance, mission scenario, communications analysis, ground tracks and cost estimates are contained herein. The study flow is depicted in Figure 3. Entry environments for outer planet probes were used to establish the simulation requirements. Boosters which can be launched from Shuttle were examined to determine the entry conditions that could be achieved to deploy an entry vehicle. Predictions of the entry environments were made in order to compare with the simulation requirements. After establishing the mission feasibility, the details of the mission and vehicle design were worked out. Also a planetary entry flight experiment handbook was prepared (Volume III) to aid in continuing the design of such an experiment.

The authors appreciate the significant contributions made to the study by: D. W. Dugan (NASA-ARC), W. E. Nicolet (Aerotherm), H. J. Fivel, W. H. Gustin, H. E. Hommes, L. J. Mockapetris and C. D. Poore of MDAC-E.

PLANETARY STUDY FLOW

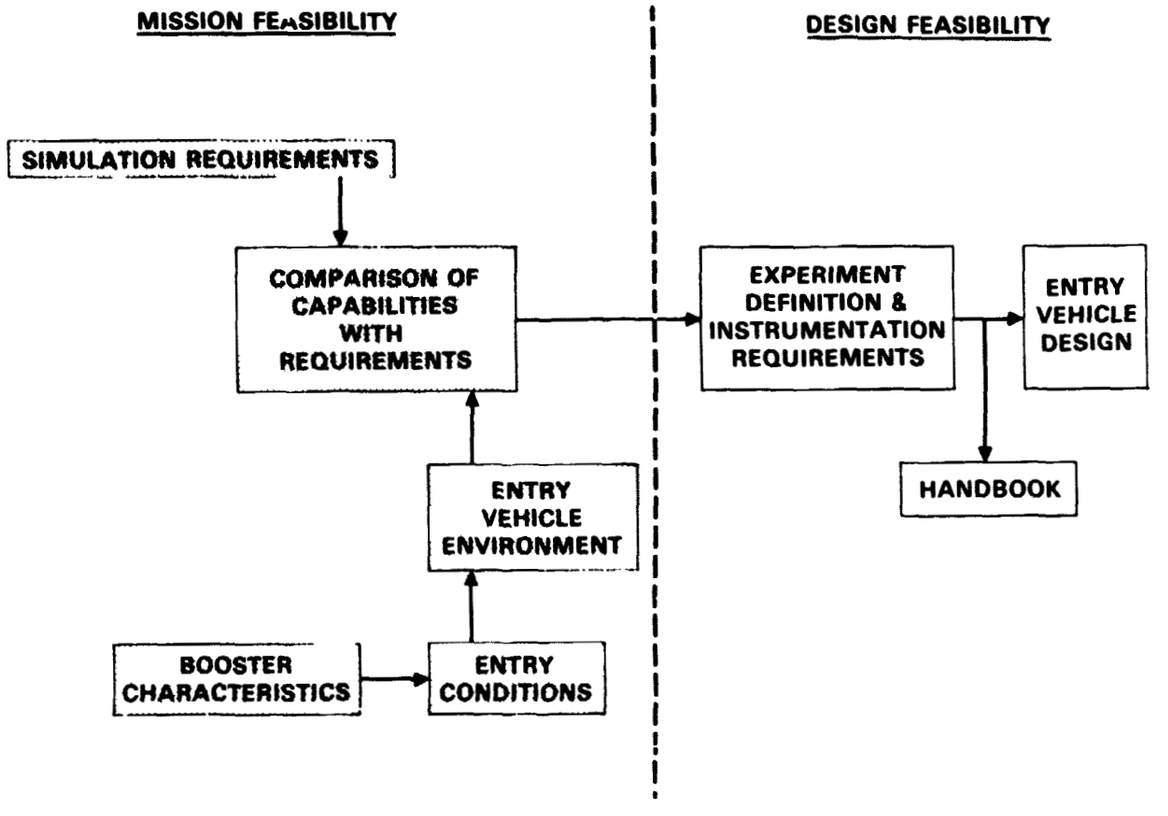

FIGURE 3

2.0 SUMMARY

The technical feasibility of launching a high speed, low β, earth entry vehicle from Shuttle to advance technology for the exploration of the outer planets' atmospheres has been established. Disciplines of thermodynamics, orbital mechanics, aerodynamics propulsion, structures, design, electronics and system integration focused on the goal of producing outer planet environments on a probe shaped vehicle during an earth entry. This study addressed seven major aspects of analysis and vehicle design. They included: planetary environments, earth entry environment capability, mission maneuvers, capabilities of Shuttle upper stages, a comparison of earth entry planetary environments, experiment design and vehicle design.

The planetary entry parameters that are required to be simulated were analyzed and related data assimilated. Entry into the outer planets is characterized by a radiant dominated heating pulse. Consequently, detailed studies were conducted centering on the understanding of the intense radiative heating emanated from the shock layer. In particular, the effects on the spectral energy distribution from adiabatic, cooled and mass injected shock layers were characterized for both carbonaceous and hyperpure silica heat shields. Uncertainties in the Jovian entry angle (3 degrees spread) results in a 58% increase in radiative heating, a 19% increase in convective heating and a 10% rise in stagnation pressure. The two candidate heat shields also influenced the radiative environment. The blowing of the carbonaceous shield reduced the incident radiative heating by 46% whereas the mass injection from the silica shield caused 18% reduction. However, due to silica's excellent reflectance properties, only 1.7 kW/cm^2 had to be accommodated by the heat shield whereas carbon with its high absorptance (.8) had to absorb 9.1 kw/cm^2 at peak heating conditions.

In parallel, trajectories and shock layers for high speed earth entry were investigated to determine what environments could be achieved. Comparable radiative heating levels were computed and the influence of shock layer properties on radiative heating were similar to those obtained for the outer planets. The spectral distribution of energy for earth showed a shift to a larger percentage in the vacuum ultra violet (VUV). Trajectory parametrics were computed and showed that not as high an entry velocity is required on earth as the outer planets to achieve the same heating.

Detailed mission analyses studies including ΔV requirements, impulsive and finite burn trajectories and ground tracks were performed. Hohmann transfer tra-

jectories with apoapsis up to 40 earth radii were computed. Only trajectories up to 6.5 earth radii were needed to achieve the required heating. Depending on the mission, once the system is deployed from Shuttle 6 to 13 hours are required to complete the mission.

At the beginning of this study, the IUS concept had not been selected. Consequently, four classes of boosters were analyzed to determine their ability to accomplish the Hohmann transfer and deorbit. They included a cryogenic (Centaur), a storable propellant (Transtage), a compact booster constructed using the Shuttle's altitude control propulsion components and a solid rocket motor (SRM) booster. Performance maps including the entry environments that would be obtained on a nominal entry vehicle were prepared for each class of booster. Midway through the study the decision to develop the SRM IUS was made by the government. All the booster concepts employed a TE364-4 as the final stage in order to obtain the desired entry velocity. The final stage and the entry vehicle were spin stabilized. Details of the booster performance were studied and factored into a comparison of simulated conditions against requirements.

In the comparison of attainable earth entry environments with the required planetary environments, the importance of simulating radiative heating over shadowed other parameters. Although earth entry conditions can be selected that result in matching peak radiative heating for Saturn or Jovian entries, the precise matching of all parameters is not possible. Entering at 20 degrees produced the best match for Jupiter and a steeper angle was required for the Saturn simulation. Detailed studies using shock layer flow field/radiation computer codes were conducted to show the effect of shock layer temperature distribution, wall temperature and species concentration on the incident heating. These sensitivity studies showed that the incident heat is significantly reduced due to cooling effects in the shock layer and blowing of ablation products. It appears that both the incident and net radiative heat flux incident on a carbonaceous heat shield during a Jovian entry can be duplicated during an earth entry but more net flux results on a silica heat shield when the incident radiative flux is duplicated. The difference in conditions on the silica shield is due to the higher percentage of energy in the VUV for air where silica's reflectance is low. Despite this mismatch, the silica shield has to accommodate approximately half the radiant flux that a carbonaceous shield. This increase in het heat also means that a closer match in total heat will be achieved. Radiative heating is significantly reduced when heat shield mass injection occurs.

This occurs more so during entry into earth than Jupiter. Hence entry energy must be increased to achieve simulation when considering blowing. Trajectories to 15 or 16 earth radii are required to produce the energetic conditions needed to meet the maximum design Jovian entry heating (blowing). The Transtage/TE364-4 booster will achieve these conditions whereas a more powerful SRM IUS booster, than the one studied, needs to be used. Even so, very high radiative dominated heating environment can be achieved using the SRM IUS.

The pertinent information assembled during this study were organized into a handbook (Volume III) to aid mission planners.

Experiments were designed to measure the environment and heat shield performance. A complement of experiments were selected to meet the measurement objectives. Instruments included:

1. Thermocouples; surface, indepth stack and interior
2. Pressure probes
3. Accelerometers
4. Strain gauges
5. Electrostatic probes
6. Radiometer

Two candidate radiometer designs were developed that fit compactly into the earth entry vehicle. These designs warrant further study and testing.

Design studies were accomplished for the earth entry vehicle. The heat shield, experiment/equipment, power and communications along with the structure and mid-air recovery system were married into an integrated design. Figure 4 is a composite of the entry vehicle profile, equipment/instrument locations, and a shared launch configuration. If the short length booster were used, the entry experiment could be sandwiched between other cargo. Even if the Transtage or SRM IUS were used only 3/8 of the Shuttle cargo bay would be occupied and 57% of the Shuttle's payload weight capability would be available for other cargo. This will permit a shared launch and a low experiment cost.

EARTH ENTRY VEHICLE – EQUIPMENT/INSTRUMENTATION

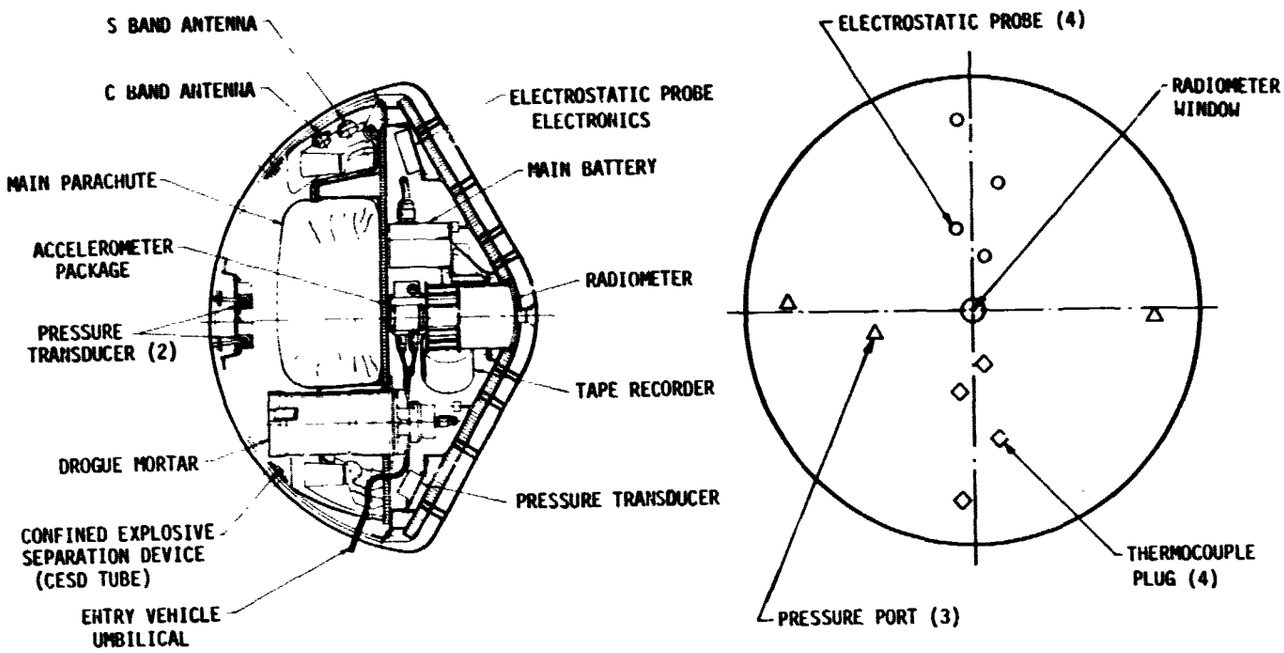

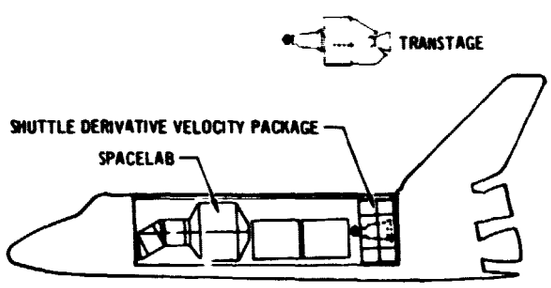

CANDIDATE BOOSTER ARRANGEMENTS

FIGURE 4

3.0 PLANETARY ENVIRONMENT SIMULATION REQUIREMENTS

Several investigators (3, 4 and 5) have been actively involved in predicting the environments that can be expected when entering the outer planets; Jupiter, Saturn and Uranus. Nominal environments that influence the design and performance of a probe include: peak radiative heating, peak convective heating, total heat, heat pulse duration, peak stagnation pressure and deceleration loads. The prediction of these quantities is of course dependent on the atmospheric model, trajectory, vehicle ballastic coefficient and the methodology. Trajectories are continuing to be evaluated so a typical atmosphere trajectory for a typical probe vehicle was used to establish entry environments. The radiative heating predicted for planetary entry is severe and dependent on the analytical model. The difference between analytical models stems from the assumptions regarding temperature and species concentrations across the shock layer.

Predictions have been compiled for: adiabatic shock layers, cooled shock layers and shock layers with species concentrations resulting from blowing of the ablation heat shield materials. In an adiabatic shock layer, all the gas is at the shock temperature and consequently produces the highest radiative heating. In a cooled shock layer, the gas temperature drops to the wall temperature near the wall and the radiative heating is lower. In a shock layer with mass injection, the region of low temperature is expanded further and the radiative heating is further reduced.

A compilation of outer planet entry environments is contained in the following sections and summarized in Figure 5. The radiative heating reported in the figure is for a cooled shock layer. Also included for reference are the entry environments anticipated for the forthcoming Venus probe mission as well as those experienced in earth by Project FIRE.

High heating parameters are the dominant environment associated with entry into the outer planets but stagnation pressure and decelerations are also important. Compared with earth entry, outer planet entry is characterized by high velocity, high radiative and convective fluxes and short entry times. Further, the heating environment is dominanted by shock layer radiation as opposed to the convective dominated earth entry.

The general environments associated with the outer planets are presented first in parametric curves followed by analyses of the spectral heating sensitivities and

SIMULATION REQUIREMENTS SUMMARY

	OUTER PLANETS				VENUS (PIONEER/ VENUS 78)	EARTH (PROJECT FIRE)
	JUPITER	SATURN	URANUS			
ENTRY CONDITIONS (INERTIAL)						
VELOCITY (KM/SEC)	59.6	36.7	24.9		11.6	11.3
ANGLE (DEGREES)	−7.5	−40	−50		−20 TO −90	−15
ATMOSPHERE						
DESIGNATION	NOMINAL	COOL	NOMINAL	COOL	CO_2/N_2	AIR
MASS FRACTION (H_2 – He)	.75–.23	.55–.40	.65–.16	.20–.80		
ENVIRONMENT						
PEAK HEATING RATE (KW/CM^2)						
RADIATIVE	38	20.5	0	33	2 TO 5	0.4
CONVECTIVE	15	12.5	4	11	3 TO 5	0.7
TOTAL HEAT (KJ/CM^2)	440	74	31	80	14 TO 21	13
HEAT PULSE DURATION (SEC)	14	10	15	4	3 TO 11	40
PEAK STAGNATION PRESSURE (ATM)	8	12	8	18	7 TO 8	0.5
PEAK DECELERATION (G)	300	700	500	700	200 TO 500	85

FIGURE 5

the influence of heat shield material on the heating.

It became apparent during the course of this study that various investigators have used slightly different values for planetary models and entry parameters. This is due to a continuing effort by the scientific community to upgrade our knowledge of the solar system. Where applicable these variations will be assessed in this report.

3.1 Planetary Environments - Worst case design environments are tabulated for each outer planet. However, emphasis is placed on parametrically describing stagnation point conditions as a function of entry angle, type of atmosphere and entry vehicle ballistic coefficient. It allows evaluation of future changes in mission and vehicle evolution and provides insight into how closely a given parameter should be simulated.

Jupiter Entry Environment - Mission and configuration parameters derived from available results of current outer planet probe studies were utilized to predict environments. Nominal parameters are as follows:

- Jupiter nominal atmosphere - 85% H_2-15% He by volume
- Inertial entry velocity - 59.70 km/sec
- Inertial entry angle - -7.5°
- Latitude - 5.0 (North)
- Relative velocity - 47.244 km/sec
- Relative entry angle - -9.5°
- Entry altitude - 450 km
- Ballistic coefficient - 141.8 kg/m^2

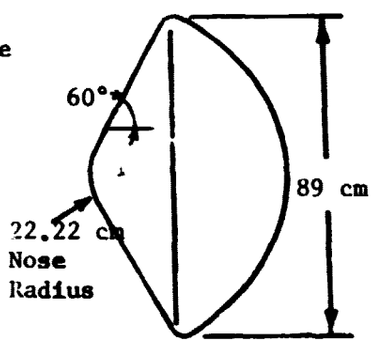

Entry radiative and convective heat pulses for this case are shown in Figure 6. Heating builds rapidly and then diminishes as rapidly. The convective rate is approximately 1/3 of the combined radiative and convective flux at peak heating conditions. However on the basis of total heat, convection (187 KJ/cm^2) accounts for 43% of the total heat (440 KJ/cm^2). Distributions of convective heating shock standoff distance, surface pressure and radiative heating on the heat shield at selected times during the Jovian entry are contained in Figures 7 and 8. As shown in Figure 8 up through maximum heating conditions (43.7 seconds) the radiative heating near the end of the conical section (S/R = 2.2) builds to values larger than that impinging on the stagnation point. Further analysis and testing are recommended to verify these results. The radiant heating in this region may be significantly altered by the presence of species injected from the heat shield. As shown in Figure 9, the flux aimed at the ablator is drastically reduced by blowing of ablation

HEATING HISTORIES FOR JOVIAN ENTRY PROBE

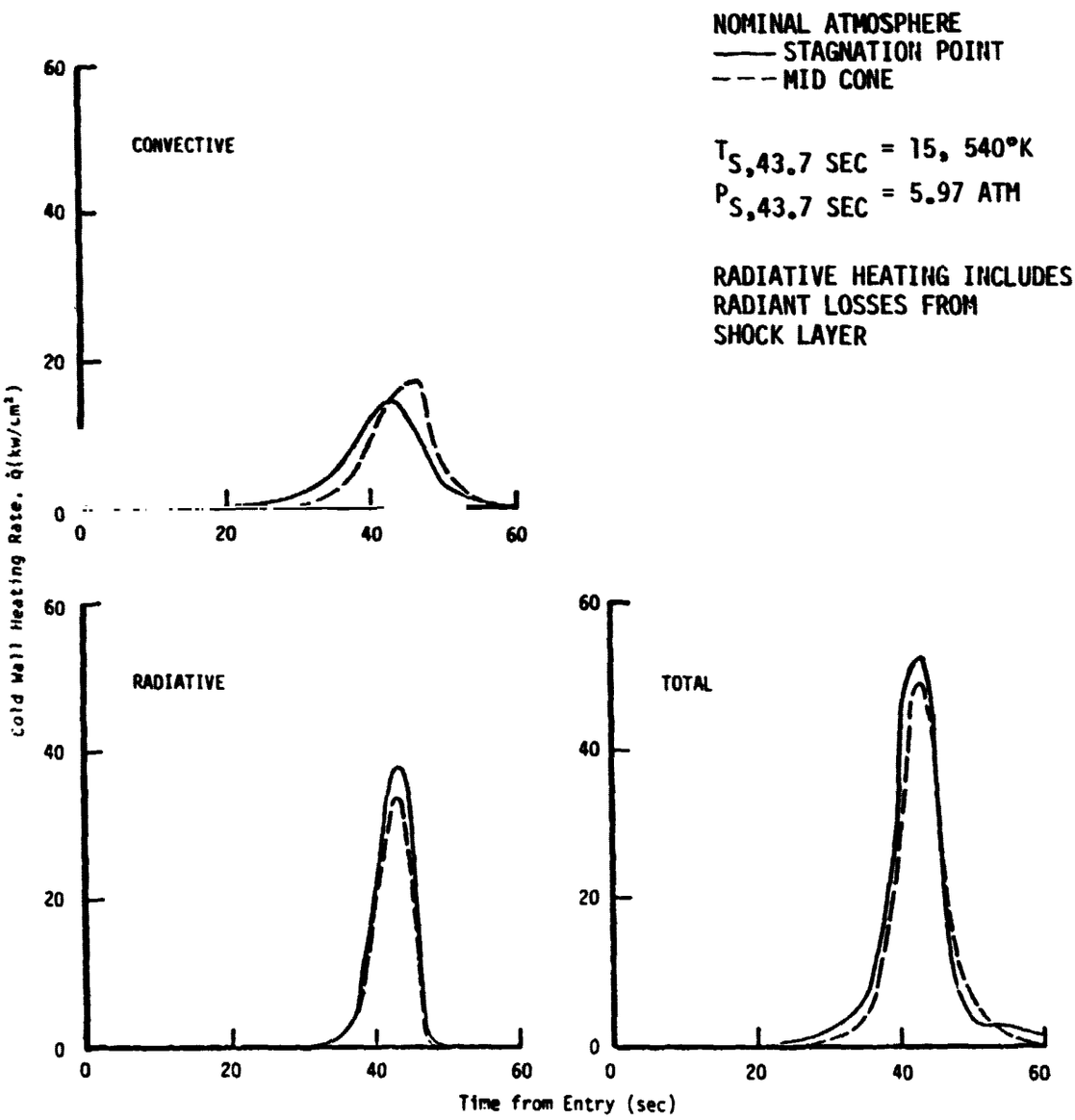

FIGURE 6

COLD WALL CONVECTIVE HEATING DISTRIBUTIONS ON A JOVIAN ENTRY PROBE

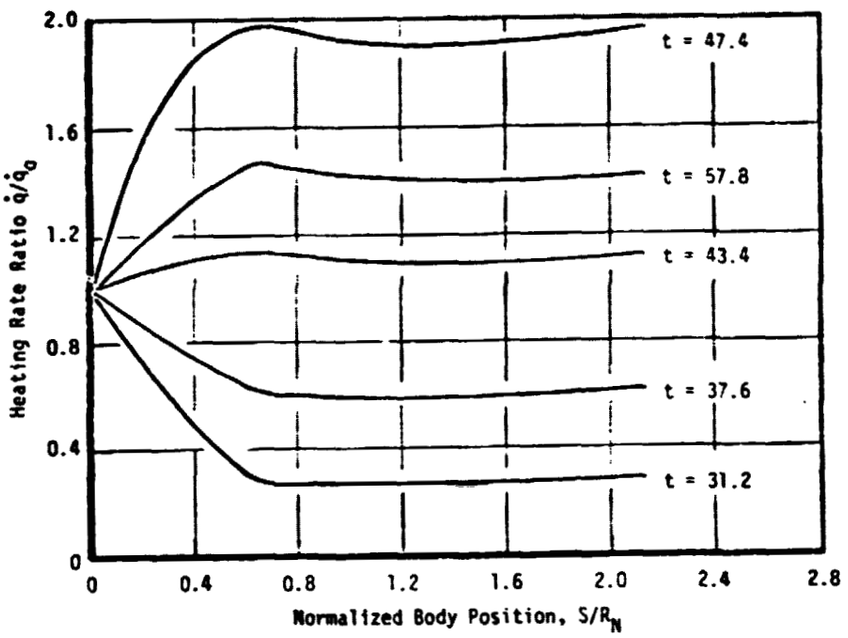

FIGURE 7

ENVIRONMENT DISTRIBUTIONS ON THE FORWARD HEAT SHIELD OF A JOVIAN ENTRY PROBE

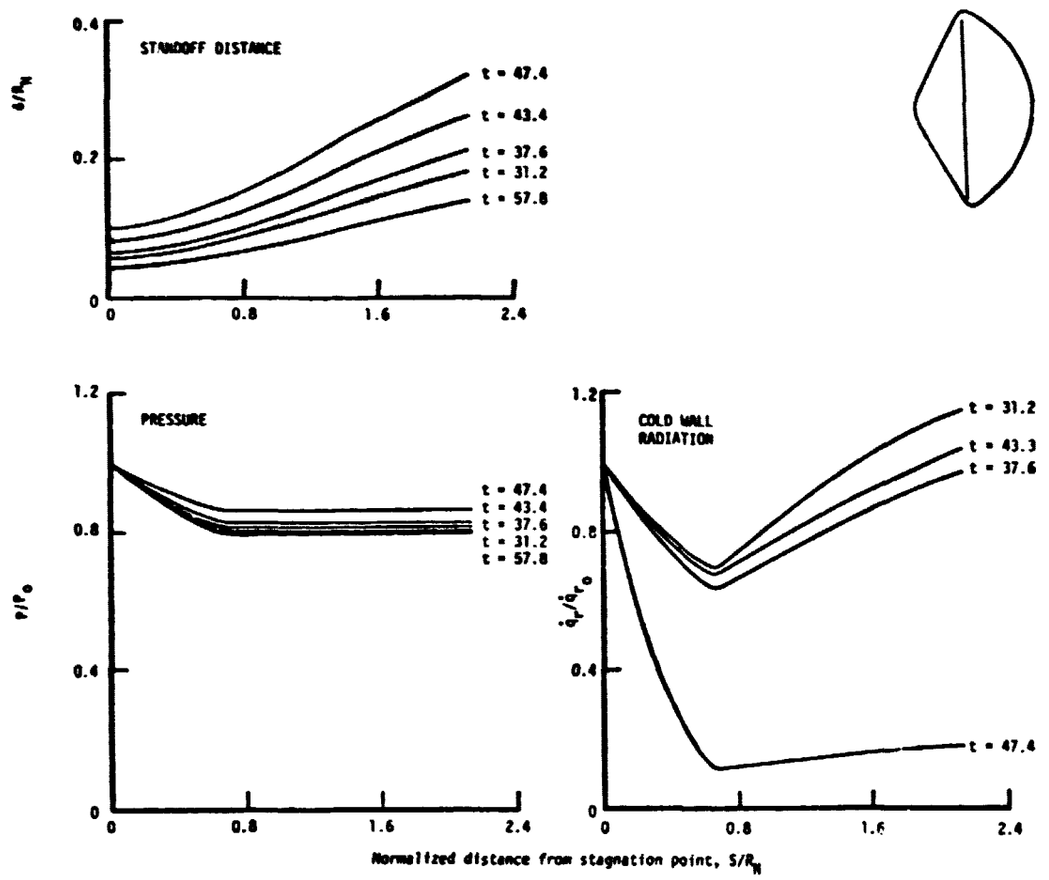

FIGURE 8

HEATING REDUCTION DUE TO BLOWING (JOVIAN ENTRY)

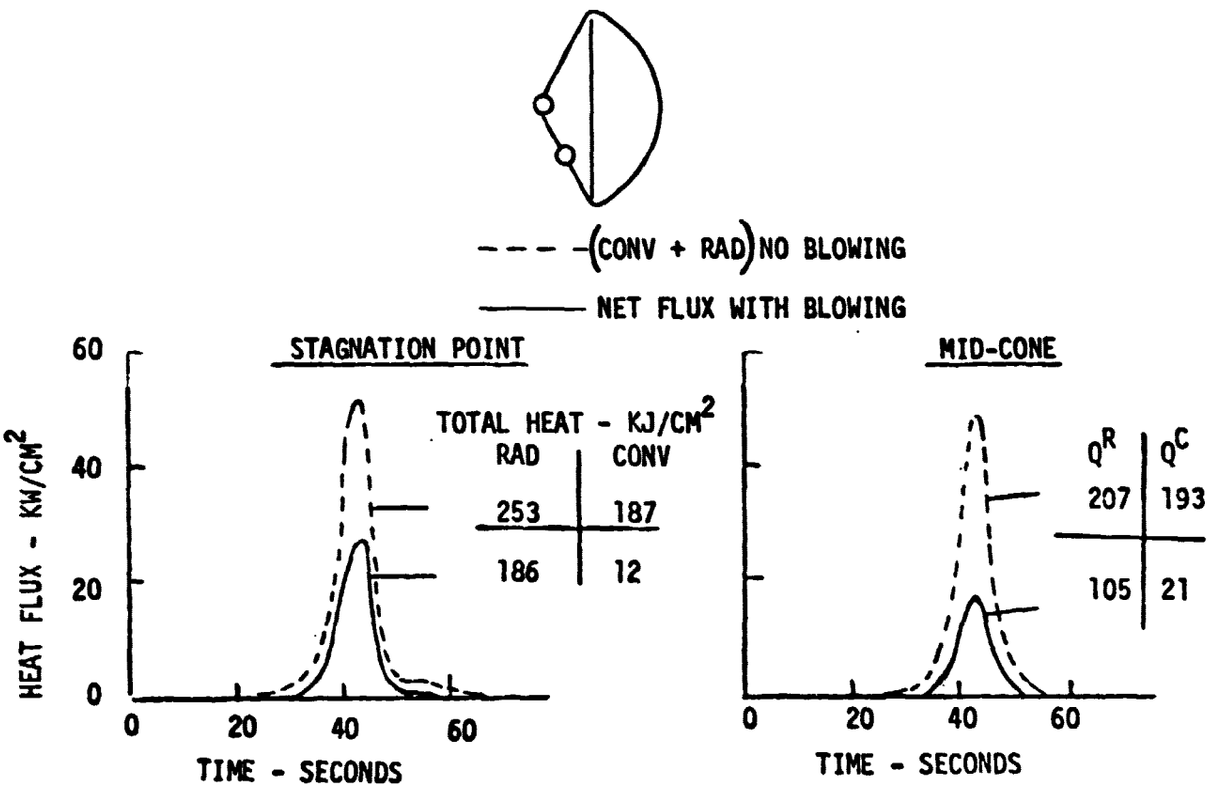

FIGURE 9

products. At the stagnation point the combined incident heat flux is halved and on the cone it is reduced by 68%. When blowing is accounted for, convective contributes only 6% of the total heat at the stagnation point and 17% on the cone.

The selection of entry angle and atmosphere model are of particular interest because of their uncertainties. The initial entry angle corresponds to a shallow entry mission nominally targeted for a relative angle of -9.5 degrees which has a typical uncertainty of $\pm$1.5 degrees. Applying this uncertainty results in a worst case condition of -11 degrees. This small uncertainty allows targeting for shallow entry and reflects the accurate knowledge of Jupiter ephemeris and physical data obtained from recent Pioneer missions.

The effect of entry angle, atmosphere model and ballistic coefficient variations on peak radiative flux, convective flux and pressure level are shown in Figures 10, 11 and 12. Atmospheric composition uncertainties were accounted for by parametrically considering the cool, nominal and warm models described in Reference 6.

JUPITER RADIATIVE FLUX ENVIRONMENT

- o V_{REL} = 47 km/sec
- o ALT = 450 km
- o R_N = .22m
- o R_N/R_B = .50
- o STAGNATION POINT
- o NON BLOWING

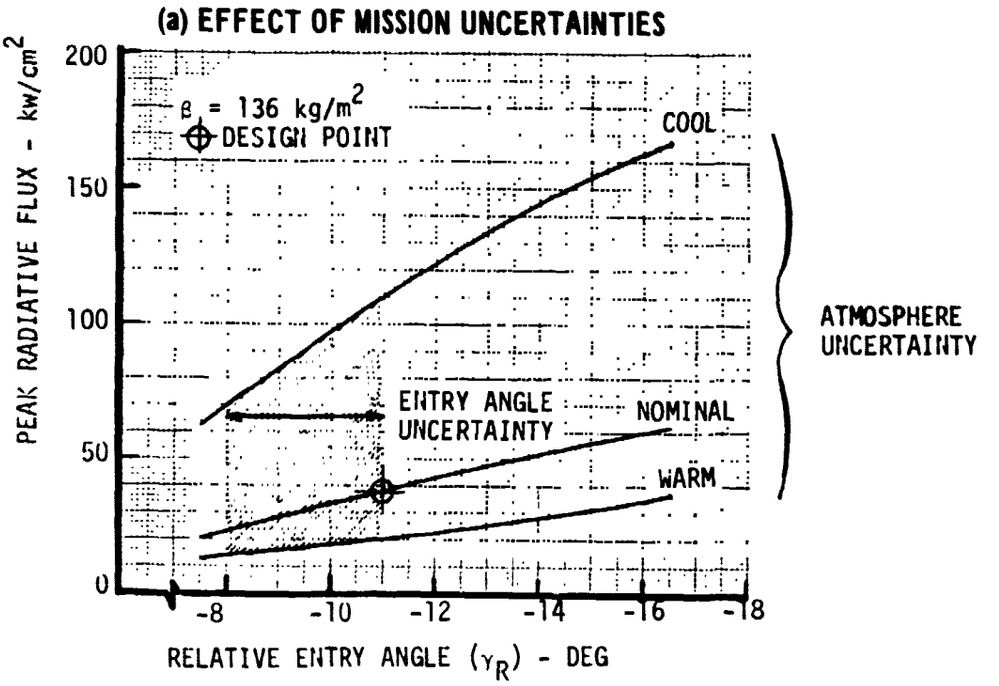

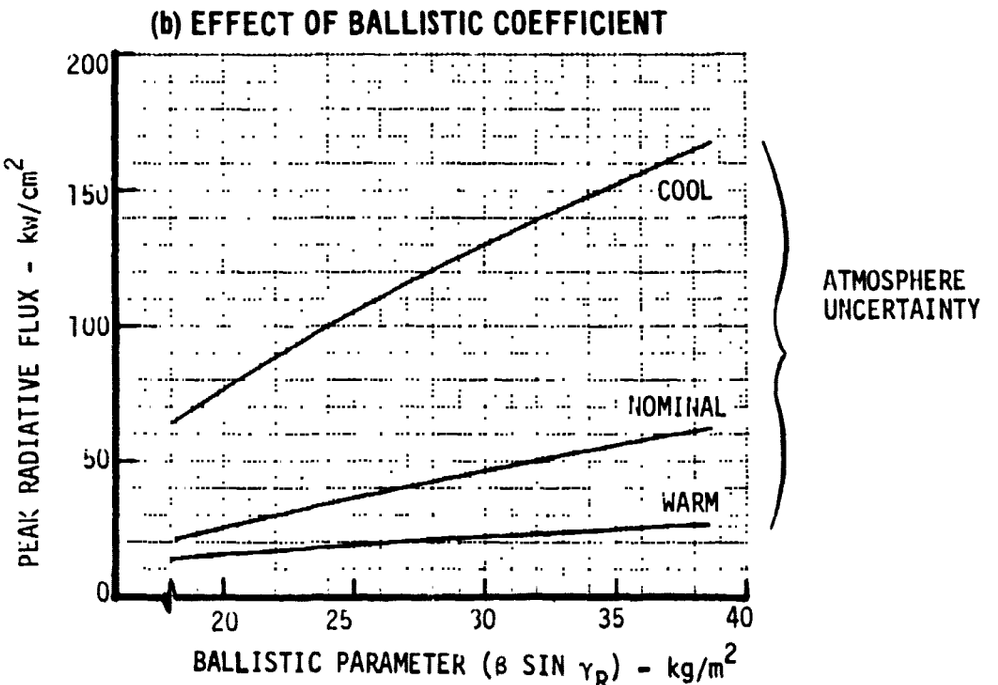

FIGURE 10

JUPITER CONVECTIVE FLUX ENVIRONMENT

- o V_{REL} = 47 km/sec
- o ALT = 450 km
- o R_N = .22 m
- o R_N/R_E = .50
- o STAGNATION POINT
- o NON BLOWING

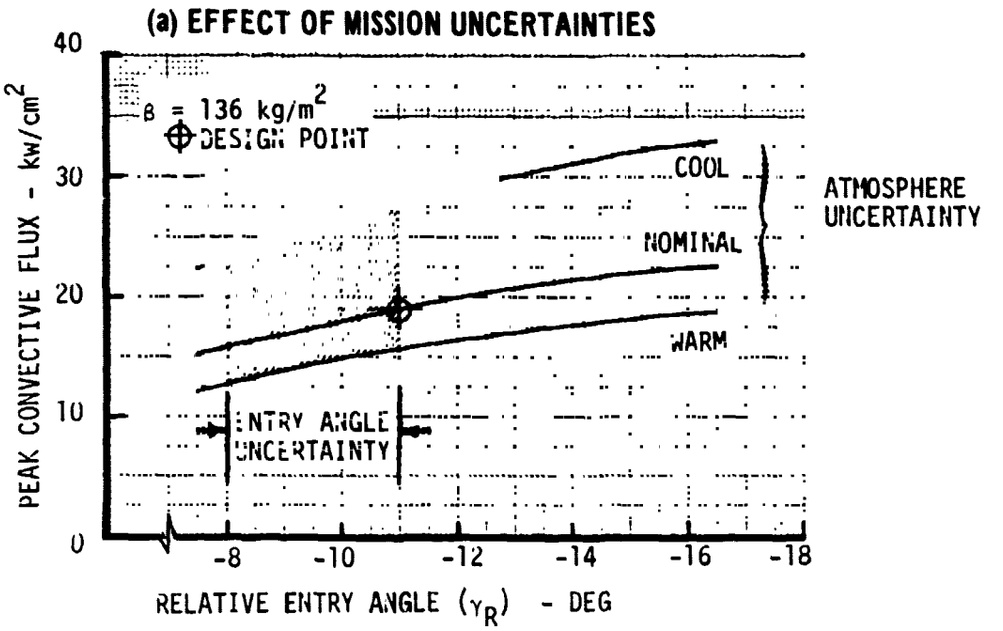

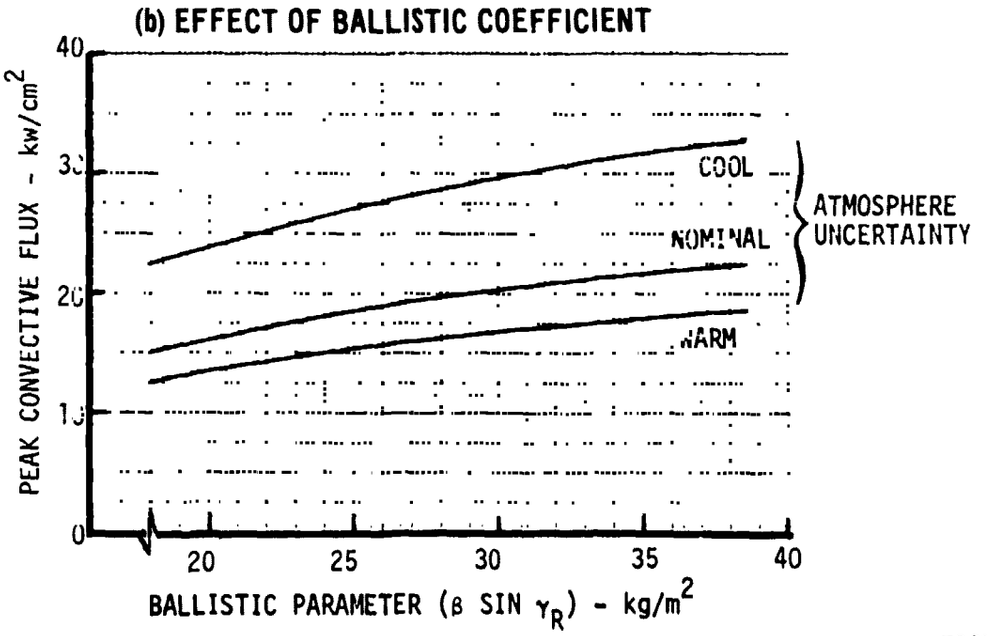

FIGURE 11

JUPITER PRESSURE ENVIRONMENT

- o V_{REL} = 47 km/sec
- o ALT = 450 km
- o R_N = .22m
- o R_N/R_B = .50
- o STAGNATION POINT
- o NON BLOWING

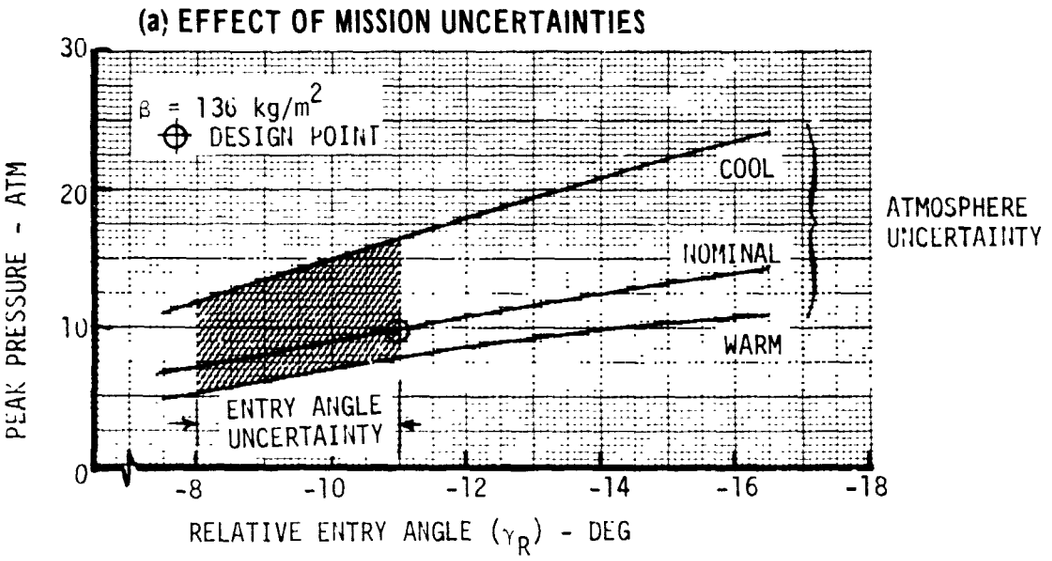

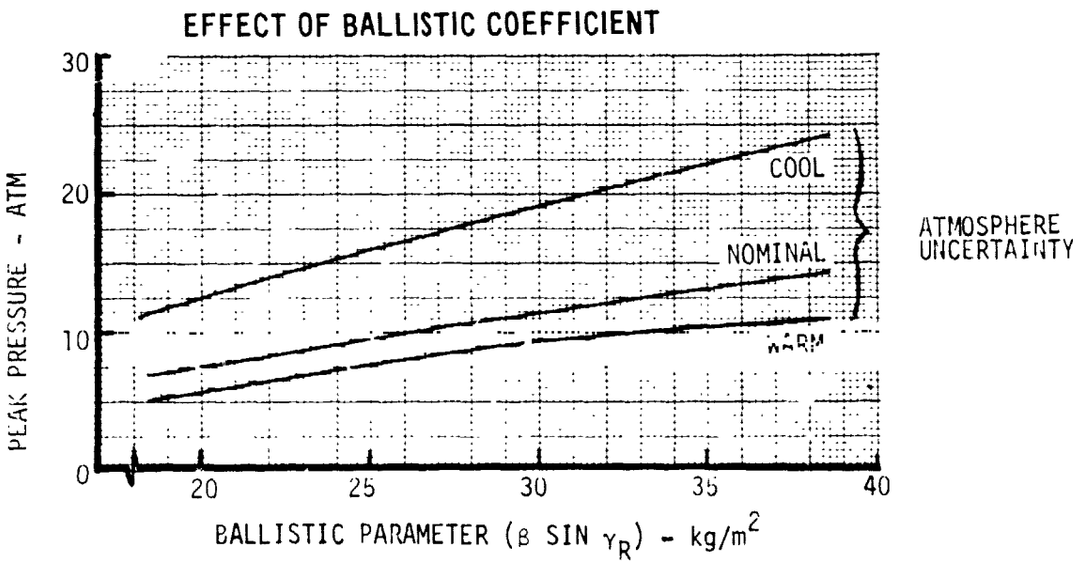

FIGURE 12

	Percent by Volume		Upper Atmosphere Temperature
	H_2	He	
Cool	68%	31%	110°K
Nominal	86%	13%	140°K
Warm	94%	6%	Decreases from 500°K to 120°K

The nominal model was assumed to establish the maximum design condition. Ordinarily a cool atmosphere would be used since it results in a more severe environment. However, Pioneer II flight data indicates that the cool model is no longer valid and that the nominal atmosphere as currently defined represents a realistic worst case. The uncertainties in entry angle (-8 to -11 degrees) increases the radiative heating by 58% to 38 kw/cm^2. The Jovian radiative heating is not as sensitive to changes in ballistic coefficient, a 10% change in β results in a 8% change in radiative flux. The 3 degree uncertainty in entry angle accounts for a 19% increase in convective heating, while a 10% change in β results in a 5% change in convective heating. The 3 degree uncertainty in entry angle causes the stagnation pressure to increase by 43% and a 10% increase in β causes a 10% change in pressure. These senstivities were factored into a maximum environment assessment. In summary, the maximum environments selected for simulation of a Jovian entry (including uncertainty effects) are:

Peak radiative heating	- 38 kw/cm^2
Peak convective heating	- 19 kw/cm^2
Total heat load (radiative plus convective)	- 440 KJ/cm^2
Heat pulse duration	- 14 sec
Peak pressure	- 10 atmosphere
Peak deceleration load	- 300 "g"

Jupiter entry produces the most severe heating environment of any planet considered. This is primarily due to a very high entry velocity (47 km/sec) which is a fundamental result of Jupiters massiveness and hence very high gravitational field. Additional factors include a steep atmospheric density gradient (large inverse scale height) induced by the high gravity and a high vehicle ballistic coefficient resulting from the large mass of a thick heat shield. However, the peak stagnation pressure and "g" loads are relatively moderate. This is a result of the rather shallow initial entry angle.

Saturn Entry Environments - Physical characteristics of a Saturn entry probe were selected to be very similar to the Jovian probe. Nose radius equals 22.2 cm

for a symmetrical sphere-cone vehicle with an 89 cm diameter based diameter. Environments are based on References 3 and 10 Saturn/Uranus studies where the initial entry velocity (relative) was 32 km/sec at an altitude of 600 km. The compiled data also reflect an uncertainty in the knowledge of Saturn location and physical nature. Unlike Jupiter, Saturn ephemeris and physical properties have not yet been investigated by flyby missions. The earliest opportunity for such refinement will be the Pioneer II flyby in 1979. As a result, large uncertainties in entry angle (±10 degrees) contributes to a rather steep (-48 degrees) design entry. The influence of atmosphere model and ballistic coefficient as well as entry angle on peak radiative heating, convective heating and pressure level are contained in Figures 13, 14 and 15. The atmosphere models are based on Reference 8. Additional models (Reference 9) have been developed and mission analyses need to be performed for this new model. For the purposes of determining a set of design environments, the most conservative atmosphere model (cool) was selected. The maximum environments selected for simulation of entry into Saturn are as follows and includes uncertainty effects.

Peak radiative heating	- 20.5 kw/cm^2
Peak convective heating	- 12.5 kw/cm^2
Total heat load (Radiative plus convective)	- 74 kJ/cm^2
Heat pulse duration	- 10 sec
Peak pressure	- 18 atm
Peak deceleration load	- 700 "g"

Saturn entry produces the highest stagnation pressures and deceleration loads of any planet considered. This is a direct result of selecting a steep entry into a cool atmosphere for purposes of design. The heating environment, however, is less severe than that encountered during a shallow Jupiter entry. This is primarily due to a lower entry velocity (32 km/sec).

Uranus Entry Environment - At present, the Uranus entry environment is considered best described by assuming it the same as Saturn. Available data is insufficient for a separate Uranus presentation because of special problems involved in selecting an atmosphere model. The current cool atmosphere, which results in radiative heating of Jupiter proportions, is now considered invalid because of excessively high helium content relative to solar abundance. Use of the nominal atmosphere model eliminates the radiative component altogether. Hence, until more accepted atmosphere models become available and used in entry heating analysis, the Saturn environment is considered the best available approximation.

SATURN RADIATIVE ENVIRONMENT

- o V_{REL} = 32.0 km/sec
- o ALT = 600 km
- o R_N = .22m
- o R_N/R_B = .5
- o STAGNATION POINT
- o NON BLOWING

(a) EFFECT OF MISSION UNCERTAINTIES

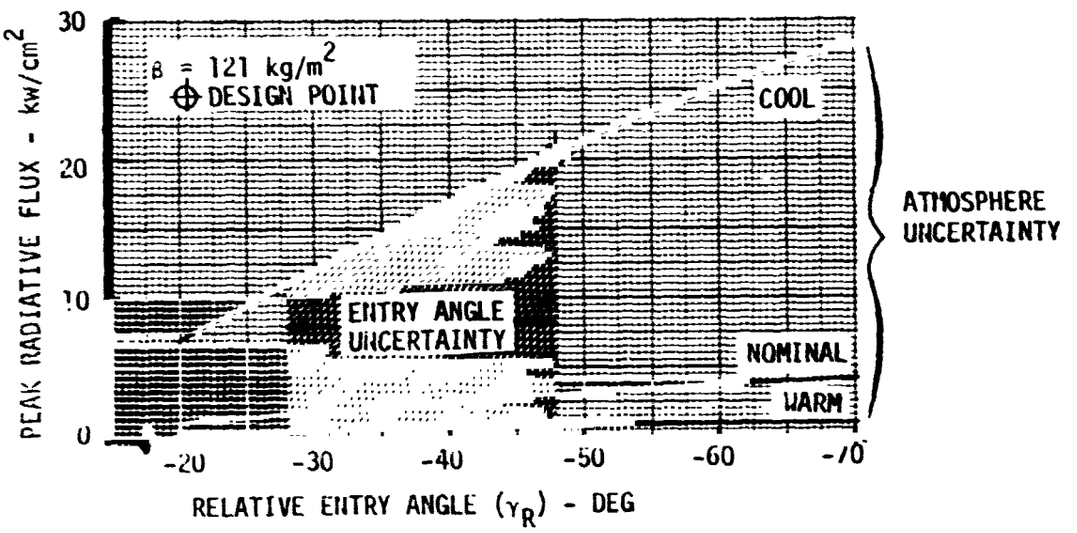

(b) EFFECT OF BALLISTIC COEFFICIENT

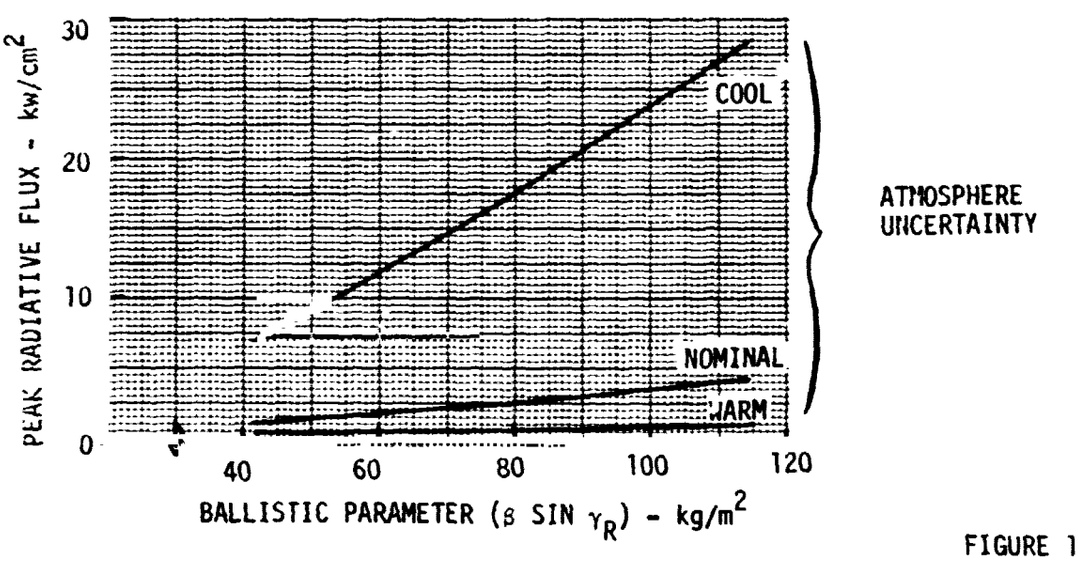

FIGURE 13

SATURN CONVECTIVE FLUX ENVIRONMENT

- o V_{REL} = 32.0 km/sec
- o ALT = 600 km
- o R_N = .22m
- o R_N/R_E = .5
- o STAGNATION POINT
- o NON BLOWING

(a) EFFECT OF MISSION UNCERTAINTIES

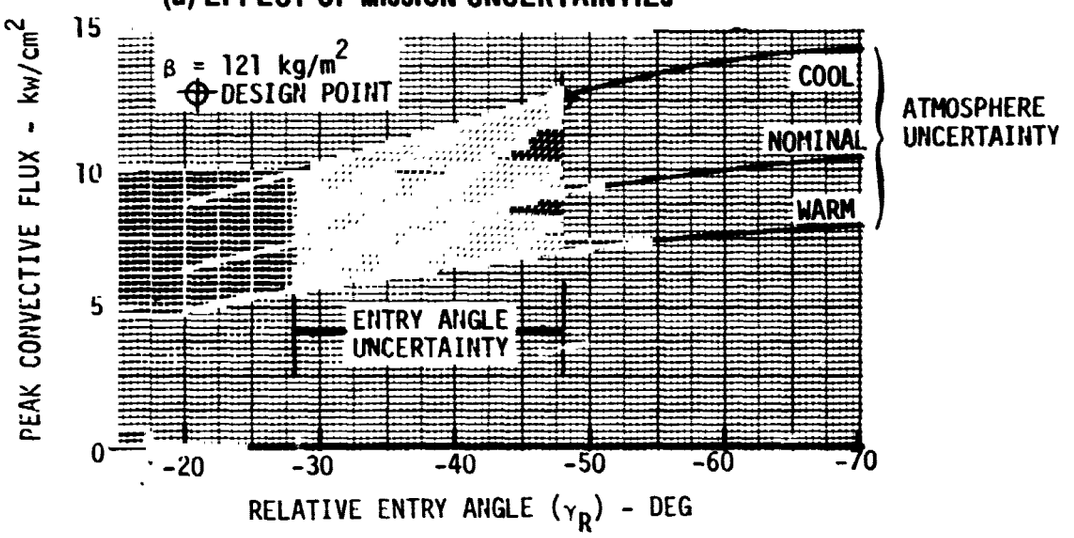

(b) EFFECT OF BALLISTIC COEFFICIENT

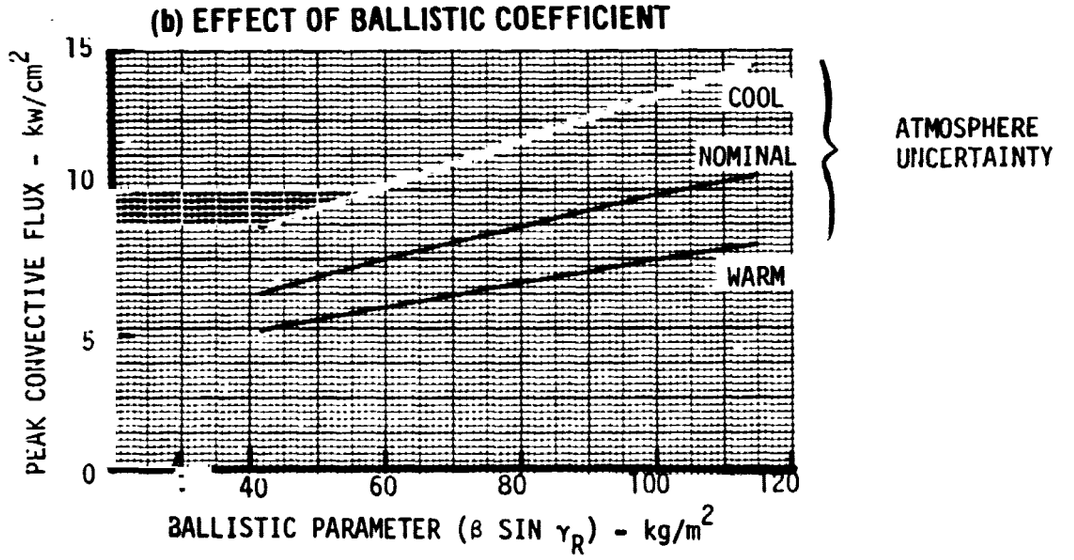

FIGURE 14

SATURN PRESSURE ENVIRONMENT

- o V_{REL} = 32.0 km/sec
- o ALT = 600 km
- o R_N = .22m
- o R_N/R_E = .5
- o STAGNATION POINT
- o NON BLOWING

(a) EFFECT OF MISSION UNCERTAINTIES

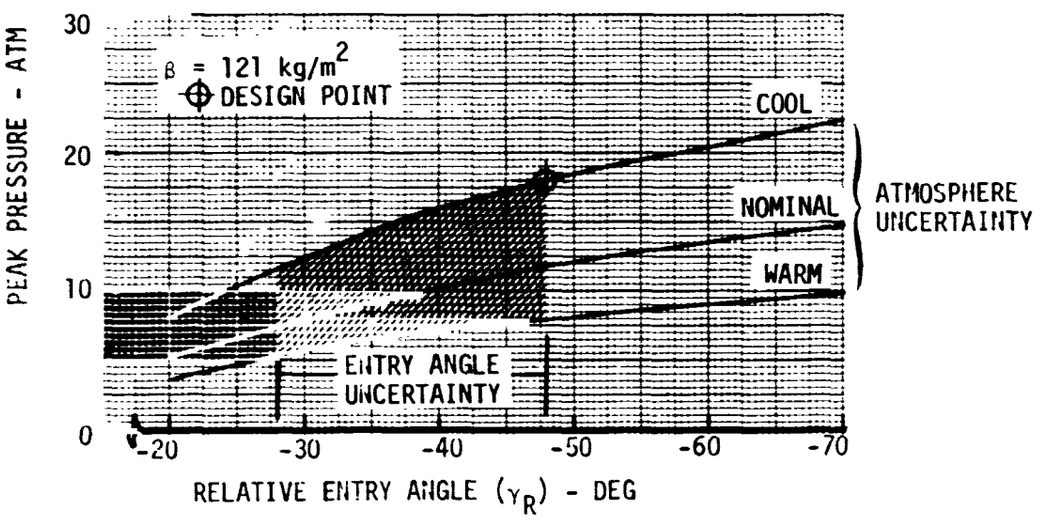

(b) EFFECT OF BALLISTIC COEFFICIENT

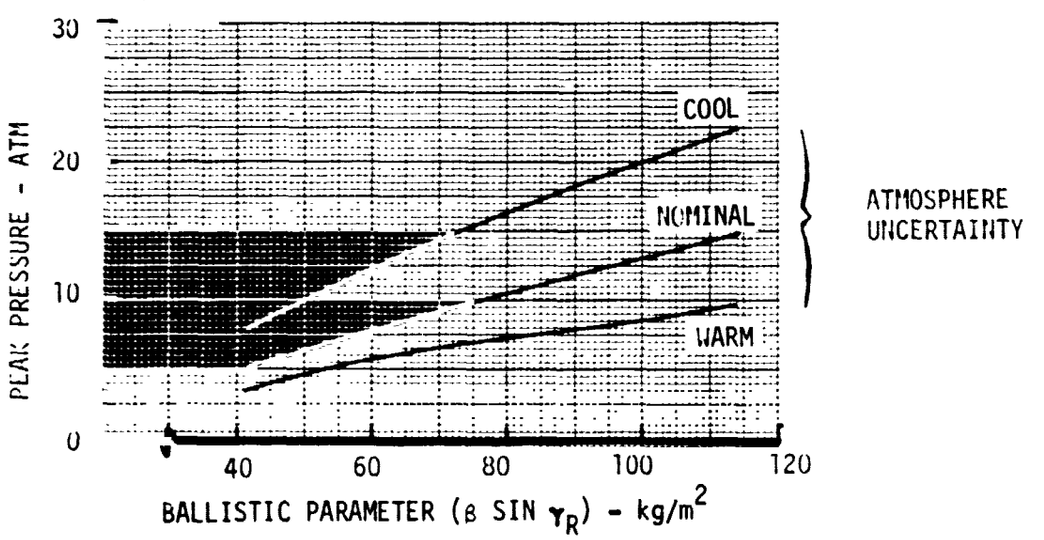

FIGURE 15

3.2 Jovian Radiative Heating Influence Factors - Prediction of the radiative heating was performed with very sophisticated computational codes that have been developed in the past few years specifically for outer planet entries. The presence of hydrogen-rich outer planet atmospheres simplifies the continuum and spectral calculations, since the radiation characteristics of the simple hydrogen atom are well known, and have been substantiated by solar spectroscopic experiments. Nominal maximum conditions were selected for this detailed analysis to show the effect of an adiabatic shock layer, a cooled shock layer and a shock layer with carbon injection. The majority of analyses were performed for:

V_∞ (free stream velocity) = 39.09 km/sec
ρ_∞ (free stream density) = 0.00039 kg/m^3
R_N (nose radius) = 22.22 cm
} Condition II (Reference 4)

A stagnation temperature of 15974°K and a stagnation pressure of 5.32 atm resulted with a shock standoff distance of 1.54 cm. For the adiabatic shock condition the entire zone between the shock and the heat shield would then be at 15974°K and produce a total radiative heating of 49 kW/cm^2 (25 kW/cm^2 due to continuum and 24 kW/cm due to line radiation). It should be remembered that this heating is significantly higher than what would actually be encountered. The temperature distribution across the shock layer and the species concentrations significantly affects the incident heat.

Ablative heat shields are principally composed of carbonaceous material and the injection of ablation products into the shock layer can increase the shock standoff distance by 15%. Nominal temperature and carbon concentration distributions across the shock layer for a Jovian entry as developed in Reference 4 (reproduced in Figure 16) and used as a basis for investigating radiant heating patterns. The sensitivity of radiant heating to shock standoff distance and type of shock layer is contained in Figure 17. As can be noted the adiabatic shock layer heating is much higher than the cooled shock layer (no mass injection) which is in turn higher than the cooled shock layer with mass injection. The incident flux is roughly composed of equal parts of continuum and line radiation. In this comparison the edge and wall temperatures, along with pressure, were held the same. However, the resulting shock layer temperature distributions are changed slightly due to a thicker shock layer for the injection case. Carbon injection drops the incident flux (13.81 kW/cm^2) to 56% of the nominal cooled shock value. As can also be noted in the figure the sensitivity in radiative heating to changes in standoff dis-

TEMPERATURE AND INJECTANT PROFILES FOR JOVIAN SHOCK LAYER

RADICAL/69 COOLED SHOCK LAYER

T_S = 15947°K
T_W = 4564°K
P_S = 5.32 ATM

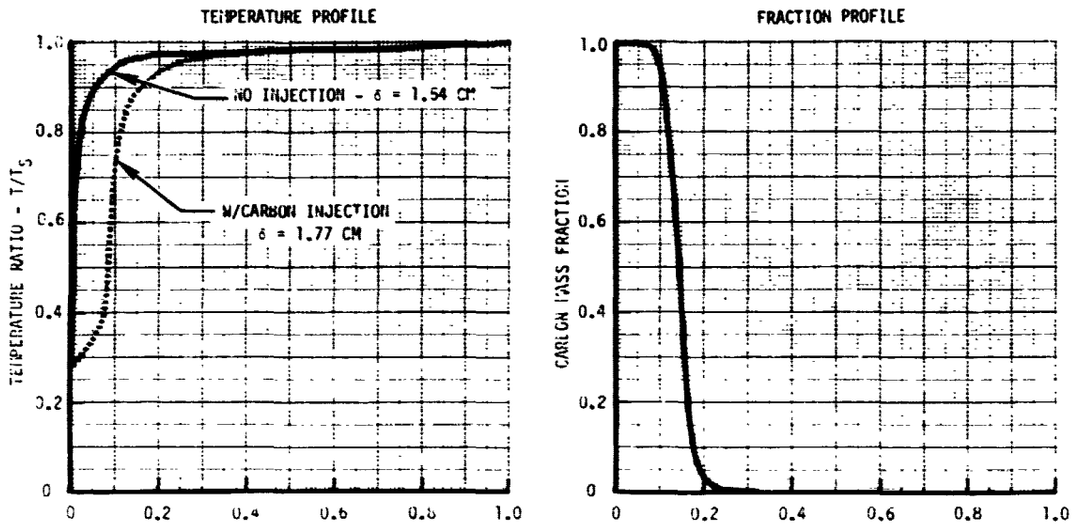

FIGURE 16

SENSITIVITY OF JUPITER RADIATIVE HEATING TO SHOCK LAYER THICKNESS AND CARBON INJECTION

T_S = 15947°K
T_W = 4564°K
P_S = 5.32 ATM

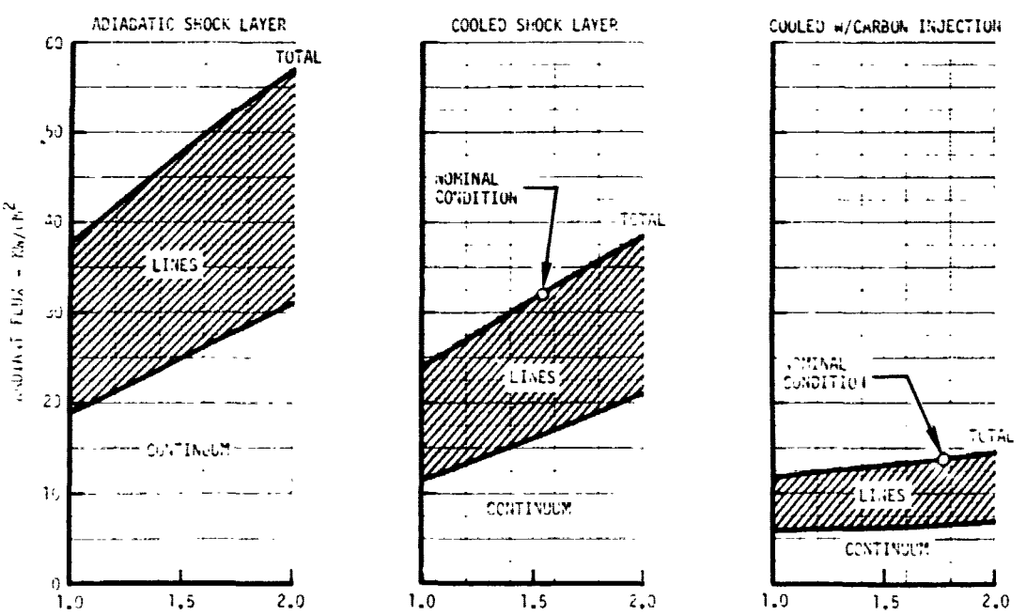

FIGURE 17

tance is much less for carbon injection than either the adiabatic or cooled case. The sensitivities of radiative heating to variations in flow field conditions will be further quantitized in following sections. The spectral distribution for the cases without and with carbon injection are shown respectively in Figures 18 and 19. Many similar spectral distribution curves were prepared to generate the previous figures. The presence of carbon species essentially eliminates the high energy line photon energy transitions and much of the lower contributing energy bands.

Variations in shock pressure for a given temperature distribution alters the chemical equilibrium composition and hence the radiant heating expected for a Jupiter entry. The sensitivity of pressure level on radiant flux is shown in Figure 20. As the pressure in the shock layer is increased a larger portion of the radiant flux is due to the continuum radiation produced by electron reaching ionization energy from lower energy levels as compared to line transition which accounts for electrons going from one energy level to a level which is less than the ionization level.

The spectral distribution for the Jupiter entry with an adiabatic shock layer at slightly different conditions than presented previously is shown in Figure 21. Note the increase in energy in the various wave bands as compared to the cooled and injection cases. Superimposed is a reflectance curve for hyperpure silica, one of the candidate heat shield materials for an outer planet probe. The reflectance approaches zero between 8 and 10 eV, which is the threshold of the vacuum ultraviolet range of the spectrum. Consequently, most of the radiant energy below vacuum ultraviolet will be reflected.

3.3 Heat Accommodation of Heat Shield Materials for Jovian Entry - Both carbonaceous and hyperpure silica materials are viable heat shield materials for a probe entering the Jovian atmosphere. The carbonaceous heat shield functions as a high performance ablator but it has a lower reflectance than the silica material and hence would be required to dissipate more radiant heat flux. Detailed computer investigations were performed for a representative high speed flight condition. Results of the investigation to compare the effectiveness of two heat shield materials in a Jupiter environment are shown in Figure 22. Reflectances of both a silica heat shield and a carbon heat shield were used in the analysis. The analysis was performed for conditions where there was mass injection as well as for a clean hydrogen/helium atmosphere. Temperature profiles (with and without injectant) and the injectant mass fraction profile (Figure 16) for a typical Jupiter entry shock layer were used in the comparison.

SPECTRAL DISTRIBUTION FROM A COOLED SHOCK LAYER (NOMINAL JUPITER ENTRY)

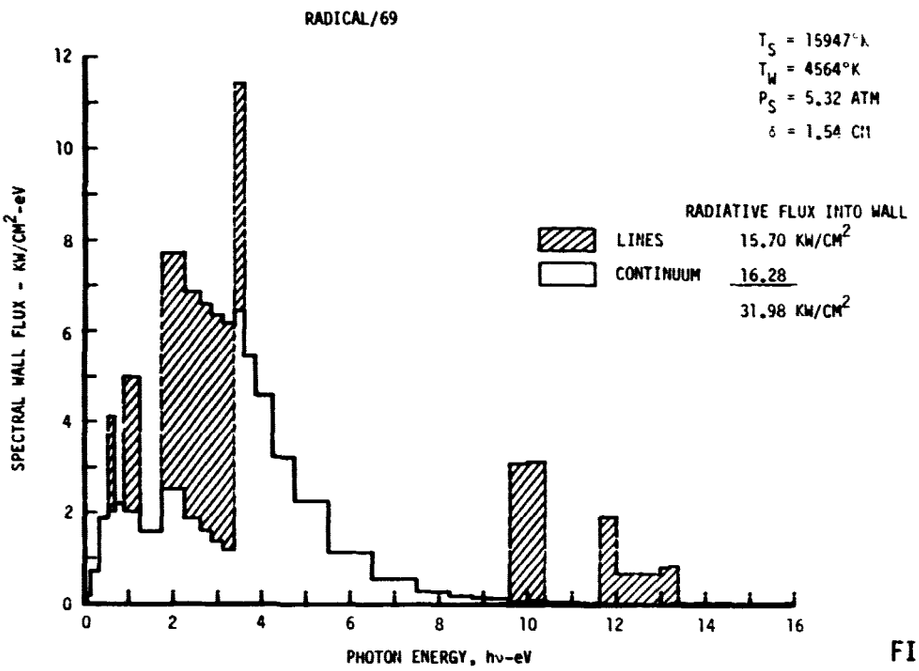

FIGURE 18

SPECTRAL DESTRIBUTION FOR NOMINAL JUPITER ENTRY WITH CARBON INJECTION

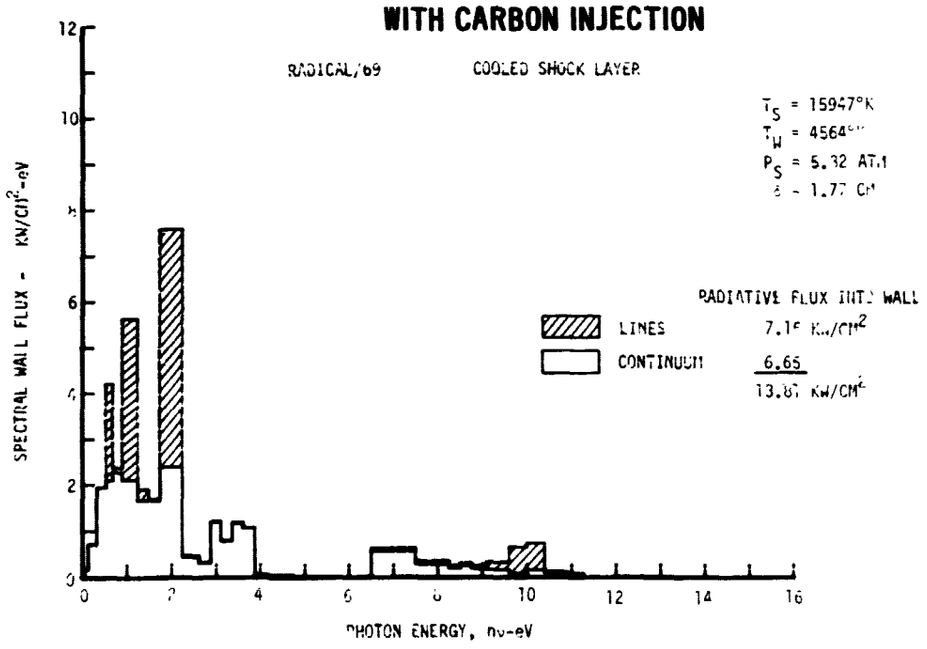

FIGURE 19

EFFECT OF PRESSURE ON JUPITER RADIATIVE HEATING

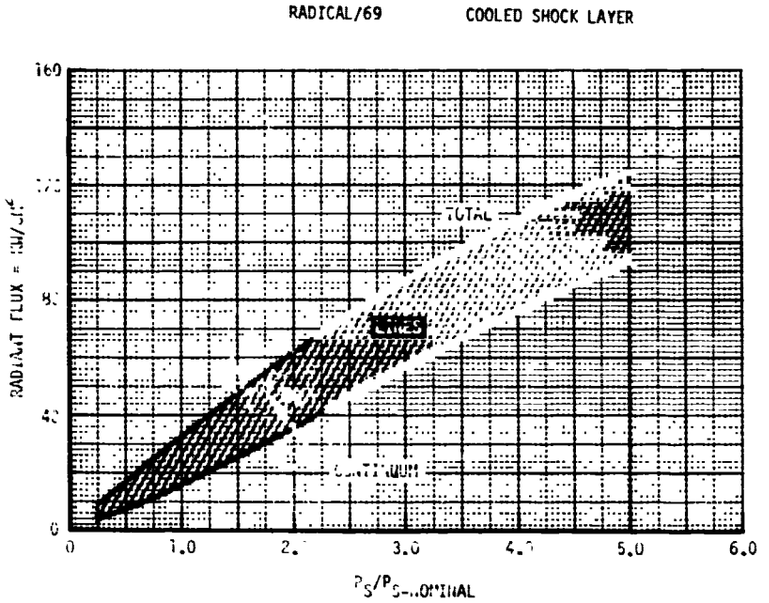

T_S = 15947°K
T_W = 4564°K
P_S = 5.32 ATM
δ = 1.54 CM

FIGURE 20

SPECTRAL HEATING FROM AN ADIABATIC SHOCK LAYER (NOMINAL JUPITER ENTRY)

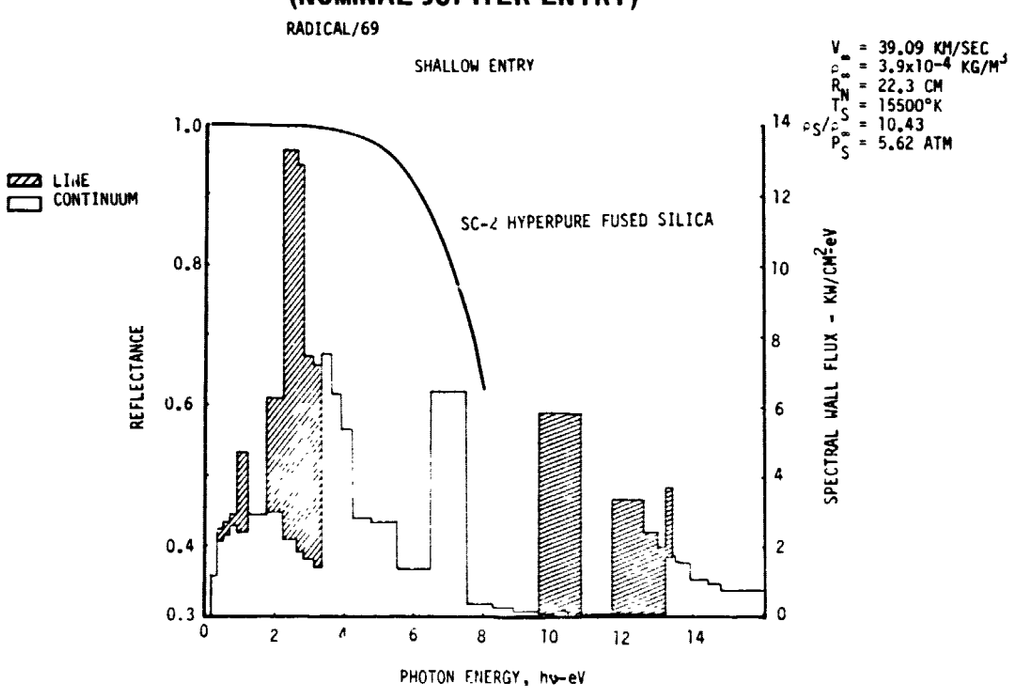

V_∞ = 39.09 KM/SEC
ρ_∞ = 3.9x10⁻⁴ KG/M³
R_N = 22.3 CM
T_S = 15500°K
P_S/P_∞ = 10.43
P_S = 5.62 ATM

FIGURE 21

RADIANT HEATING COMPARISON OF SEVERAL INJECTANTS IN JUPITER ENTRY SHOCK LAYER

ATMOSPHERIC COMPOSITION (WEIGHT FRACTION)
HELIUM (He) 0.21
HYDROGEN (H_2) 0.79

T_S = 15947°K

P_S = 5.32 ATM

	FLUX TOWARD WALL (KW/CM^2)			FLUX AWAY FROM WALL (KW/CM^2)			NET FLUX TO ABLATOR (KW/CM^2)
	CONTINUUM	LINES	TOTAL	CONTINUUM	LINES	TOTAL	
NO INJECTANT	16.280	15.700	31.980				
SILICON (Si) INJECTION SILICA ABSORPTANCE T_W = 3450°K	13.577	8.275	21.853	13.210	8.267	21.477	0.376
SILICON (Si) INJECTION ABSORPTANCE = 0.5 T_W = 3450°K	13.577	8.275	21.853	7.191	4.141	11.332	10.521
SILICA (SiO_2) INJECTION SILICA ABSORPTANCE T_W = 3450°K	13.182	11.070	24.252	12.692	10.586	23.279	0.973
CARBON (C) INJECTION ABSORPTANCE = 0.8 T_W = 4564°K	6.650	7.160	13.810			4.730	9.080

FIGURE 22

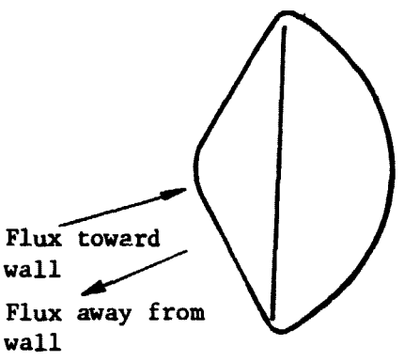

Radiant flux values are compared in Figure 22. It can be seen that the addition of ablation material to the shock layer reduces the radiant flux directed toward the wall, with carbon having the greatest reduction (about 46%). The silica injection was considered in two forms - first as silicon (Si), and then as silica (SiO_2). The flux directed away from the wall is a function of the wall spectral absorptance (α_i) or emittance (ϵ_i) and the temperature assumed for black body o radiant. The absorptance was calculated assuming no radiant transmission through the wall material and the customary relationship involving reflectance (ρ_i):

$$\alpha_i = \epsilon_i = 1 - \rho_i$$

Analysis were performed for two absorptances and two wall temperatures. The spectral reflectance for silica in Figure 23 was used as one of the conditions for Si injection. An additional condition considered a constant value of absorptance equal to 0.5. Both were used with two wall temperatures for the black body radiation 0°K and 4564°K. Figure 24 gives a comparison of the spectral flux distributions between the flux incident on a silica heat shield and that reflected. Note the shift in the line and continuum spectral bands.

The last column of Figure 22 compares the net radiative flux which the ablator must accommodate. Although the carbon reduces the heat flux incident on the wall more than does the silica, the nature of the reflective surface of the silica makes it a better heat shield material on a net flux basis (1.68 kw/cm^2 vs 9.08 kw/cm^2). Testing of the silica and carbonaceous materials should be performed to substantiate these values.

REFLECTANCE OF HYPERPURE SILICA

REFERENCE:-
MDC E1139
OCTOBER 1974

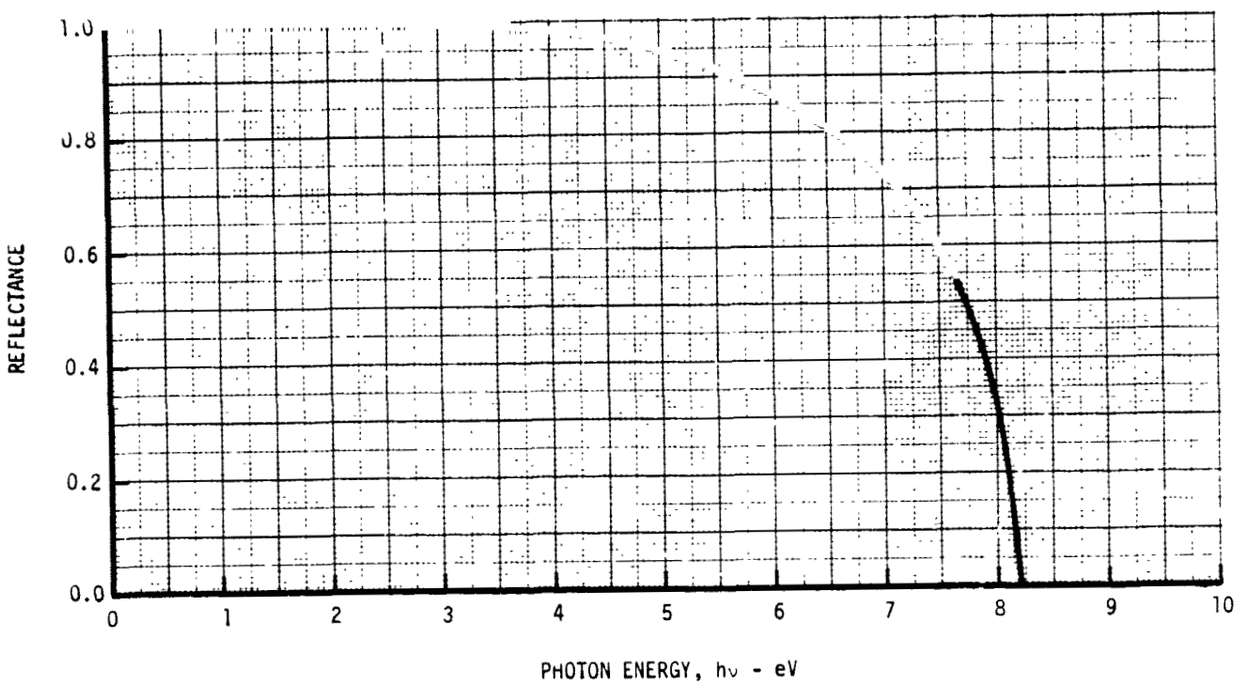

FIGURE 23

SILICA HEAT SHIELD SPECTRAL DISTRIBUTIONS OF INCOMING AND REFLECTED FLUXES (JUPITER ENTRY)

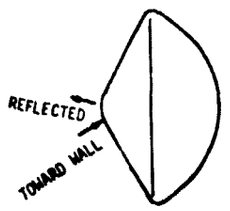

TOWARD WALL

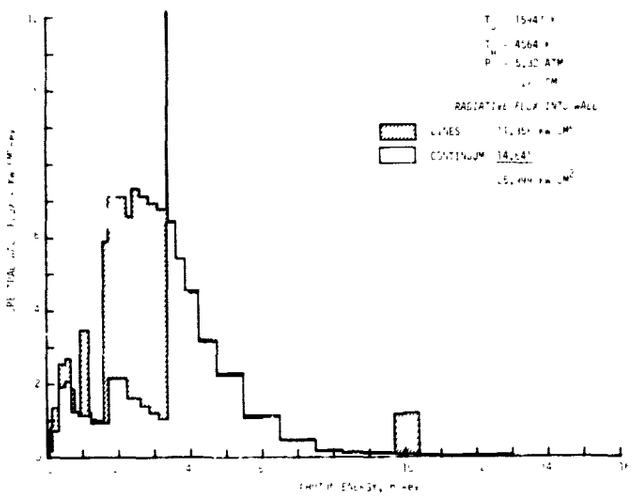

REFLECTED

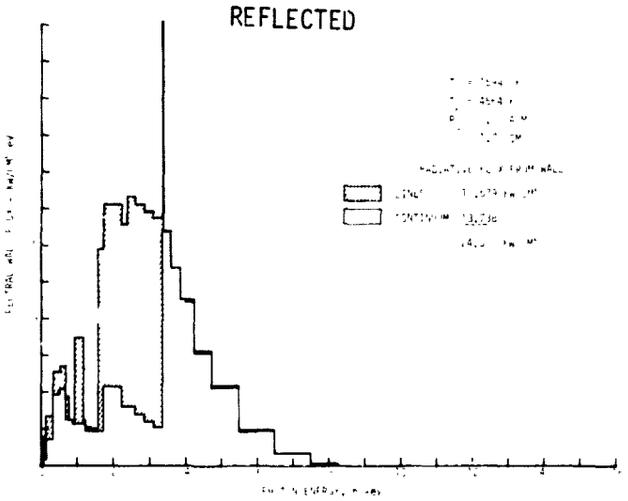

FIGURE 24

3.4 Carbon Phenolic Heat Shield Sizing (Jovian Mission) - Detailed analysis of heat shield requirements have been made by Jovian entry probe designers. The effects of mechanical erosion, thermochemical recession and the heat shield insulation were included in the analysis to limit the bondline to 533°K. Current designs of a carbon phenolic heat shield relay on maintaining the adhesive integrity between carbon phenolic layer and the honeycomb support structure. Adhesives used for this purpose are limited to 533°K. As can be seen from Figure 25 approximately 7.2 cm of carbon phenolic are required for the stagnation point ($S/R_N = 0$) and 5.0 cm on the cone.

CARBON PHENOLIC HEAT SHIELD REQUIREMENTS (JUPITER ENTRY)

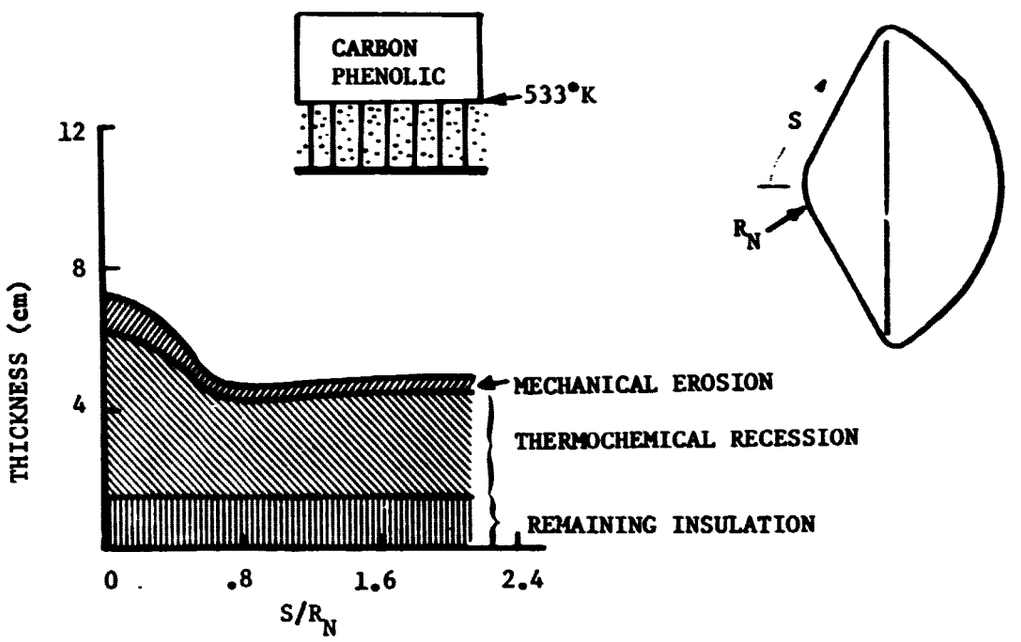

FIGURE 25

4.0 EARTH ENTRY ENVIRONMENT SIMULATION CAPABILITY

One of the prime objectives of this study centers on obtaining environments during a high speed entry on earth which are similar to those predicted for an outer planet probe. Moreover it is important to understand the characteristics of the environments, the sensitivity to changes in entry conditions, flow field conditions, and heat shield design. Because of the intense radiative heating predicted for Jovian entry, the understanding of this parameter during an earth entry is necessary. To these ends maps of entry environments, sensitivity studies, shock layer analysis and heat shield performance evaluations were performed for high speed earth entry flights.

4.1 Non-Blowing Earth Entry Environments - The environments that can be produced by high speed entry into the earth's atmosphere are presented in this section. Data are shown for the range of initial entry conditions generally attainable by Shuttle launched boosters. This information identifies the capability of earth flights to simulate planetary entry environment and the associated initial entry conditions.

The environmental parameters shown are intentionally the same as those used previously to describe the planetary entry environment. Stagnation point heating characteristics are emphasized but do not include the effect of re-radiation or boundary layer mass injection. These effects will be assessed in later sections.

The range of initial earth entry velocity needed to simulate planetary heating is much lower than actual planetary mission entry velocities. This is due to differences in atmosphere composition. The outer planet atmospheres are composed primarily of hydrogen-helium mixtures at about the solar abundance ratio, whereas the earth atmosphere is nearly 21 percent oxygen and 79 percent nitrogen. From basic thermodynamics it is known that the low molecular weight gases, hydrogen and helium, have a much higher heat capacity than air. Thus simulation of similar shock layer temperatures or heating rates in air require a much lower entry speed than that of planetary entries. The higher molecular weight of air also results in a steeper atmospheric density gradient which enhances simulation of the peak environment conditions but reduces the heating duration.

A 3 degree of freedom point mass trajectory computer program was used to compute earth entry trajectories. The earth model was a spherical rotating earth. All trajectories began at 121.92 km with the inertial velocity and flight path angle defined. In addition to computing altitude, velocity, flight path angle, latitude, longitude and heading as a function of reentry time, the program also

determined the trajectory conditions at peak stagnation point radiative heat flux, dynamic pressure, and deceleration. This was accomplished by automatic monitoring of these parameters as the trajectory was computed. Once a peak value was passed, the trajectory parameter immediately preceeding the peak were stored. Upon completion of a trajectory, smaller time step trajectory segments were computed about the peak values to provide a precise definition of the peak values. The dynamic pressure and decleration result from the solution to the equations of motion. The stagnation point convective heat flux (kw/cm^2) was determined by the following equation:

$$\dot{q}_c = 0.01464 \frac{\rho^{1/2} V^{3.15}}{R_N^{1/2}}$$

where ρ = atmospheric density (kg/m^2)

V = velocity (km/sec)

R_N = nose radius (meters)

This equation was evaluated at each point on the computed trajectory and integrated over the full trajectory to give the total convective heating at the stagnation point. The stagnation point radiative heat flux was determined from a table look-up of data for a cooled shock layer from Reference 11. These data provide stagnation point radiative heat flux as a function of altitude, nose radius, and velocity. A table look-up of radiative heat flux was performed at each point on the trajectory and the values integrated to give stagnation point total radiative heating.

4.1.1 Reference Vehicle Environment - Detailed entry environment descriptions are presented for a cone/hemisphere shared entry body having a ballistic coefficient (β) of 120 km/m^2 and a nose radius (R_N) of 22.2 cm. A single reference vehicle configuration was chosen to allow a full yet concise presentation of the various environment and entry conditions parameters. The selected configuration is typical of outer planet probes currently under study.

Figures 26 through 28 are computer summaries that detail the peak stagnation point values of radiative flux, convective flux and pressure/"g" loads. Data is presented as a function of initial entry conditions and describes the flight conditions at which the peak value of each environment parameter occurs.

Each is composed of 48 cases which are subdivided into 6 groups of 8 cases each. As shown in the second and third columns, each of the 6 groups correspond to a different entry velocity while the 8 cases within each group represent a different entry angle. Note that these initial entry conditions are given as inertial coordinates. This is done for ease of comparison with the booster capability information presented in Section 6.

CONDITIONS AT PEAK RADIATIVE HEAT FLUX FOR EARTH ENTRY OF A HIGH SPEED – LOW β(120 kg/m^2) VEHICLE

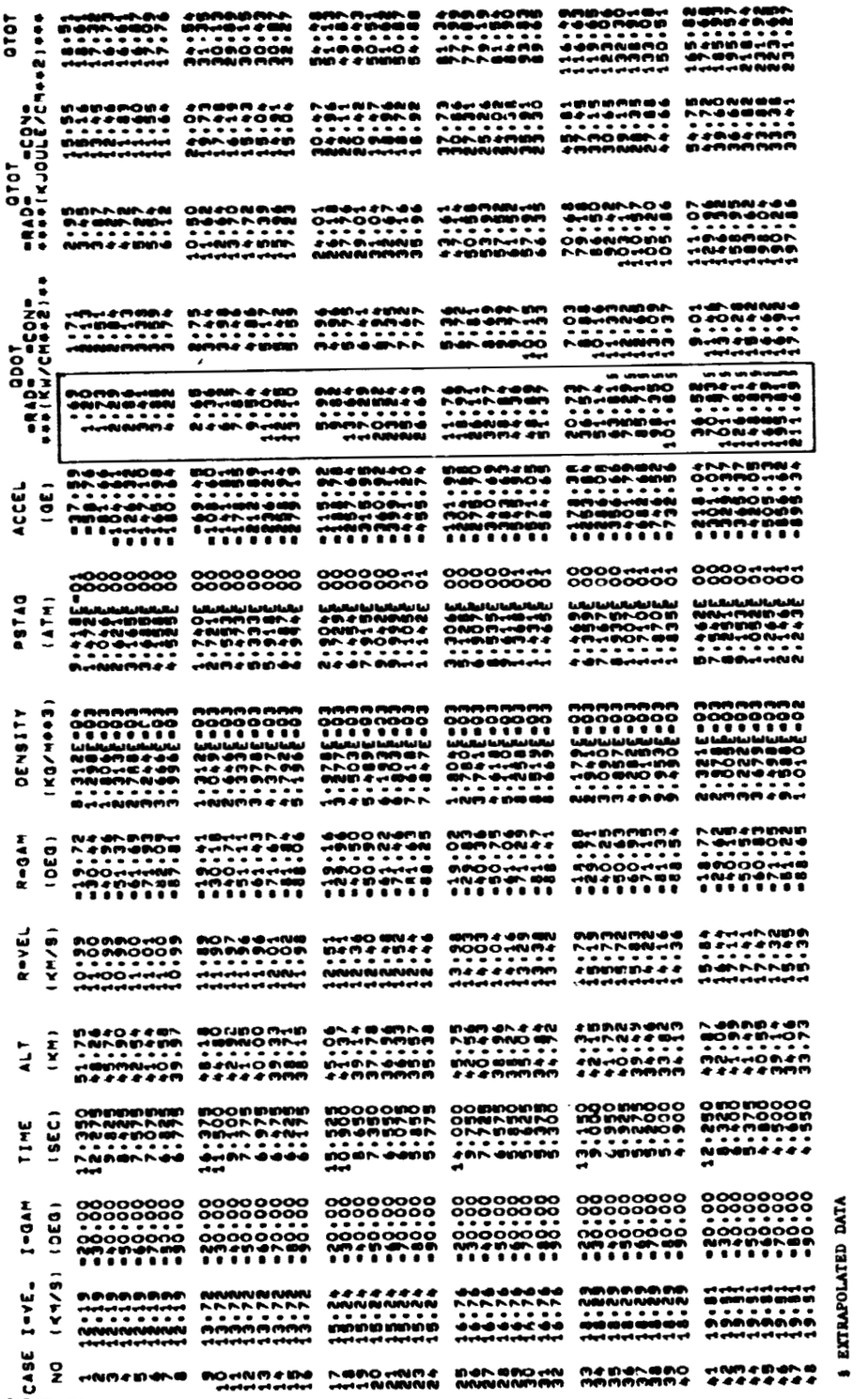

ORIGINAL PAGE IS
OF POOR QUALITY

FIGURE 26

CONDITIONS AT PEAK CONVECTIVE HEAT FLUX FOR EARTH ENTRY OF A HIGH SPEED – LOW β(120 kg/m^2) VEHICLE

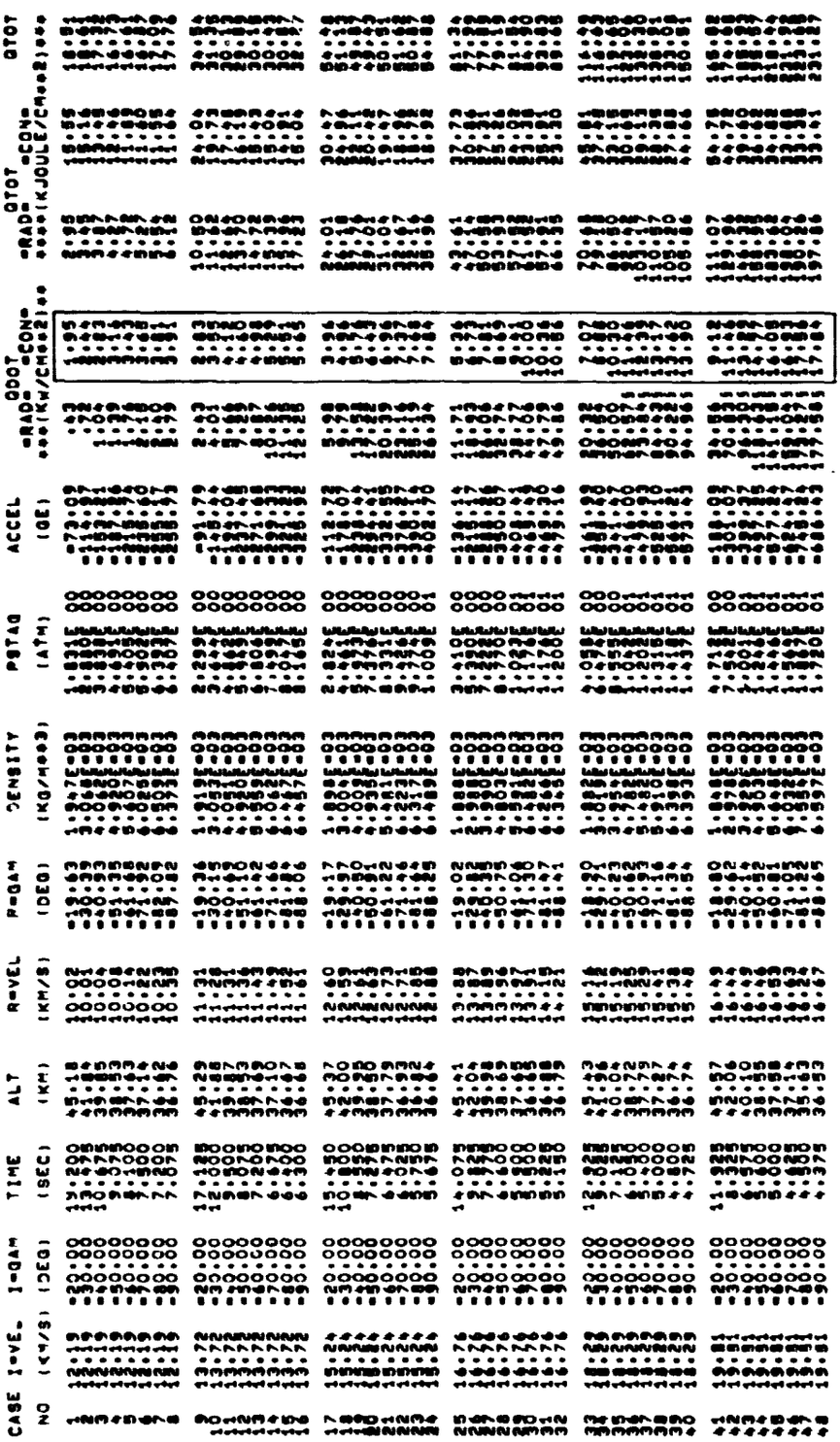

FIGURE 27

CONDITIONS AT PEAK DECELERATION AND STAGNATION PRESSURE FOR EARTH ENTRY OF A HIGH SPEED–LOW β(120 kg/m^2) VEHICLE

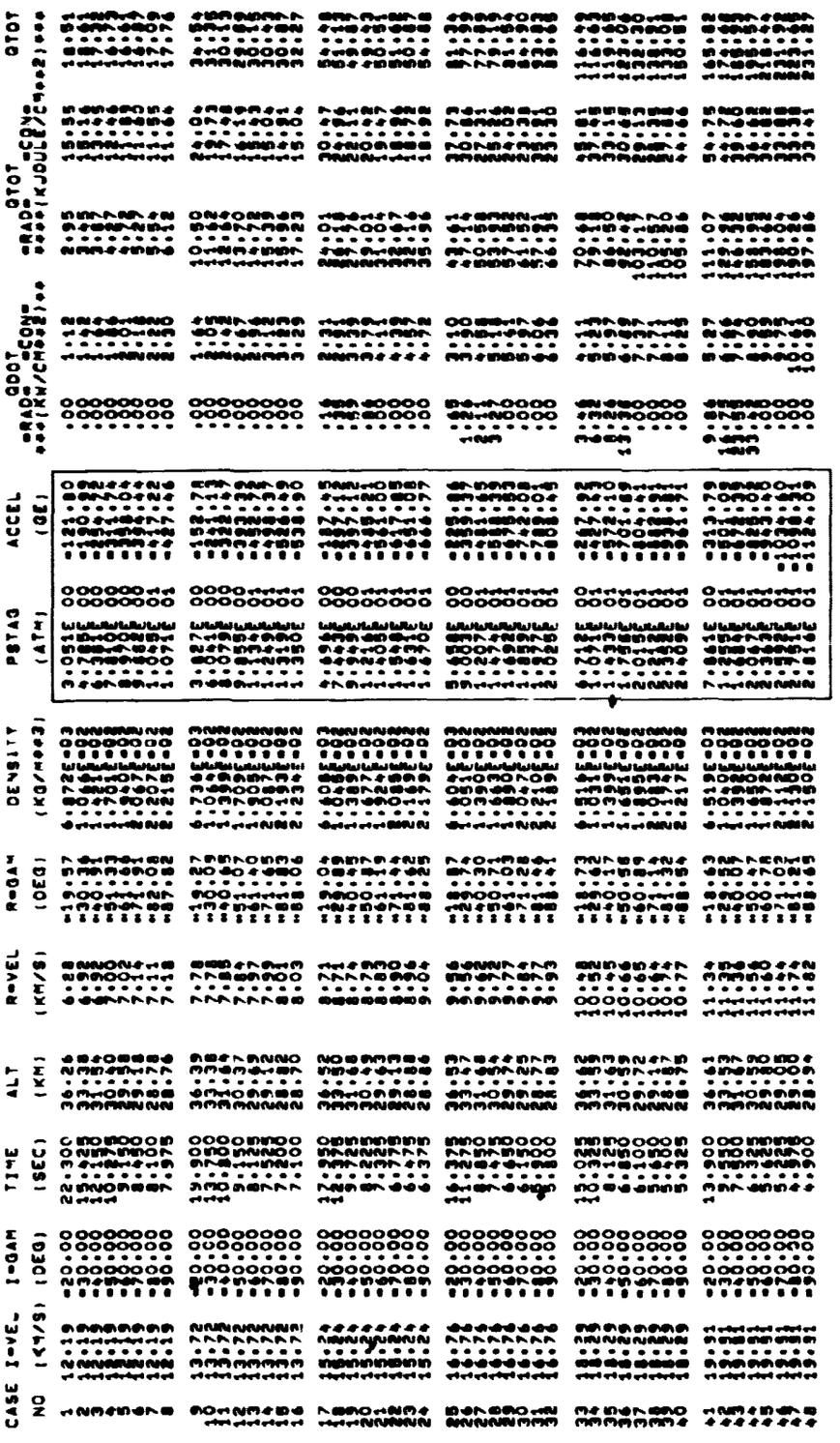

FIGURE 28

The fourth through eighth columns provide a definition of that point in the mission at which the peak environment parameter occurs. The time shown refers to the length of time it takes to pass from an altitude of 122 km (400,000 ft) to the peak environment point. The individual values of altitude, relative flight conditions and free stream density are based on a due east entry into a 1962 U.S. Standard Atmosphere and a spherical, rotating earth.

The ninth through twelfth columns list the magnitude of the environmental parameters of interest. Peak values are indicated by enclosure in a rectangular box. For example, Figure 26 presents the peak level of radiative flux. The corresponding levels of convective flux, pressure and "g" loads do not represent maximum values but rather the magnitude of these parameters that exist at the time of peak radiative heating. Similarly Figure 27 shows peak convective flux while Figure 28 indicates maximum pressure levels and "g" loads. It should be pointed out that peak radiative flux values in excess of about 50 km/cm^2 are an extrapolation of the computed data. Values so noted should be treated with caution.

The final three columns shown the total stagnation point heat load. Radiative and convective components are listed as well as the sum total. These are total mission values and hence are the same on each table.

Graphical presentations of these tabular data are also presented. Figures 29 through 34 illustrate the effect of initial entry conditions on peak heating rates, pressure, "g" loads and total heat load. Figures 35 and 36 indicate the duration of the radiative and convective heat pulse. Figures 37 through 40 show the initial entry angle and velocity combination necessary to achieve a given maximum level of heat flux, pressure and "g" loads.

4.1.2 Environment Sensitivity to Configuration - The effect of variations in ballistic coefficient (β) and nose radius (R_N) are shown in this section in terms of their effect on peak heating rates, pressure and "g" loads. Information is presented in the form of normalized sensitivity factors and also by illustrating the change in initial entry conditions required to achieve selected levels of radiative heat flux. These data are intended to provide a simplified scaling method that can be applied over a wide range of initial entry conditions. They reflect the combined results of many point design computer runs. However, a degree of environment approximation is incorporated to achieve the desired range of entry condition applicability with a simple presentation of data. Hence these predicted environment variations with vehicle configuration should be considered first order trend data as opposed to precise, point design solutions.

EARTH ENTRY HEATING RATES

- o STAGNATION POINT
- o NON-BLOWING
- o INERTIAL ENTRY CONDITIONS
- o β = 120 kg/m^2
- o R_N = .22 m

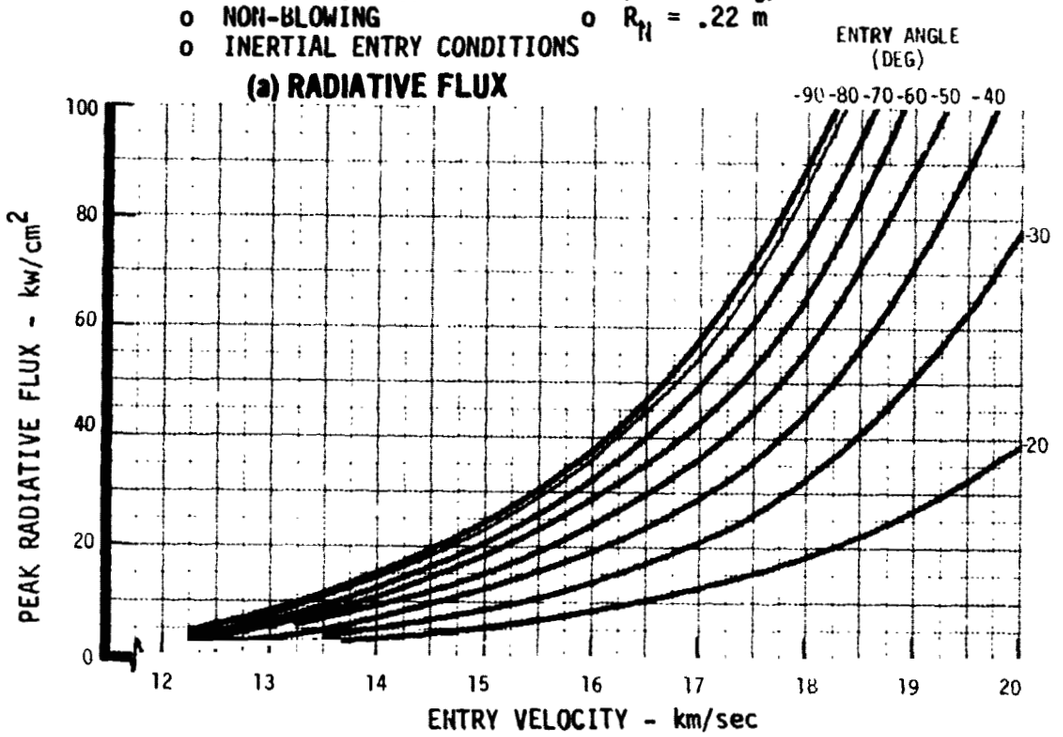

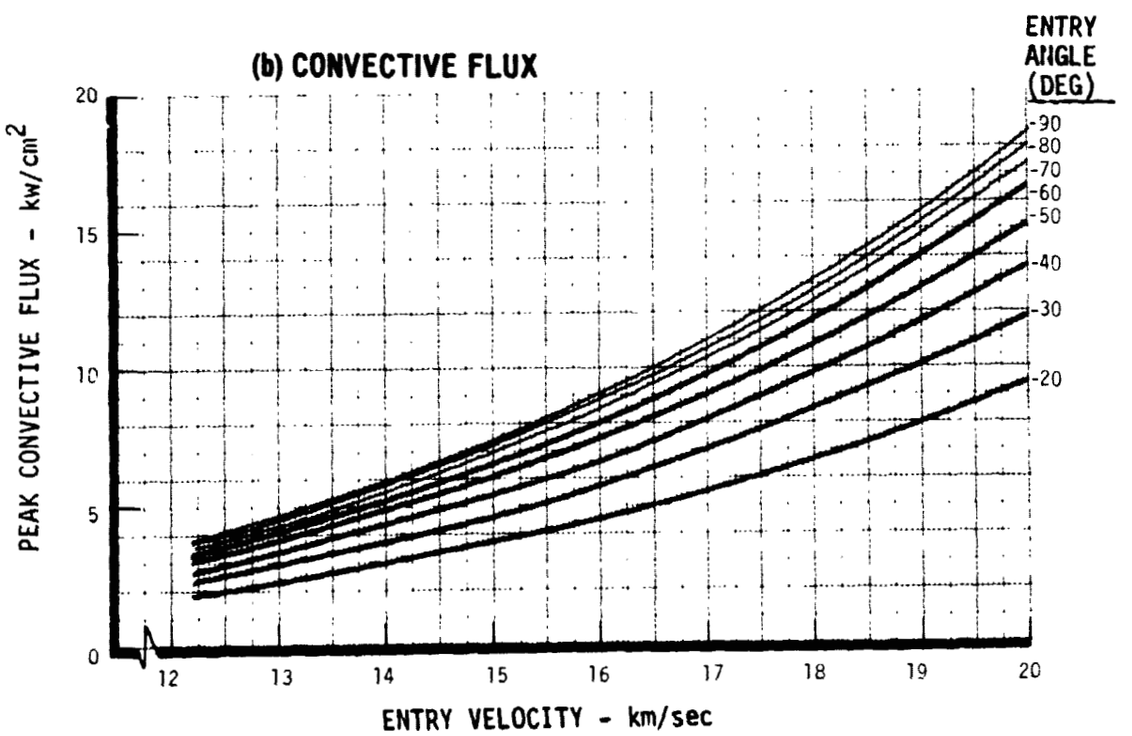

FIGURE 29

EARTH ENTRY DECELERATION LOADS

- o STAGNATION POINT
- o NON-BLOWING
- o β = 120 kg/m^2
- o INERTIAL ENTRY CONDITIONS

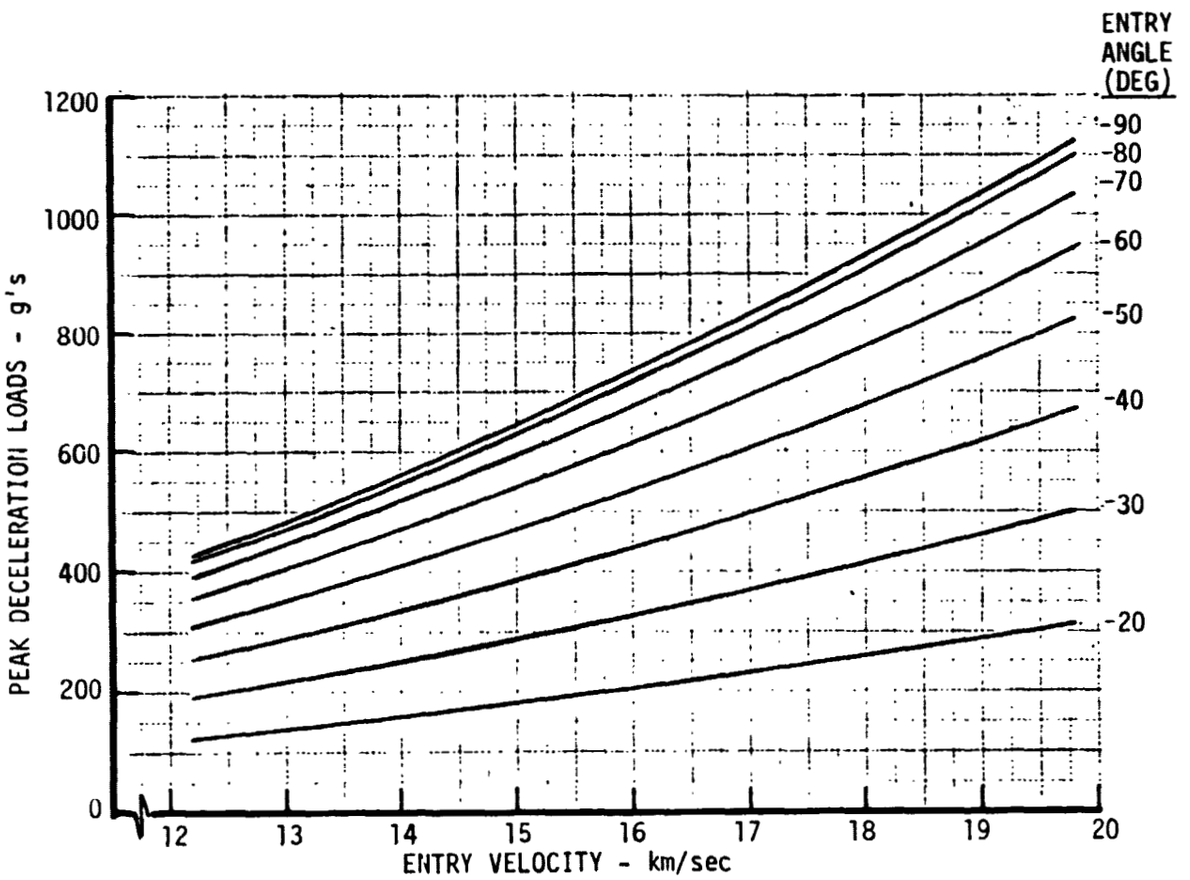

FIGURE 30

EARTH ENTRY PRESSURE

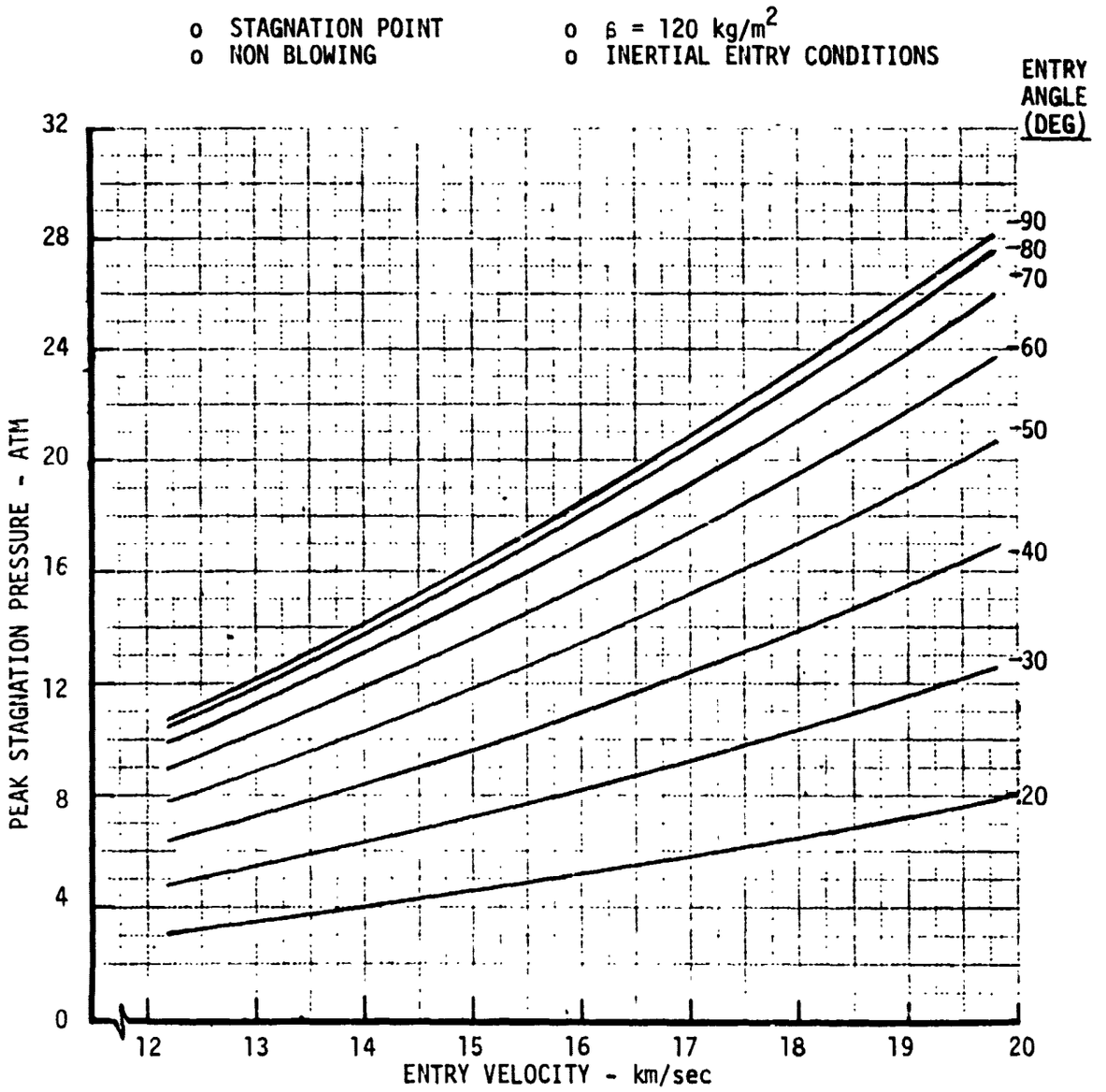

FIGURE 31

EARTH ENTRY RADIATIVE HEAT LOAD

- o STAGNATION POINT
- o NON-BLOWING
- o INERTIAL ENTRY CONDITIONS
- o β = 120 kg/m^2
- o R_N = .22 m

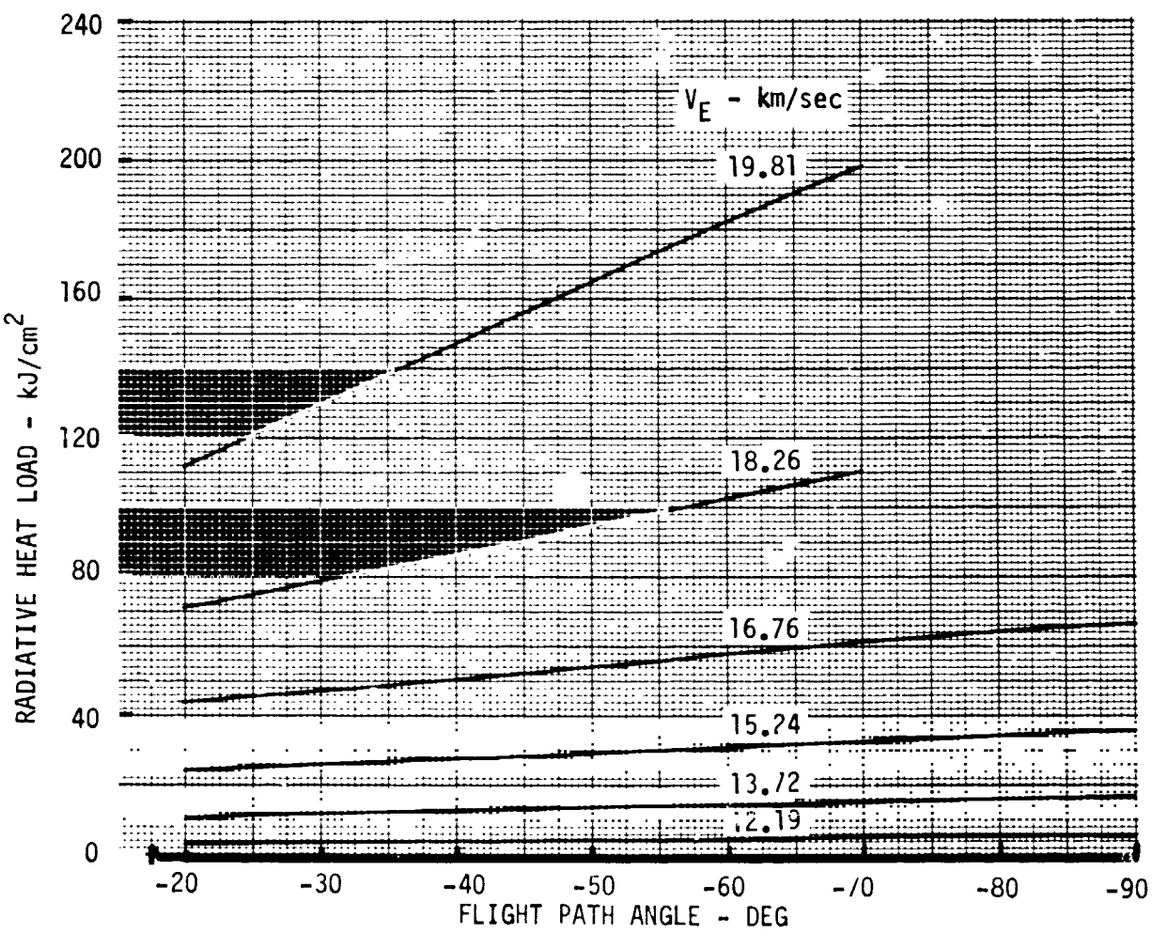

FIGURE 32.

EARTH ENTRY CONVECTIVE HEAT LOAD

- o STAGNATION POINT
- o NON-BLOWING
- o INERTIAL ENTRY CONDITIONS
- o β = 120 kg/m^2
- o R_N = .22 m

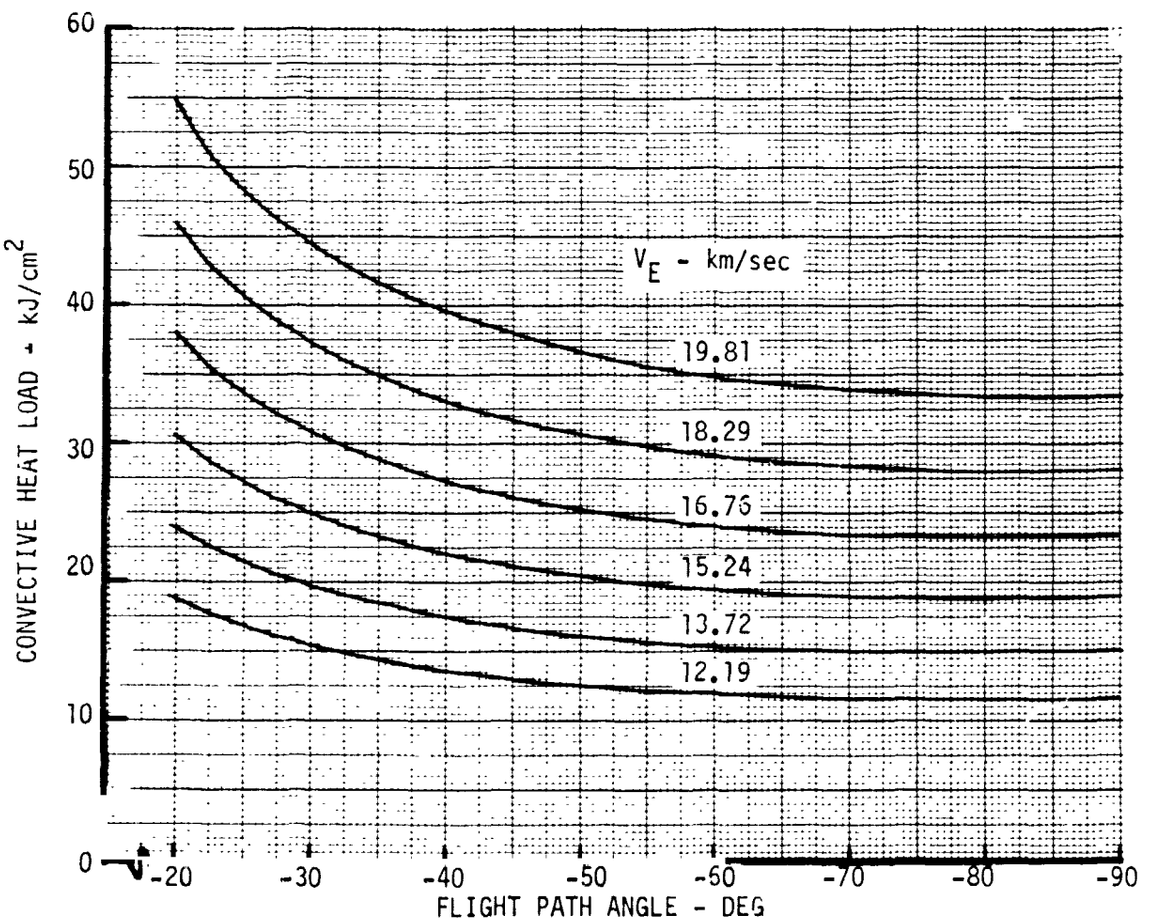

FIGURE 33

EARTH ENTRY TOTAL HEAT LOAD

- o STAGNATION POINT
- o NON-BLOWING
- o INERTIAL ENTRY CONDITIONS
- o β = 120 kg/m^2
- o R_N = .22 m

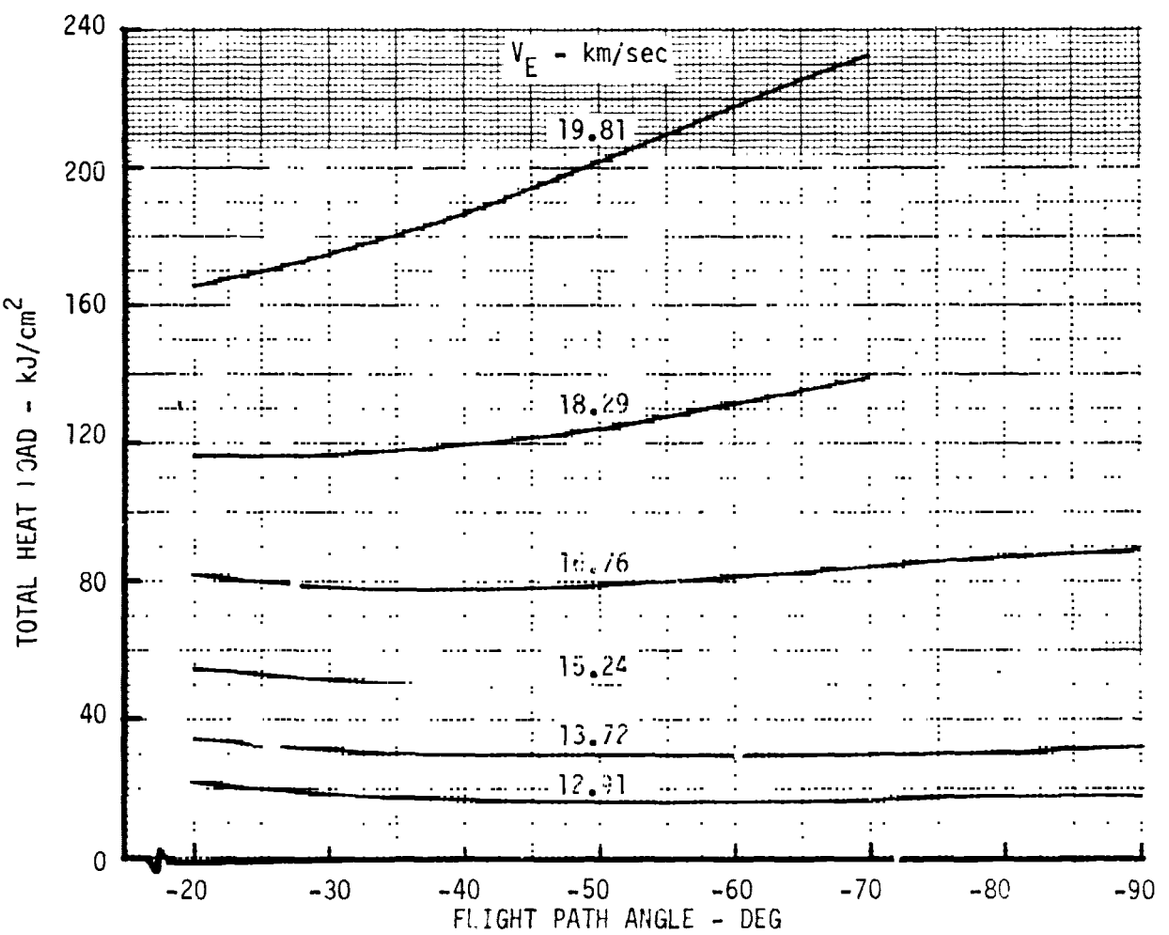

FIGURE 34

EARTH ENTRY HEAT PULSE DURATION

- o 0.5 kw/cm^2 THRESHOLD
- o β = 120 kg/m^2
- o R_N = .22 m

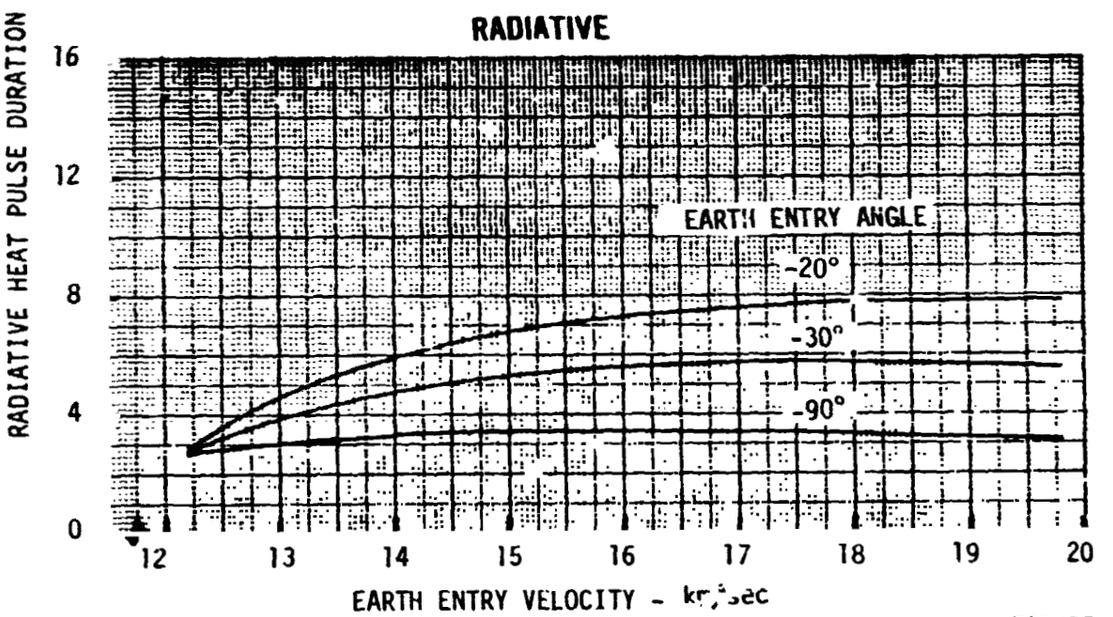

FIGURE 35

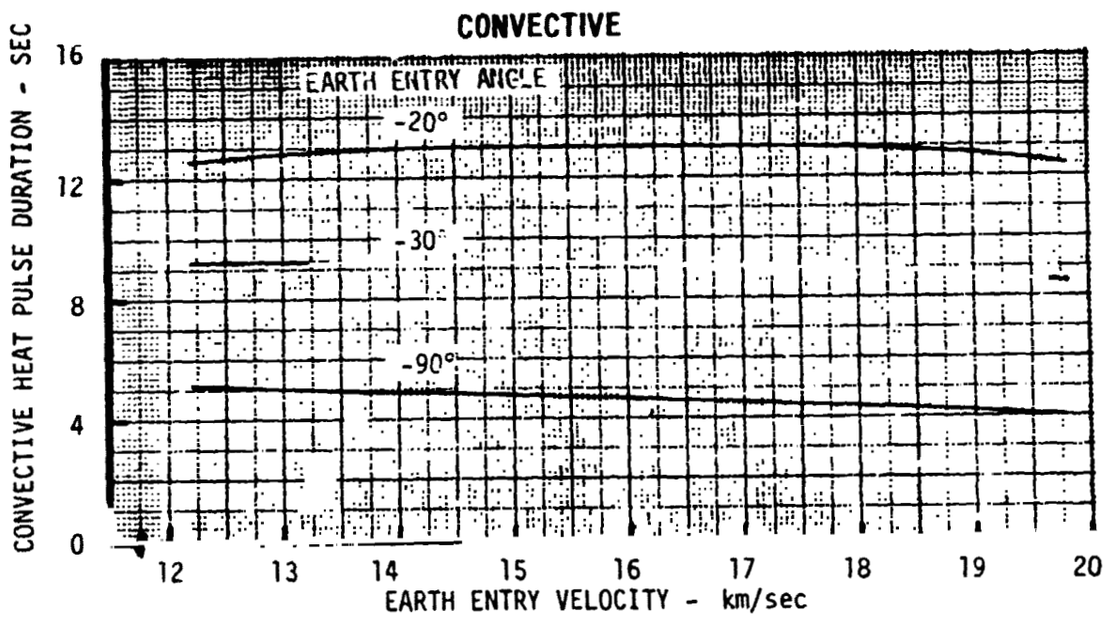

FIGURE 36

EARTH ENTRY CONDITIONS TO SIMULATE RADIATIVE HEAT FLUX

o β = 120 kg/m^2 o R_N = .22 m

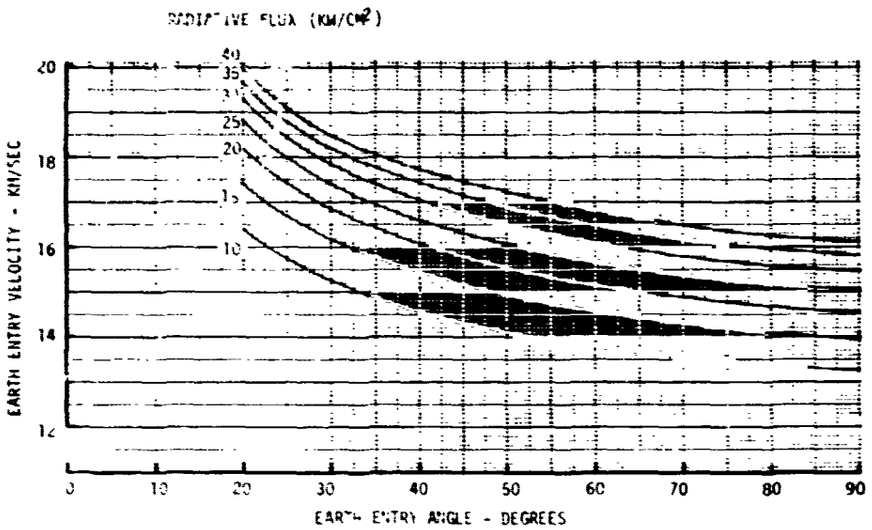

FIGURE 37

EARTH ENTRY CONDITIONS TO SIMULATE CONVECTIVE HEAT FLUX

o β = 120 kg/m^2 o R_N = .22 m

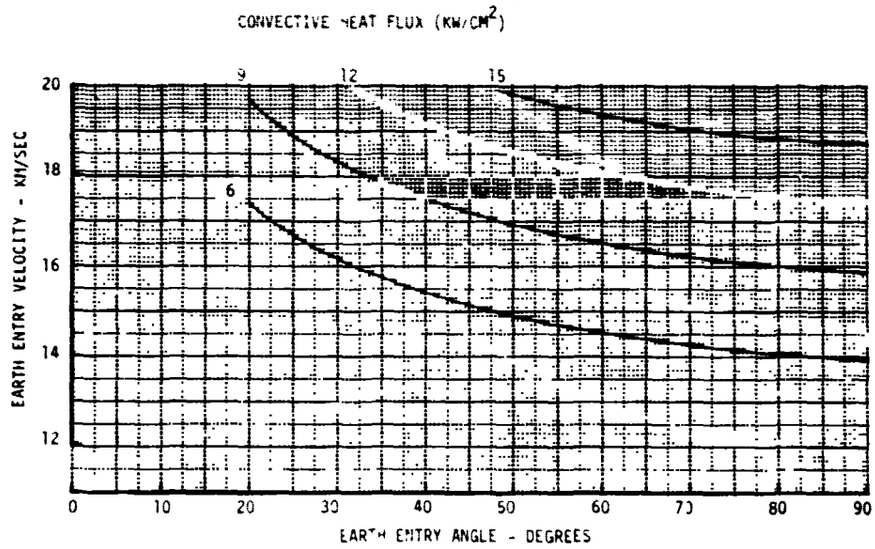

FIGURE 38

EARTH ENTRY CONDITIONS TO SIMULATE PEAK STAGNATION PRESSURE

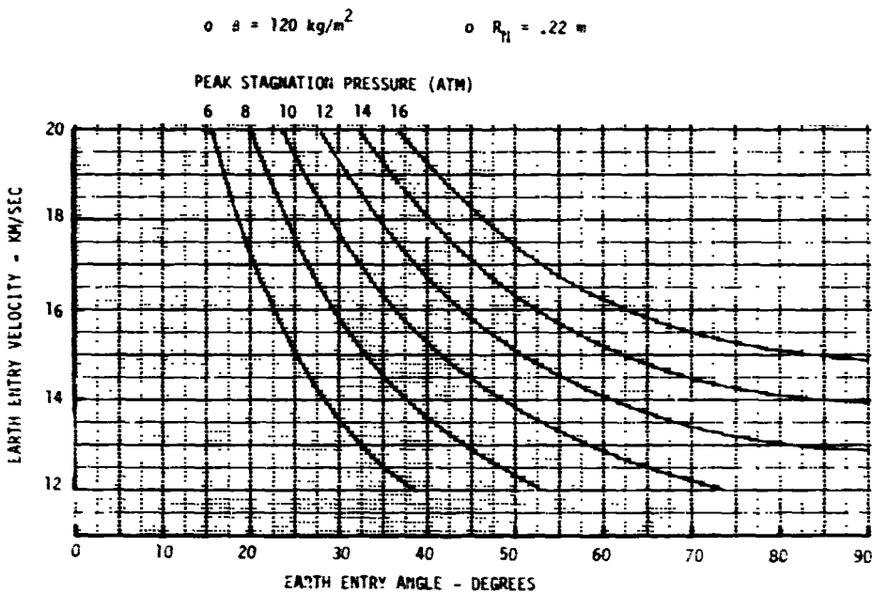

FIGURE 39

EARTH ENTRY CONDITIONS TO SIMULATE DECELERATION LOADS

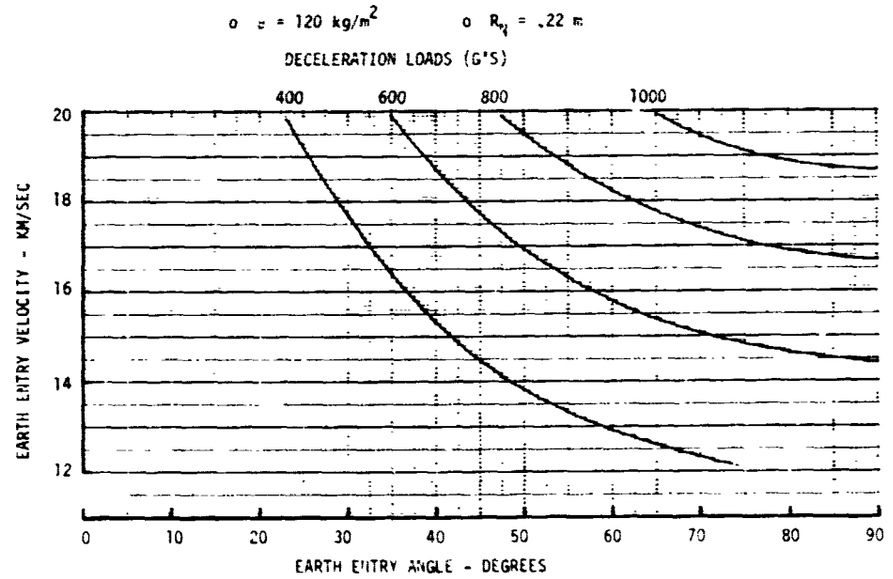

FIGURE 40

Normalized sensitivity factors are summarized in Figure 41 and presented graphically in Figures 42 through 45. Vehicle characteristics are referenced to the β and R_N values employed in Section 4.1.1 Similarly, the environment parameters are referenced to the values shown in Section 4.1.1 for any given entry angle and velocity combination. As indicated, both radiative and convective flux levels are influenced by both β and R_N. However, pressure level is a strong function of β but independent of R_N while deceleration "g" loads are essentially independent of both vehicle parameters. These unequal dependences on vehicle configuration infers that various combinations of environment parameters can be produced by proper manipulation of vehicle design characteristics.

Vehicle configuration variations also influence entry condition requirements if the level of environment simulation is fixed. This influence is illustrated in Figures 46 through 50 for representative levels of radiative heat flux. Figures 46 through 48 show the effect of β changes only (R_N = reference) while Figures 49 through 51 indicate the β effect with a smaller R_N (higher convective flux). These data show the increasing β can be used to substantially lower either the entry angle or the entry velocity requirement for a specified heating level. This also implies that a reduction in required booster size may be possible. If β is increased by mass addition, the reduction in booster ΔV required (lower entry conditions) may be greater than the reduction in booster ΔV capability (payload mass increase).

4.2 Factors Influencing Radiative Heating for Earth Entry - The computation of continuum and line spectral radiation from a shock layer is more involved for an earth entry than for a Jovian entry. This is primarily due to the increased number of species and the states that can be attained with air as compared to the simpler, hydrogen-helium atmosphere. An investigation was performed to document the differences between computational procedures, the sensitivities of radiant flux due to changes in shock layer structure and the presence of carbon species.

4.2.1 Sensitivities of Earth Entry Radiant Heating - The radiant heating table used in Section 4.1 to generate entry heating trajectory curves was generated by Kenneth Sutton using NASA-LRC SUTO computer code. The SUTO code computes the inviscid flow field as well as the radiant heating whereas Aerotherm RASLE also includes boundary layer computation. The radiant heating portion of RASLE and SUTO

EARTH ENTRY ENVIRONMENT SENSITIVITIES SUMMARY

- o STAGNATION POINT
- o NON BLOWING

- o $\beta_{REF} = 120\ kg/m^2$
- o $(R_N)_{REF} = .22\ m$

CONFIGURATION FACTORS β/β_{REF}	$R_N/(R_N)_{REF}$	$\frac{\dot{q}_R}{(\dot{q}_R)_{REF}}$	$\frac{\dot{q}_c}{(\dot{q}_c)_{REF}}$	$\frac{P_{STAG}}{(P_{STAG})_{REF}}$	$\frac{G's}{(G's)_{REF}}$
0.5	0.5	.346	.983	.474	.948
	1.0	.434	.696	.474	.948
	1.5	.480	.568	.474	.948
	2.0	.522	.492	.474	.948
1.0	0.5	.788	1.414	1.000	1.000
	1.0	1.000	1.000	1.000	1.000
	1.5	1.563	.816	1.000	1.000
	2.0	1.283	.707	1.000	1.000
1.5	0.5	1.268	1.731	1.540	1.027
	1.0	1.631	1.241	1.540	1.027
	1.5	1.893	1.007	1.540	1.027
	2.0	2.115	.872	1.540	1.027
2.0	0.5	1.756	2.033	2.094	1.047
	1.0	2.325	1.438	2.094	1.047
	1.5	2.725	1.174	2.094	1.047
	2.0	3.073	1.017	2.094	1.047

FIGURE 41

EARTH ENTRY ENVIRONMENT SENSITIVITY TO BALLISTIC COEFFICIENT

- o STAGNATION POINT
- o NON BLOWING
- o β_{REF} = 120 kg/m^2
- o $(R_N)_{REF}$ = .22 m

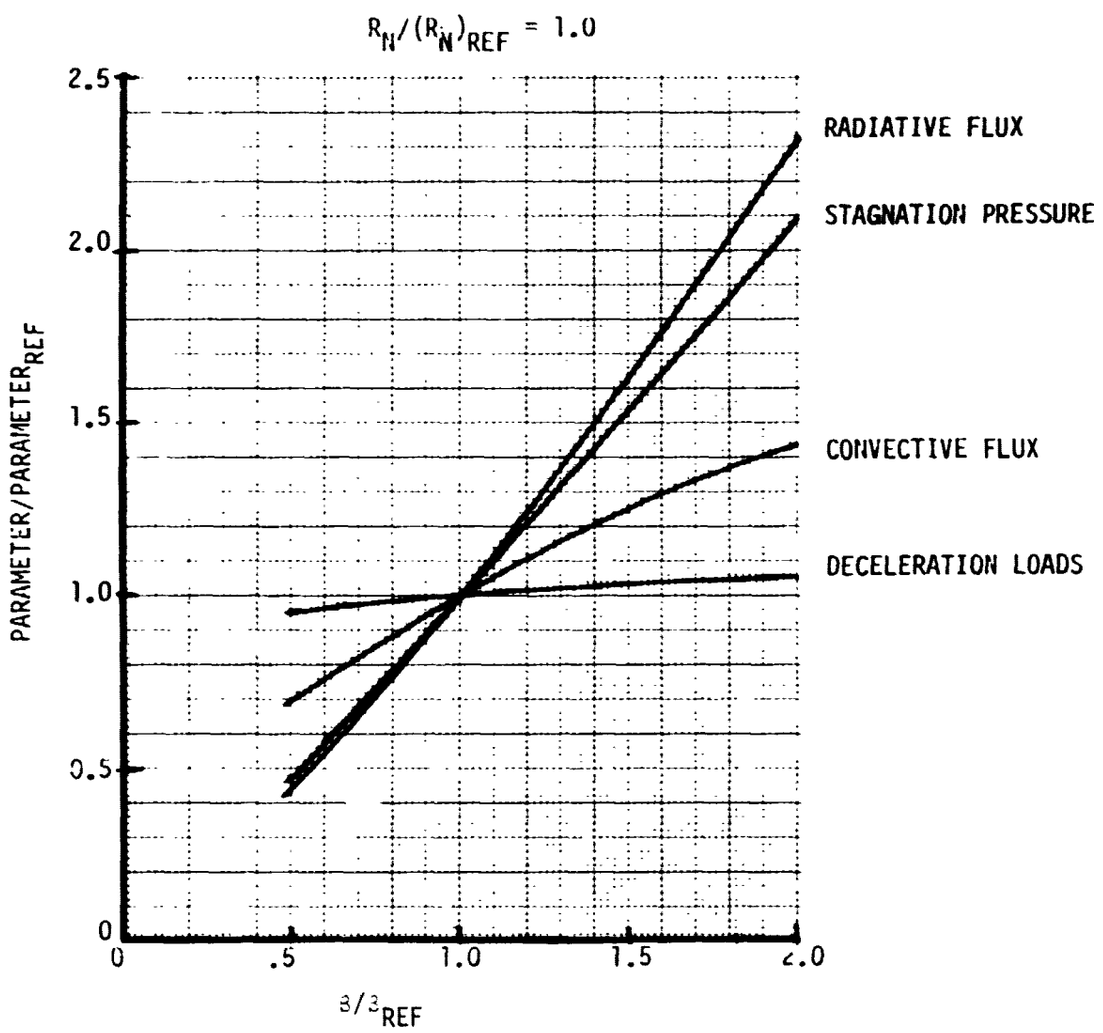

FIGURE 42

EARTH ENTRY ENVIRONMENT SENSITIVITY TO NOSE RADIUS

- o STAGNATION POINT
- o NON BLOWING

$\beta_{REF} = 120\ kg/m^2$

$(R_N)_{REF} = .22\ m$

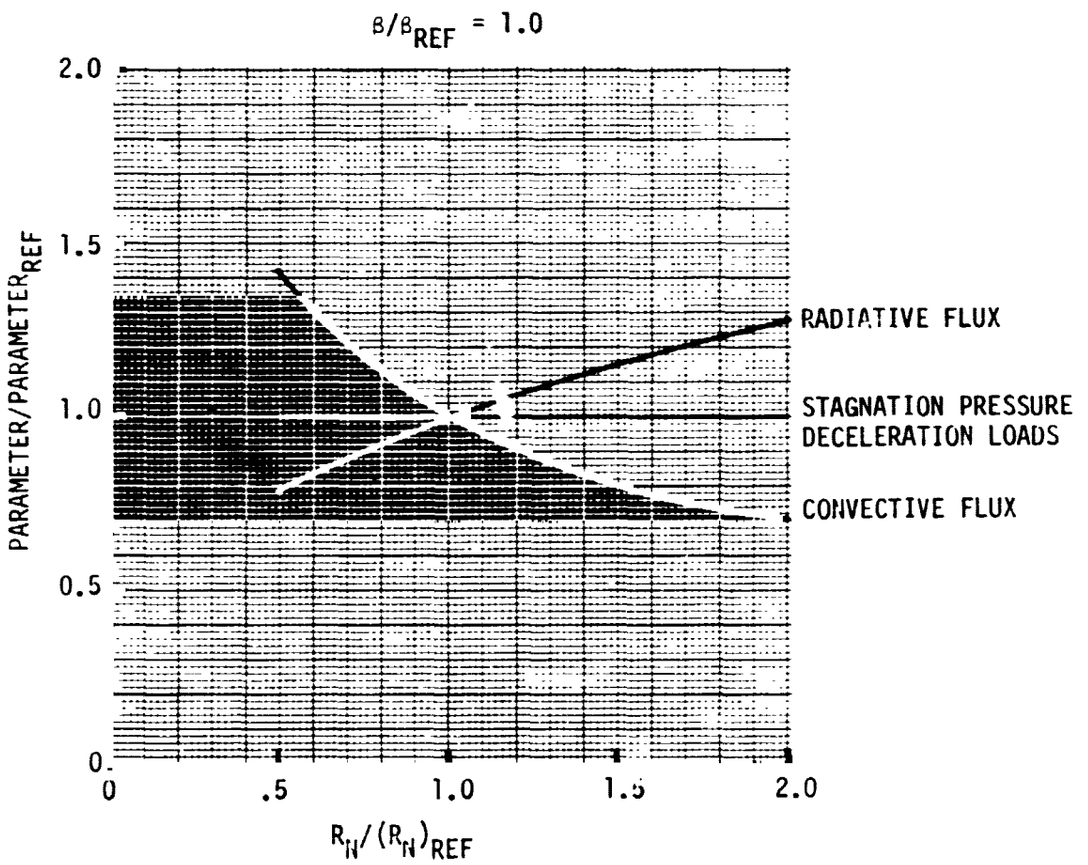

FIGURE 43

RADIATIVE FLUX SENSITIVITY TO VEHICLE CONFIGURATION

- o EARTH ENTRY
- o STAGNATION POINT
- o NON-BLOWING
- o β_{REF} = 120 kg/m^2
- o $(R_N)_{REF}$ = .22 m

(a) BALLISTIC COEFFICIENT

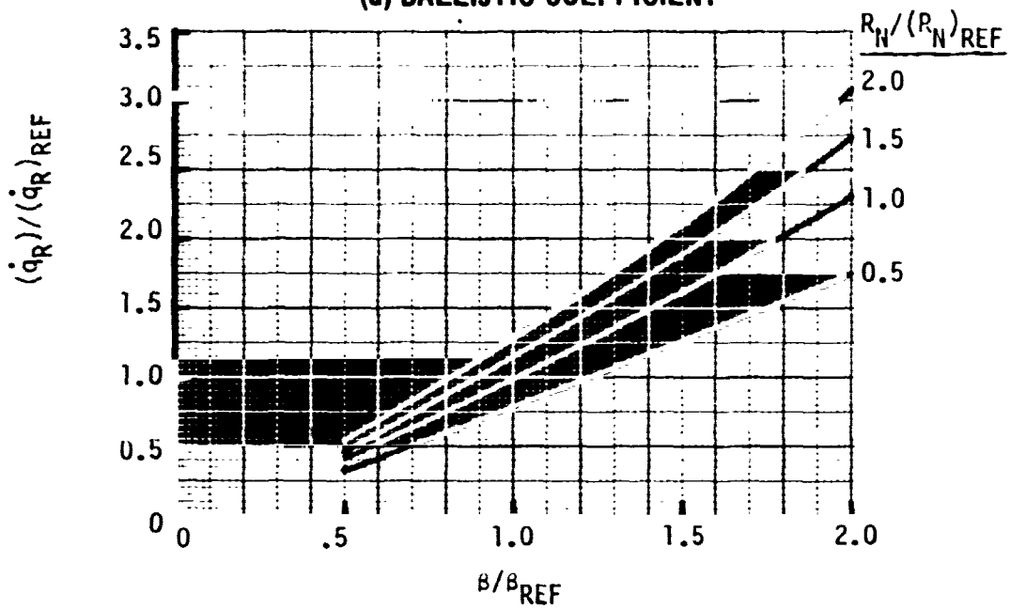

(b) NOSE RADIUS

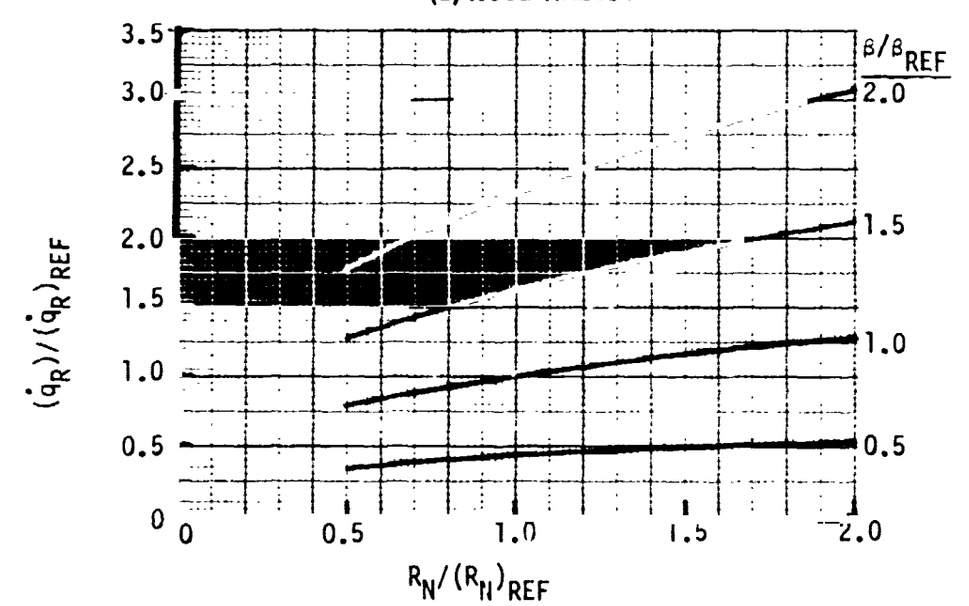

FIGURE 44

CONVECTIVE FLUX SENSITIVITY TO VEHICLE CONFIGURATION

- EARTH ENTRY
- STAGNATION POINT
- NON BLOWING
- β_{REF} = 120 kg/m^2
- $(R_N)_{REF}$ = .22 m

(a) BALLISTIC COEFFICIENT

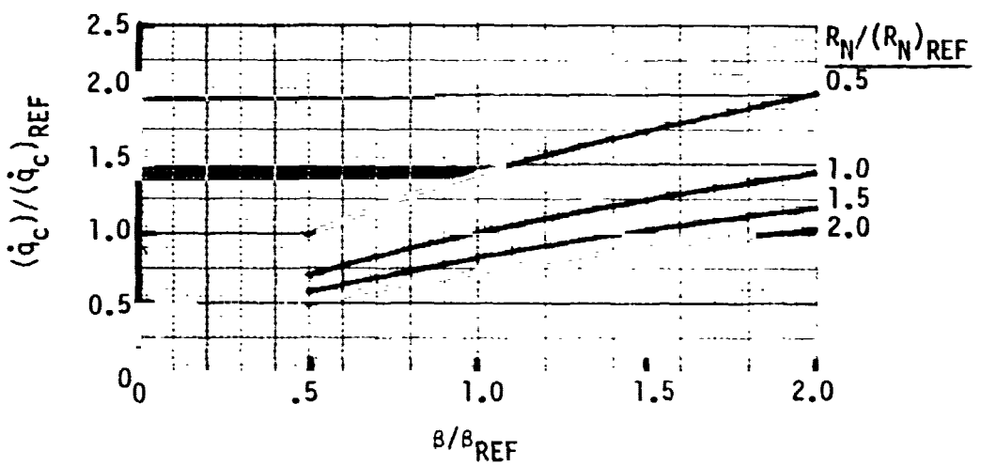

(b) NOSE RADIUS

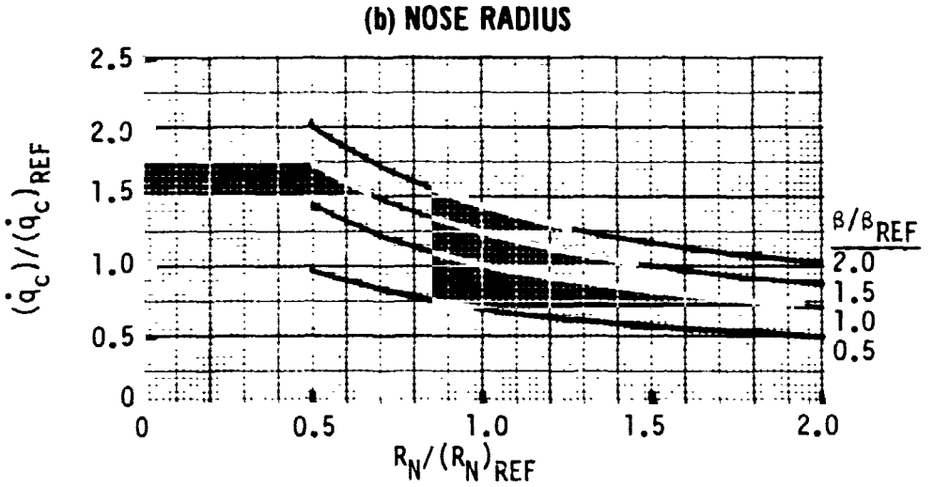

FIGURE 45

ENTRY CONDITION SENSITIVITY TO BALLISTIC COEFFICIENT FOR RADIATIVE FLUX SIMULATION

($\dot{q}_R$ = 10 kw/cm^2, $R_N/(R_N)_{REF}$ = 1.0)

- o EARTH ENTRY
- o STAGNATION POINT
- o NON BLOWING
- o β_{REF} = 120 kg/m^2
- o $(R_N)_{REF}$ = .22 m

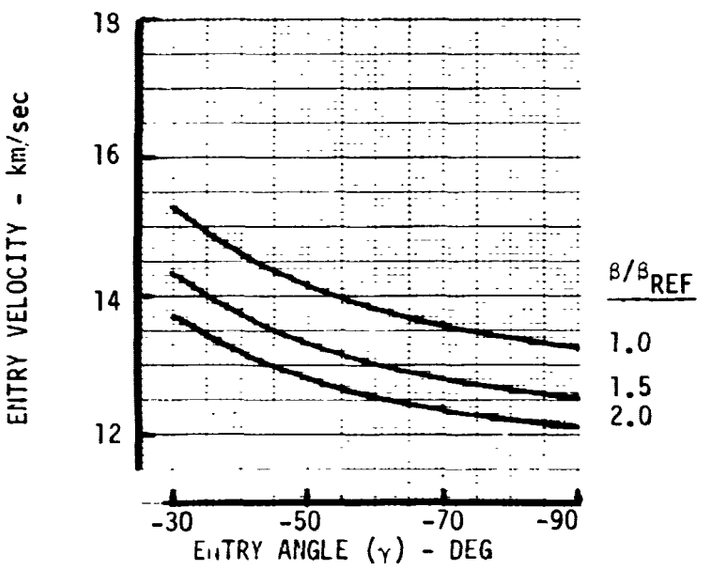

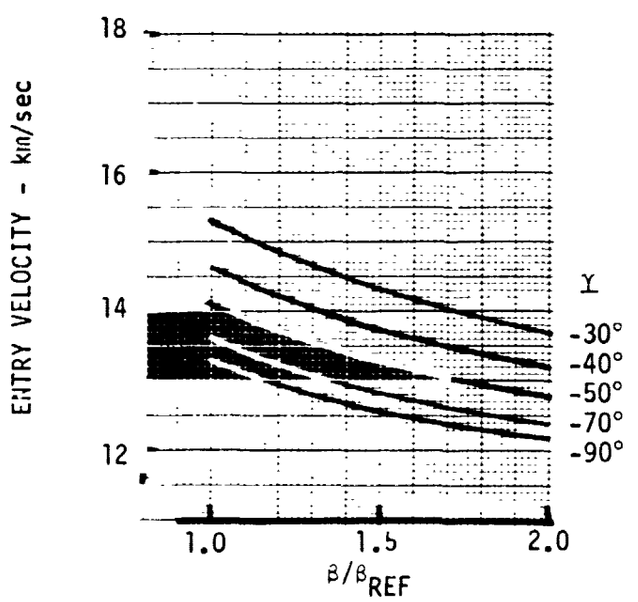

FIGURE 46

ENTRY CONDITION SENSITIVITY TO BALLISTIC COEFFICIENT FOR RADIATIVE FLUX SIMULATION

($\dot{q}_R$ = 17 kw/cm^2, $R_N/(R_N)_{REF}$ = 1.0)

- o EARTH ENTRY
- o STAGNATION POINT
- o NON BLOWING
- o β_{REF} = 120 kg/m^2
- o $(R_N)_{REF}$ = .22 m

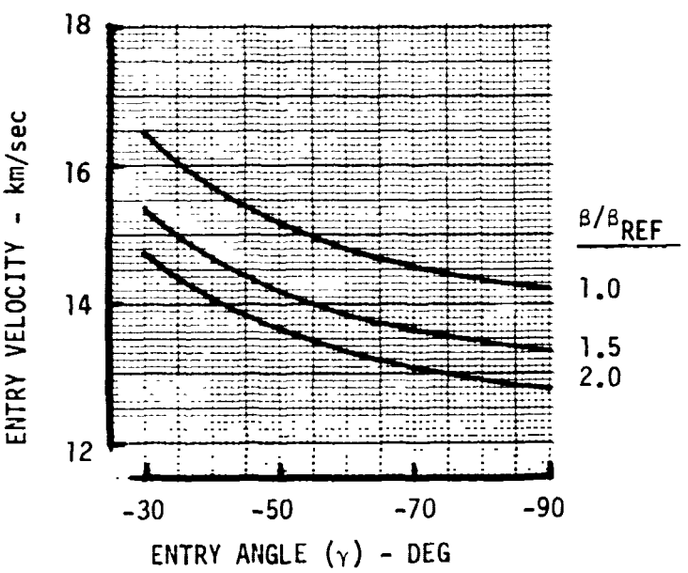

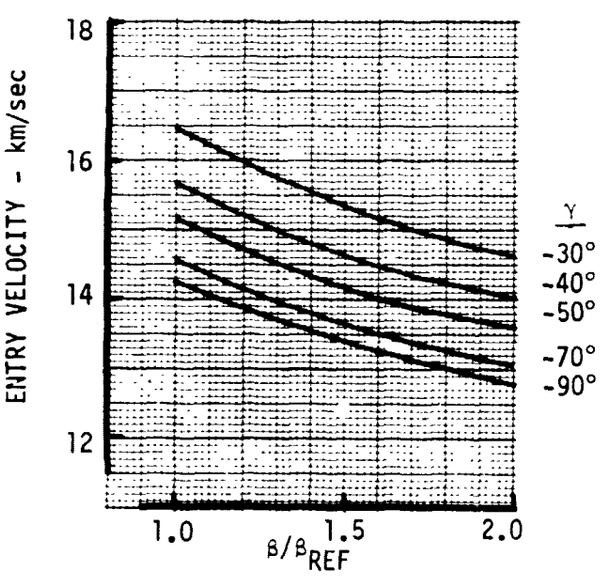

FIGURE 47

ENTRY CONDITION SENSITIVITY TO BALLISTIC COEFFICIENT FOR RADIATIVE FLUX SIMULATION

($\dot{q}_R$ = 40 kw/cm^2, $R_N/(R_N)_{REF}$ = 1.0)

- o EARTH ENTRY
- o STAGNATION POINT
- o NON BLOWING
- o β_{REF} = 120 kg/m^2
- o $(R_N)_{REF}$ = .22 m

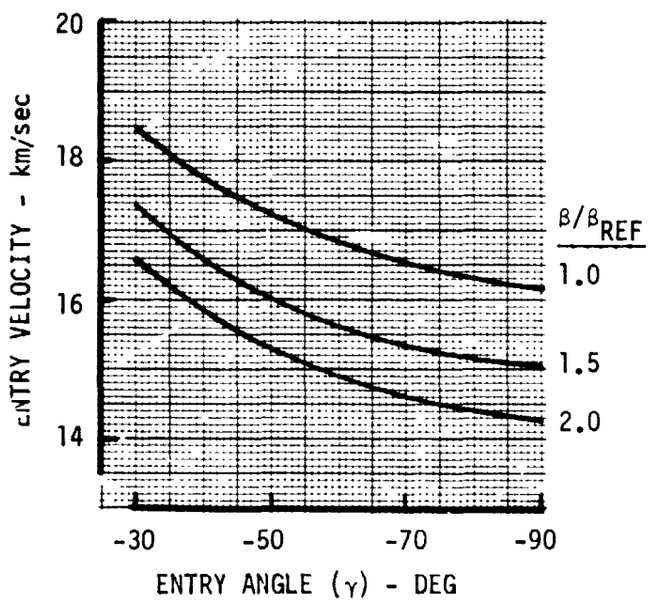

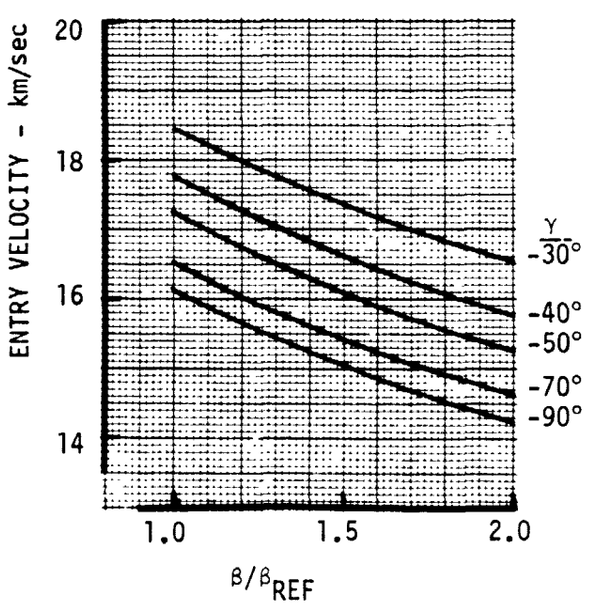

FIGURE 48

ENTRY CONDITION SENSITIVITY TO BALLISTIC COEFFICIENT FOR RADIATIVE FLUX SIMULATION

($\dot{q}_R$ = 10 kw/cm^2, $R_N/(R_N)_{REF}$ = 0.5)

- o EARTH ENTRY
- o STAGNATION POINT
- o NON BLOWING
- o β_{REF} = 120 kg/m^2
- o $(R_N)_{REF}$ = .22 m

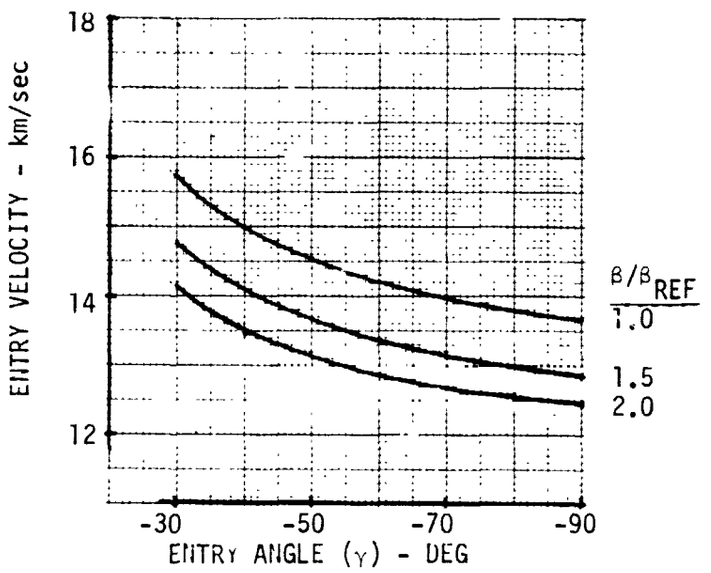

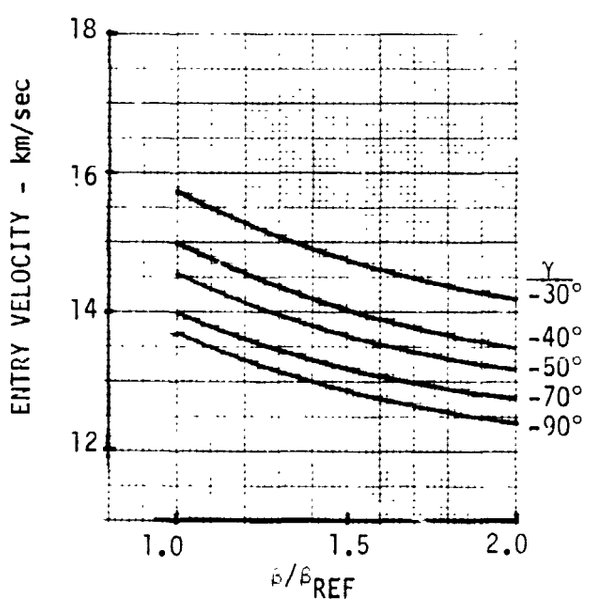

FIGURE 49

ENTRY CONDITION SENSITIVITY TO BALLISTIC COEFFICIENT FOR RADIATIVE FLUX SIMULATION

(q_R = 17 kw/cm^2, $R_N/(R_N)_{REF}$ = 0.5)

- o EARTH ENTRY
- o STAGNATION POINT
- o NON BLOWING
- o β_{REF} = 120 kg/m^2
- o $(R_N)_{REF}$ = .22 m

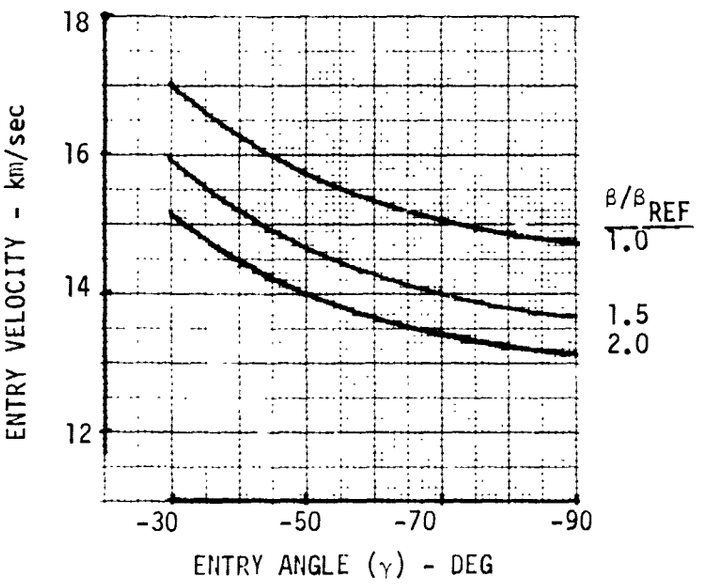

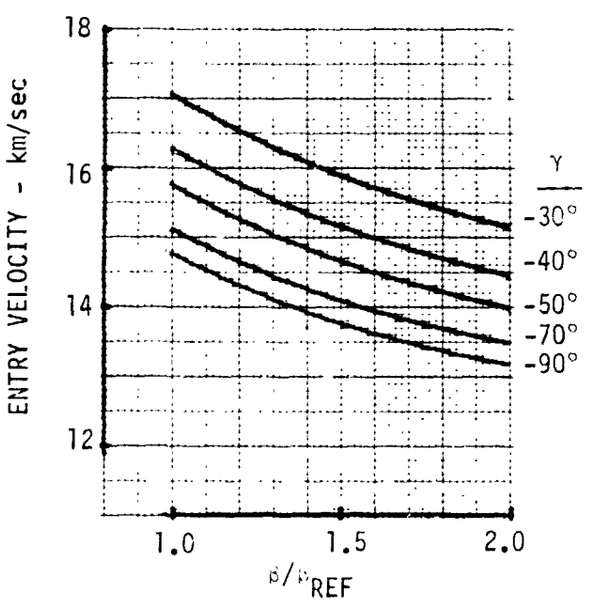

FIGURE 50

ENTRY CONDITION SENSITIVITY TO BALLISTIC COEFFICIENT FOR RADIATIVE FLUX SIMULATION

($\dot{q}_R$ = 40 kw/cm^2, $R_N/(R_N)_{REF}$ = 0.5)

- o EARTH ENTRY
- o STAGNATION POINT
- o NON BLOWING
- o β_{REF} = 120 kg/m^2
- o $(R_N)_{REF}$ = .22 m

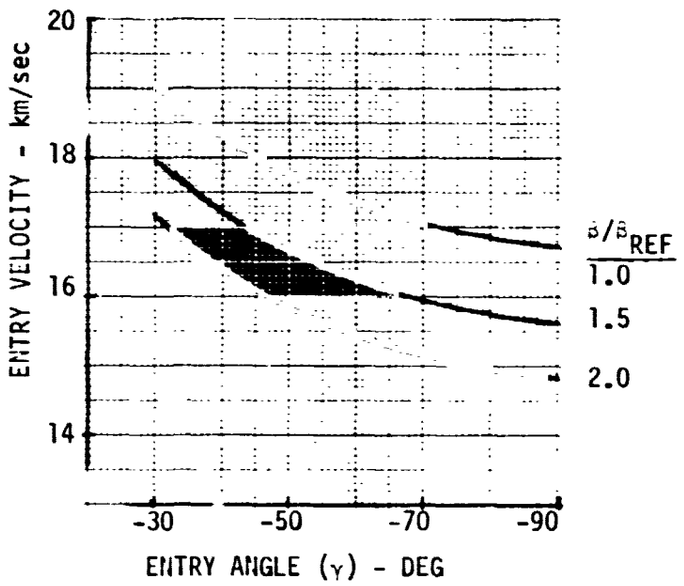

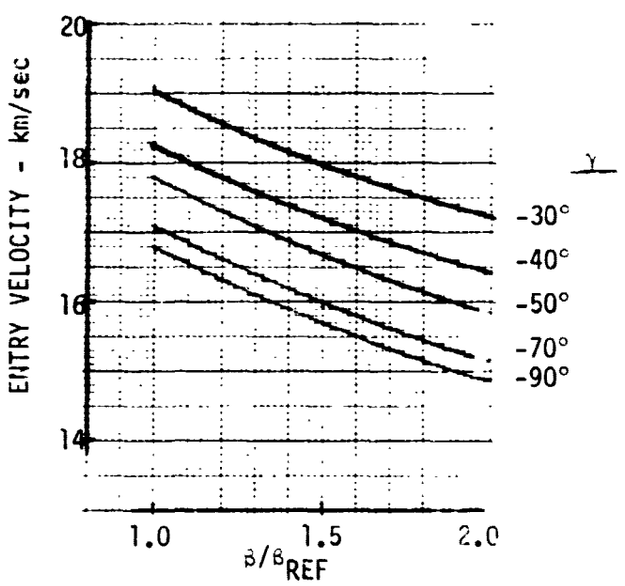

FIGURE 51

have their genius in the RADICAL/69 computer code. A copy of RADICAL/69 is operational on the MDAC-E computers and used extensively in this study. A two conditions evaluation emerged to evaluate radiant heating computed by the three codes. Both adiabatic and cooled shock layer conditions were evaluated. Figure 52 lists the flow field conditions and the resulting heating for adiabatic and cooled shock layer. The adiabatic computations were made with a uniform temperature across the shock layer and the cooled shock layer computations employed temperature profiles. SUTO modeled only the inviscid portion of the shock while RASLE included boundary layer effects at the wall. The two temperature profiles are shown in Figure 53. Of course the profile including boundary layer effects is closer to what would be expected in flight. As can be seen in Figure 52 by examining the adiabatic shock results, the shock temperature (T_S) drives the incident flux. The effect of temperature profile on incident flux is evident by examining the cooled shock layer results. Using the higher temperature of the boundary layer edge produces high heating than accounting for the temperature drop in the boundary layer. The RADICAL/69 results compare quite favorably with SUTO results and are within 10 percent of RASLE results.

Spectral distributions of the wall flux are contained in Figures 54 through 57 as obtained using the RADICAL/69 calculations. The RADICAL/69 calculation method was used for the remainder of this study.

Changes in free stream flow conditions result in a change in the overall temperature level of the shock layer, while a change in vehicle nose radius directly affects the shock standoff distance and consequently effects the so called "shock layer thickness". The sensitivity of radiant heating to several temperature levels over a range of shock layer thicknesses or standoff distances is shown in Figure 58. To obtain the other temperature levels, the "condition 1" temperature distribution was multiplied by a constant factor throughout. It appears that temperature level has more effect than the shock standoff distance. For ease in interpolating the total flux, a carpet plot is presented in Figure 59. Figure 60 compares the spectral flux distribution at the extremes of the conditions analyzed. The zones (photon energy) where radiant energy is released are essentially the same for the three conditions plotted, only the magnitude of the energy release changes. It is very apparent that a shock layer with a 90% temperature distribution with a thinner thickness (0.75 cm) releases much less energy than the nominal condition layer. Conversely if the temperature level is high (10%)than predicted and the shock thickness is (1.25 cm) much more energy is released. An additional carpet plot showing the effect of a constant temperature shock layer is presented in Figure 61.

RADIATIVE HEATING METHOD COMPARISON (EARTH ENTRY)

		RADICAL/69 COOLED SHOCK LAYER	RADICAL/69 ADIABATIC SHOCK LAYER	SUTO COOLED SHOCK LAYER	SUTO ADIABATIC SHOCK LAYER	RASLE COOLED SHOCK LAYER
CONDITION 1						
V_∞ = 14.0 KM/SEC	LINES	8.63	18.60	8.88	19.79	--
h = 42.0 KM						
T_S = 15721°K	CONTINUUM	11.83	26.75	11.56	25.39	--
P_S = 5.41 ATM						
T_W = 12242°K	TOTAL (KW/CM^2)	20.46	45.35	20.44	45.18	--
CONDITION 2						
V_∞ = 14.15 KM/SEC	LINES	8.89	22.90	11.0	25.2	13.37
h = 40.5 KM						
T_S = 16100°K	CONTINUUM	14.95	33.70	15.4	34.3	10.90
P_S = 6.80 ATM						
T_W = 4370°K	TOTAL (KW/CM^2)	23.85	56.64	26.4	59.5	24.27

RADICAL/69 OPERATIONAL AT MDAC
SUTO OPERATIONAL AT NASA LRC
RASLE OPERATIONAL AT AEROTHERM

FIGURE 52

TEMPERATURE DISTRIBUTIONS ACROSS COOLED SHOCK LAYER (EARTH ENTRY)

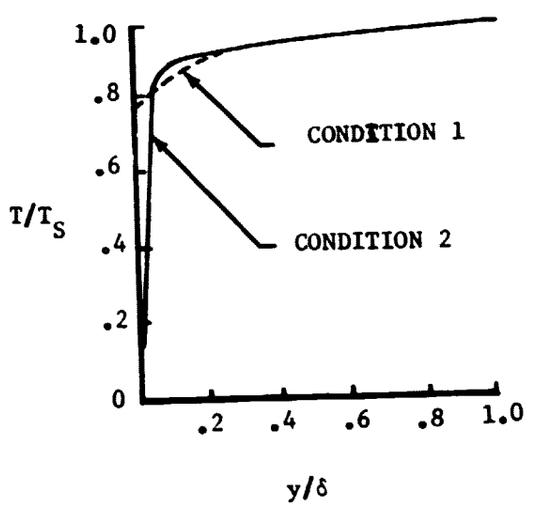

FIGURE 53

SPECTRAL WALL FLUX, ADIABATIC SHOCK LAYER (CONDITION 2) (EARTH ENTRY)

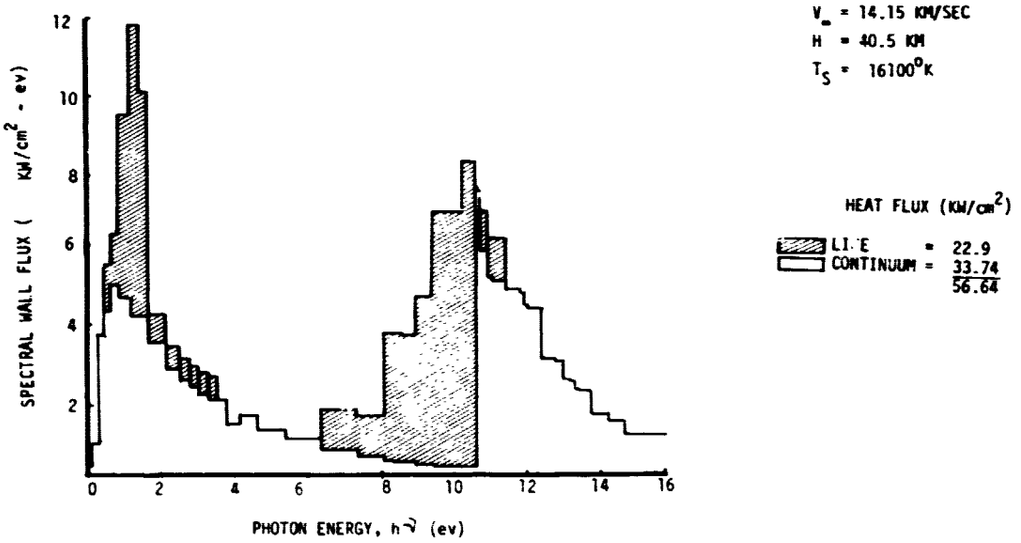

FIGURE 54

SPECTRAL WALL FLUX, CONDITION 2 COOLED SHOCK LAYER (EARTH ENTRY)

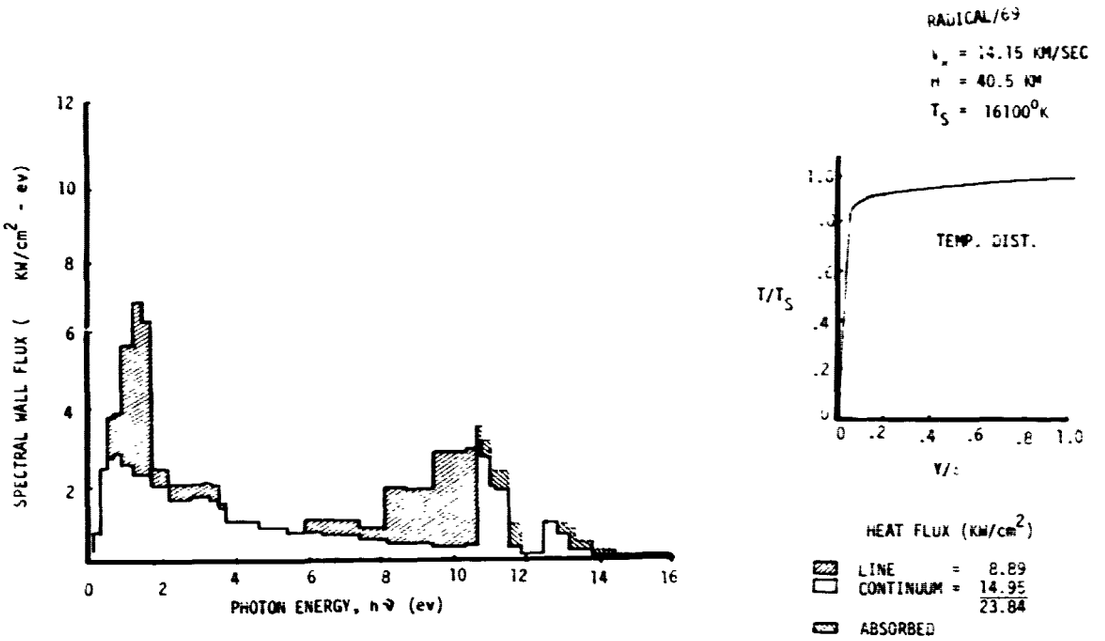

FIGURE 55

SPECTRAL WALL FLUX, ADIABATIC SHOCK LAYER (CONDITION 1) (EARTH ENTRY)

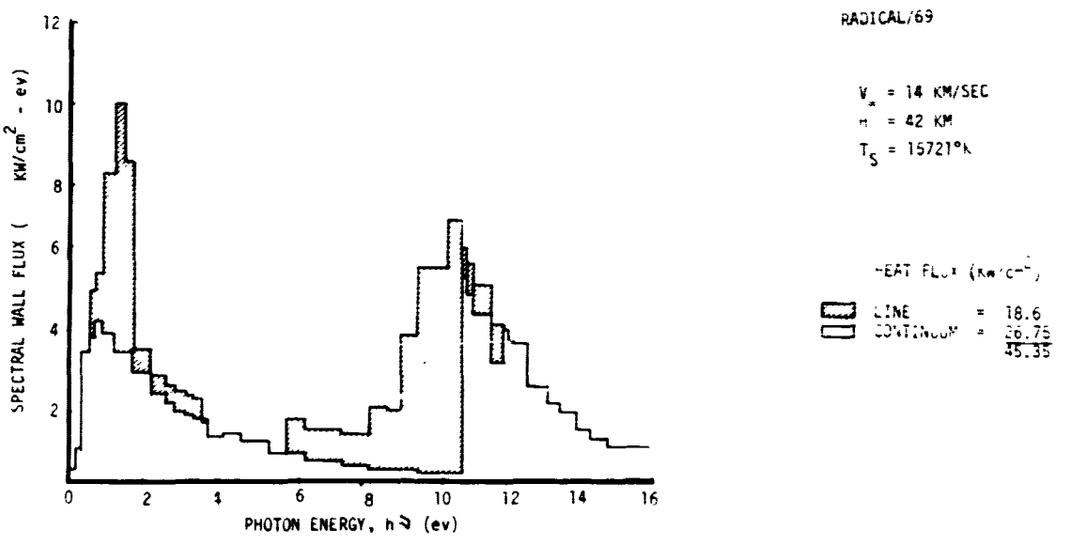

FIGURE 56

SPECTRAL FLUX FOR CONDITION 1 COOLED SHOCK LAYER (EARTH ENTRY)

V_∞ = 14.0 KM/SEC
H = 42KM
T_S = 15721°K

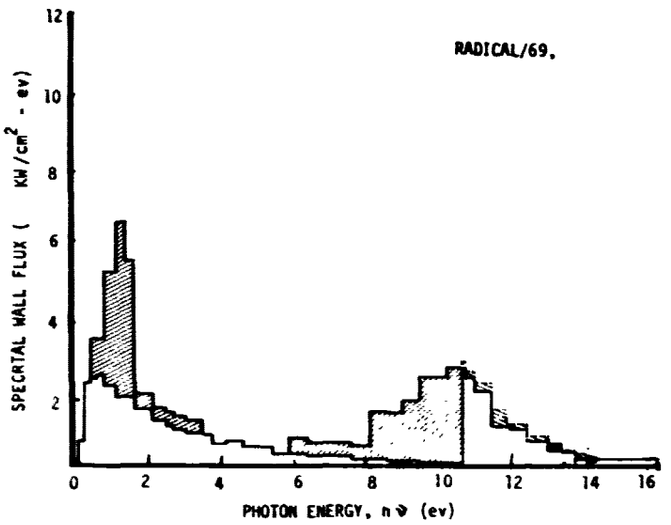

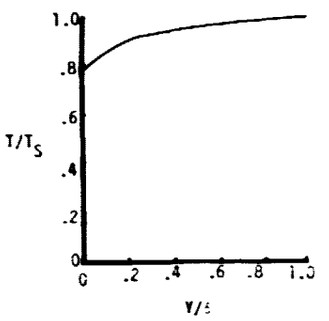

HEAT FLUX (KW/cm²)
LINE = 8.63
CONTINUUM = 11.83
20.46
ABSORBED

FIGURE 57

SENSITIVITY OF RADIANT HEATING TO SHOCK LAYER TEMPERATURE AND THICKNESS

EARTH ENTRY
RADICAL/69, COOLED SHOCK LAYER

V_∞ = 14.0 KM/SEC
h = 42 KM
T_S = 15721°K
P_S = 5.41 ATM

"T" REPRESENTS CONDITION 1 TEMPERATURE DISTRIBUTION

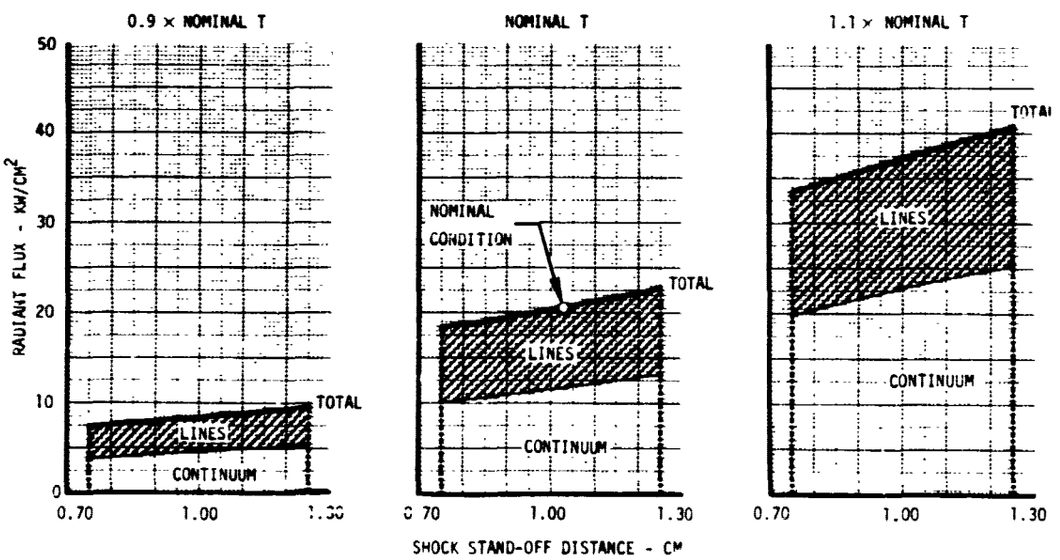

FIGURE 58

EFFECT OF SHOCK LAYER TEMPERATURE AND THICKNESS ON RADIANT HEATING

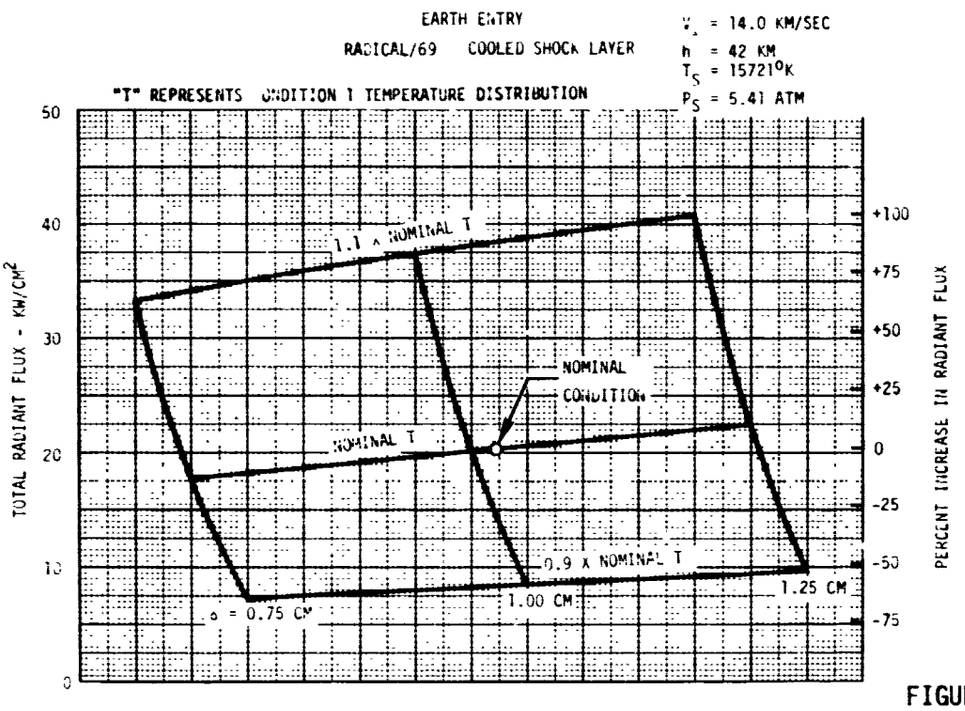

FIGURE 59

SENSITIVITY OF SPECTRAL FLUX DISTRIBUTION TO SHOCK LAYER TEMPERATURE AND THICKNESS

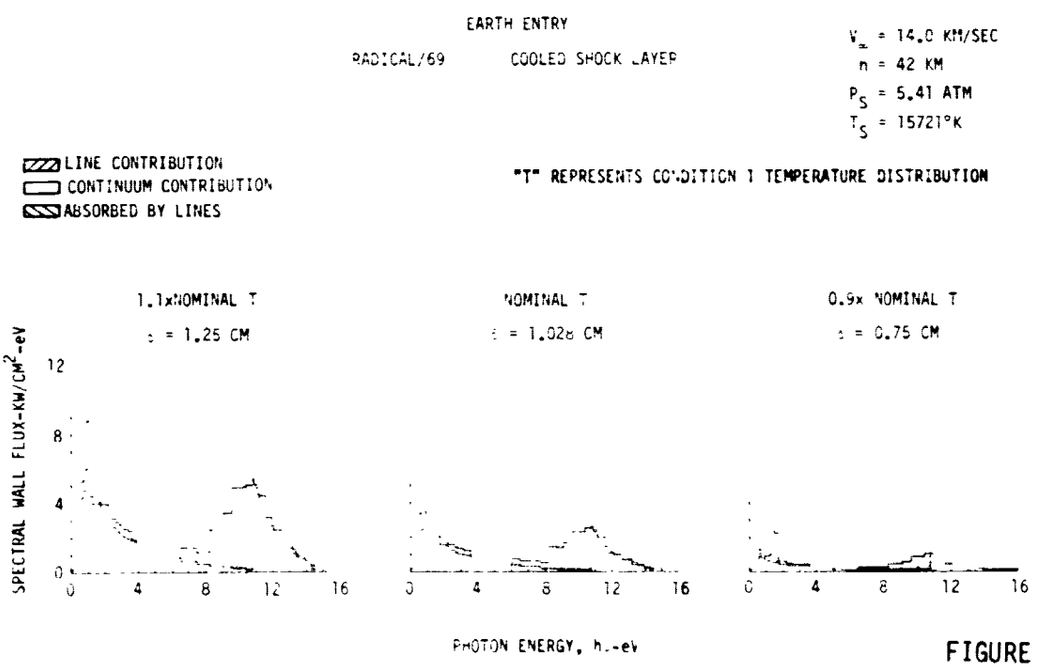

FIGURE 60

The effects of the expected temperature distribution across the shock layer is contained in Figure 62. For this sensitivity analysis several temperature distributions for the zone ($\delta/Y < .5$) near the wall were faired into the nominal temperature distribution computed by Sutton. These temperature distributions were used to compute incident radiant flux as a function of wall temperature. As can be seen in the figure for the cooler wall conditions which are expected for carbon phenolic or silica ablators the incident flux is only moderately sensitive to wall temperature. The spectral flux distribution at several wall temperatures is compared in Figure 63. The sensitivity of radiant flux (Figure 64) to temperature distribution across the shock layer was further studied by fixing the wall at 4370°K (nominal sublimation temperature of carbon phenolic) and varying the profile adjacent to the wall to give the influence of boundary layer thickness for the same shock layer thickness. The thicker (Y_B) the boundary layer the lower the incident heat flux.

An overall comparison of different actual flight conditions is shown in Figure 65, which presents the spectral flux distribution. The wall temperature is the same for all three cases and the normalized temperature distribution away from the wall effects is also the same and follows the basic Sutton distribution.

4.2.2 Evaluation of Profile Definition - Several highly sophisticated automated procedures are in use to compute radiation transport through the shock layer. There is a RADICAL/69, the RASLE, the code used by G. Moss and the SUTO code used by K. Sutton, just to name a few. A few benchmark calculations are being made using the RASLE for a fully coupled flow field for the design of the earth entry probe. Radical/69 is essentially the radiation code in RASLE and SUTO and used to study the characteristics of the radiant environment. The computer cost for each code can be high depending on the fineness of the lattace size through the shock layer. One of the key factors governing the radiative heat transport is the definition of the temperature profile across the shock layer. Consequently this investigation centered on the numerical definition of the temperature profile, the uncertainties of the profile, and the computational cost savings that could be realized by using fewer points to define the curve. Figure 66 graphically describes the coupled temperature distribution across the shock layer and Figure 67 contains the computed heating. Using the temperatures printed out by the RASLE code (to the nearest degree kilven) results in a radiant flux of 22.5 kw/cm^2. Reducing the number of points defining the temperature profile reduces the computer run time accordingly and results in a considerable savings (about 40%). However, taking every other point from the original array does not yield the same result, nor

EFFECT OF ADIABATIC TEMPERATURE AND SHOCK THICKNESS ON RADIANT HEATING (EARTH ENTRY)

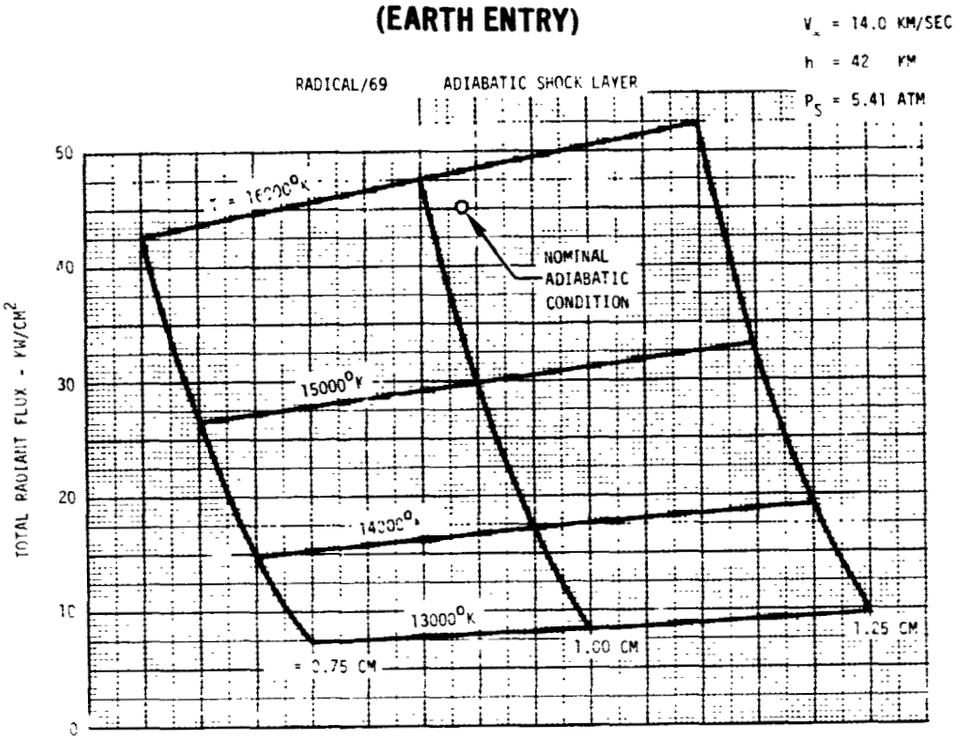

FIGURE 61

EFFECT OF WALL TEMPERATURE ON RADIATIVE HEATING

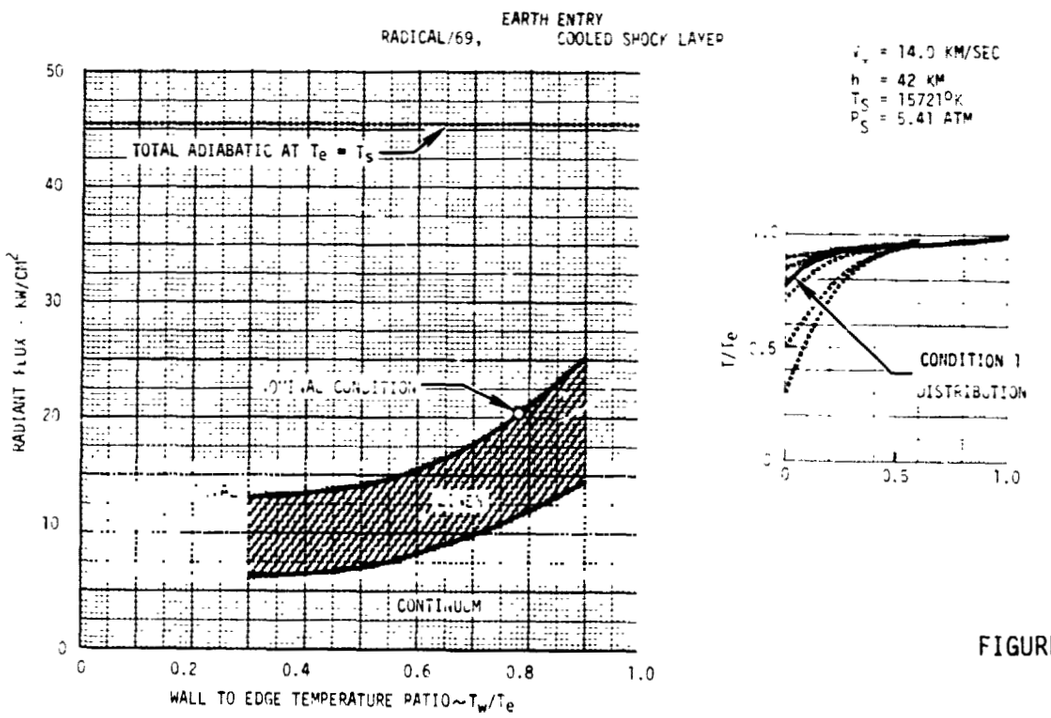

FIGURE 62

EFFECT OF WALL TEMPERATURE ON SPECTRAL FLUX DISTRIBUTION

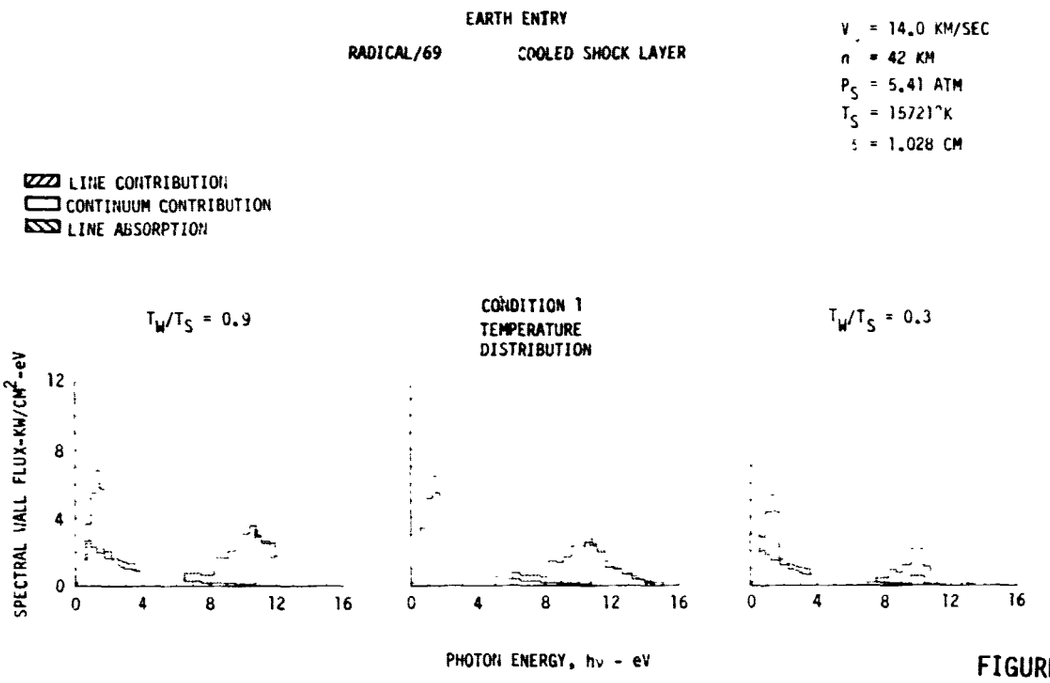

FIGURE 63

EFFECT OF TEMPERATURE PROFILE ON RADIATIVE FLUX

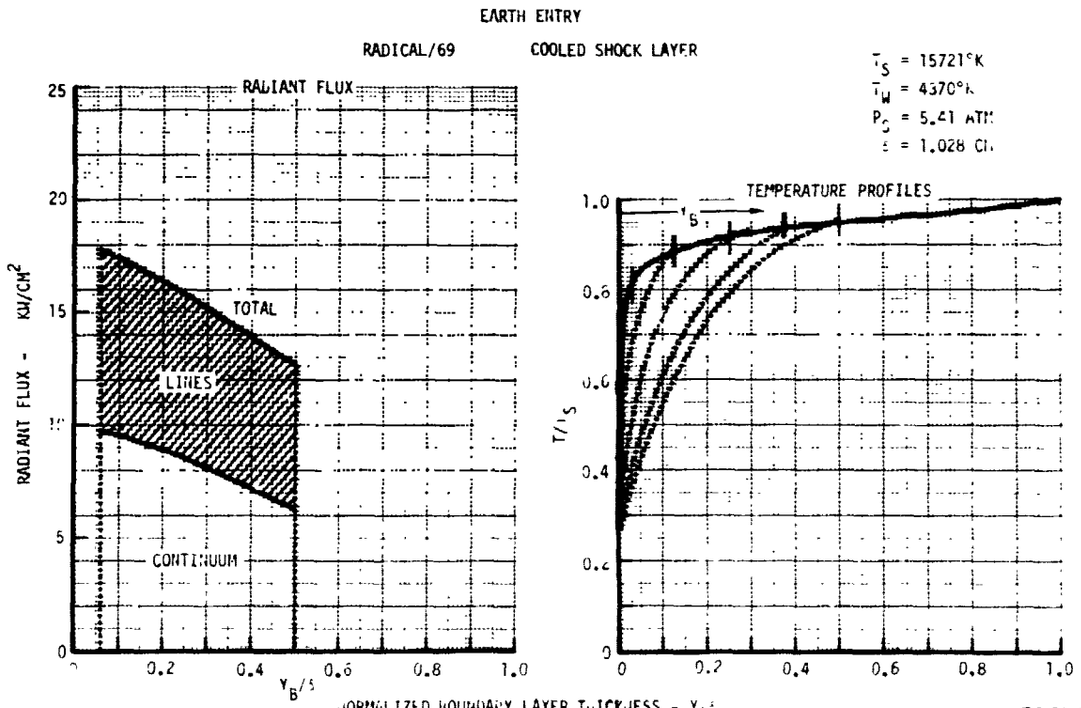

FIGURE 64

EFFECT OF FLIGHT CONDITIONS ON SPECTRAL DISTRIBUTION

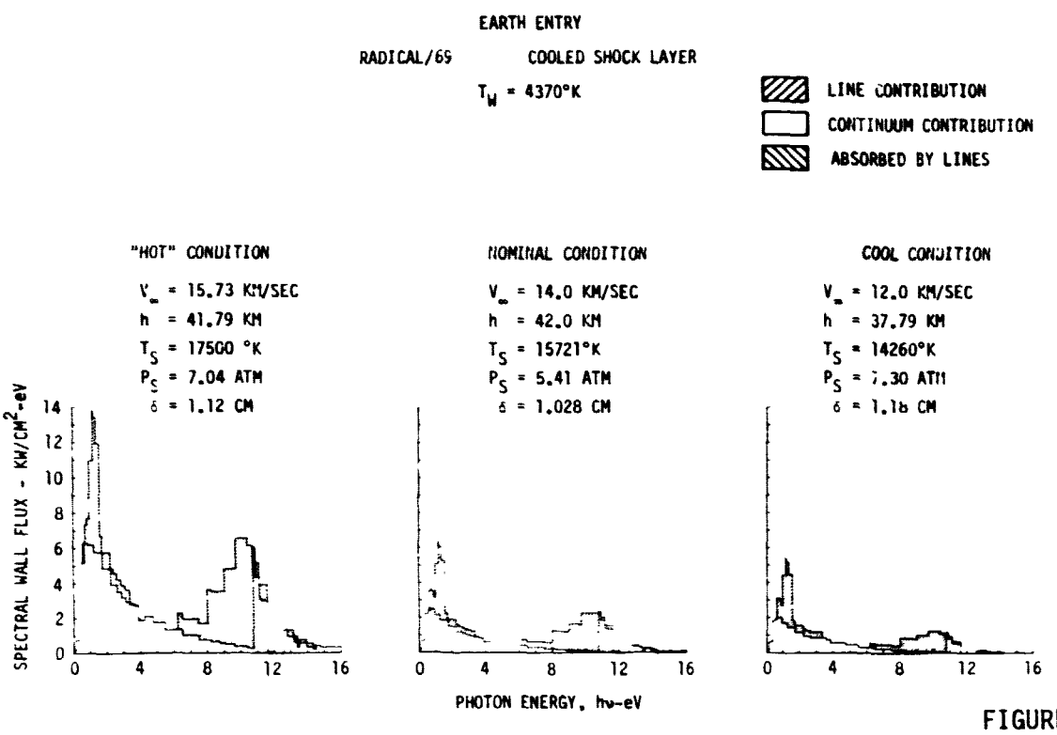

FIGURE 65

TEMPERATURE PROFILE ANALYZED FOR EARTH ENTRY SHOCK LAYER

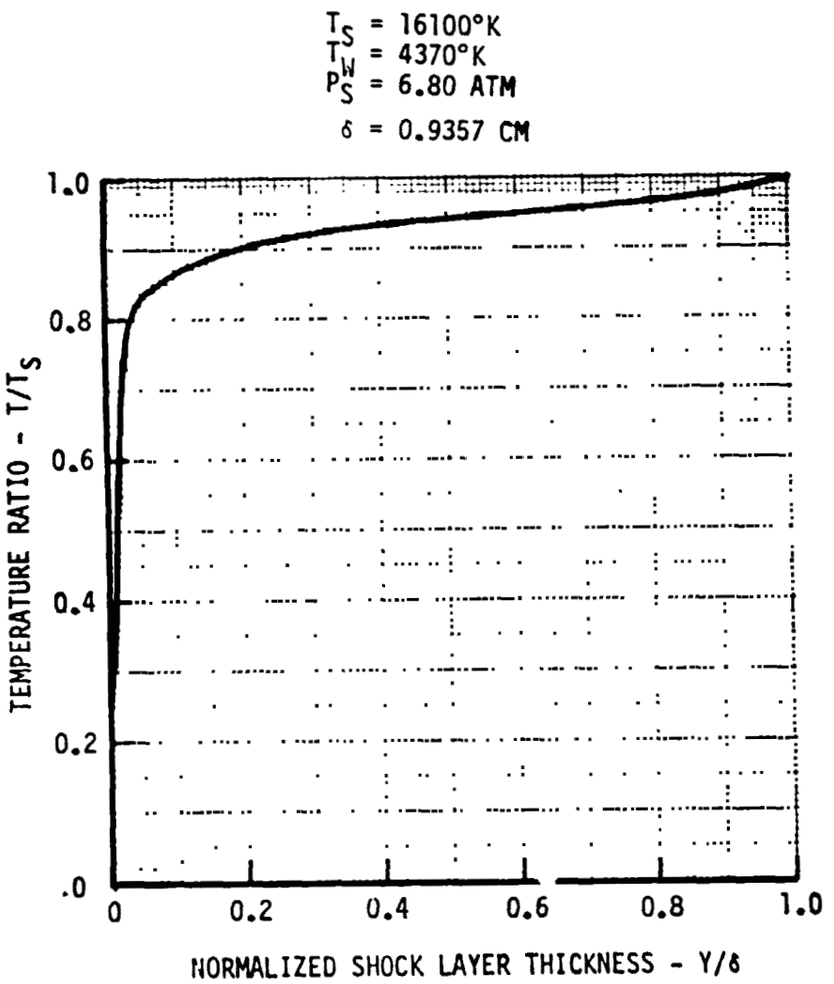

FIGURE 66

TEMPERATURE PROFILE DEFINITION ANALYSIS (FOR USE IN RADICAL/69)

ATMOSPHERIC COMPOSITION (WEIGHT FRACTION)
OXYGEN (O_2) 0.227
NITROGEN (N_2) 0.773

P_S = 6.8 ATM
δ = 0.9357 cm

	ALL RASLE POINTS	EVERY OTHER RASLE POINT	LOW ROUND-OFF	HIGH ROUND-OFF	DEFINE KNEE POINTS	CONSTANT ΔY	
Y/δ	T(°K)					Y/δ	T(°K)
0.0	4370	4370	4365	4374	4370	0.0	4370
0.000528	4930					0.060	13524
0.001075	5480	5480	5475	5484		0.125	14136
0.001935	6080				6080	0.250	14699
0.002827	6490	6490	6485	6494		0.375	14957
0.006221	7350						
0.008469	7760	7760	7755	7764	7760	0.500	15118
0.010098	8030					0.625	15295
0.011857	8310	8310	8305	8314		0.750	15456
0.013746	8630					0.875	15681
0.015831	9040	9040	9035	9044		1.000	16100
0.018143	9690				9690		
0.029023	11800	11800	11750	11849	11800		
0.048534	13200				13200		
0.103583	14000	14000	13950	14049	14000		
0.204234	14500				14500		
0.475570	15100	15100	15050	15149	15100		
0.814332	15600						
1.000000	16100	16100	16050	16149	16100		
RADIATIVE HEATING (kw/cm^2)							
CONTINUUM	12.632	11.687	11.379	11.983	12.792		12.519
LINES	9.851	8.905	8.769	9.041	9.906		10.018
TOTAL	22.483	20.592	20.148	21.024	22.698		22.537
CP TIME (SEC)	210.9	127.0	127.2	126.5	122.4		114.8

RASLE SOLUTION (Kw/cm^2)

CONTINUUM	LINES	TOTAL
13.37	10.9	24.27

FIGURE 67

does altering the values in such a way that round-off, either on the high or low side, results in the same three significant digits. What is required for this particular profile is a better definition at the knee in the curve, yet still with the reduced number of points. This may be accomplished by selecting more points in this area and reducing the number of points closer to the wall. What appears to be just as effective in this case are points equally spaced through the shock layer.

Results from the RADICAL/69 solution are eight to ten percent lower than from the RASLE code. The radiation calculations in the RASLE code have been updated and such a comparison was anticipated by Bill Nicolet who wrote both computer programs.

4.2.3 Impact of Shock Layer Carbon Concentration on Radiant Heating - The effect of carbon injection on earth entry radiative flux is presented in Figures 68, 69 and 70. The effect of a constant level of carbon through the entire shock layer for the adiabatic condition is shown in Figure 68. The effect of two different carbon distributions for the cooled shock layer temperature distributions previously presented in Figure 62 is shown in Figure 69 The presence of carbon species released into the shock layer by ablation tends to increase heating at high wall temperatures whereas at cooler wall temperatures the presence of carbon decreases heating. Figure 70 compares the spectral flux distribution with and without carbon injection as affected by wall temperature.

4.2.4 Sensitivity of Maximum Radiative Heating - In the previous sections, the impact of changing a particular environment factor on radiative heating has been analyzed. The gross changes in radiative heating are summarized in Figure 71. Knowledge of the temperature distribution in the shock layer compares with the temperature behind the shock as the main factors affecting radiative heating. Pressure is the next important factor but the uncertainties in pressure calculation methods is minimal. The other factors fall into the third category of importance. It should be pointed out that the presence of an ablation gas (carbon) in the shock layer strongly affects the temperature distribution and hence the heating. This point will be addressed in a later section.

4.3 Heat Accommodation of Heat Shield Materials for Earth Entry - To form the basis for comparison between earth entry radiant heat and that for a Jovian entry (See Section 7), a series of analyses were performed for the maximum heating point, various entry angles, wall emittance/reflectances and injectants. Figure 72 contains the detailed results including continuum/lines for the flux toward the wall

EFFECT OF CARBON CONCENTRATION ON ADIABATIC SHOCK LAYER RADIANT HEATING

EARTH ENTRY
RADICAL/69 ADIABATIC SHOCK LAYER

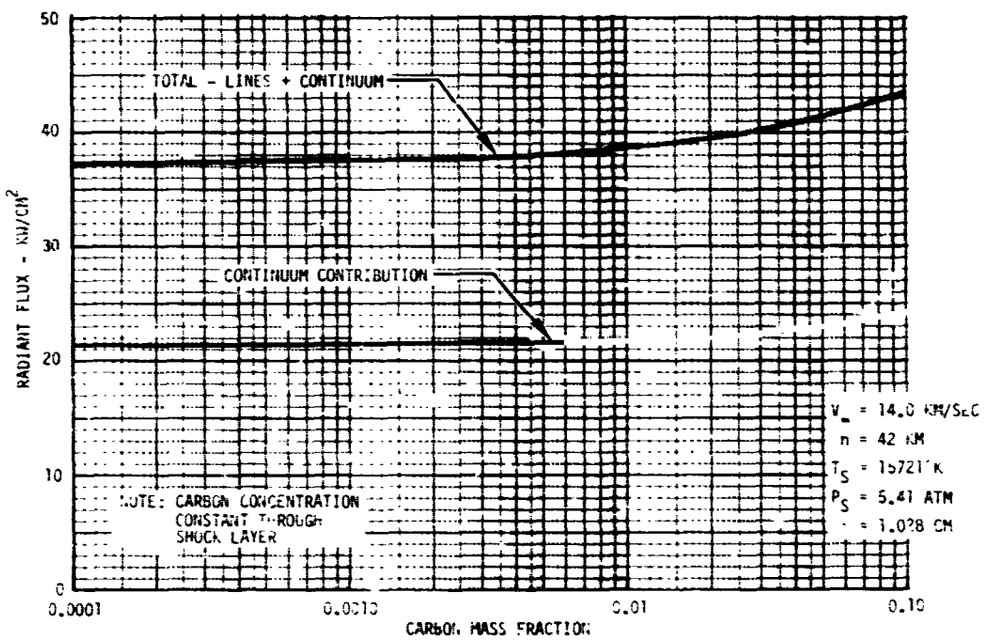

FIGURE 68

EFFECT OF WALL TEMPERATURE ON RADIATIVE HEATING WITH CARBON INJECTION

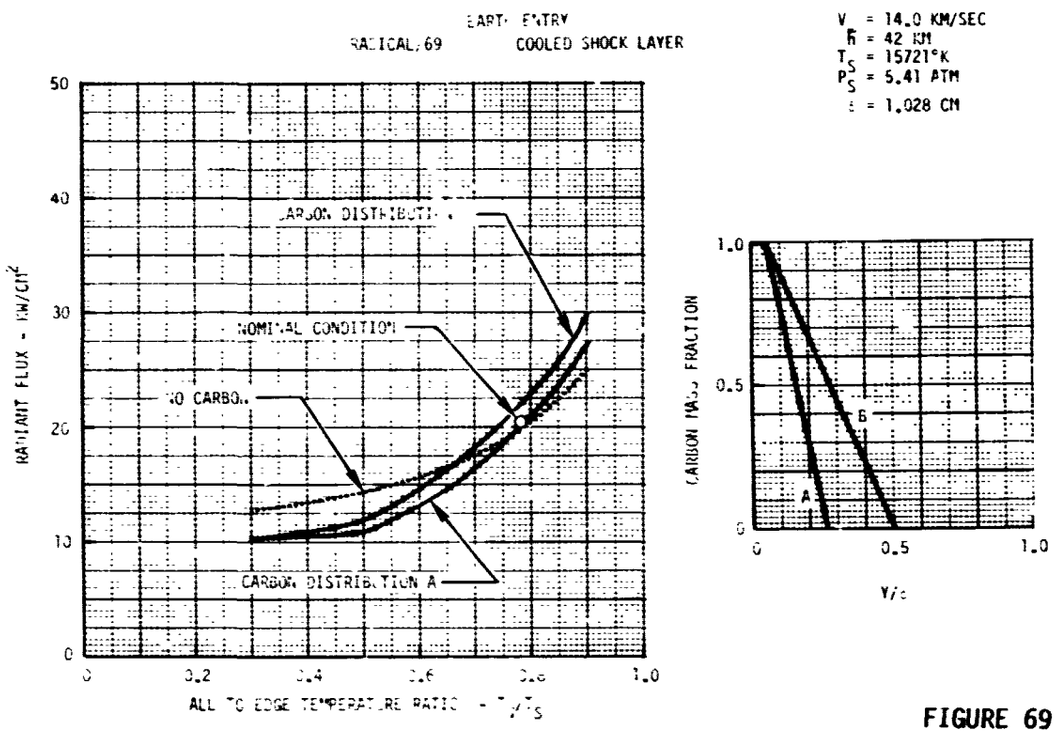

FIGURE 69

EFFECT OF WALL TEMPERATURE ON SPECTRAL FLUX WITH CARBON INJECTION

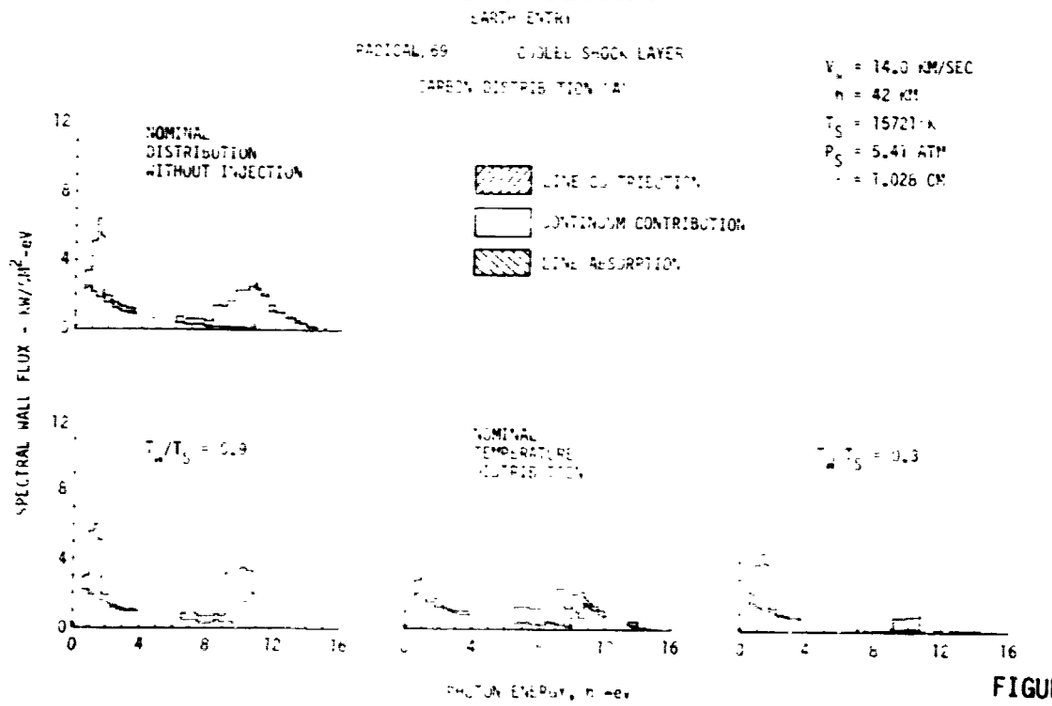

FIGURE 70

SENSITIVITY OF MAXIMUM RADIATIVE HEATING EXPERIMENTAL OBJECTIVES

CONDITION	$\frac{\Delta Q}{\Delta C}$	
	JOVIAN ENTRY	EARTH ENTRY
SHOCK LAYER TEMPERATURE LEVEL		
– UNIFORM TEMPERATURE	—	8.75
– NOMINAL TEMPERATURE DISTRIBUTION	—	8.5
BOUNDARY LAYER THICKNESS	—	-0.24
WALL TEMPERATURE	—	0.1-1.5
SHOCK LAYER THICKNESS	0.6	0.5
SHOCK LAYER PRESSURE	2.2	—
PRESENCE OF ABLATION GASES (CARBON)	-0.39	-0.31

Q $\triangleq$ NORMALIZED HEATING RATE
C $\triangleq$ NORMALIZED CONDITION
NOTE: $\Delta Q/\Delta C$ OF 0.10 MEANS THAT "Q" CHANGES BY 10% FOR A 100% CHANGE IN "C"

FIGURE 71

RADIANT HEATING COMPARISON OF SEVERAL INJECTANTS AT PEAK RADIATIVE HEATING FOR EARTH ENTRY

Atmospheric Composition (Weight Fraction)
Oxygen (O_2) 0.227
Nitrogen (N_2) 0.773

V_E = 16.76 km/sec
δ = 120 kg/m^2

SILICA WALL T = 3450°K
CARBON WALL T = 4370°K

		Flux Toward Wall (kW/cm^2)			Flux Away From Wall (kW/cm^2)			Net Flux To Ablator (kW/cm^2)
		Continuum	Lines	Total	Continuum	Lines	Total	
γ_E = -20°	No injectant-SiO_2 Wall	4.983	4.579	9.562	3.037	2.022	5.059	4.503
Altitude = 45.75 km Velocity = 13.98 km/sec	No injectant - C Wall	5.001	4.584	9.584	2.647	1.917	3.564	6.020
T_S = 15235.1°K P_S = 3.2521 ATM	Silica (SiO_2) Injection	6.577	2.769	9.346	3.595	1.419	5.014	3.422
δ = 1.06803 cm	Carbon (C) Injection	5.007	5.361	10.368	2.648	1.074	3.722	6.646
γ_E = -30°	No injectant-SiO_2 Wall	9.127	7.510	16.636	6.523	3.586	10.109	6.527
Altitude = 42.56 km Velocity = 14.03 km/sec	No injectant - C Wall	9.141	7.525	16.667	3.475	1.505	4.980	11.687
T_S = 15718.7°K P_S = 5.0393 ATM	Silica (SiO_2) Injection	10.697	4.086	14.783	7.451	4.010	11.462	3.321
δ = 1.08969 cm	Carbon (C) Injection	9.567	8.650	18.217	3.560	1.732	5.292	12.925
γ_E = -40°	No injectant-SiO_2 Wall	12.776	9.888	22.663	9.511	4.723	14.234	8.439
Altitude = 40.50 km Velocity = 14.15 km/sec	No injectant - C Wall	12.792	9.906	22.698	4.205	1.981	6.186	16.512
T_S = 16100.0°K P_S = 6.8000 ATM	Silica (SiO_2) Injection	14.218	5.315	19.533	10.746	5.243	15.990	3.543
δ = 0.93574 cm	Carbon (C) Injection	13.493	11.296	24.788	4.345	2.262	6.607	18.181

FIGURE 72

and that reflected. In making this analysis the premise was made that a correspondence between the temperature and concentration distributions across the shock layer exists between a Jovian and earth entry. Consequently, the normalized distributions in Figure 16 are applicable to earth entry.

Four states were investigated:

1) No injectant and the wall exhibited hyperpure silica radiative properties.
2) No injectant and the wall was carbonaceous (emittance = 0.8).
3) Silica injection and hyperpure silica radiative properties.
4) Carbon injection and 0.8 wall emittance .

The incident radiative flux decreased with mass injection. Even though the incident flux on the wall was slightly higher for silica than for the carbon injection, the heat reflected by the silica was much greater and consequently the carbon material has to accommodate more radiant energy than the silica. For the steeper entry (-40°), the carbon heat shield has to accommodate almost twice the energy.

4.3.1 Coupled Solutions - A second set of detailed flow field analyses were performed at the maximum heating condition for the γ_E= -40°, V_E=16.76 km/sec case. RASLE code was used to analyze three situations: no injection, carbon phenolic injection and silica injection. The RASLE code computes the velocity profile, concentration profile and the ablation rate based on an energy balance at the ablator surface . For the no injection case, the radiative flux toward the wall was 24.27 kW/cm^2 as compared to 22.698 kW/cm^2 using the RADICAL/6º code. The eight percent difference is due to technique for computing partition function. The solution for the carbon phenolic case produced a temperature distribution, as expected, that was significantly different from the no injection case and cooler than the carbon injection case. Figure 73 shows the temperature profiles. The spectral distribution (Figure 74) for carbon phenolic injection shows where the heating is reduced or eliminated as compared to the no injection case. The carbon phenolic blowing caused a thick zone of cooler gas near the wall and hence a lower heating rate. The carbon phenolic case has 25 species in the shock layer as opposed to 20 species for the carbon heat shield. Each specie has its own continuum and line radiation descriptors and hence greater computations are required for the carbon phenolic. The perinent results from the RASLE solutions are contained in Figure 75. Only a small part of the reduction in radiant flux can be attributed to a lower ablation temperature (4020°K) used for the carbon phenolic as compared

DISTRIBUTIONS ACROSS SHOCK LAYER, EARTH ENTRY

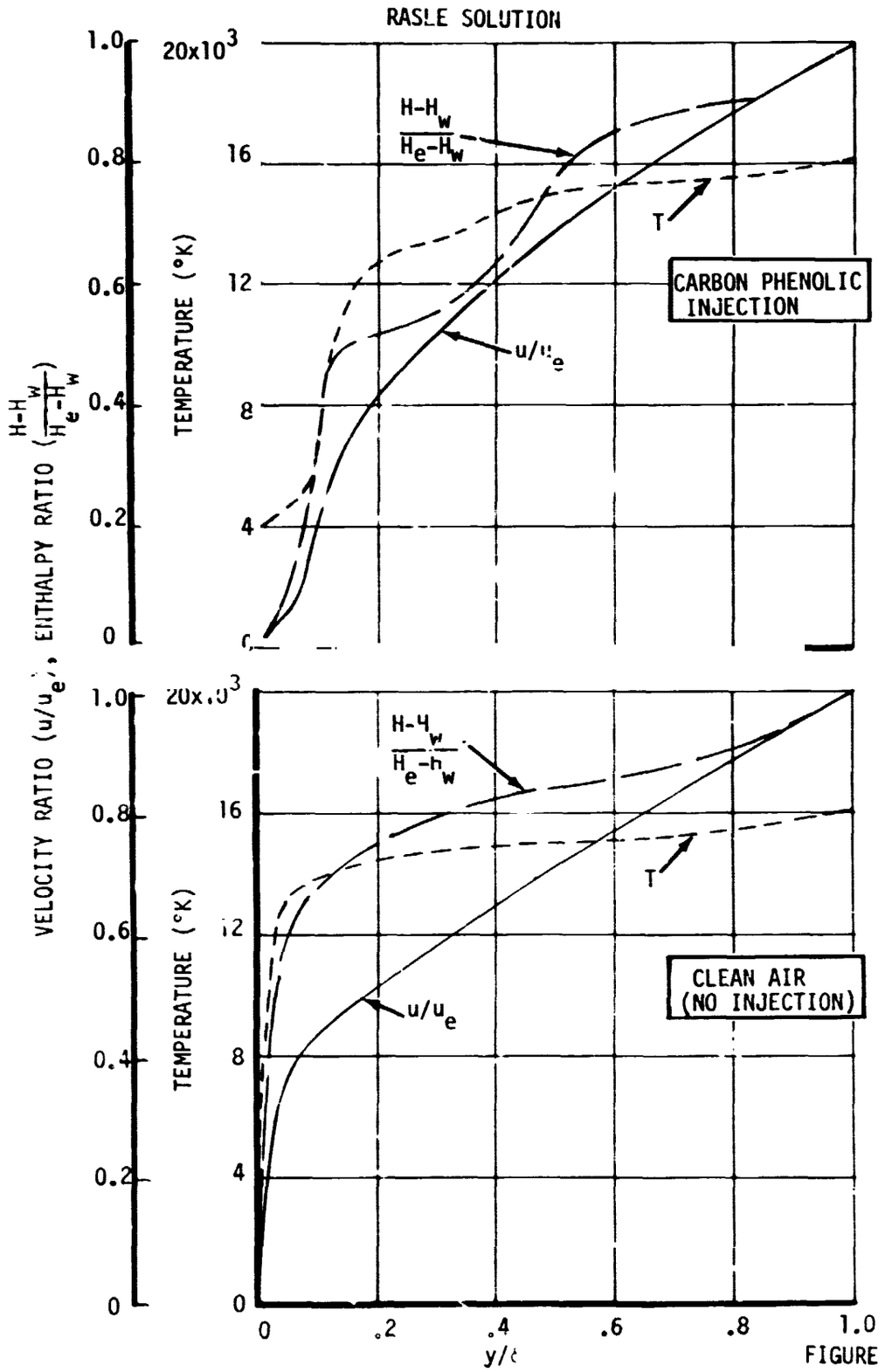

FIGURE 73

CARBON PHENOLIC ABLATION REDUCTION IN SPECTRAL HEATING, EARTH ENTRY

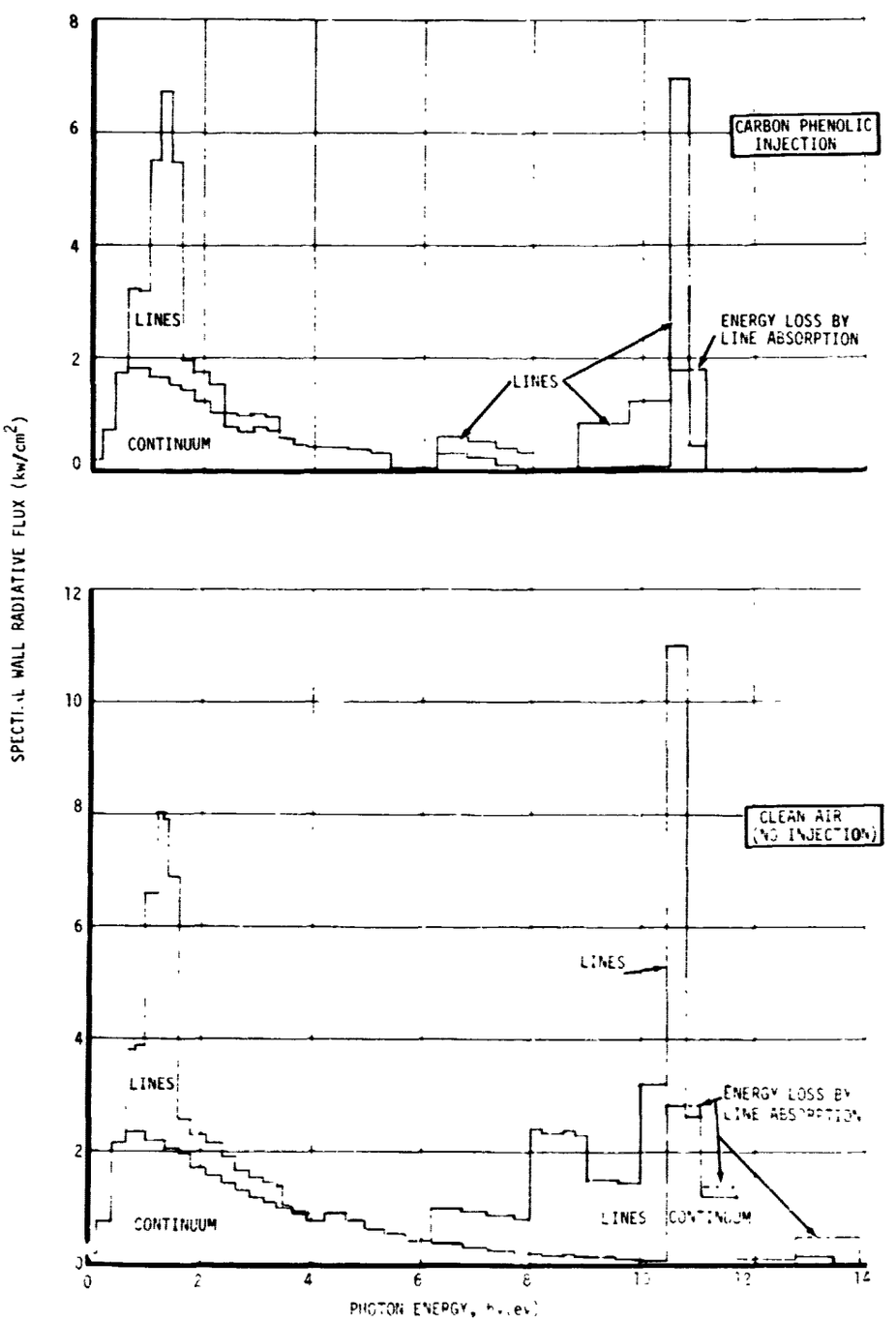

FIGURE 74

RESULTS FROM COUPLED SOLUTIONS FOR EARTH ENTRY

V_∞ = 14.1427 km/sec
ρ_∞ = 0.0037 kg/m^3
P_S = 6.80 ATM
R_N = 0.222 m

	CLEAN AIR	CARBON PHENOLIC INJECTION	SILICA INJECTION	
			RASLE	RADICAL
$\dot{m}$ ($\frac{kg}{m^2 sec}$)	--	4.606	2.846	--
δ(cm)	0.936	1.027	1.039	1.039
T_{WALL} (K)	4370.	4020.	3450.	3450.
q_{cw} (kW/cm^2)	6.52	0.379	0.554	--
q_{rw} (kW/cm^2)	24.27	12.474	14.356	16.5
$q_{Reflected} + q_{emitted}$	--	2.554	9.062 (1)	15.082 (2)

(1) CONSERVATIVE ESTIMATE OF SILICA REFLECTANCE, 90% REFLECTANCE BELOW 6.0 eV

(2) HYPERPURE SILICA REFLECTANCE, FIGURE 23, HIGH REFLECTANCE

FIGURE 75

to the no injection case (4370°K). The carbon phenolic injection case shows about a 50% reduction in radiative heating and almost a complete elimination of convective heating (from 6.52 to 0.379 kW/cm^2).

The silica injection case had a temperature distribution that was different than the other cases examined (See Figure 76). Twenty species were considered in the analysis. Also the ablation temperature (3450°K) used for silica was much lower than that for the other materials. Even so, the radiative flux (14.356 kW/cm^2) was higher than that predicted for carbon phenolic (12.474 kW/cm^2). A similar increase was experienced in the first study of carbon and silica injection.

The radiative flux computed for the 3450°K silica wall was 14.356 k $/cm^2$ as opposed to 25.481°K for the 4370°K silica wall. Cooling the wall temperature rapidly decreases the radiative flux.

EFFECT OF INJECTION ON SHOCK LAYER TEMPERATURE DISTRIBUTION

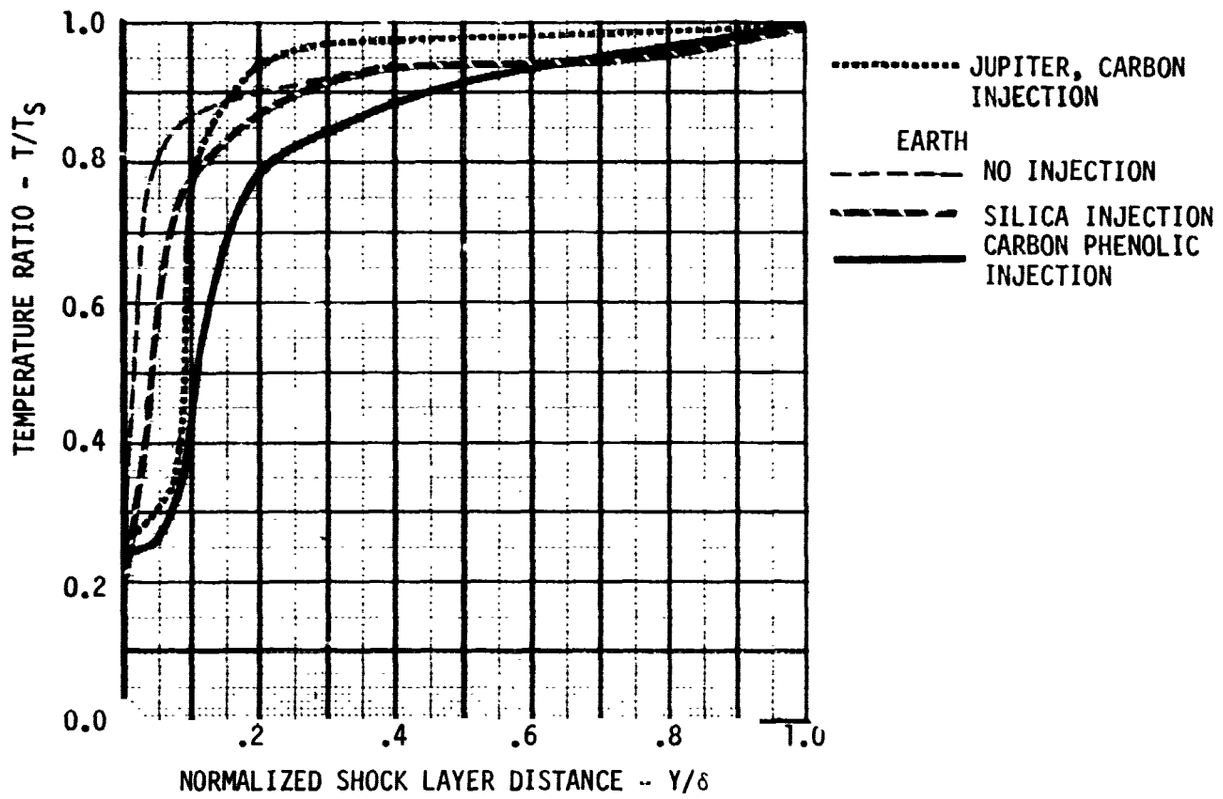

FIGURE 76

5.0 EARTH ENTRY MANEUVERS

The maneuver requirements necessary to achieve a range of steep, fast entry conditions are developed in this section. This information gives experiment planners an initial insight into the scope and nature of the orbital mission phase. Additionally, these data provide a means of comparing the initial entry conditions required for environment simulation (Section 3) with the performance capability of typical Shuttle launched boosters (Section 7).

The earth orbit maneuver requirements is divided into four parts. The first describes the basic, high apoapsis deorbit maneuver necessary to produce the extreme entry conditions of interest. The second part defines the required velocity increments for each maneuver burn as a function of entry conditions. The third part shows representative mission profiles in terms of ascent and descent ground tracks. The fourth part illustrates the correlation of environment simulation with velocity increment requirements using radiative heat flux as the example.

5.1 Deorbit Maneuvers - The selected deorbit maneuver strategy is pictorially described in Figure 77. This highly elliptical trajectory technique, suggested by NASA-Ames, allows high speed and angle entries to be efficiently achieved from a low, circular initial orbit. Compared with a direct deorbit from low altitude, this maneuver strategy reduces required thrust to those normally attainable with typical Shuttle upper stages and minimizes the velocity increment (ΔV) needed for steep entries.

As shown in Figure 77, three maneuver burns are used to accomplish deorbit beginning in a 296 km circular orbit. This initial orbit selected as typical of Shuttle insertion conditions. The first maneuver is a tangential, posigrade burn that initiates Hohmann transfer to a preselected apoapsis altitude (R_a). The value of R_a is treated as a basic mission variable and was varied from 2 to 40 earth radii above the earth's center. The second maneuver is a tangential, retrograde burn applied at apoapsis to achieve the desired entry angle. This maneuver also adjusts the trajectory so that entry occurs at a proper location relative to the desired impact point. Any plane change corrections required to attain such an entry location would be included in the second burn by vector summing. The third maneuver burn is applied along the flight path just before entry to increase velocity to the desired value.

DEORBIT MANEUVER STRATEGY

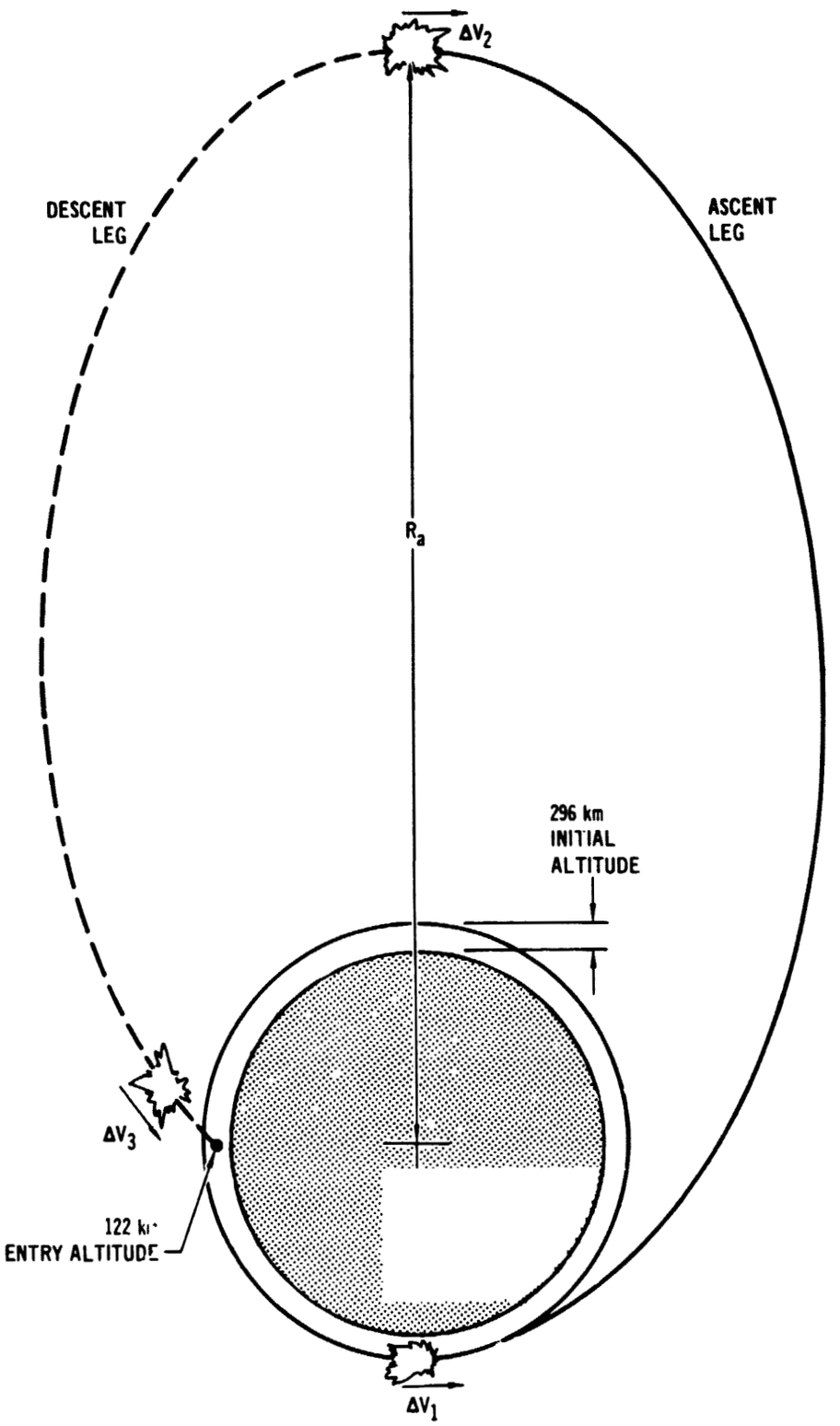

FIGURE 77

Figure 78 shows the entry velocity that would result if only the first two maneuver burns were accomplished. As indicated, each combination of entry angle and apoapsis distance produce a unique value of entry velocity that decreases with steeper angles and increases with high apoapsis distances. As apoapsis increases, the effect of entry angle diminishes to essentially zero and entry velocity approaches an upper limit of about 11 km/sec. This is well below the 13 to 20 km/sec range of required entry velocity (reference Section 3.0). Hence a third burn is always required, the mangitude of which is the difference between the required entry velocity and that achieved by a two burn maneuver.

Figure 79 shows the mission time interval required to accomplish the deorbit maneuver. This is the elapsed time between the first maneuver burn and the beginning of atmospheric entry at 122 km (400,000 ft). As shown, the time interval required is a strong function of apoapsis altitude but essentially independent of entry angle.

TWO BURN MANEUVER ENTRY VELOCITY (V*)

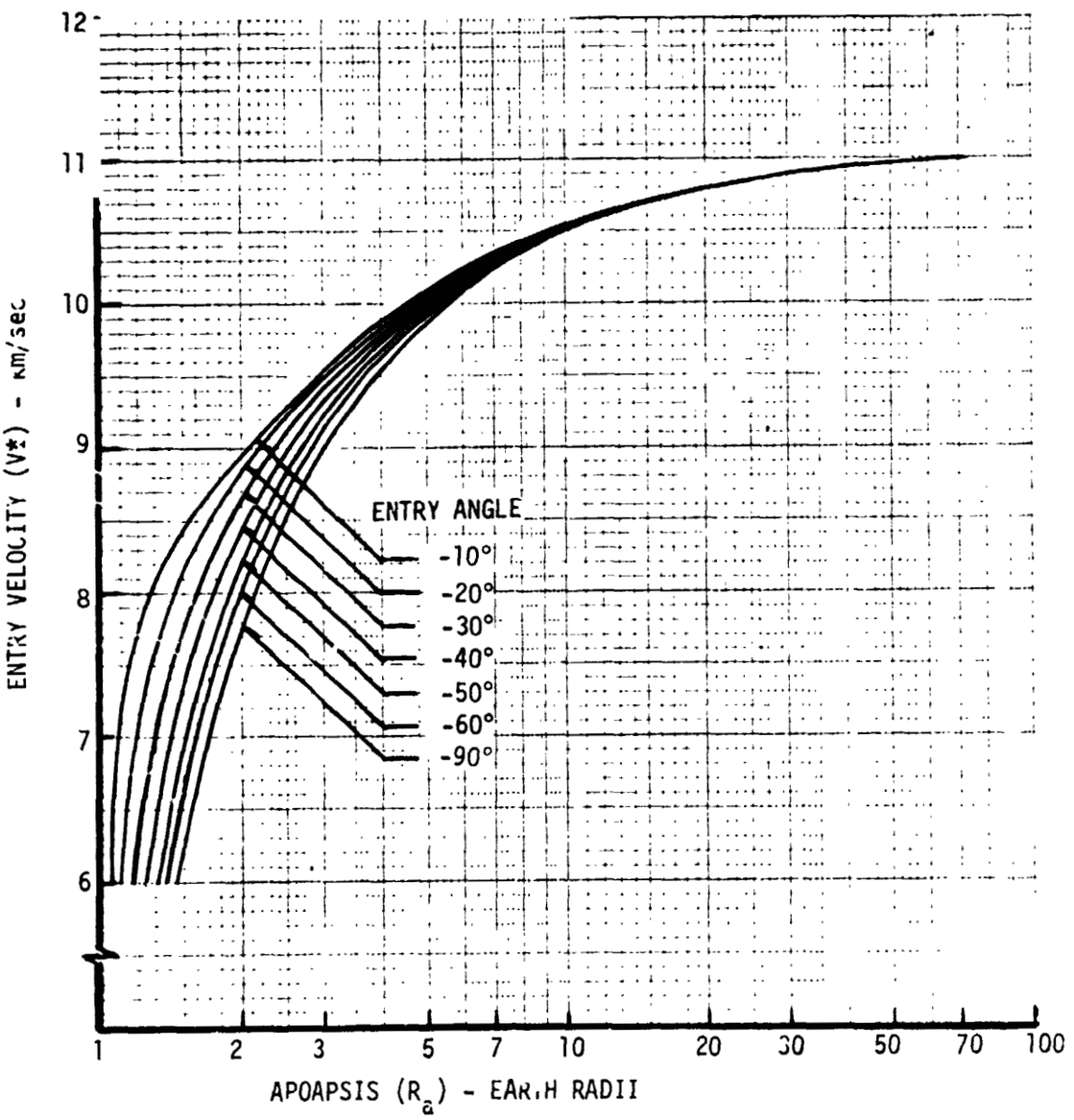

FIGURE 78

DEORBIT MANEUVER TIMES

- TIME FROM FIRST MANEUVER BURN TO ENTRY

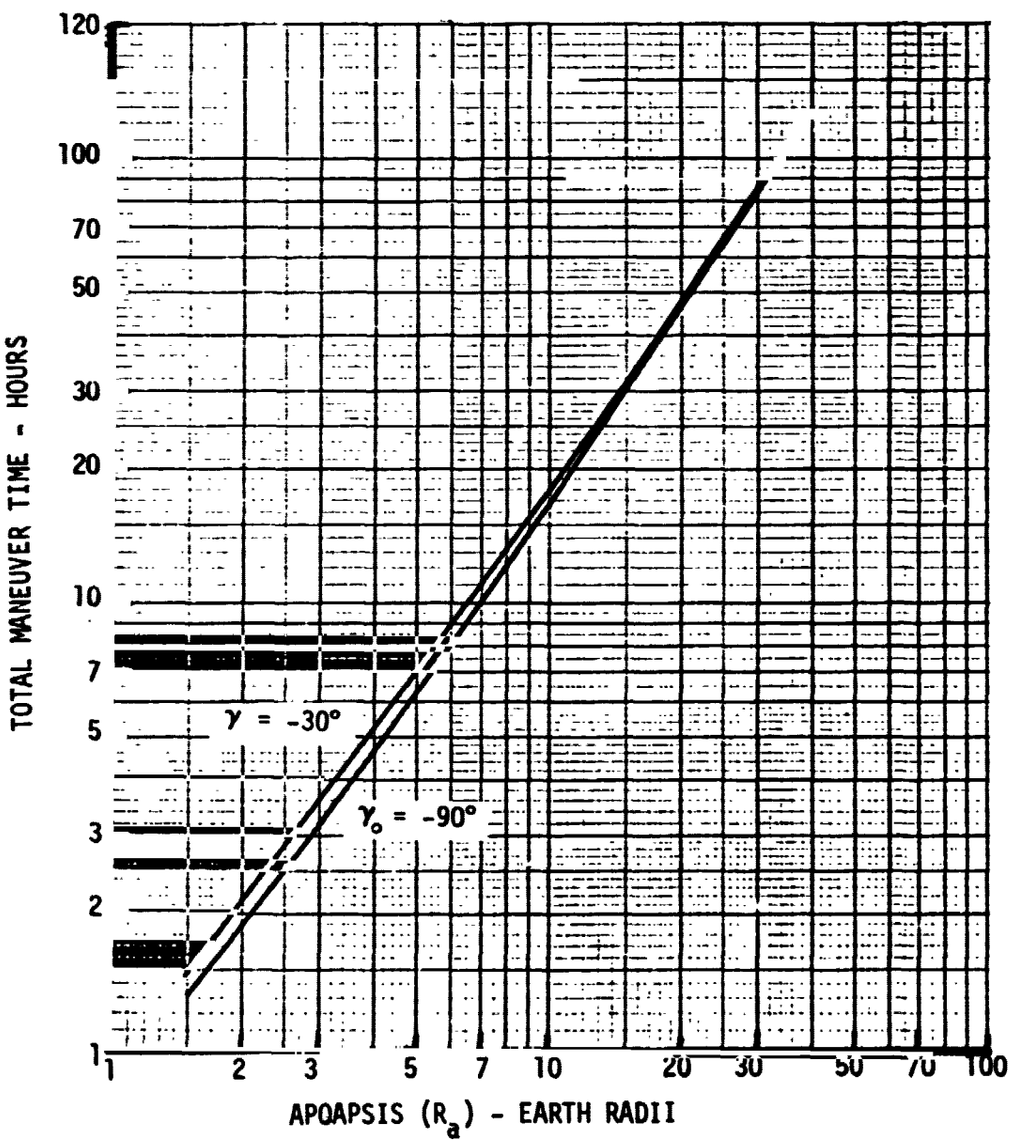

FIGURE 79

5.2 Velocity Increment Requirements - The inplane velocity increment (ΔV) required to accomplish the deorbit maneuvers are summarized in Figures 80 through 84. These data illustrate that the ΔV requirements are large but that they can be minimized by increasing apoapsis altitude, particularly for steep entry angles.

The ΔV required for the first or hohmann transfer burn (Figure 80) increases with apoapsis but is independent of entry angle. However, the second or apoapsis burn ΔV requirements (Figure 81) reduce with increasing apoapsis and increase as entry angle becomes steeper. The net effect is illustrated by the Figure 82 summation of ΔV_1 and ΔV_2. At entry angles steeper than about -50 degrees, increasing apoapsis reduces the total two burn ΔV requirements. This trend becomes very pronounced as entry angle approaches -90 degrees. However, for shallow entries, a moderate ΔV penalty results from increasing apoapsis.

The ΔV required for the third or velocity adjustment burn is presented in Figure 83 as a function of desired entry velocity. As noted in the previous subsection, this ΔV_3 is the difference between the desired entry velocity and the entry velocity resulting from a two burn velocity only (reference Figure 78). Hence the ΔV_3 requirement decreases as apoapsis altitude increases. The trend is similar with entry angle although at high apoapsis, the ΔV dependency on entry angle diminishes to essentially zero.

The total deorbit maneuver ΔV requirements, summarized in Figure 84, increase linearly with entry velocity for a given apoapsis altitude and entry angle. Lowering entry angle reduces the total ΔV required as does increasing apoapsis altitude, particularly for steep entries.

An example of the ΔV penalty associated with out-of-plane maneuvers is illustrated in Figures 85 and 86. These values represent ΔV increments that must be added to the second burn, in plane requirements to achieve a preselected impact point location. The example shown assumes impact near Ascension Island and a due east launch of Shuttle from ETR. The Shuttle orbit numbers shown correspond to deorbit maneuver initiation (ΔV_1) sometime during the second, third or fourth Shuttle orbits following initial insertion. This is discussed further in the following subsection.

These data show that plane change ΔV penalties reduce with increasing apoapsis altitude and can be minimized by selecting a relatively steep entry angle. However, for apoapsis above 3 earth radii, this ΔV penalty is small to negligible compared to the total inplane ΔV requirements of Figure 84.

FIRST BURN VELOCITY INCREMENT (ΔV_1) REQUIREMENTS

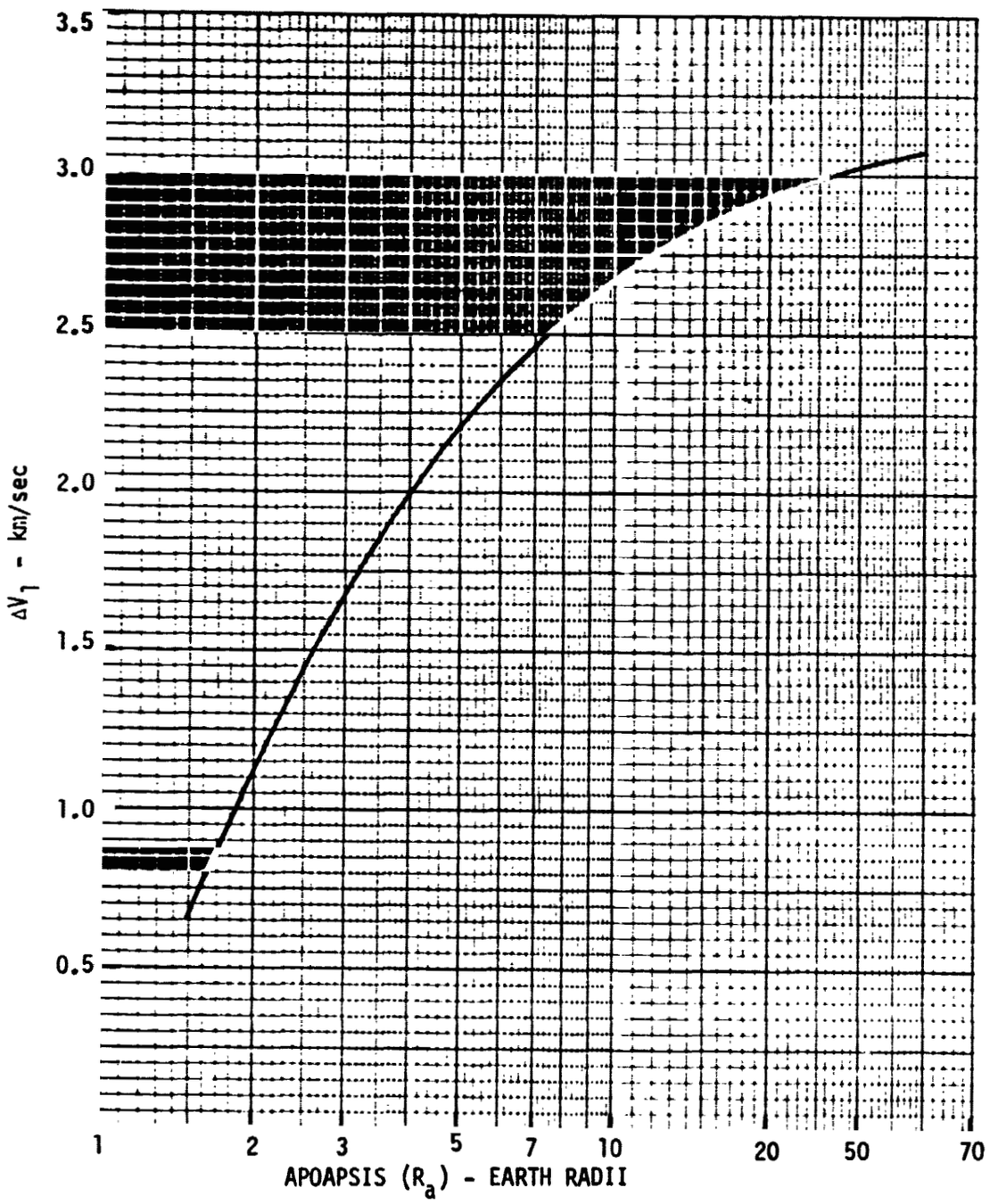

FIGURE 80

SECOND BURN VELOCITY INCREMENT (ΔV_2) REQUIREMENTS

o IN PLANE MANEUVER

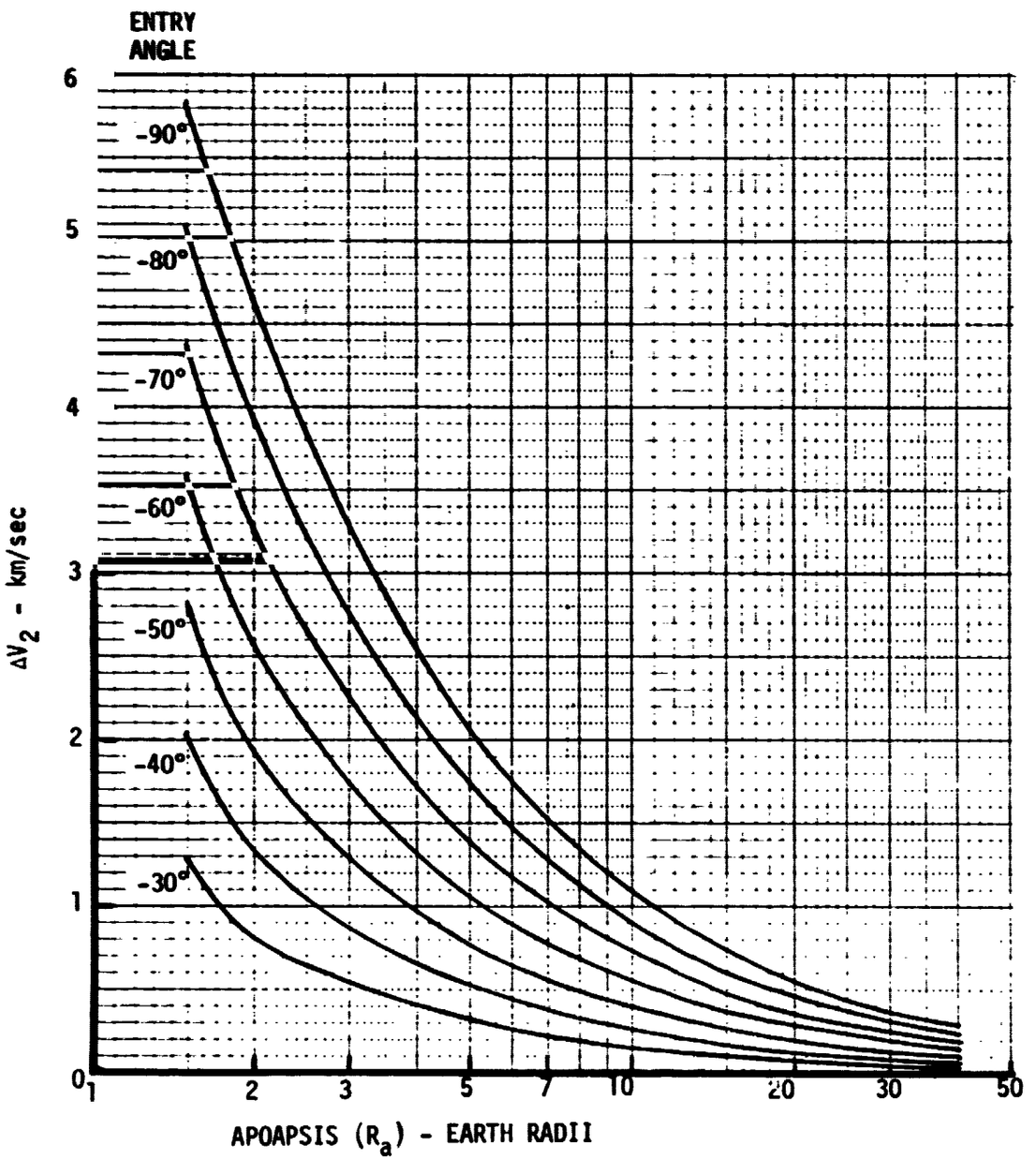

FIGURE 81

ASCENT PLUS ENTRY ANGLE VELOCITY INCREMENT ($\Delta V_1 + \Delta V_2$) REQUIREMENTS

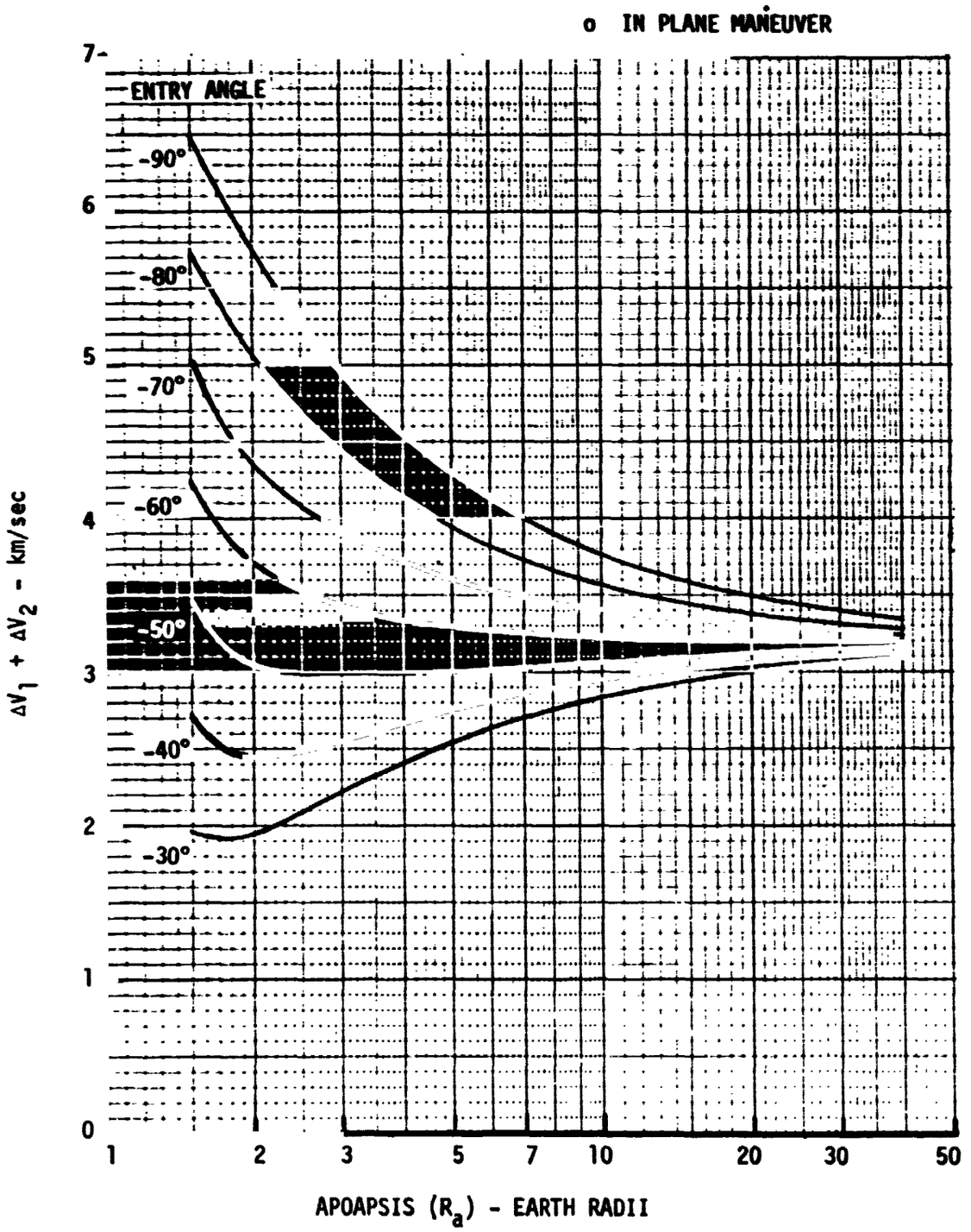

FIGURE 82

THIRD BURN VELOCITY INCREMENTS (ΔV_3) REQUIREMENT

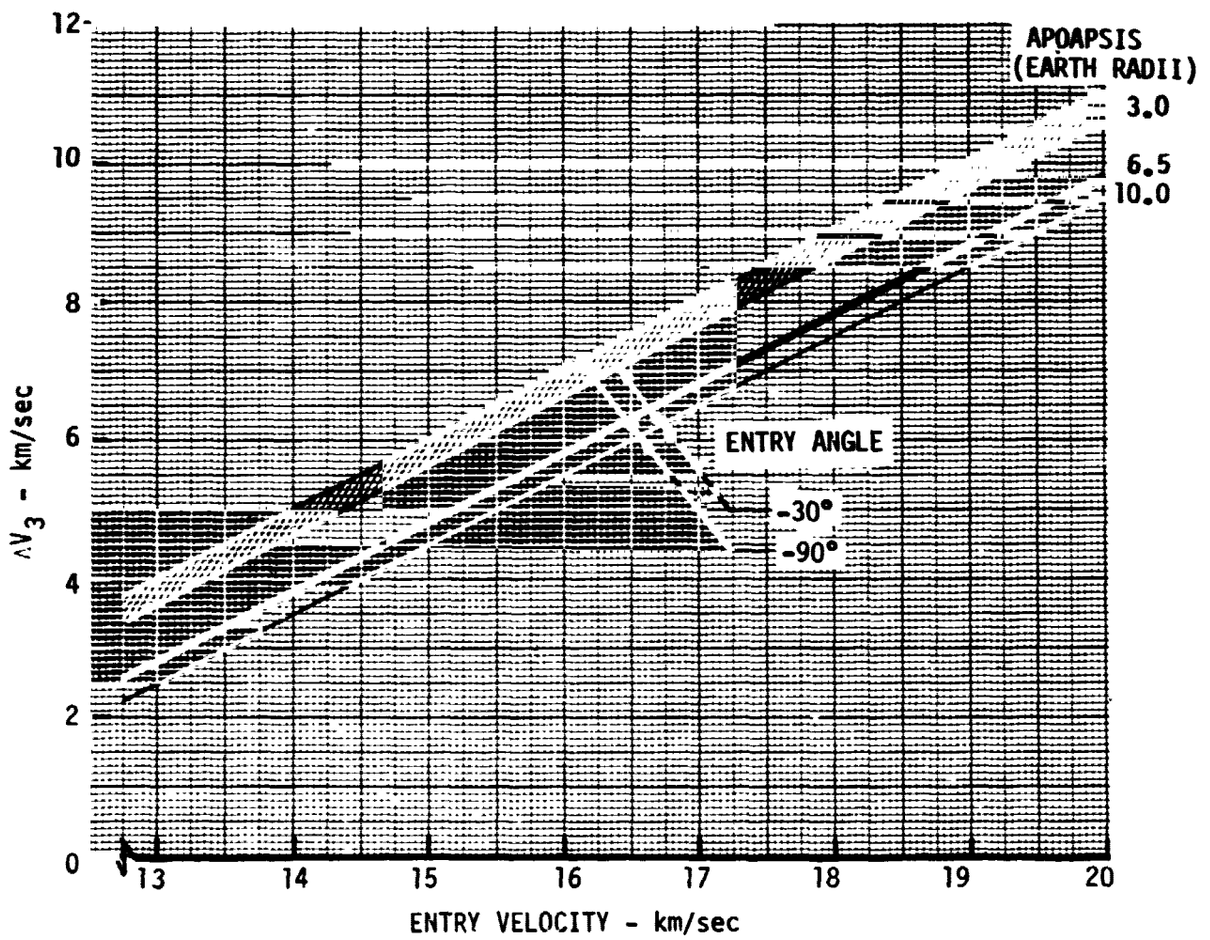

FIGURE 83

TOTAL VELOCITY INCREMENT (ΔV_{TOT}) REQUIREMENT

- IN PLANE MANEUVERS

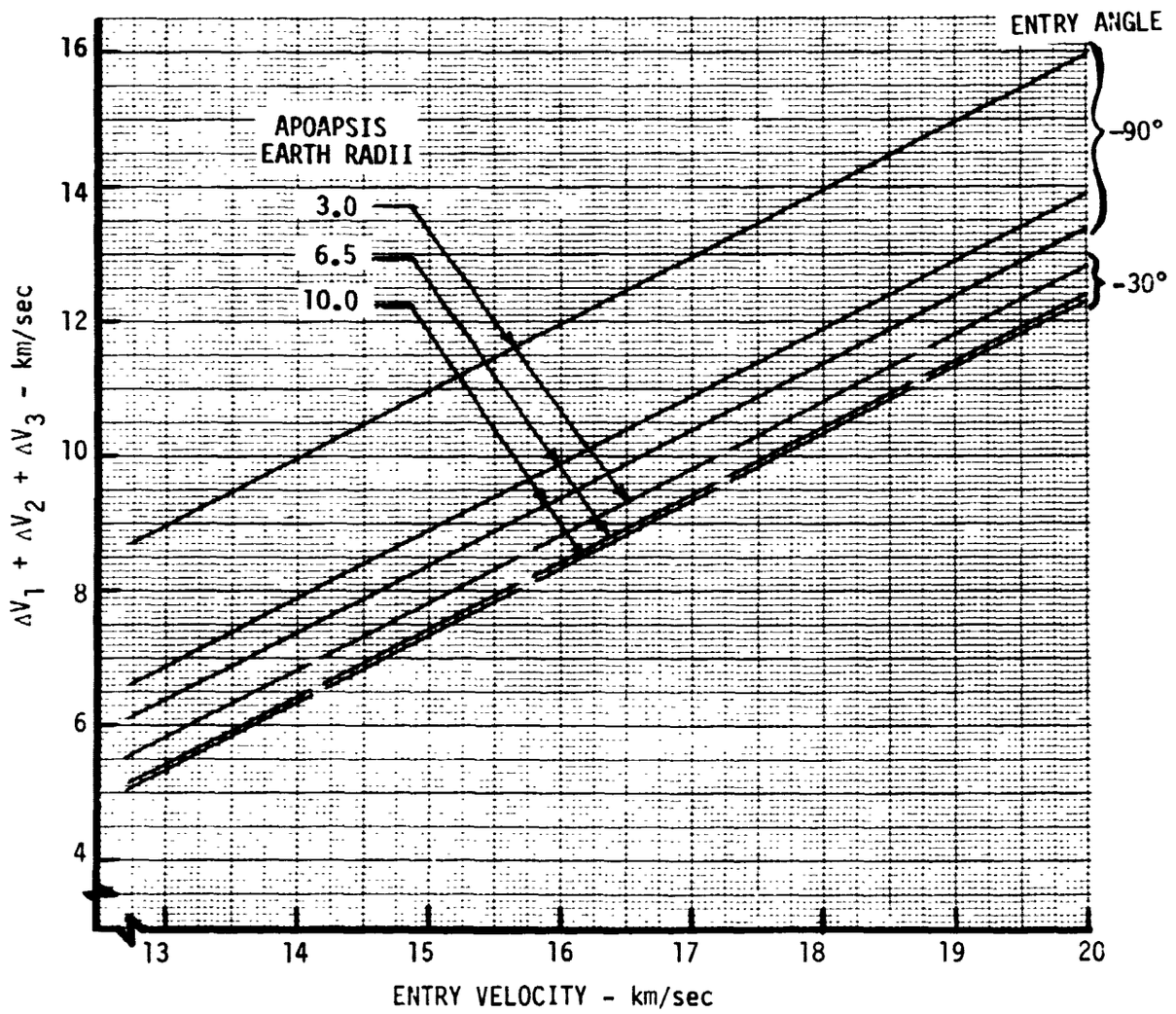

FIGURE 84

PLANE CHANGE ΔV PENALTY – R_a = 6.5

- TOTAL $\Delta V_2 = \Delta V_2$ (IN PLANE) + $\Delta(\Delta V_2)$
- DUE EAST LAUNCH FROM ETR TO 296 KM CIRCULAR ORBIT
- ASCENSION ISLAND RECOVERY ZONE

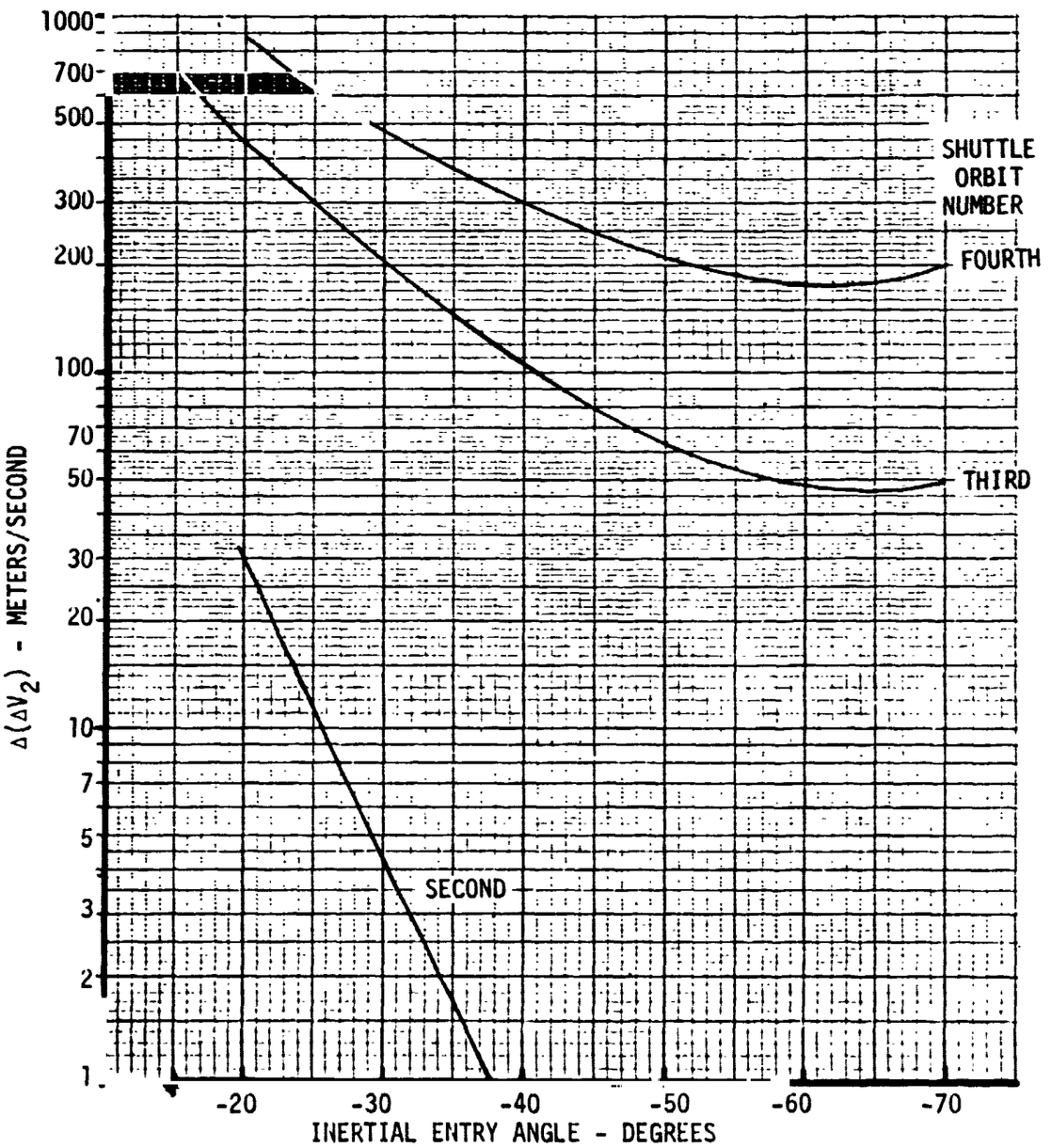

FIGURE 85

PLANE CHANGE ΔV PENALTY – R_a = 3.0

- o TOTAL $\Delta V_2 = \Delta V_2$ (IN PLANE) + $\Delta(\Delta V_2)$
- o DUE EAST LAUNCH FROM ETR TO 296 KM CIRCULAR ORBIT
- o ASCENSION ISLAND RECOVERY ZONE

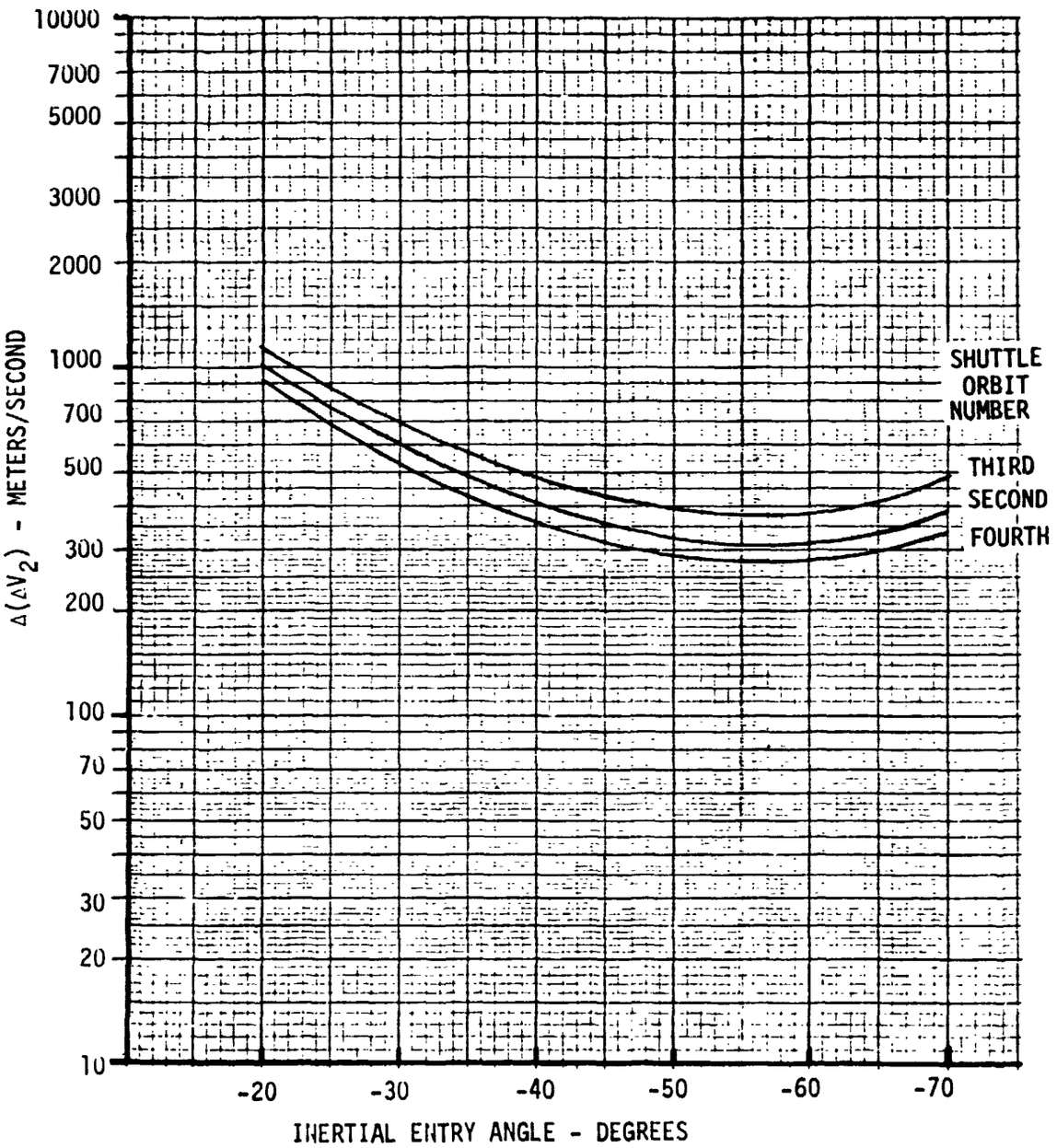

FIGURE 86

5.3 Ground Tracks - In the previous sections the booster ΔV requirements for each burn and the resultant inertial entry conditions have been defined. This section identifies the latitude and longitude of the first and second booster burns, the resultant entry conditions for impact at Ascension Island, the Shuttle orbits from which these can be achieved, and two representative ground tracks.

To establish these parameters, the following deorbit strategy was used. The first burn of the Hohmann transfer was assumed to be made from a point on the Shuttle orbit and at the same heading as the Shuttle, i.e., no plane change was associated with the first burn. The location of apoapsis on the Hohmann transfer orbit is then at a latitude equal in magnitude but opposite in sign to the first burn latitude. The apoapsis longitude will be the first burn longitude plus 180 degree minus the earth's angular velocity, Ω , multiplied by the Hohmann transfer time, T, from the first burn to apoapsis, i.e.,

$$\theta_{apogee} = \theta_{perigee} + 180 - \Omega T$$

Once the apoapsis location was determined, the trajectory from apoapsis to impact at Ascension was computed as follows. First the impact point latitude and longitude at Ascension was selected as -7.95 deg (7.95 deg south),345.667 deg (14.333 deg west), respectively. Then the deorbit trajectory required to hit the impact point from apogee was computed along with the inertial entry conditions at the pierce point. The deorbit trajectory velocity, flight path angle, and azimuth at apoapsis is established by the second burn of the booster. The vectorial difference between pre-burn and post-burn conditions at apogee establish the ΔV requirements for the booster. This analysis identifies a latitude and longitude for the first and second burns on specified Shuttle orbits and the resultant velocity, flight path angle, and azimuth that can be achieved at Ascension Island. The trajectory from entry to impact neglects atmospheric effects. This does not affect the results significantly.

The first question to be resolved was: what Shuttle launch azimuth should be used from KSC? Fortunately, a due east launch from KSC to a 296 km circular orbit provides impact at Ascension with essentially no plane change requirements at apogee and entry velocities (prior to the third burn) of more than 10 km/sec over a wide range of flight path angles. Figure 87 is a summary table defining potential first burn locations and resultant entry conditions for a 6.5 earth radii deorbit trajectory. The Shuttle longitude and latitude correspond to 10 deg increments along the orbital path. The particular values selected provide inertial entry conditions in

DEORBIT CONDITIONS FOR R_a = 6.5 TRAJECTORY

SHUTTLE ORBIT ALTITUDE = 160 NMI

SHUTTLE ORBIT #	FIRST BURN CONDITIONS LONG. (DEG)	LAT. (DEG)	AZIMUTH (DEG)	ENTRY INERTIAL CONDITIONS V_E (KM/SEC)	γ_E (DEG)	AZIMUTH (DEG)	BOOSTER ΔV AT APOGEE ΔV_2 (KM/SEC)	ΔΔV (KM/SEC)	TIME SINCE FIRST ORBIT TIME (MIN)
2	174.04	13.80	64.82	10.29	-19.60	39.90	113.81	32.310	75.26
	182.90	17.86	67.42	10.28	-23.97	60.83	160.27	13.59	77.77
	192.17	21.44	70.76	10.27	-28.57	61.51	218.40	5.595	80.28
	201.90	24.41	74.81	10.26	-33.37	62.00	288.73	2.248	82.79
↓	212.07	26.64	79.48	10.25	-38.36	62.35	371.64	.845	85.30
2	222.58	28.03	84.61	10.24	-43.51	62.56	467.20	.275	87.80
3 & 2	233.28	28.50	90.00	10.23	-48.82	62.66	575.24	.062	90.31
3	254.49	26.64	100.52	10.21	-59.81	62.57	825.39	.005	95.33
	264.66	24.41	105.19	10.20	-65.44	62.42	965.00	.021	97.84
3	274.39	21.44	109.24	10.19	-71.10	62.23	1111.69	.033	100.34
3	169.06	21.44	70.76	10.29	-19.76	46.65	115.38	454.28	170.59
	178.79	24.41	74.81	10.28	-23.87	51.29	159.07	327.97	173.10
	188.96	26.64	79.48	10.27	-28.26	54.81	214.08	234.90	175.61
↓	199.47	28.03	84.61	10.26	-32.87	57.67	280.90	167.34	178.11
3 & 4	210.17	28.50	90.00	10.25	-37.69	60.13	359.91	120.27	180.62
4	220.88	28.03	95.39	10.24	-42.68	62.37	451.24	88.92	183.13
	231.39	26.64	100.52	10.23	-47.84	64.56	554.68	68.74	185.64
	241.55	24.41	105.19	10.22	-53.13	66.85	669.37	56.33	188.15
	251.28	21.44	109.24	10.21	-58.50	69.47	794.09	49.37	190.65
	260.56	17.86	112.58	10.20	-63.92	72.78	926.83	46.76	193.16
	269.42	13.80	115.18	10.19	-69.31	77.45	1064.63	48.63	195.67
↓	277.94	9.39	117.03	10.18	-74.52	84.93	1202.55	56.93	198.18
4	286.23	4.753	118.13	10.18	-79.27	98.95	1330.94	78.59	200.69
4	165.85	26.64	79.48	10.29	-20.40	38.36	121.62	863.33	265.92
4	176.36	28.03	84.61	10.28	-23.99	46.00	160.43	684.69	268.42
4 & 5	187.06	28.50	90.00	10.39	-27.05	51.80	209.65	546.27	270.93
5	197.77	28.03	95.39	10.27	-32.14	57.09	269.80	437.12	273.44
	208.28	26.64	100.52	10.26	-36.59	61.52	341.14	351.69	275.95
	218.44	24.41	105.19	10.25	-41.23	65.64	423.67	286.61	278.46
	228.17	21.44	109.24	10.24	-46.01	69.74	516.97	239.04	280 96
	237.45	17.86	112.58	10.23	-50.90	73.95	620.13	206.30	283.47
	246.31	13.80	115.18	10.22	-55.84	78.70	731.28	186.41	285.98
	254.83	9.39	117.03	10.21	-60.73	84.39	847.82	177.97	288.49
	271.29	0.0	118.50	10.19	-69.83	101.62	1078.21	199.15	293.51
	279.45	-4.75	118.13	10.19	-73.49	115.77	1174.98	238.79	296.02
↓	287.74	-9.39	117.03	10.18	-75.90	135.46	1239.54	313.63	298.53
5	296.26	-13.80	115.18	10.18	-76.43	159.02	1253.79	438.86	301.03

FIGURE 87

the 10 km/sec velocity range and flight path angles between -20 and -79 deg. The azimuth on the Shuttle orbit is the inertial value and corresponds to the payload azimuth during the first burn. The entry azimuth is an inertial azimuth at the entry altitude of 121.92 km. The inplane ΔV requirement, ΔV_2, and the ΔV penalty, $\Delta\Delta V$, for plane change at apoapsis are also provided. Finally, the time between the end of the first orbit and the first Hohmann transfer burn is given. For the first window on orbit 2 and 3 almost no plane change penalty is incurred. During later Shuttle orbits, the plane change ΔV penalty is minimum for the intermediate values of flight path angles. Deorbit opportunities are available on three consecutive Shuttle orbits with at least a 25 minute launch window on each orbit (at the sacrifice of entry flight path angle). This allows for very flexible mission planning.

Figure 88 tabulates the same type of data for a deorbit trajectory with a 3.0 earth radii apogee. The first Hohmann transfer burn must occur further east than for the higher apoapsis deorbit discussed previously. This is due to the shorter flight time of the low apoapsis mission. The entry velocities are between 9 and 9.5 km/sec and the approach azimuth is more from the west than the previous case. The most significant difference is the higher plane change ΔV penalty which on the first opportunity exceeds 300 km/sec for all cases.

To provide mission planning information, the times given in the last column of Figures 87 and 88 are plotted as a function of the inertial entry angle in Figure 89. For a given entry angle this time can be added to the total deorbit times given in Figure 79 to give the total time from end of first orbit to impact at Ascension. The end of the first orbit is used as the initial time because Shuttle orbit insertion requires most of the first orbit. Depending upon the procedure for circularizing the Shuttle orbit, the time for the first orbit can vary significantly.

The data provided in Figures 87, 88 and 89 can be used for mission planning and to define ground tracks. Figures 90 and 91 provide typical ground tracks for the 6.5 and 3.0 earth radii missions, respectively. The deorbit maneuvers are made from the second Shuttle orbit and the entry conditions are noted on the figures. For the high apogee case of Figure 90, the first burn occurs near Hawaii and could be tracked from there. The Hohmann transfer ground track goes over Mexico and the northern coast of South America. As the payload approaches apoapsis the relative ground speed is faster than the payload velocity and the ground track reverses. The second burn occurs at apoapsis just off the east coast of South America. After the apoapsis burn, the ground track continues westward until the

DEORBIT CONDITIONS FOR R_a = 3.0 TRAJECTORY

SHUTTLE ORBIT ALTITUDE = 160 NMI

SHUTTLE ORBIT #	FIRST BURN CONDITIONS LONG. (DEG)	LAT. (DEG)	AZIMUTH (DEG)	ENTRY INERTIAL CONDITIONS V_E (DEG)	γ_E (DEG)	AZIMUTH (DEG)	BOOSTER ΔV AT APOGEE ΔV_2 (KM/SEC)	ΔΔV (KM/SEC)	TIME SINCE FIRST ORBIT TIME (MIN)
2	96.214	-24.408	74.81	9.50	-19.83	114.80	247.75	1047.64	52.68
	105.944	-21.440	70.76	9.47	-23.30	110.36	327.41	847.89	55.19
	115.221	-17.861	67.42	9.44	-27.05	106.62	426.21	692.03	57.70
	124.082	-13.803	64.82	9.41	-31.09	103.27	546.31	569.59	60.21
	132.605	- 9.393	62.97	9.37	-35.42	100.09	689.92	474.99	62.72
	140.892	- 4.753	61.87	9.32	-40.05	96.86	859.02	404.58	65.23
	149.059	0	61.50	9.27	-44.98	93.38	1054.90	355.21	67.74
	157.225	4.753	61.87	9.22	-50.19	89.40	1277.56	324.49	70.24
	165.512	9.393	62.97	9.17	-55.64	84.52	1524.79	311.38	72.75
	174.035	13.803	64.82	9.12	-61.20	78.11	1790.13	317.59	75.26
	182.897	17.861	67.42	9.08	-66.67	69.03	2061.11	349.53	77.77
	192.17	21.44	70.76	9.05	-71.61	55.19	2312.95	424.15	80.28
	201.90	24.41	74.81	9.04	-75.18	33.69	2498.18	579.76	82.79
2	212.07	26.64	79.48	9.03	-76.14	5.23	2548.30	874.81	85.30
3	92.111	-17.861	67.42	9.51	-18.10	107.20	212.38	1312.40	148.01
	100.972	-13.803	64.82	9.49	-21.35	101.73	281.24	1067.79	150.52
	109.496	- 9.393	62.97	9.46	-24.89	97.27	367.69	879.84	153.03
	117.783	- 4.753	61.87	9.43	-28.71	93.40	473.90	731.88	155.54
	125.949	0	61.50	9.39	-32.81	89.81	601.84	615.28	158.05
	134.116	4.753	61.87	9.35	-37.20	86.29	753.46	525.36	160.55
	142.403	9.393	62.97	9.30	-41.88	82.63	930.29	458.87	163.06
	150.926	13.803	64.82	9.25	-46.84	78.59	1132.88	413.43	165.57
	159.787	17.861	67.42	9.20	-52.05	73.86	1360.19	387.45	168.08
	169.064	21.440	70.76	9.16	-57.41	67.98	1607.85	381.29	170.59
	178.794	24.408	74.812	9.11	-62.78	60.18	1867.26	398.54	173.10
	188.958	26.640	79.480	9.08	-67.87	49.14	2121.60	449.29	175.61
3	199.47	28.03	84.61	9.05	-72.13	32.78	2339.75	556.47	178.11
3 & 4	210.17	28.50	90.00	9.04	-74.64	9.51	2469.74	762.47	180.62
4	94.673	- 4.753	61.866	9.50	-19.13	90.13	233.04	983.70	245.85
	102.804	0	61.500	9.48	-22.60	86.08	310.27	790.90	248.36
	111.006	4.753	61.866	9.45	-26.34	82.56	406.44	642.56	250.86
	119.294	9.393	62.969	9.41	-30.36	79.42	523.67	527.08	253.37
	127.817	13.803	64.816	9.37	-34.67	76.43	664.21	483.44	255.88
	136.678	17.861	67.416	9.33	-39.28	73.41	830.12	372.47	258.39
	145.955	21.440	70.761	9.28	-44.20	70.16	1022.97	325.82	260.90
	155.685	24.408	74.812	9.23	-49.41	66.46	1243.34	295.87	263.41
	165.849	26.640	79.480	9.18	-54.88	61.98	1489.45	281.19	265.92
4	176.359	28.028	84.614	9.13	-60.52	56.18	1756.79	282.53	268.42
4 & 5	187.063	28.500	90.00	9.09	-66.15	48.04	2035.26	304.59	270.93
5	197.766	28.028	95.386	9.05	-71.45	35.61	2304.60	360.66	273.44
	208.276	26.640	100.52	9.03	-75.65	15.44	2522.65	483.85	275.95
5	218.44	24.41	105.19	9.03	-77.41	135.72	2614.84	739.84	278.46

FIGURE 88

velocity again exceeds earth rotational speed near the west coast of South America. The ground track then proceeds northeast until impact at Ascension. Because of the apogee altitude of 6.5 earth radii, the second burn is observable from Ascension.

The ground track for the low apoapsis deorbit is quite different as shown in Figure 91. The first Hohmann transfer burn occurs over Indonesia and north of Australia - considerably west of the previous case. The Hohmann transfer orbit track is only slightly different from a typical Shuttle track until it passes over the coast of Mexico. Apoapsis is achieved over northern South America. At this altitude the second burn will be observable from Ascension. The ground track from apogee to impact then approaches Ascension from the west as compared to the south-west approach for the higher apoapsis.

The time line for the R_a = 3.0 and 6.5 missions are summarized in Figure 92. The R_a = 3.0 mission takes about six hours and the R_a = 6.5 mission takes just under 13 hours.

In conclusion, a due east launch from KSC provides multiple opportunities for payload targeting at Ascension. Opportunities exist during the second, third, or fourth orbits. The plane change penalty at apoapsis can be minimized by selecting appropriate launch points on the Shuttle orbit. Coverage of the second burn is excellent from Ascension; coverage of the first burn may be possible from Hawaii, KMR, or Guam for specific entry conditions.

TIME IN INITIAL ORBIT

o TIME MEASURED FROM END OF 1ST ORBIT TO FIRST MISSION BURN

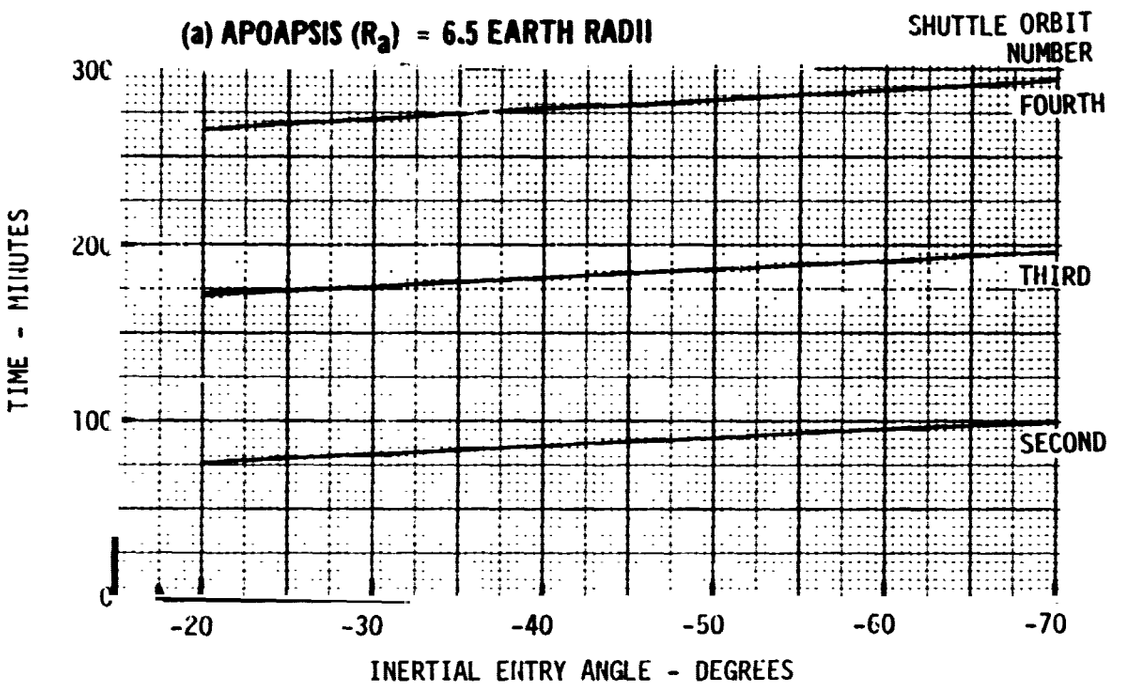

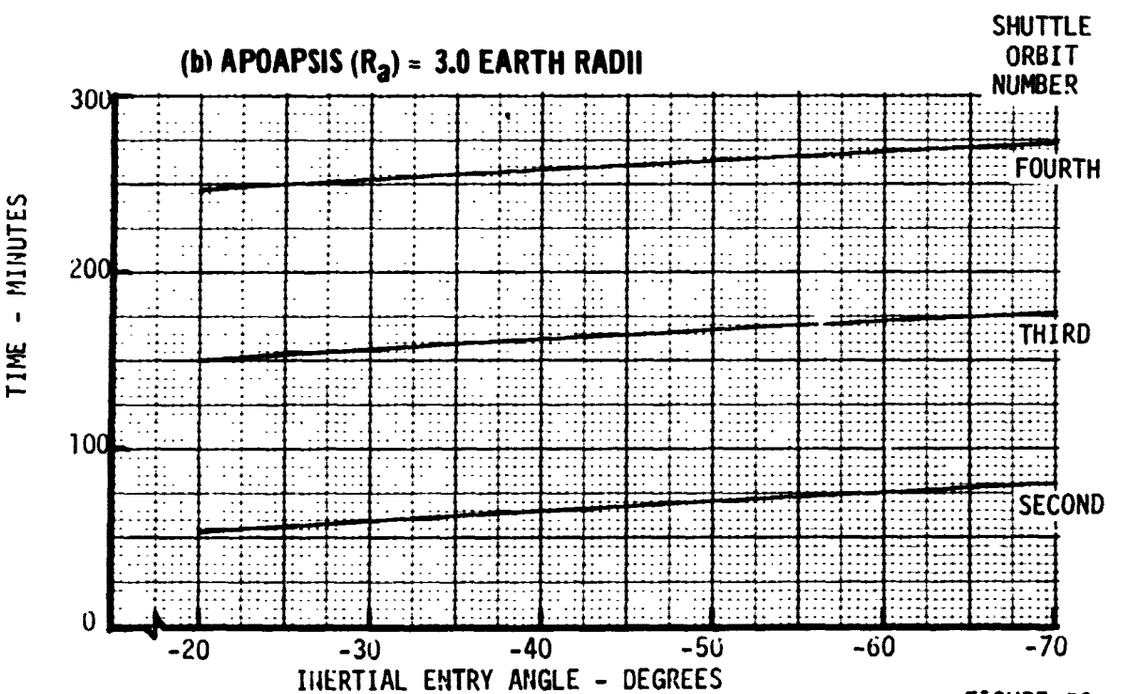

FIGURE 89

PLANETARY ENTRY GROUND TRACKS
(APOAPSIS = 6.5 EARTH RADII)

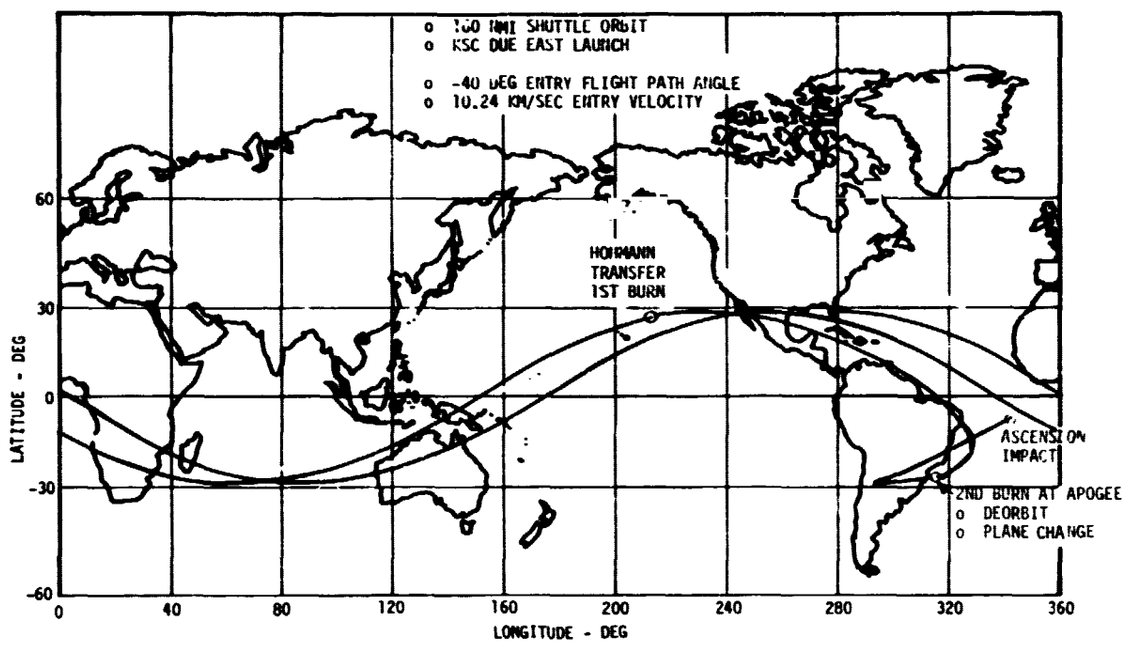

FIGURE 90

PLANETARY ENTRY GROUND TRACKS
(APOAPSIS = 3.0 EARTH RADII)

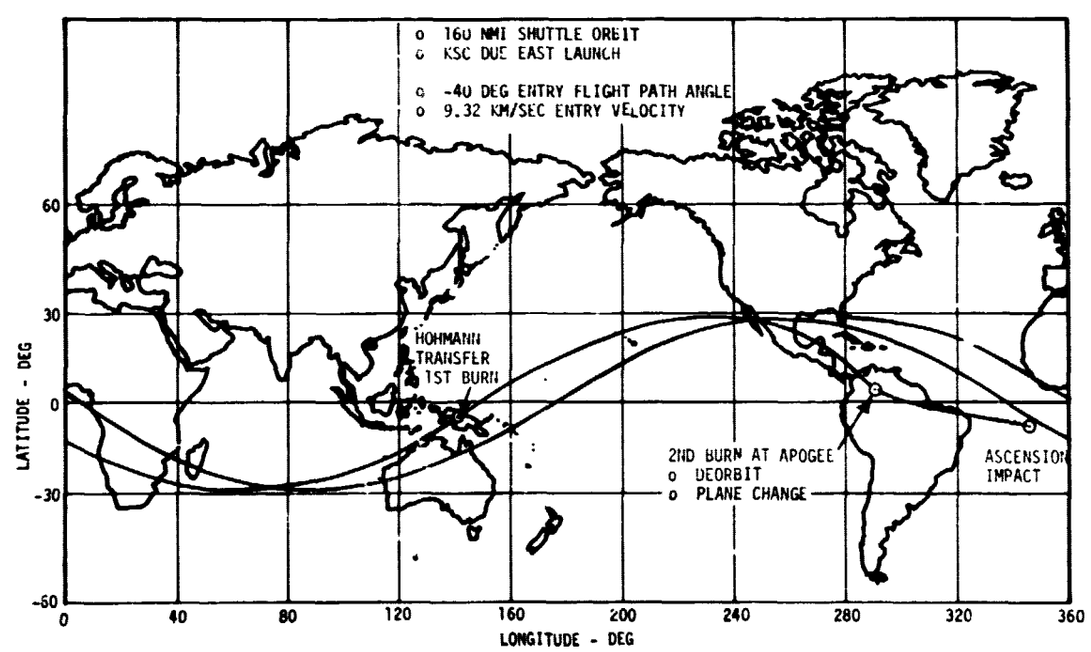

FIGURE 91

PLANETARY ENTRY MISSION EVENT SEQUENCE

TIME (HR: MIN)		EVENT
Ra = 6.5	RA = 3.0	
00:00	00:00	LIFTOFF
01:27	01:27	OMS SHUTDOWN-160 NMI CIRCULAR ORBIT
02:25	02:02	DEPLOY IUS
02:55	02:32	IGNITE IUS FOR FIRST BURN OF HOHMANN TRANSFER
08:06	04:34	IGNITE IUS FOR SECOND BURN AT APOAPSIS
12:32	05:55	IGNITE IUS FOR THIRD BURN TO INCREASE ENTRY VELOCITY
12:37	06:00	ENTRY AT 121.92 KM
12:41	06:04	IMPACT

FIGURE 92

5.4 Typical Environment Simulation - The previous subsections have addressed the deorbit maneuver requirements in the general terms of initial entry conditions. However, these requirements can also be expressed more directly in terms of environment parameter simulation. For example, the deorbit maneuver ΔV requirements are presented in Figures 93 through 94 using peak radiative flux as the specific environment parameter.

The optimum entry angle (γ) is shown in Figure 93 as a function of apoapsis distance (R_a). This is the γ that minimizes the total inplane ΔV needed to simulate a given level of radiative flux. Figure 94 graphically illustrates the procedure for identifying the optimum value of γ. Note that the option is rather flat; variations of ± 5 degrees around the optimum γ do not significantly effect ΔV requirements.

Figure 94 presents the total ΔV required as a function of apoapsis distance and radiative flux level. The beneficial effect of increasing R_a is quite pronounced at low altitudes but diminishes rapidly above an R_a of about 4 earth radii. The effect of radiative flux level or ΔV is nearly linear above about 20 kW/cm^2.

OPTIMUM ENTRY ANGLE FOR RADIATIVE FLUX SIMULATION

o MINIMUM ΔV REQUIREMENTS o IN PLANE MANEUVERS ONLY

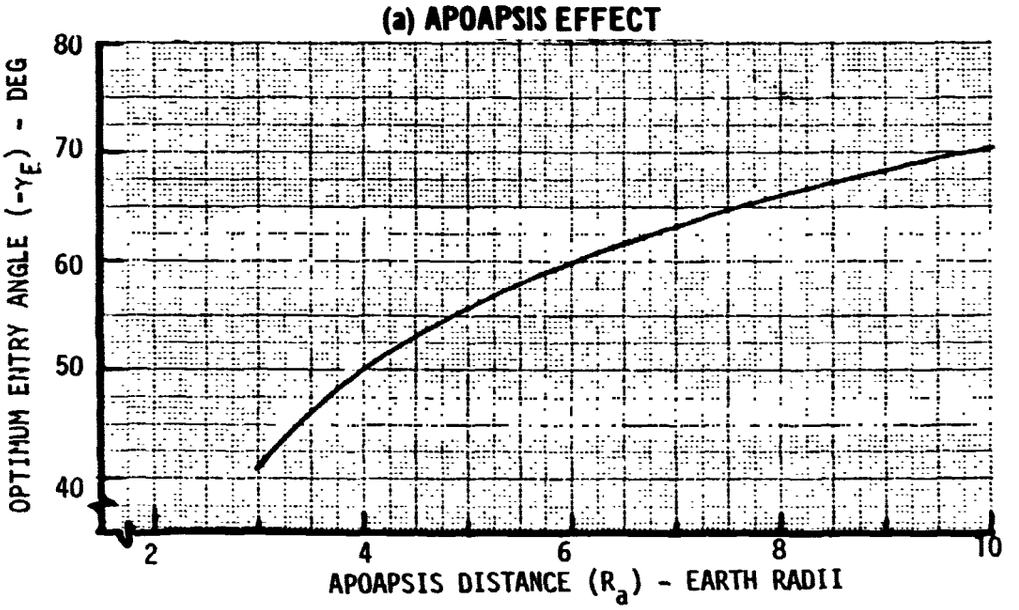

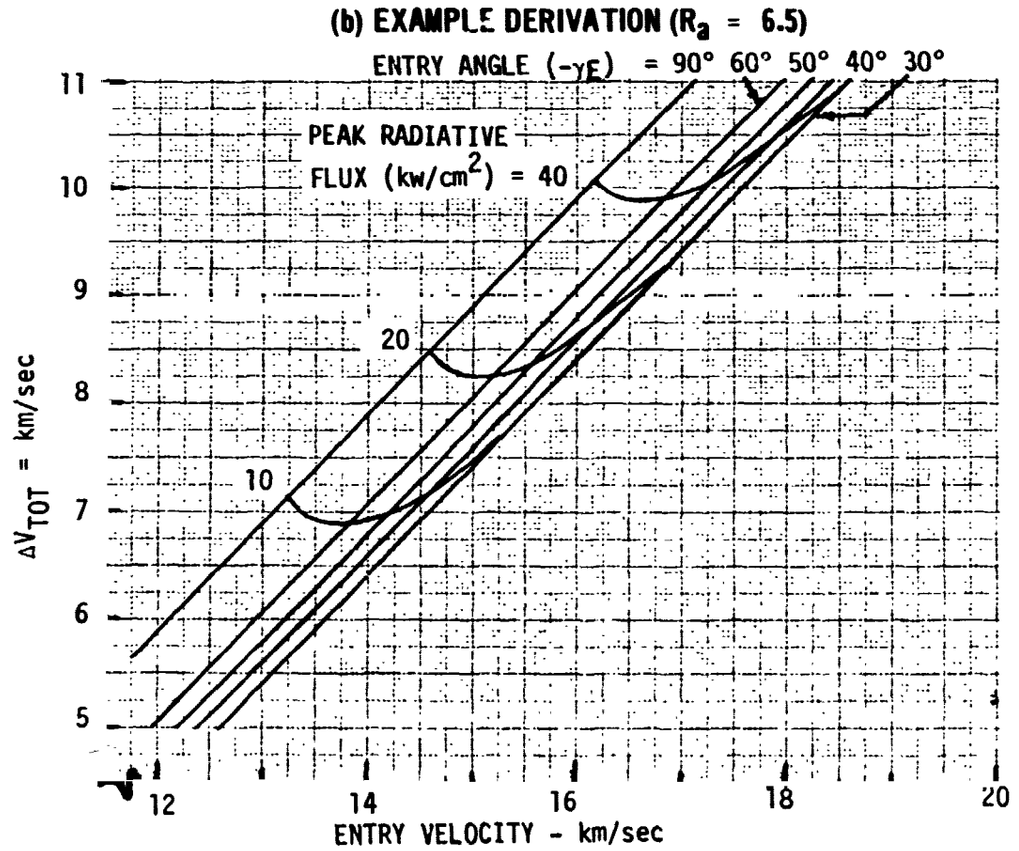

FIGURE 93

RADIATIVE FLUX SIMULATION ΔV REQUIREMENTS

- o STAGNATION POINT
- o NON BLOWING
- o β = 120 kg/m^2
- o R_N = .22 m
- o OPTIMUM γ_E
- o IN PLANE MANEUVER

(a) APOAPSIS EFFECT

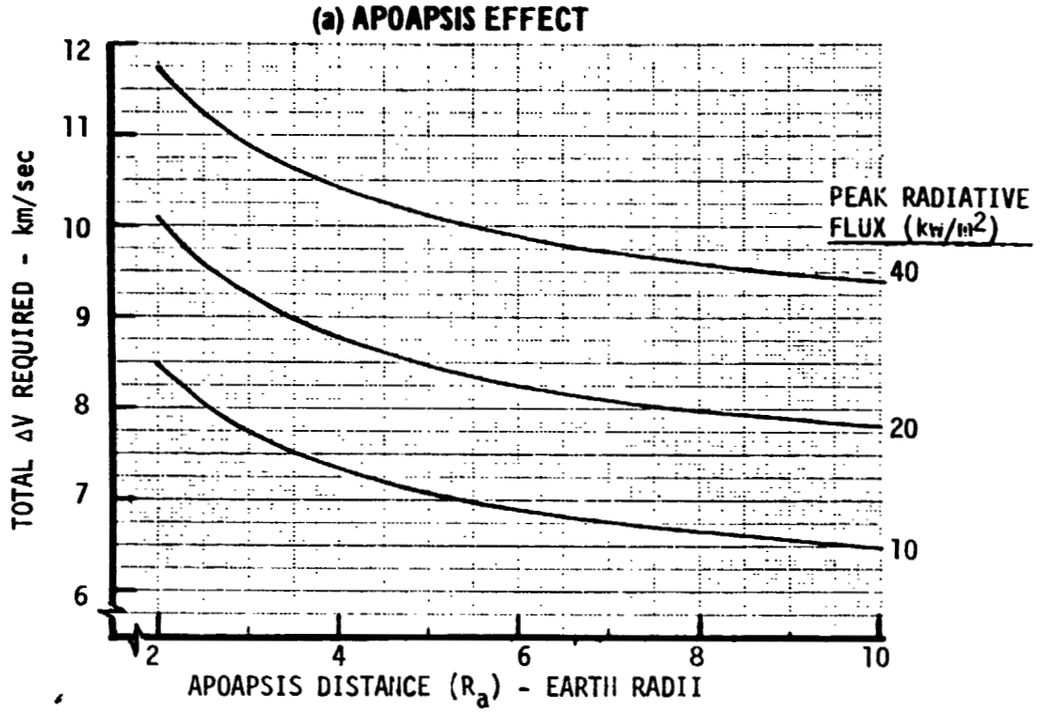

(b) RADIATIVE FLUX LEVEL EFFECT

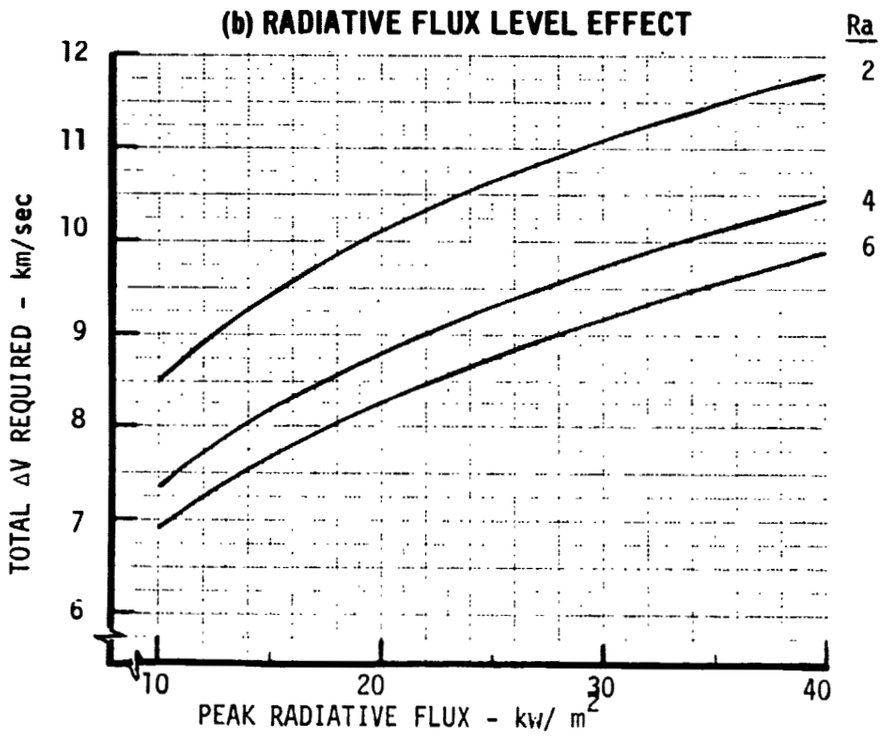

FIGURE 94

6.0 SHUTTLE LAUNCHED BOOSTERS

The physical characteristics and performance capabilities of typical Shuttle launched boosters are summarized in this section. The purpose of these data is to provide an understanding of the payload mass versus earth entry condition constraints imposed by current technology, Shuttle upper stages. Figure 95 shows the candidates boosters and assembled vehicles in relation to the Shuttle.

These boosters fall into four categories which cover the existing technology range of upper stage performance and physical size. Each class is illustrated by a representative design. Category 1 is a cryogenic propellant class of booster such as the Centaur. This class represents the highest available performance but also the biggest. Category 2, an existing storable propellant booster, such as the Transtage, is presented as an example of intermediate size and performance. Agena and Delta also fall into this category. Category 3 is a storable propellant design based on using components from the Shuttle auxiliary propulsion system. This multi-stage velocity package is an example of a very compact configuration that allows maximum opportunity for shared payload launches of the Shuttle. Category 4, a solid propellant booster, is shown using the best available definition of the recently selected Interim Upper Stage (IUS) concept.

Each booster class is described by a survey (including References 11, 12 and 13) of dimensional and mass characteristics and by parametric performance curves. The performance capability is shown in terms of payload mass versus velocity increment (ΔV) and also by the entry angle versus velocity attainable for selected values of apoapsis distance and payload mass.

6.1 Existing Cryogenic Booster - The Centaur, which is the only cryogenic (O_2/H_2) stage currently in use, is shown as the example design for this class of booster. Figure 96 presents the mass, dimensional and propulsion characteristics of the Centaur plus a spin stabilized, TE364-4 solid motor second stage. Although the Centaur alone performance is within the entry simulation range of interest, it is less than the other candidate, multi-stage, vehicles. Adding the TE364-4 stage, make the performance of this system the highest of any considered. Hence, this two stage configuration is presented as an example of the maximum performance capability available.

Figure 97 illustrates performance capability in terms of payload mass versus velocity increment (ΔV). Figure 98 describes the entry conditions that can be

CANDIDATE BOOSTERS

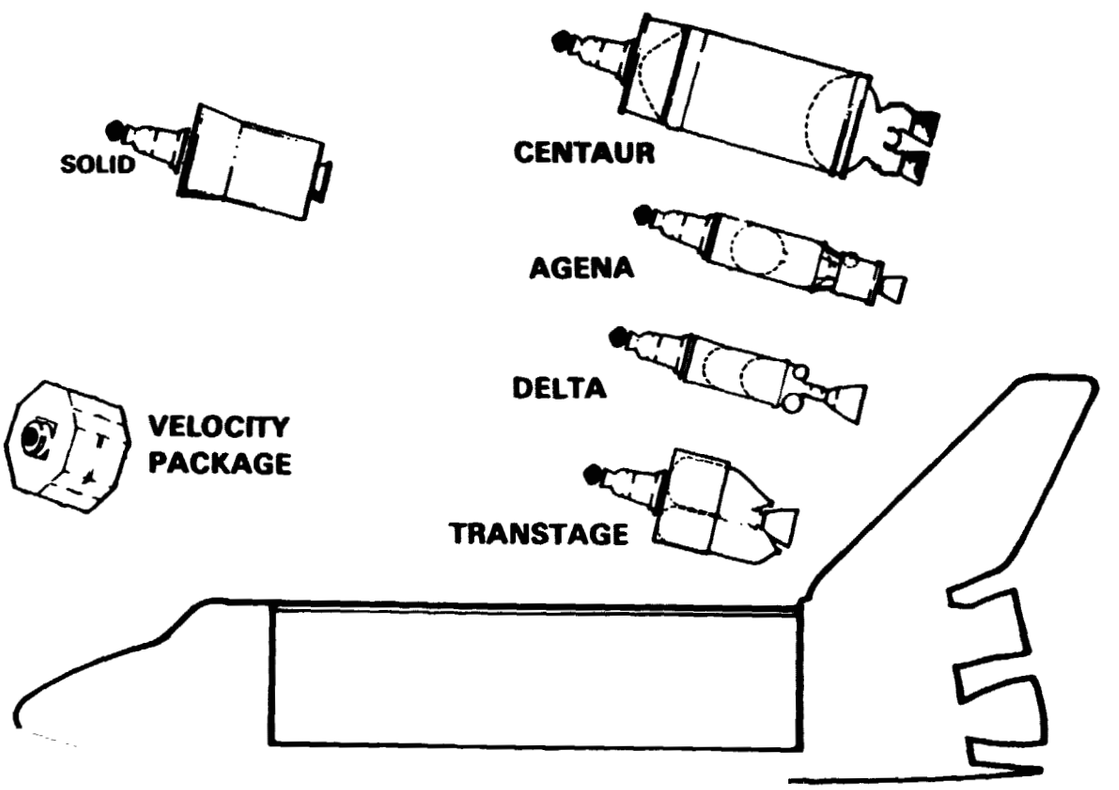

FIGURE 95

TYPICAL CRYOGENIC PROPELLANT BOOSTER DESCRIPTION (CENTAUR/TE364-4)

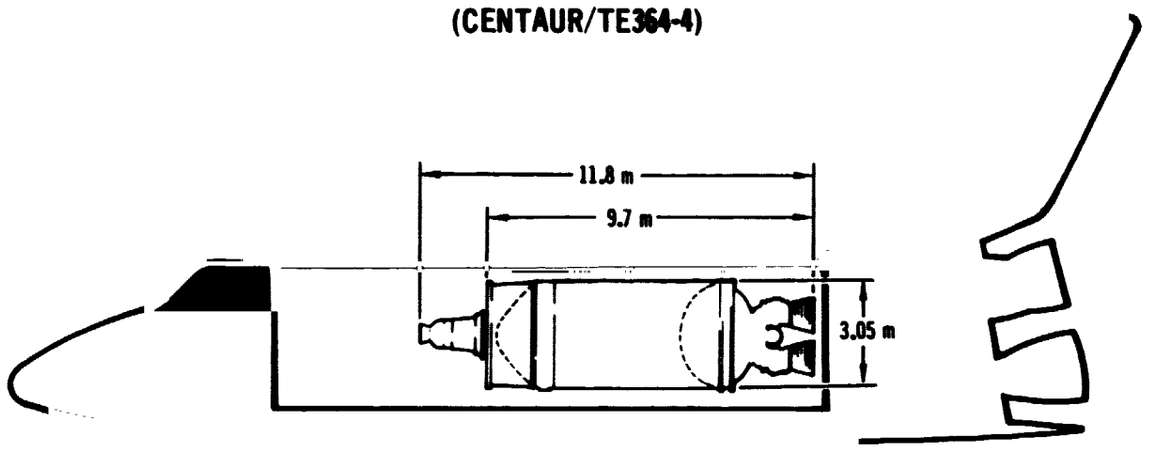

STAGE	MASS kg (lb)		THRUST N (lb)	I_{SP} n/sec (sec)
SECOND STAGE	ADAPTER	0 0	68,500 (15400)	2782 (283.8)
	INERT	75.8 (167.0)		
	BURNOUT	75.8 (167.0)		
	EXPENDED	1045.5 (2305.0)		
	IGNITION	1121.3 (2472.0)		
FIRST STAGE	INTERSTAGE *	86.7 (191.2)	129,900 (29200)	4311 (439.6)
	INERT **	2495.0 (5501.0)		
	BURNOUT	3703.0 (8164.2)		
	EXPENDED	13532.0 (29833.0)		
	IGNITION	17235.0 (37997.2)		

* INCLUDES 2ND STAGE SPIN TABLE
** INCLUDES AVIONICS

FIGURE 96

CENTAUR/TE364-4 PAYLOAD MASS CAPABILITY

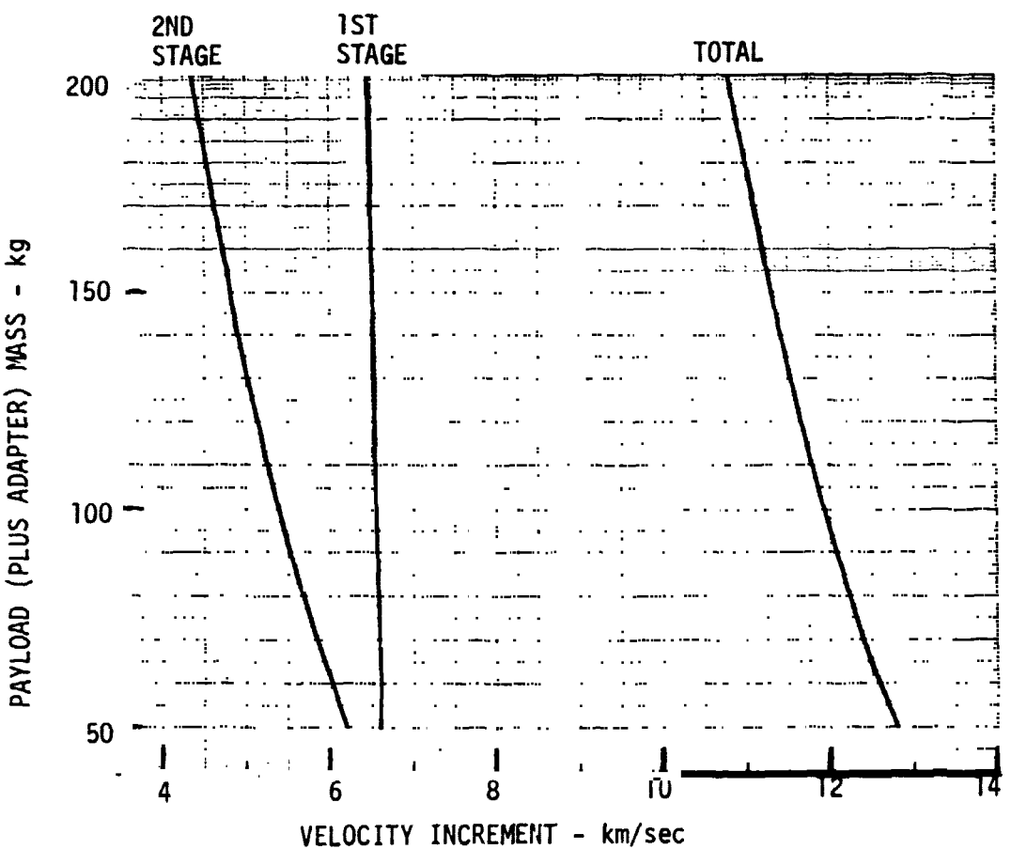

FIGURE 97

CENTAUR/TE364-4 ENTRY CONDITIONS CAPABILITY

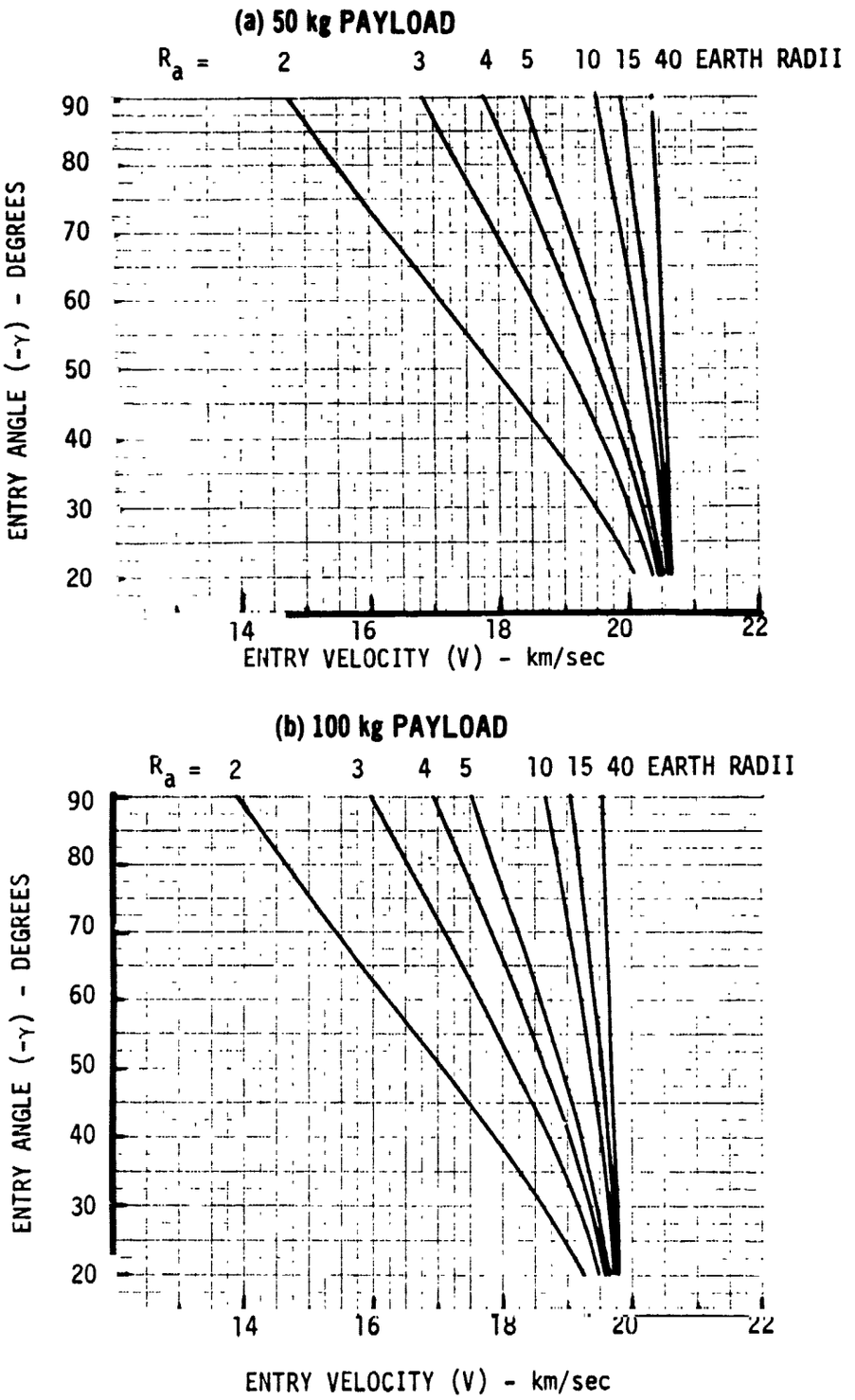

FIGURE 98

CENTAUR/TE364-4 ENTRY CONDITIONS CAPABILITY (Continued)

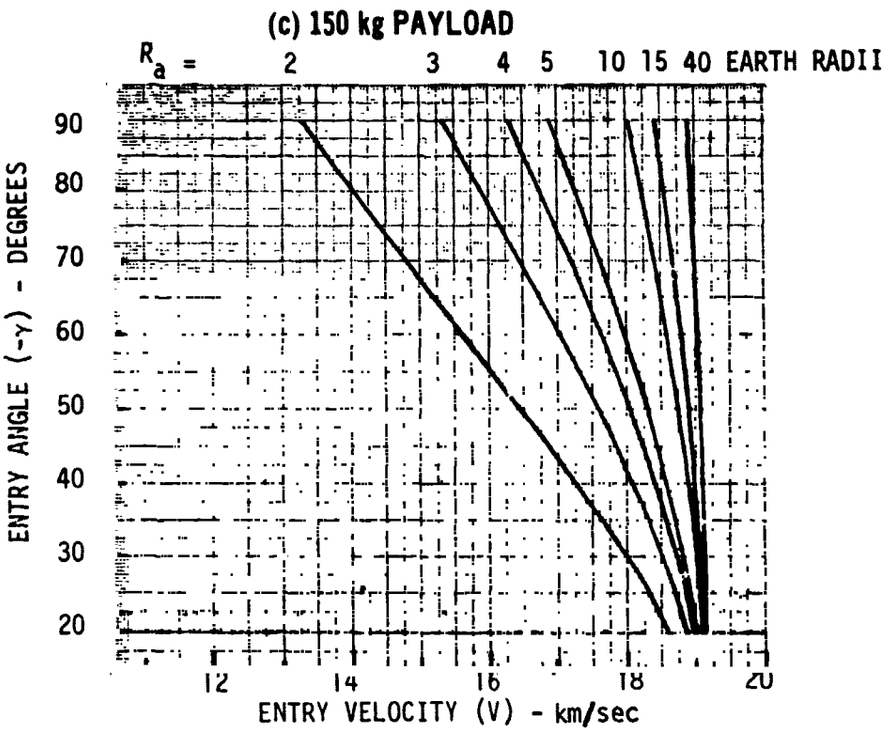

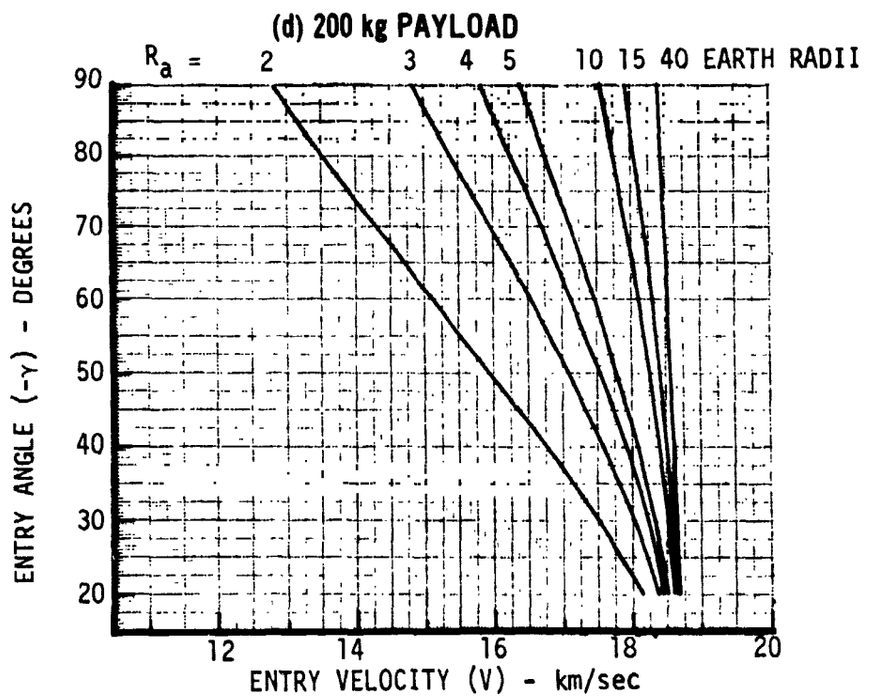

FIGURE 98 (CONT)

achieved for selected values of apoapsis distance and payload mass (50, 100, 150 and 200 kg). Note that as apoapsis (R_a) is increased, higher entry velocities can be attained at steeper entry angles. In all cases, the Centaur stage accomplishes the first and second maneuver burn and a portion of the third or final burn while the solid motor is used to complete the final burn.

6.2 Existing Storable Booster - The Transtage is selected as the example design for this booster class on the basis that it provides maximum performance capability with minimum modification. Of the designs considered were the Delta and Agena stages. Physical and propulsion characteristics of the Transtage plus a TE364-4 solid motor upper stage are described in Figure 99. An auxiliary stage is necessary to achieve performance levels high enough to be of interest for environment simulation missions.

Figures 100 and 101 present the Transtage/TE364-4 performance capability in terms of payload mass and entry conditions respectively. The second stage restart line of Figure 101 reflects the limited ΔV capability of the Transtage plus the single start limitation of current solid motors. To achieve steep entries at lower apoapsis altitudes, the first two maneuver burns require more ΔV than is available from the Transtage alone. Hence the second stage must be used to complete the second or apoapsis burn. It must then be shut down during the coast to low altitude and restarted to accomplish the third or velocity adjustment burn.

6.3 Short Length Existing Component Storable Booster - A multi-stage velocity package composed of Shuttle Auxiliary Propulsion System Components is shown to illustrate a short length high ΔV class of storable (N_2O_4/MMH) boosters. The compact velocity package is an example of how existing components can be configured to best utilize the wide but length limited shape of the Shuttle payload bay. This maximizes opportunity for shared payload launches of the Shuttle. In contrast, the other booster classes represent relatively long, narrow upper stages that were originally designed for ground launched, expendable boosters.

Figure 102 describes the physical and propulsion characteristics of the three stage velocity package. The first two stages are identical and composed of tank, engine and flow control components being developed for the Reaction Control System (RCS) of Shuttle. The third stage is a spin stabilized, TE364-4 solid motor.

Figure 103 shows the basic payload mass versus ΔV performance capability of each stage while Figure 104 presents the entry condition capability for representative apoapsis distances and payload masses. The third stage restart limit of

TYPICAL EARTH STORABLE PROPELLANT BOOSTER DESCRIPTION (TRANSTAGE/TE364-4)

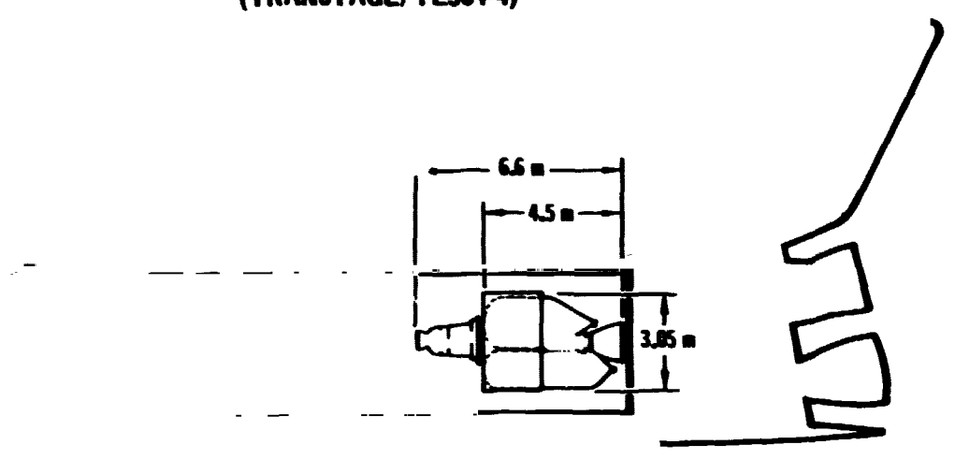

STAGE	MASS	kg	(lb)	THRUST N (lb)	I_{sp} m/sec (sec)
SECOND STAGE	ADAPTER	0	0	68500 (15400)	2782 (283.8)
	INERT	75.8	(167.0)		
	BURNOUT	75.8	(167.0)		
	EXPENDED	1045.5	(2305.0)		
	IGNITION	1121.3	(2472.0)		
FIRST STAGE	INTERSTAGE *	86.7	(191.2)	69900 (15733)	2955 (301.3)
	INERT **	1701.0	(3750.7)		
	BURNOUT	2989.0	(6413.9)		
	EXPENDED	10447.0	(23032.0)		
	IGNITION	13356.0	(29445.9)		

* INCLUDES 2ND STAGE SPIN TABLE
** INCLUDES AVIONICS

FIGURE 99

TRANSTAGE/TE364-4 PAYLOAD MASS CAPABILITY

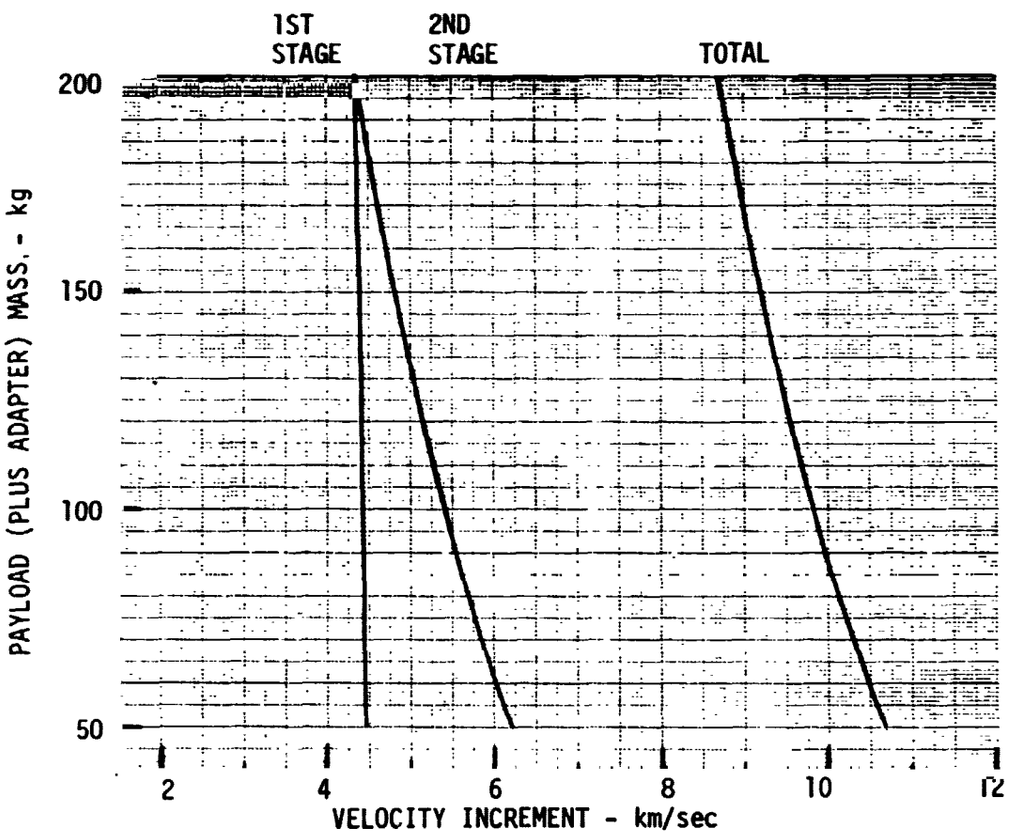

FIGURE 100

TRANSTAGE/TE364-4 ENTRY CONDITION CAPABILITY

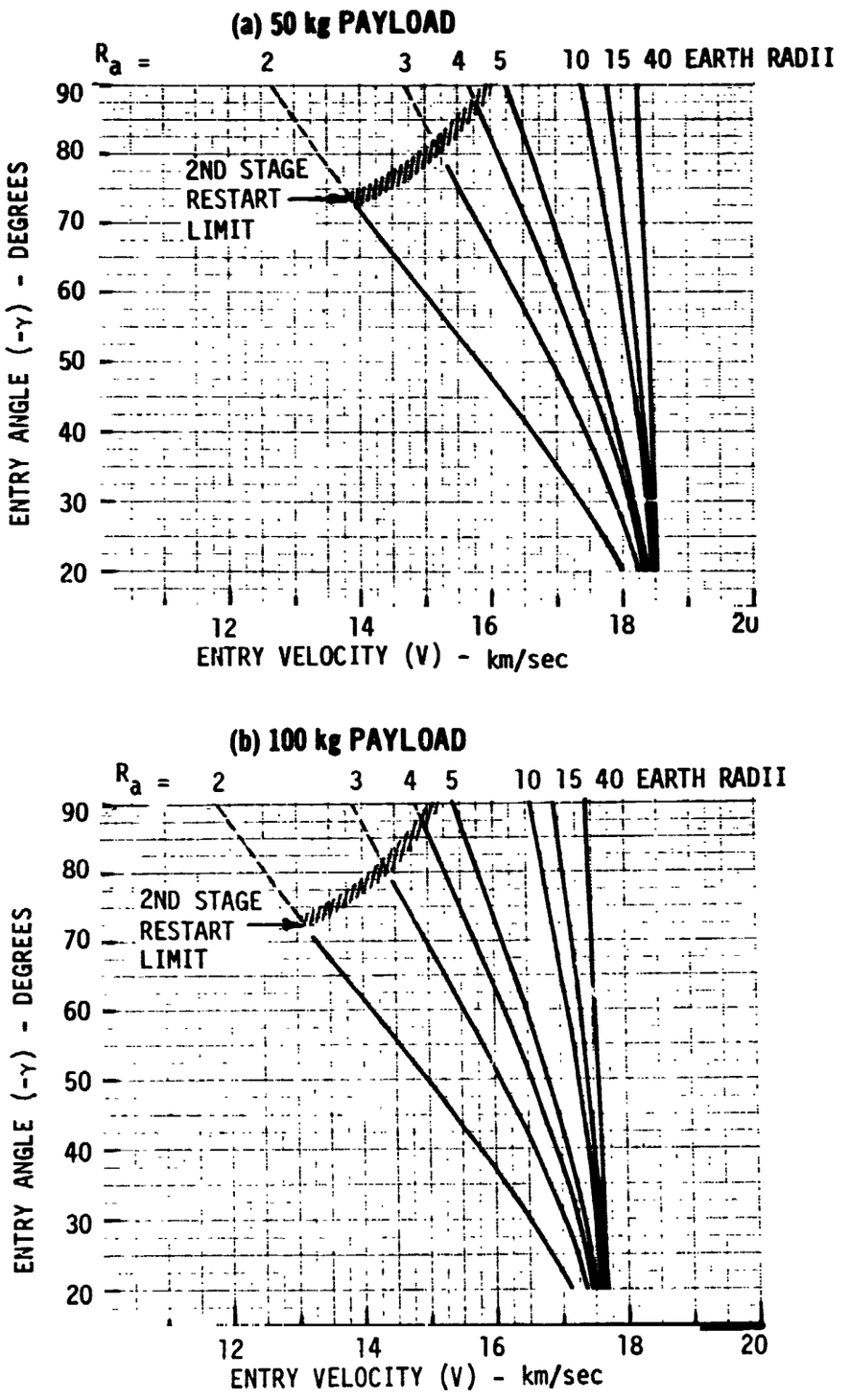

FIGURE 101

TRANSTAGE/TE364-4 ENTRY CONDITION CAPABILITY (Continued)

(c) 150 kg PAYLOAD

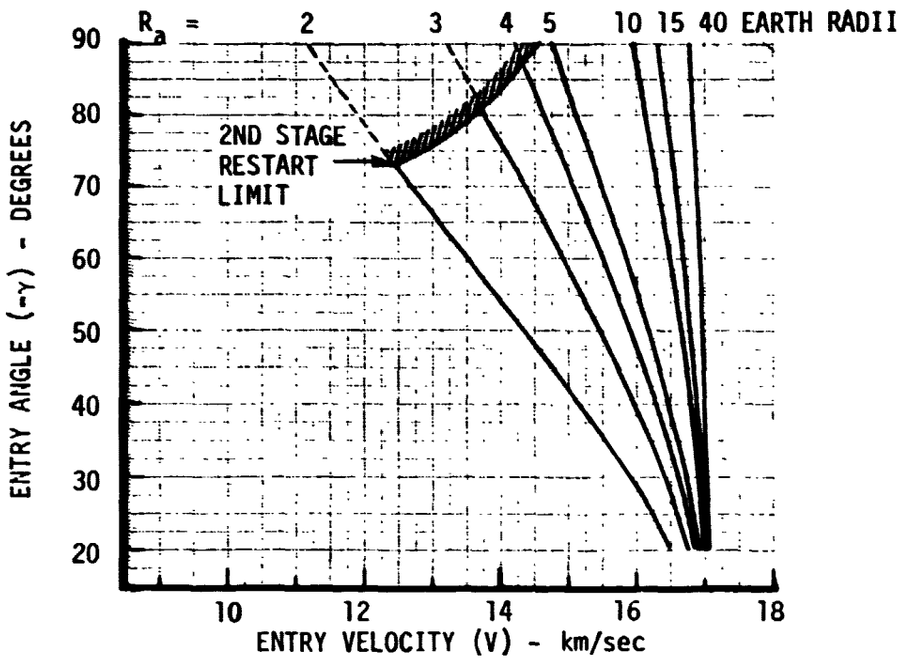

(d) 200 kg PAYLOAD

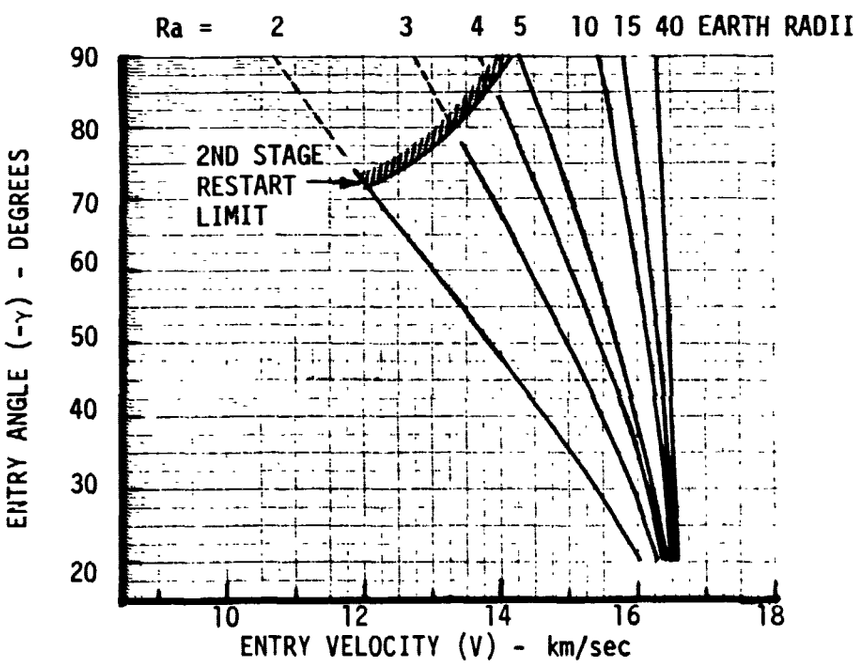

FIGURE 101 (CONT)

TYPICAL "SHORT LENGTH" BOOSTER DESCRIPTION (SHUTTLE COMPONENT VELOCITY PACKAGE)

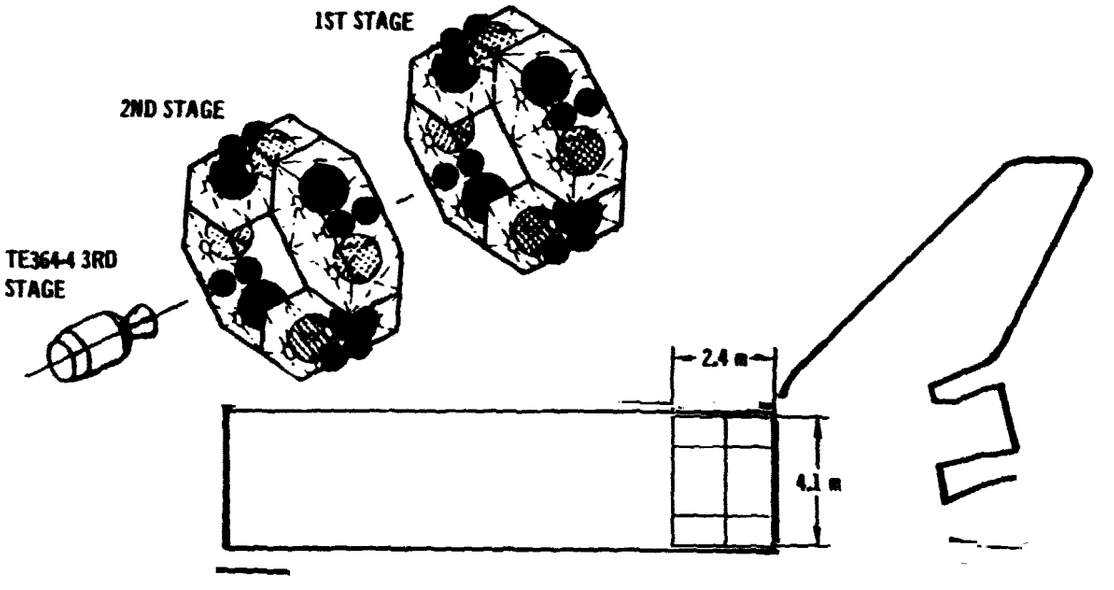

STAGE	MASS kg (lb)		THRUST N (lb)	I_{SP} m/sec (sec)
THIRD STAGE	ADAPTER	0 0	68,500 (15400)	2782 (283.8)
	INERT	75.8 (167.0)		
	BURNOUT	75.8 (167.0)		
	EXPENDED	1045.5 (2305.0)		
	IGNITION	1121.3 (2472.0)		
SECOND STAGE	INTERSTAGE *	349.0 (770.0)	15984 (3600)	2834 (289)
	INERT	1316.0 (2902.0)		
	BURNOUT	2786.3 (6144.0)		
	EXPENDED	3931.0 (8667.0)		
	IGNITION	6717.3 (14811.0)		
FIRST STAGE	INTERSTAGE	45.0 (100.0)	15984 (3600)	2834 (289)
	INERT	1316.0 (2902.0)		
	BURNOUT	8078.3 (17813.0)		
	EXPENDED	3931.0 (8667.0)		
	IGNITION	12009.3 (26480.0)		

* INCLUDES AVIONICS AND 3RD STAGE SPIN TABLE

FIGURE 102

VELOCITY PACKAGE PAYLOAD MASS CAPABILITY

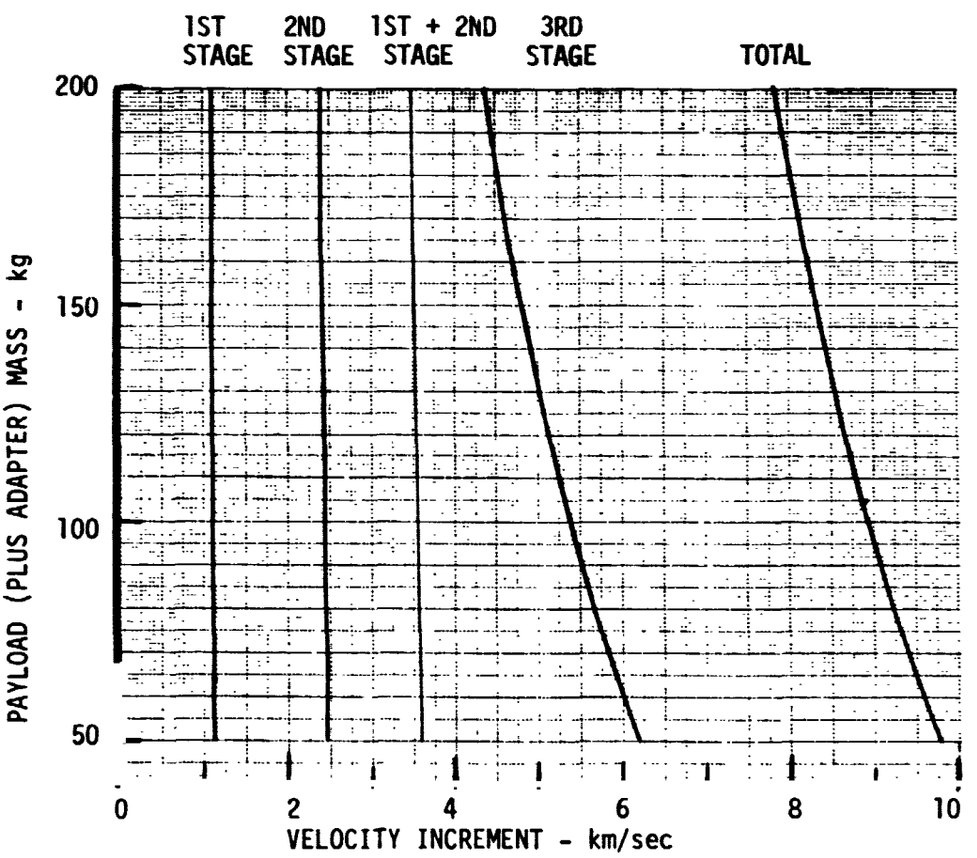

FIGURE 103

VELOCITY PACKAGE ENTRY CONDITION CAPABILITY

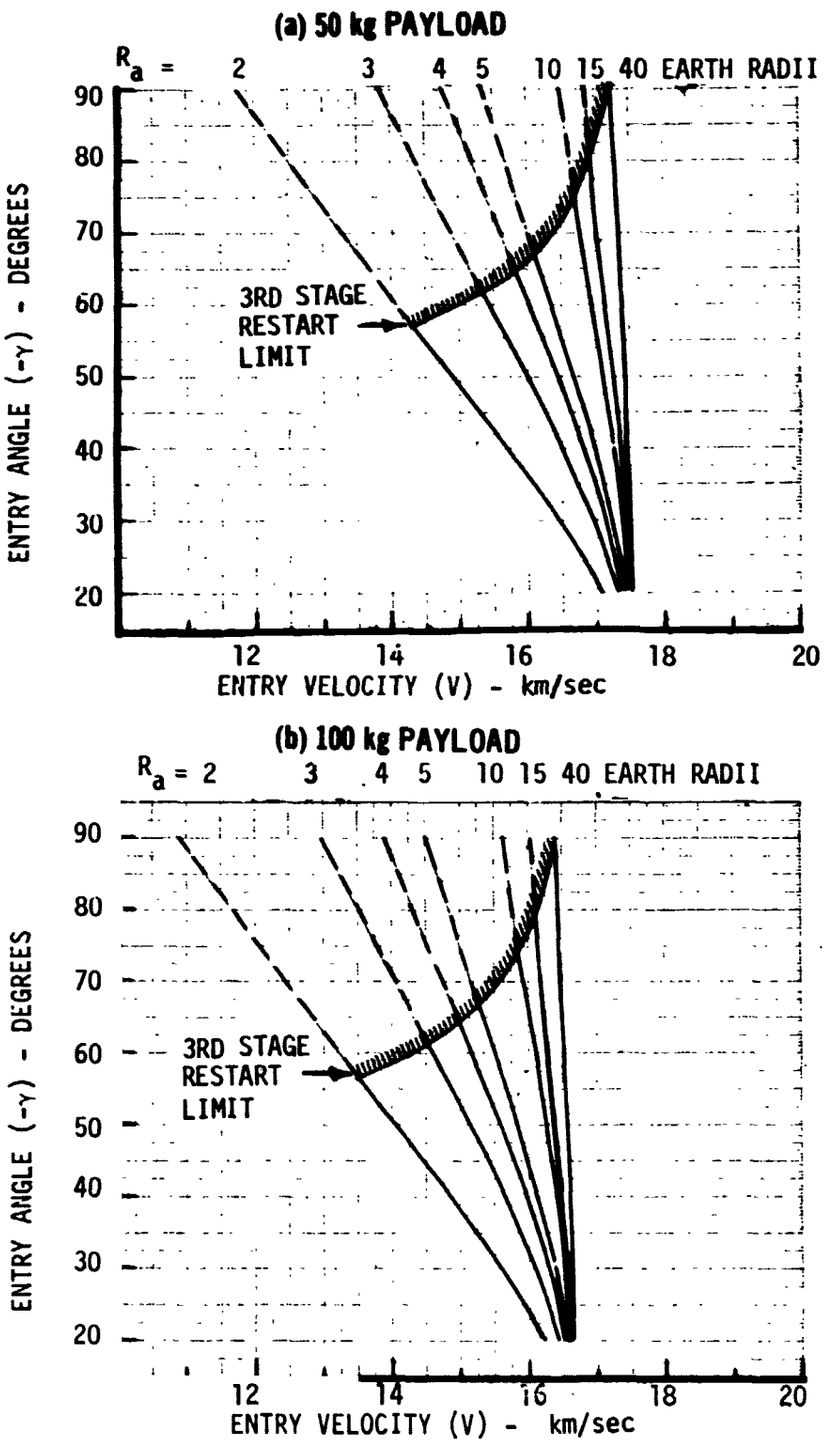

FIGURE 104

VELOCITY PACKAGE ENTRY CONDITION CAPABILITY (Continued)

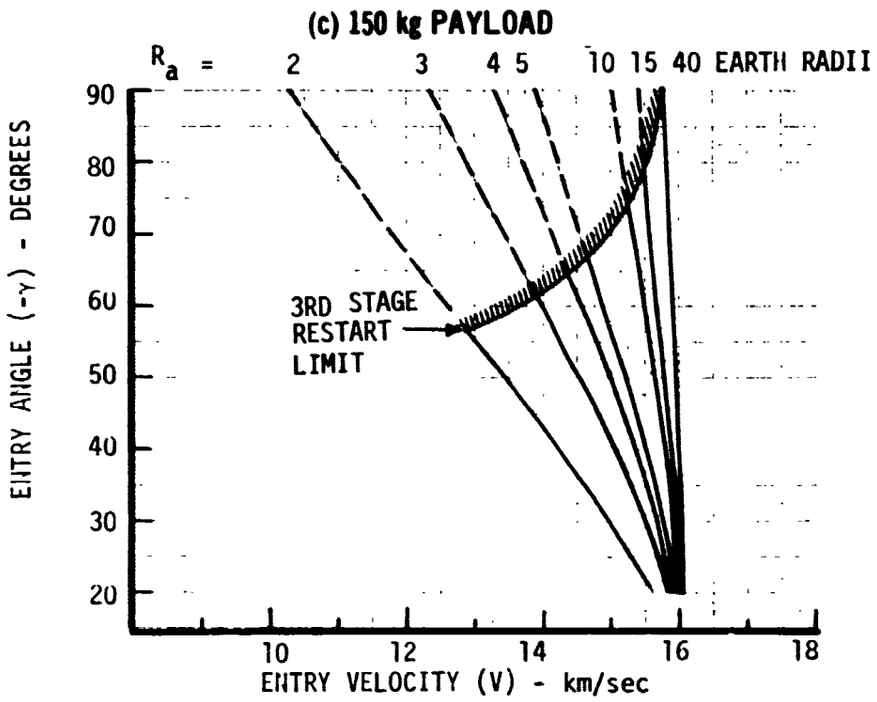

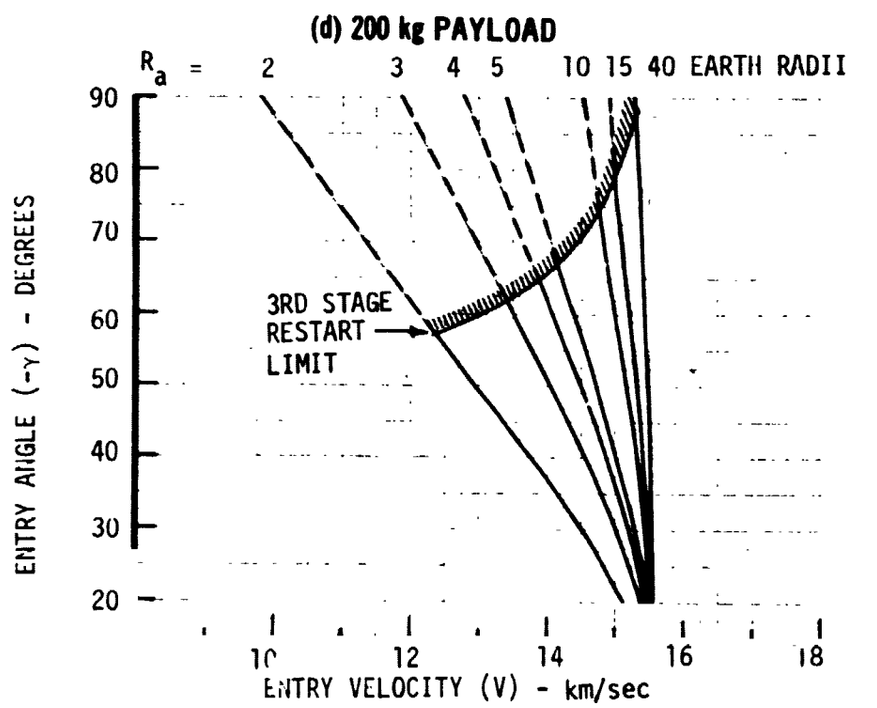

FIGURE 104 (CONT)

Figure 104 represents the same operational constraint as discussed in the preceeding subsection.

6.4 Existing Solid Motor Booster - A preliminary version of the Interim Upper Stage (IUS) is presented as an example of the solid propellant class of booster. The configuration shown is necessarily preliminary since the Air Force is in the process of awarding a contract to define the final IUS characteristics. Figure 105 summarizes the characteristics of a two stage IUS plus a spin stabilized, TE364-4 solid motor used as an auxiliary third stage. A third stage is required because of the three burn nature of the deorbit maneuver and the single start limitation of current solid motors.

The performance capability of the IUS/TE364-4 is shown in Figures 106 and 107. The third stage restart limit of Figure 107 is imposed for the same reasons as discussed in previous subsections. The first stage ΔV limit is a similar constraint arising from the single start nature of the second stage. It should be noted that the Figure 107 entry condition capability is conservative in that it was assumed that any excess ΔV from either the first or second stage was wasted by non-optimum trajectory usage. In particular, the second stage apoapsis burn can probably be applied in a manner that utilizes this excess energy to increase entry velocity. This should be the subject of detailed trajectory analysis for a given mission application.

TYPICAL SOLID PROPELLANT BOOSTER DESCRIPTION (2 STAGE IUS/TE364-4)

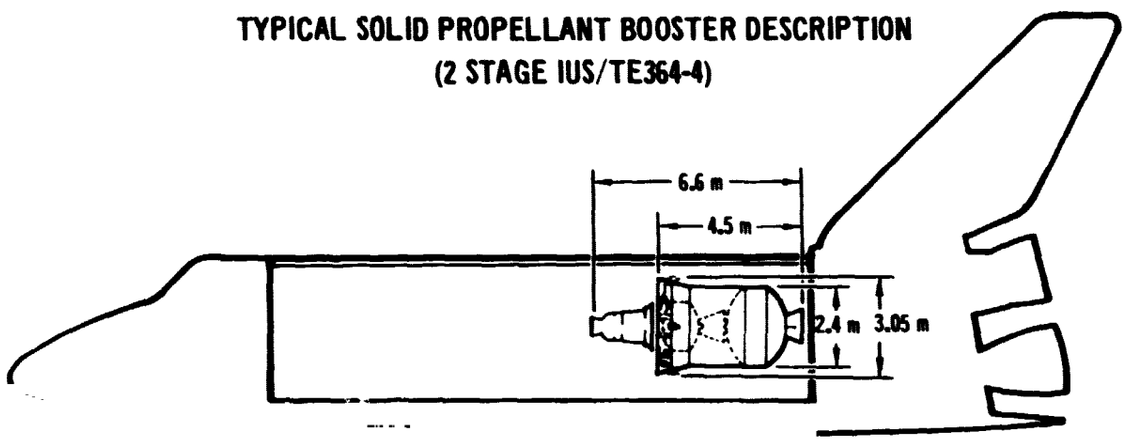

STAGE	MASS	kg	(lb)	THRUST N (lb)	I_{SP} m/sec (sec)
THIRD STAGE	ADAPTER	0	0	68,500 (15400)	2782 (283.8)
	INERT	75.8	(167.0)		
	BURNOUT	75.8	(167.0)		
	EXPENDED	1045.5	(2305.0)		
	IGNITION	1121.3	(2472.0)		
SECOND STAGE	INTERSTAGE *	86.7	(191.2)	62,720 (14100)	2909 (296.6)
	INERT **	648.5	(1430.0)		
	BURNOUT	1856.3	(4093.2)		
	EXPENDED	2161.9	(4767.0)		
	IGNITION	4018.2	(8860.2)		
FIRST STAGE	INTERSTAGE	–	–	186800 (32000)	2838 (289.4)
	INERT	932.9	(2057.0)		
	BURNOUT	4951.1	(10917.2)		
	EXPENDED	9144.7	(20164.0)		
	IGNITION	14095.8	(31081.2)		

* INCLUDES 3RD STAGE SPIN TABLE
** INCLUDES AVIONICS

FIGURE 105

SOLID IUS/TE364-4 PAYLOAD MASS CAPABILITY

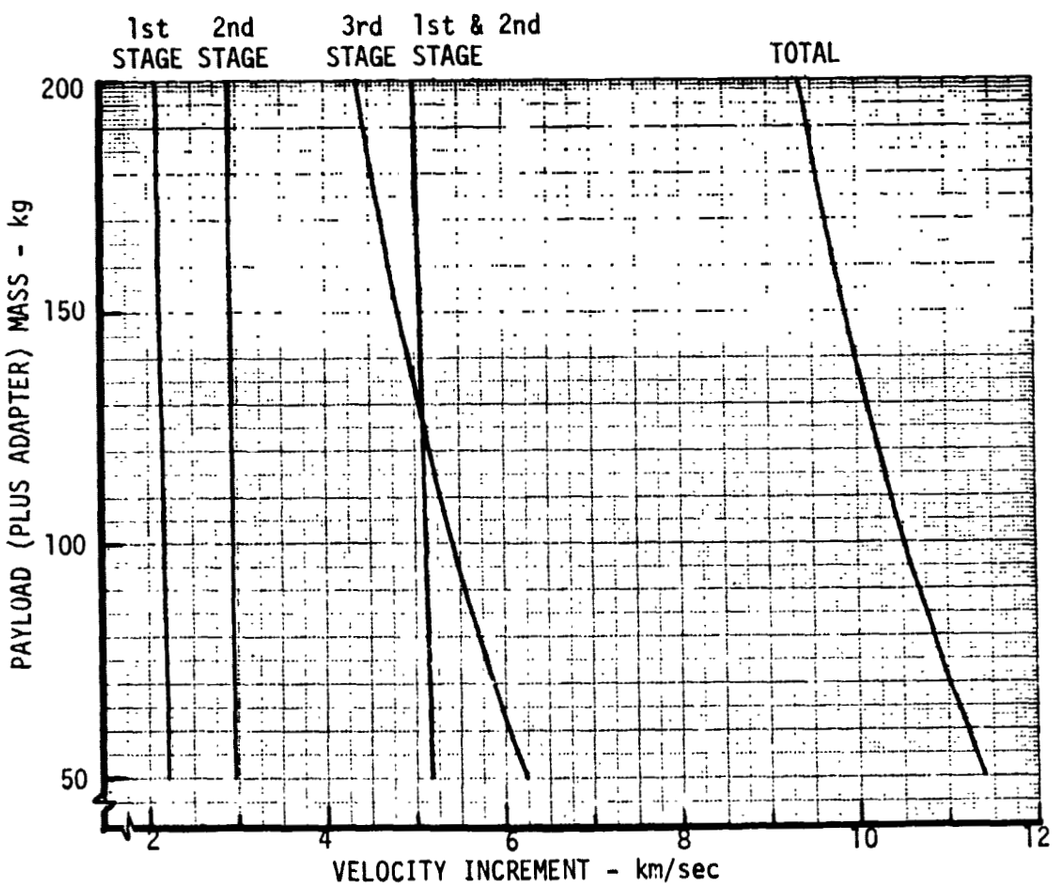

FIGURE 106

SOLID IUS/TE364-4 ENTRY CONDITION CAPABILITY

o SINGLE START PER STAGE o IN PLANE MANEUVERS

(a) 100 kg PAYLOAD

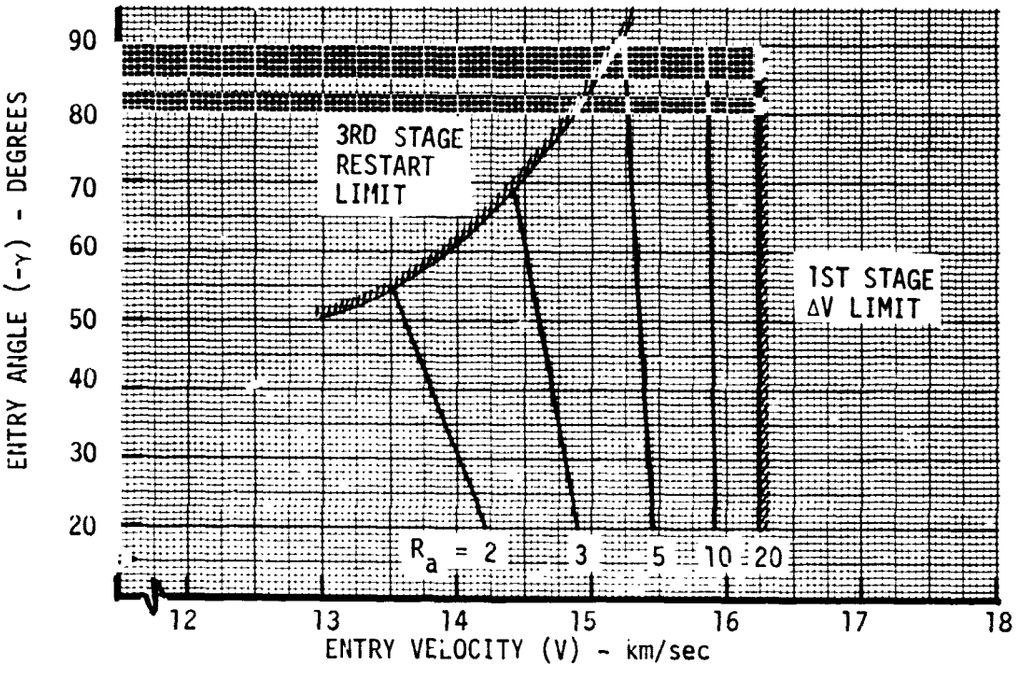

(b) 200 kg PAYLOAD

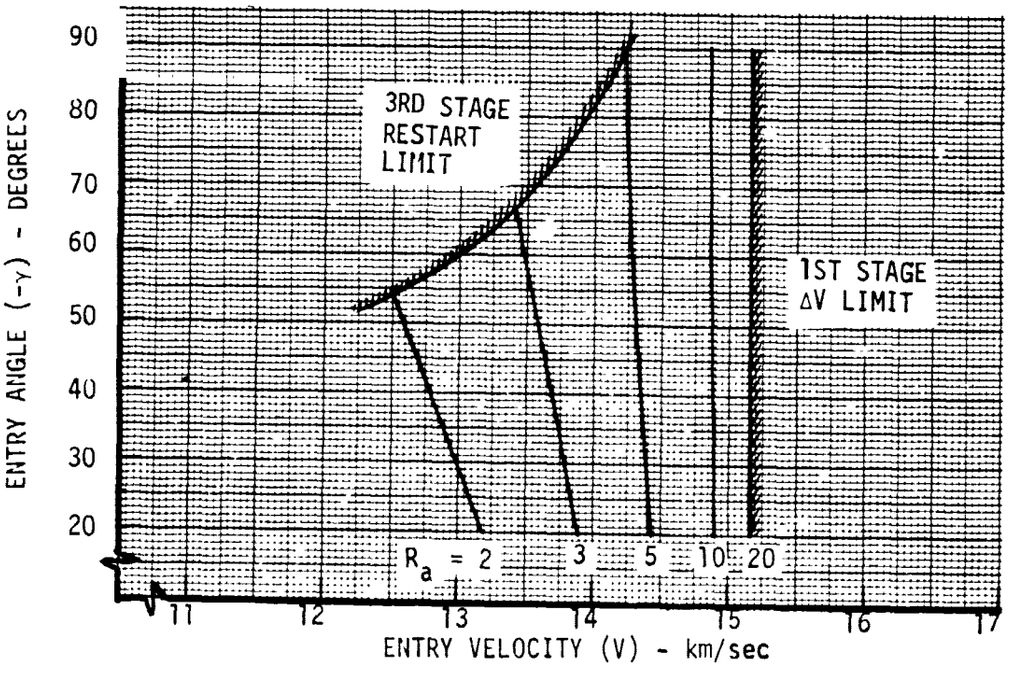

FIGURE 107

7.0 COMPARISON OF REQUIREMENTS AND CAPABILITIES

The environments that can be produced during a high speed earth entry are compared in this section with those predicted for the outer planets to determine what conditions will produce the best simulation. Four aspects of the simulation are examined. Do differences in atmospheric composition affect shock layer spectral radiative heating? What conditions can the boosters produce to best simulate peak radiative heating (nonblowing)? What conditions can the booster produce to best simulate multiple nonblowing environments? And finally, what conditions will produce the best simulation when the heating is reduced due to mass injection carbonaceous and hyperpure silica heat shields?

The atmosphere composition differences between earth and an outer planet raise the issue of shock layer radiation spectral distribution. The incident radiation spectrum is a complex function of many variables, chief among which are gas composition, total energy, density and shock layer thickness. The shock layer radiation interacts with the boundary layer gases so that the spectral intensity and total radiant energy incident on the heat shield surface can differ significantly from the initial shock layer values. While planetary entry levels of radiative heating can be simulated during earth entry, the difference in atmosphere composition results in a different spectral distribution. Spectral distributions of incident radiative flux for a Jovian and an earth entry were compared (see Figure 108) to determine similarities. There are obviously similarities as well as differences. Both have qualitatively similar distributions. The Jupiter distribution peaks in the visible spectrum and again in the VUV at about 11 electron volts. The earth distribution peaks in the near-infrared and also in the VUV at 10-11 electron volts. For the hydrogen-helium atmosphere of Jupiter most of the energy is produced in the ultra violet, visible and infrared regimes with only 20% lies in the vacuum ultra violet (VUV) region. This is not the case for an earth entry. Approximately half of the energy lies in the VUV region (photon energy greater than 6.5 ev). The reflectance of silica drops off in the VUV, so almost all the energy in this region will be absorbed. Consequently, about 50% of the incident radiation will be absorbed by the silica shield for an earth entry as compared to 25% for a Jovian entry. These percentages will change when blowing is present.

While the spectral distribution differences are of little concern for testing carbonaceous heat shields, they are a consideration in testing reflective silica heat shields. Since the reflectivity of silica is spectrally dependent as depicted

in Figure 108, only about half of the incident radiation from an air shock layer will be reflected. This is not expected to destroy the validity of such a test. Indeed if the silica heat shield can absorb the higher energy radiation in addition to the convective heating, it will demonstrate the effectiveness of a reflective heat shield in an environment even more severe than it was intended to experience.

SPECTRAL DISTRIBUTION CONSIDERATIONS

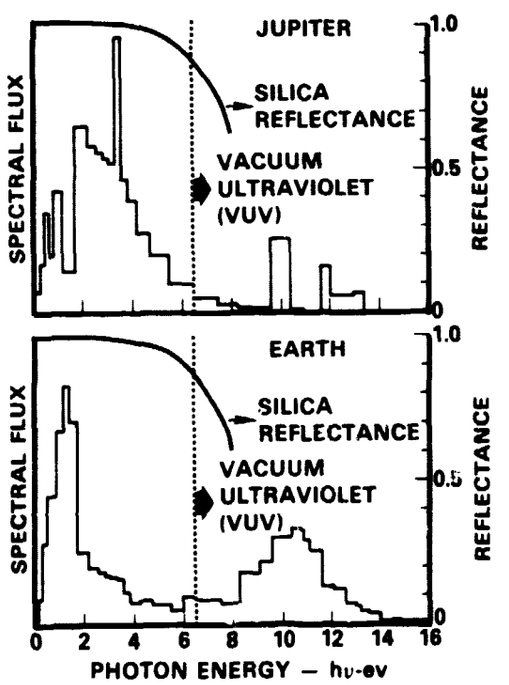

ENERGY DISTRIBUTION*	PLANET	
	JUPITER	EARTH
% BELOW VUV	80	50
% ABOVE VUV	20	50
% ABSORBED (SILICA)	26	50

*PEAK RADIATIVE FLUX STAGNATION POINT NON-BLOWING

FIGURE 108

7.1 Non-Blowing Radiative Flux Simulation - High radiation flux levels of outer planet proportions can be achieved by earth entry flights using a variety of Shuttle launched boosters. This is illustrated by Figure 109 which summarizes the comparison of planetary simulation requirements with earth flight test booster capabilities. The shaded area of Figure 109 represents the earth entry conditions required to simulate the radiative flux level range of interest. The lower bound of 10 kw/cm^2 is the minimum level to produce a radiation dominated environment. The upper bound of 40 kw/cm^2 is the maximum design level for Jupiter entry simulation. The four booster classes presented represent the range of entry condition capability available from current technology upper stages. As described in Section 6.0, the example designs used for each class are the Centaur/TE364-4 (cryogenic), the Transtage/TE364-4 (storable), a Shuttle RCS Velocity Package (short length), and the IUS/TE364-4 (solid). As shown, the entry condition capability of each booster classes is well above the minimum requirement and, in fact, exceed the 20 kw/cm^2 maximum requirement for Saturn/Uranus entry simulation. Further, the capability of the cryogenic and storable classes exceed the maximum Jupiter requirement of 40 kw/cm^2.

A more detailed comparison that includes the effect of apoapsis altitude and entry vehicle mass variations is shown in Figure 602 using the Transtage/TE364-4 (storable class) as the booster example. One point to be noted is that increasing apoapsis altitude increases the peak radiative flux level that can be simulated with a given booster and entry vehicle mass (Figure 110). This effect is particularly pronounced at low apoapsis but reaches a point of diminishing returns at an apoapsis of about 10 earth radii. Hence for a fixed booster and entry vehicle, apoapsis altitude can be used to adjust the level of radiative flux produced during entry. For instance, a 100 kg entry vehicle (reference design) could simulate a Saturn entry at an $R_a = 2$ while the same mass vehicle could simulate a Jupiter entry by increasing R_a to about 6.5.

A second point illustrated by Figure 110 is that increasing entry vehicle mass actually improves radiative flux simulation capability if C_DA is held constant. In this case, the ballistic coefficient (m/C_DA) increases directly proportional to the mass increase which causes a corresponding increase in radiative flux for the same entry conditions. Offsetting this is the reduced entry condition capability of the booster resulting from increased payload mass. However, the net effect is beneficial; the entry condition requirement for a given radiative flux level goes

RADIATIVE FLUX SIMULATION CAPABILITY VS REQUIREMENTS

- o STAGNATION POINT
- o NON BLOWING
- o PAYLOAD = 100 kg
- o β = 120 kg/m^2
- o Ra = 10 EARTH RADII
- o IN PLANE MANEUVERS

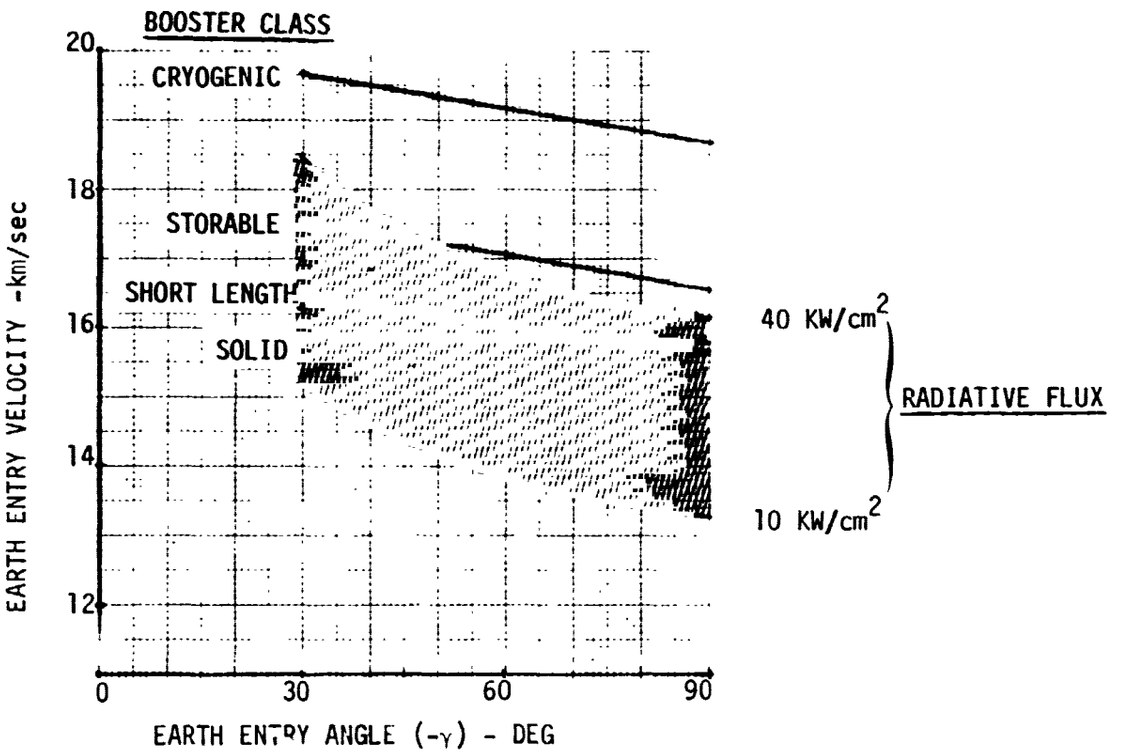

FIGURE 109

TRANSTAGE TE364-4 RADIATIVE FLUX SIMULATION CAPABILITY

- o STAGNATION POINT
- o NON BLOWING
- o IN PLANE MANEUVERS
- o OPTIMUM ENTRY ANGLE

(a) APOAPSIS EFFECT

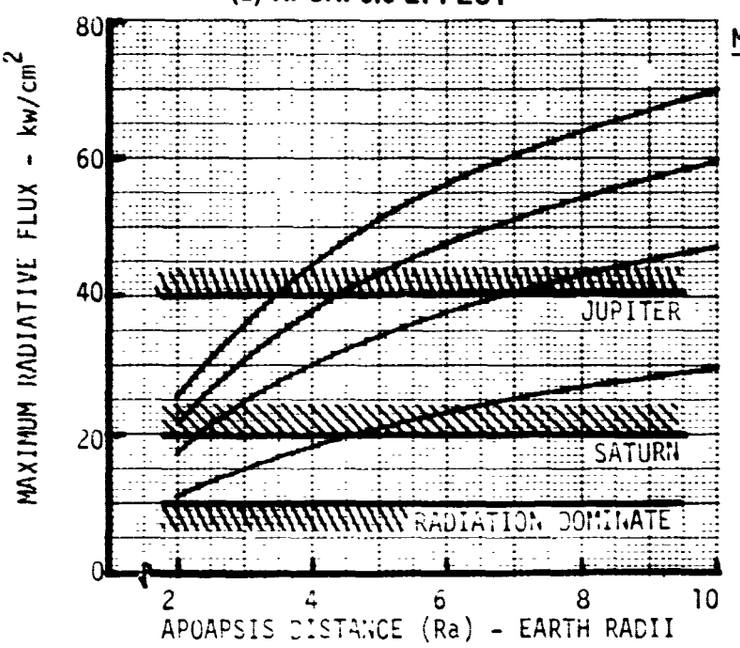

PAYLOAD MASS (kg)	β (kg/m²) *
200	240
150	180
100	120
50	60

*C_DA = CONSTANT

(b) PAYLOAD MASS EFFECT

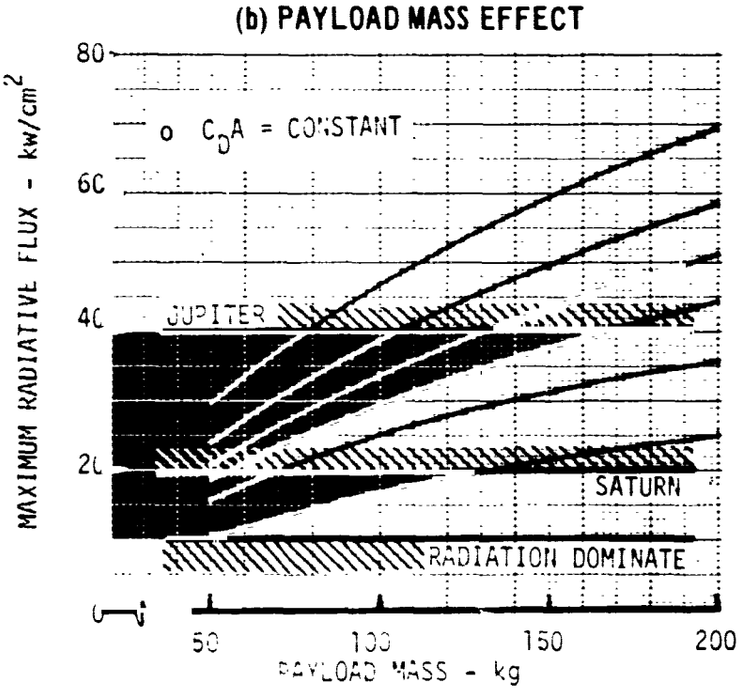

R_a
10
6.6 (SYNC. ALT.)
5
4
3
2

FIGURE 110

down faster than the booster entry condition capability. This can be seen in Figure 110 by noting that as payload mass increases, higher radiative flux levels are achievable if R_a is held constant or a lower R_a can be used if radiative flux is held constant.

7.2 Multiple Non-Blowing Parameter Simulation - Although earth entry conditions can be selected that will result in matching peak radiative heat flux levels for entry into Saturn or Jupiter, the precise simultaneous matching of all other entry parameters can only be approximated. Figure 111 presents four additional earth entry environment parameters as a function of the peak radiative heat flux. It is seen that peak convective heat flux is essentially independent of entry angle and always falls short of the planetary value by just under a factor of two. The total integrated heat load can be varied by about a factor of three depending on the selection of the entry angle. This permits one to match the total heat load for Saturn. However, even the shallowest earth entry falls short of the total heat load for Jupiter. Although this might be of some concern if the flight test is meant to qualify a Jupiter heat shield, it is not expected to be a serious deficiency when the flight test is intended to enlarge the technology base. G-loads and stagnation pressure are closely related and can be nearly matched for either Jupiter or Saturn. The best overall match can be obtained for Jupiter at a 20 degree entry angle. Referring back to Figure 109 it is seen that this requires an earth entry velocity on the order of 20 km/sec. This will of course be extremely difficult to achieve with any but the most energetic upper stage boosters.

As shown in Section 4, vehicle configuration can also influence the relative as well as the absolute level of environment parameter simulation. In addition to varying the entry velocity and flight path angle, the level of radiation flux can be altered by selecting different ballistic coefficients and different nose radii for the entry vehicle. For example, doubling the ballistic coefficient more than doubles radiative flux but increases convective flux by less than 50 percent. Similarly reducing nose radius by a factor of 2 reduces radiative flux by about 20 percent but increases convective flux by approximately 40 percent. This points out the potential use of vehicle configuration "tailoring" as a means of closer simultaneous simulation of environment parameters. For example, Figure 112 illustrates how reducing nose radius can more closely achieve simultaneous simulation of peak convective and radiative flux levels.

EARTH ENTRY SIMULATION CAPABILITY

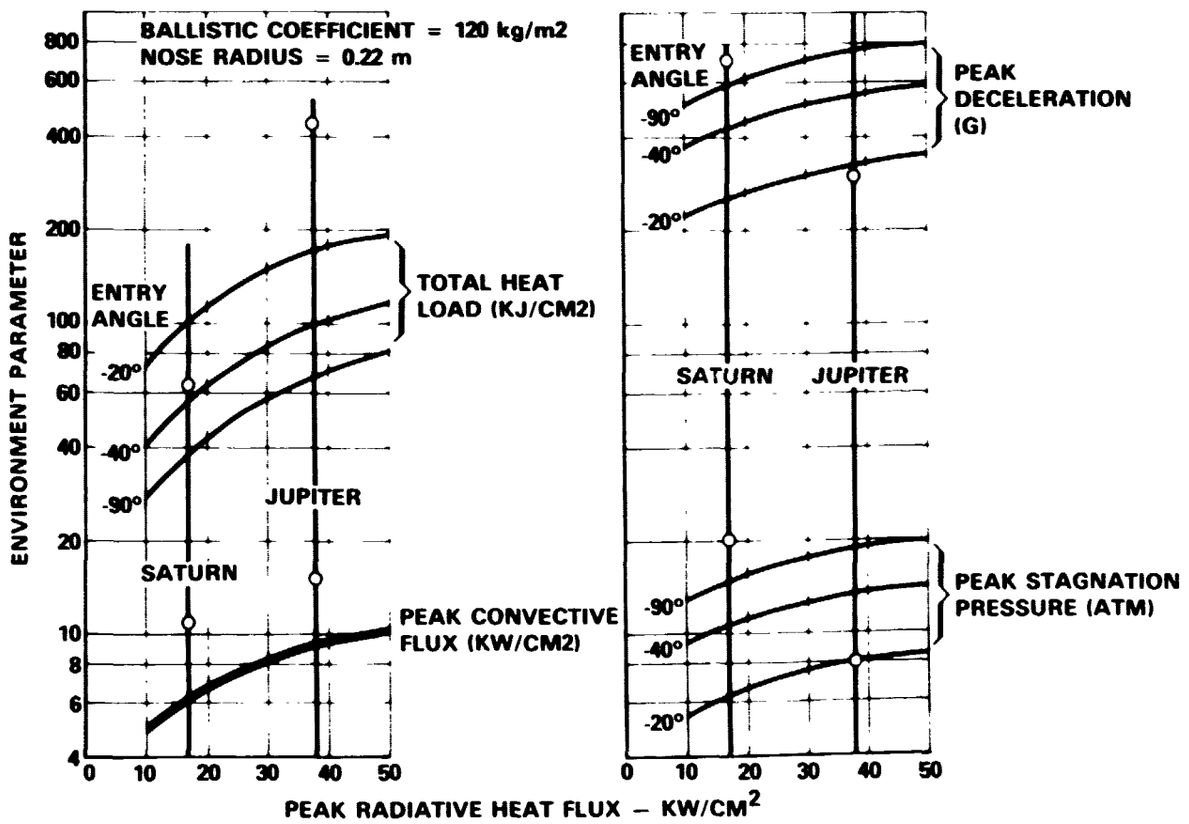

FIGURE 111

SIMULTANEOUS SIMULATION OF CONVECTIVE & RADIATIVE FLUX

- o EARTH ENTRY
- o STAGNATION POINT
- o NON BLOWING
- o $(R_N)_{REF}$ = .22 m
- o INDEPENDENT OF β & γ

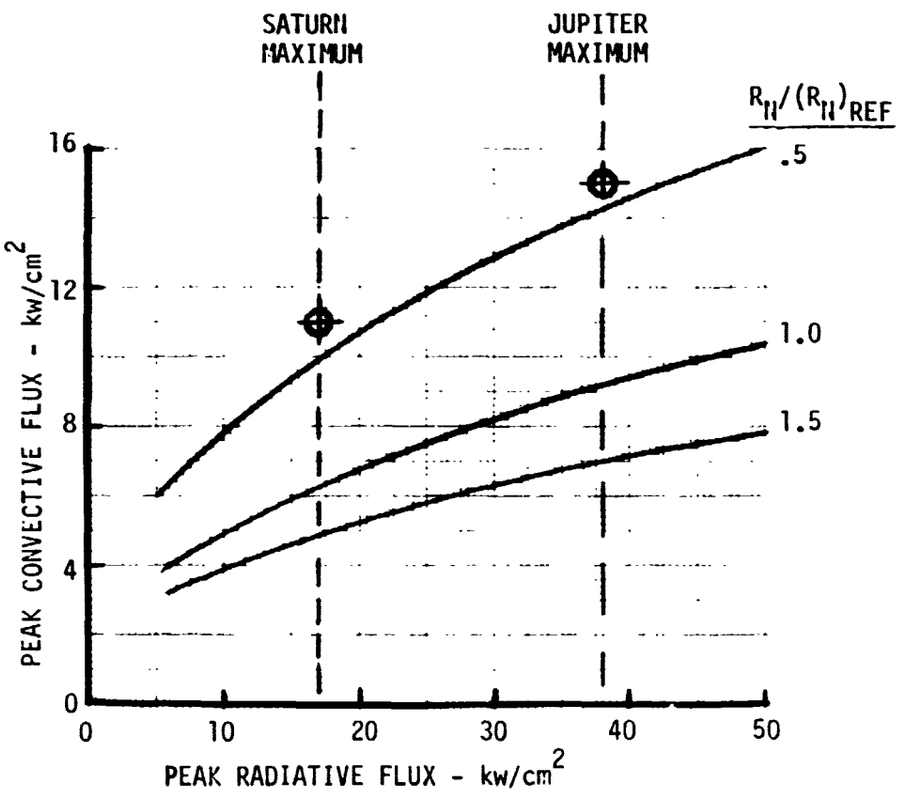

FIGURE 112

7.3 Simulation of Jovian Radiative Heating with Blowing - As mentioned previously, the computation of radiative heating in the presence of mass injection due to ablation involves sophisticated computer codes. Methodology within these codes yield slightly different values of heating due to the formulation of temperature profiles, species concentration profiles, spectral reflectance, integration technique, spectral absorption coefficients, etc. Detailed analyses were made for several Jovian flight conditions and earth flight conditions, and for three heat shield materials; carbon, carbon phenolic and hyperpure silica. First, a point comparison is presented for a typical Jovian condition followed by the parametric analysis for simulation of maximum heating.

7.3.1 Simulation of Typical Radiative Heating with Blowing - In Section 3.2, the incident and net heat flux were determined at a peak heating (condition "II") during a typical Jovian entry. For the carbon heat shield, the incident radiative flux was 13.81 kW/cm^2 and the net flux that the heat shield had to accommodate was 9.08 kW/cm^2. For the hyperpure silica heat shield, the incident flux was 24 kW/cm^2 with 1.0 kW/cm^2 that had to be accommodated. These heating values are compared in Figure 113 with peak flux produced during earth entry from V_E = 16.76 km/sec as a function of enetry angle. It should be noted that Jovian similar profiles through the shock layer were used for the earth entry computations. The shaded bands on this figure represent changes in heating that may occur due to moderate mass injection. When massive blowing occurs, a larger change in heating is obtained. The carbon shield shows a much smaller change in heating than obtained for carbon phenolic. In addition to the carbon species generated by the carbon shield the carbon phenolic liberates C-H radicals which are good absorbers of VUV radiation and hence a lower heating.

As shown on the figure both the incident and the net radiative fluxes to the carbon are matched at an entry angle of -22 degrees. The incident flux on the silica shield is matched at -48 degrees but the net flux will be substantially greater than predicted for the Jovian entry. This increase is beneficial in simulating total heat and heat shield performance. Similar results are obtained in the next section when analyzing maximum design heating simulation.

7.3.2 Simulation of Maximum Radiative Heating with Blowing - The uncertainties in Jovian entry conditions resulted in a maximum non-blown radiative heating of 38 kW/cm^2. The corresponding blown radiative heating values for the candidate heat shields are:

HEAT SHIELD RADIATION PERFORMANCE FOR EARTH ENTRY

(BASED ON JOVIAN SIMILAR SHOCK PROFILES)

V_E = 16.76 KM/SEC

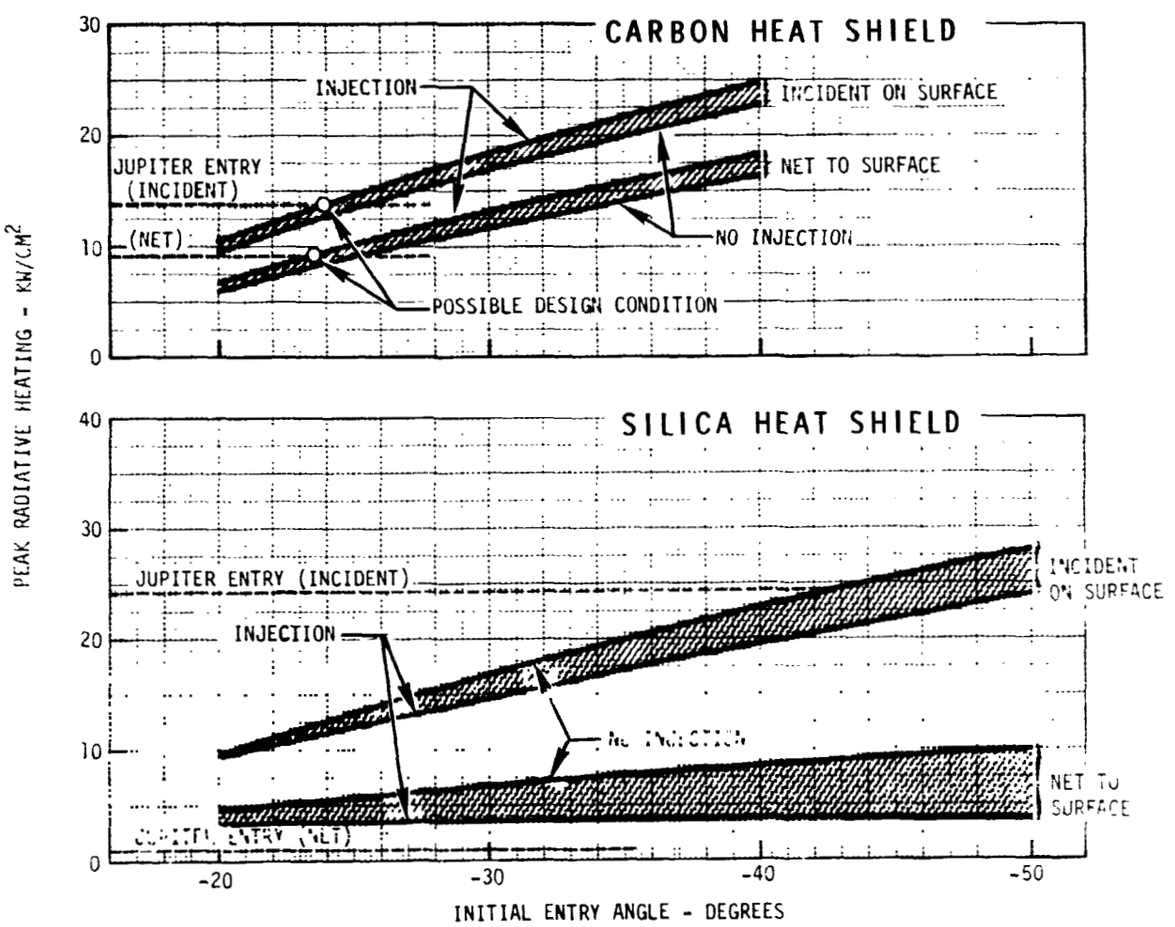

FIGURE 113

	Carbon Phenolic	Silica	Carbon
$q_{Incident}$ (Blowing)	26.6	30.5	16.42
$q_{Net\ to\ Surface}$ (Blowing)	17.48	2.0	10.79

The maximum blown heating environments on the heat shields during earth entry using the Transtage/TE364-4 and the SRM IUS/TE364-4 booster were determined to establish the degree of simulation. The comparisons are shown on Figure 114. Both the incident and net maximum heating to the carbon phenolic shield can be simulated using the Transtage booster. Simulating the maximum incident radiative flux requires a trajectory to 12 earth radii, however, the carbon phenolic shield will be required to accommodate 17% more net flux than for a Jovian entry. This additional flux improves the simulation of total heat.

A Transtage boost will also match the incident flux on the silica shield but 5-1/2 times the required net flux will be experienced causing an increase in surface recession. This is not expected to destroy the validity of such a test. Indeed, if the silica can accommodate this additional heat, it will demonstrate the capabilities of the reflective heat shield. The net flux to the silica shield can easily be simulated with either the Transtage or the SRM IUS by flying a trajectory to altitudes less than 2 earth radii. Using the SRM IUS to simulate carbon phenolic shield net flux is possible by flying to R_a = 20 but the incident flux is 22 kW/cm^2 instead of 26.6 kW/cm^2. Similarly a solid IUS boost does not produce the desired incident flux on the silica shield. A maximum of 24 kW/cm^2 is achieved. These are very high radiative heating values and obtaining data in this radiation dominated regime is worthwhile and will significantly increase the technology base. If simulation of a 30.5 kW/cm^2 radiative flux on a silica shield is absolutely required,a larger solid IUS stage would be required.

BLOWING RADIATIVE FLUX SIMULATION – EARTH

(100 kg; β = 100 kg/m^2 VEHICLE)

TRANSTAGE/TE364-4

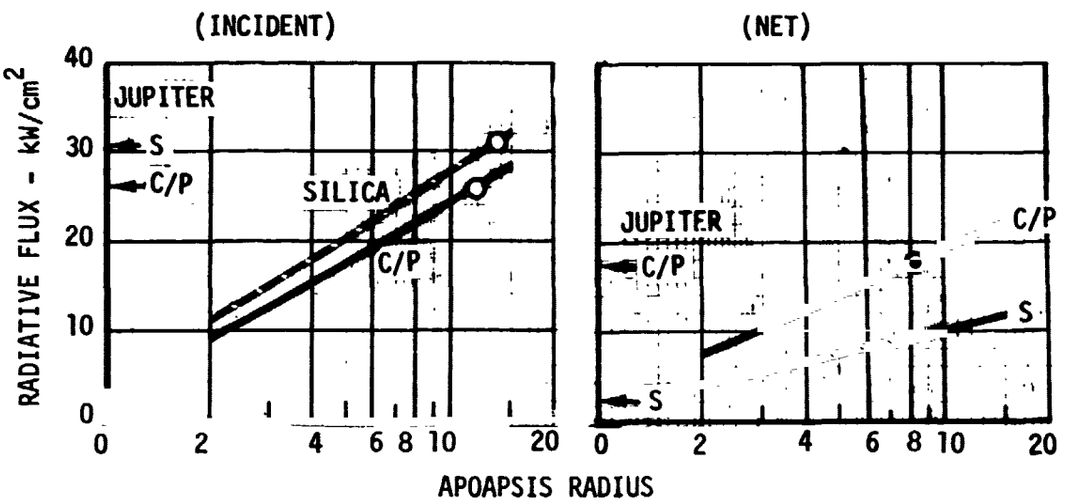

SRM IUS/TE364-4

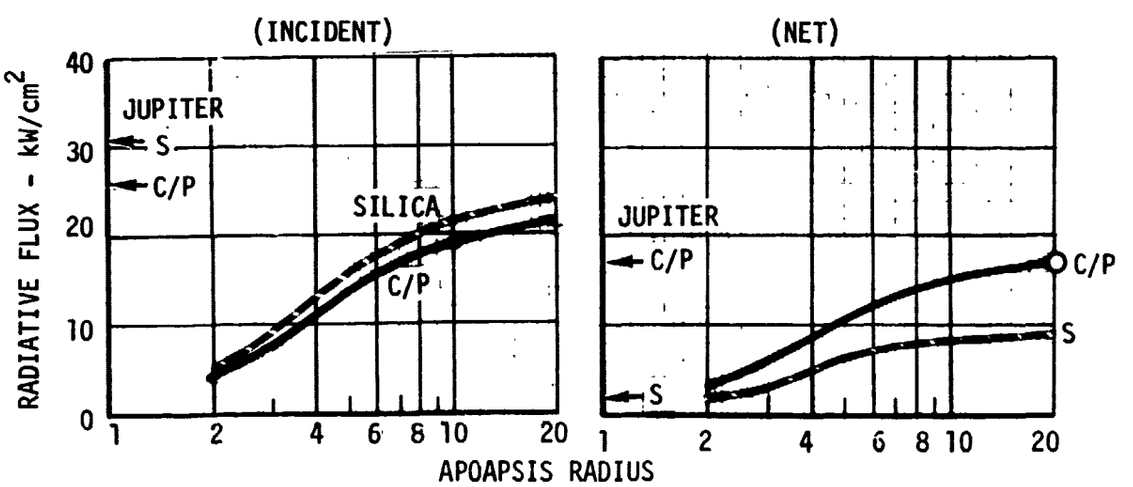

C/P - CARBON PHENOLIC
S - SILICA

FIGURE 114

8.0 ENTRY VEHICLE EXPERIMENTS

Projected technology needs for a complement of entry individual experiments were assessed by reviewing state of the art measurement goals and by conversation with outer probe teams and key NASA personnel. The experiment goals were defined and the return expected from a measuring device weighed against the impact on the vehicle design and weight increment. A recommended list of experiments was compiled and the location of instruments coordinated with the design of the entry vehicle. Because the flight experiment vehicle is primarily a heat shield/thermal environment research tool, its heat shield must be a part of the experiments in addition to providing vehicle thermal protection. In some instances the experiments and/or instrumentation drove vehicle design.

Candidate heat shield concepts were identified (Figure 115) and their attributes are as follows:

A. Single Ablator - This concept, which would employ either a reflective or non-reflective heat shield is conceptually the simplest and most reliable. For any given entry profile, it is probably also the lightest; thus this concept should permit a larger fraction of vehicle mass to be devoted to instrumentation, data management, and recovery. Separate flights would be required to address each of the candidate heat shield materials.

B. Heat Sink Approaches - The large heating rates which the entry vehicle will encounter precludes the useful application of beryllium heat sinks in the manner employed by the PAET, or FIRE vehicles (References 14 and 15). For instance, time-to-melt for a berryllium heat sink at a flux of 1 kW/cm^2 is approximately 7 seconds, at 10 kW/cm^2 it is 0.07 seconds. Because efficiency of mass transfer cooling increases with free stream enthalpy, the possibility exists that local application of transpiration cooled surfaces may be feasible. Active transpiration has been successfully employed on reentry vehicles to protect small areas from convective heating comparable in severity to the required environment. In assessing the feasibility of employing transpiration locally, the effect of the radiative environment needs to be evaluated.

C. Dual Ablator Concepts - A number of possibilities exist for using more than one ablator in the heat shield. Such an approach suggests the possibility of obtaining performance comparisons between two or more heat shield materials which have been exposed to the same environment. In addition,

HEATSHIELD CONCEPTS FOR EARTH ENTRY VEHICLES

CANDIDATE ENTRY PROBE HEAT SHIELD CONCEPTS

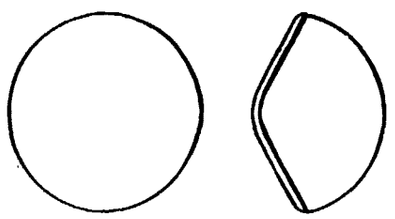

SINGLE ABLATOR

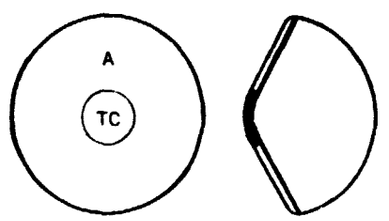

TRANSPIRATION COOLED NOSE CAP/ABALATOR

CANDIDATE MATERIALS
TRANSPIRATION COOLED (TC)
• TUNGSTEN
• POROUS CERAMICS
ABLATOR (A)
REFLECTIVE (R)
• FUSED SILICA
NON-REFLECTIVE (NR)
• CARBON PHENOLIC
• CARBITEX 100
• ATJ GRAPHITE

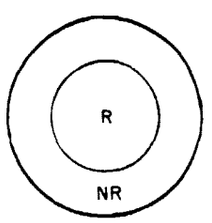

CONCENTRIC

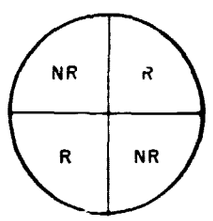

ALTERNATING QUADRANT

DUAL ABLATOR

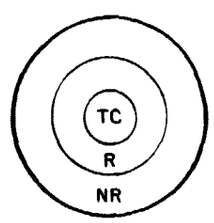

CONCENTRIC

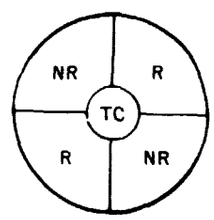

ALTERNATING QUADRANT

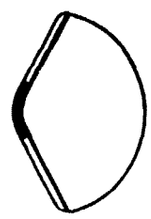

TRANSPIRATION COOLED NOSECAP/DUAL ABLATOR

FIGURE 115

there is an obvious appeal to testing two or more heat shields "for the price of one". A number of potential problems require investigation before such an approach can be judged completely feasible. Some of these are:

- o Contamination - Can inter-ablator contamination either in the boundary layer or due to liquid runoff be avoided?
- o Material Interfaces - Are problems likely to arise due to surface discontinuities at ablator material interfaces? Are chemical reactions between adjoining ablators likely to cause difficulties?
- o Vehicle aerodynamics - Are differences in recession rates between ablators likely to introduce pitching or rolling moments?
- o Trajectories - Are different test trajectories for reflective and carbonaceous ablators necessary to meet planetary entry technology needs?
- o Structural integrity - Can structural integrity be preserved with a multiple ablator heat shield?

The alternating quadrant approach shown in Figure 115 has been successfully employed to test more than one ablator. However, the vehicle geometry and flight environment were different from those envisioned for the planetary entry simulation and ground testing is necessary before flight.

The key experiment affecting vehicle design was the complexity of the heat shield design. All candidate heat shield designs were evaluated and the single material design selected. The other designs did not test candidate outer planet heat shield materials or had problems with interfaces between materials that would recede at different rates and contaminate one material by the flow of dissimilar ablation products over adjacent materials. Also a heat shield segmented with dissimilar materials would have stress and strain patterns far different than the single heat shield design used in the outer planet probes. Instrumentation location would also have to be compromised because of attachment devices and minimum edge distance requirements needed to minimize local stress concentrations.

8.1 Experiment Definition - One of the end products of this program is the design of an earth entry flight experiment which will provide valuable information for the successful entry of a probe into the atmosphere of an outer planet. In general, flight experiments are used to achieve an adequate entry technology base for future design by firming up the foundations in several areas of technology. The principal planetary entry technology needs are:

a. Verified shock layer radiation heating predictions.
b. Verified predictions of radiation blockage by ablation.
c. Verification of heat shield design
   - carbon phenolic mechanical and chemical erosion characterization
   - silica performance and structural integrity
d. Establishment of a reliable transition criteria under conditions of high energy flow and high rates of ablation.
e. Determination of turbulent heat transfer.
f. Determination of the influence of the chemical state of the shock layer and ablation product gases on radiative and convective heat transfer.
g. Development of reliable predictions of afterbody heating and loads.
h. Determination o heat shield stresses.
i. Investigate vehicle aerodynamics and stability.

It is very important to test a full heat shield so that the correct stress levels, mechanical and thermal, can be developed. Consequently, the experiments which are described in this section are based on a full ablative heat shield. The candidate experiments envisioned to meet these needs can be grouped in three categories:

a. Flow field
b. Heat shield performance
c. Aerodynamics

Measurements of various parameters can provide data with which to substantiate or update theoretical analyses or provide empirical correlations. Instrumentation available to make measurements and which can be packaged in the earth entry vehicle include:

1. Thermocouples; surface, indepth stack, and internal.
2. Pressure probes
3. Accelerometers

4. Strain gauges
5. Electrostatic probes
6. Radiometer

Other instruments such as boundary layer microphones were considered but they were eliminated because of complexity and that other instruments would provide the same data. Specific experimental objectives are summarized in Figure 116. Included on the figure is an indication of the particular instrumentation devices which can be used. The entry vehicle will be air-recoverable so that post flight heat shield and vehicle examinations can be made.

Location of the various instrumentation devices on the heat shield is shown in Figure 117 and were coordinated with the packaging of equipment within the vehicle. Furthermore the quantity of each instrument was established to produce sufficient data to meet experiment needs. An attempt has been made to locate the devices in such a way as to detect expected minima or maxima measurements in the radial direction. The entry vehicle will be spun up for stability etc. as well as the probe for outer entry. Expected radial distribution of pressure and radiative heating for a typical case is shown in Figure 118.

The electrostatic or Langmuir probe is a device from which the electron concentration flux at the wall may be determined. This device has been proven in flight to be a useful tool in comparing measurements with theoretical analytical predictions. Typical electron concentration profiles for high speed earth entry are shown in Figure 119. Probe installation and associate equipment characteristics are described in Section 9.2.

The radiometer is the primary piece of equipment and measures total radiant energy and spectral values. Most flight radiometers are tailor made for a particular job and the studies performed for the entry vehicle is no exception. Design of a radiometer is aided by examining the spectral wall flux plots shown in Figures 120 and 121. The spectral distribution of wall flux is compared for carbon injection, silica injection, and a clean atmosphere for an earth entry shock layer. Also shown in the figures (and in Figure 122) are the wavelengths selected for a multichannel radiometer in order to characterize the radiant flux. These wavelengths (12) were selected so that the same instrument can be used for measurements with either a carbon heat shield or a silica heat shield. The temperature and injectant mass fraction profiles used in the computation of the spectra are shown in Figure 123.

EXPERIMENTAL OBJECTIVES

	INSTRUMENTATION					
	RADIOMETER	THERMOCOUPLE*	PRESSURE PROBE	ACCELEROMETER	STRAIN GAUGE	ELECTROSTATIC PROBE
FLOW FIELD						
SHOCK LAYER RADIATION TRANSPORT	X					
CONVECTIVE HEAT FLUX		X				
BOUNDARY LAYER TRANSITION		X	X			X
AFTERBODY HEATING DISTRIBUTION		X	X			
AFTERBODY PRESSURE DISTRIBUTION			X			
MASSIVE BLOWING INTERACTION WITH BOUNDARY LAYER & DOWNSTREAM EFFECTS	X	X	X			X
HEAT SHIELD PERFORMANCE						
SUBLIMATION MECHANISM		X				
MECHANICAL EROSION		X				X
UNSYMMETRICAL & UNEVEN ABLATION		X				
SURFACE ROUGHNESS		X				
AERODYNAMICS						
HYPERSONIC VEHICLE MOTION PERTURBATION CAUSED BY						
MASS AND SHAPE CHANGES				X	X	
MASSIVE ABLATION PRODUCT BLOWING				X	X	
SURFACE ROUGHNESS				X	X	
REAL GAS EFFECTS				X	X	
TRANSONIC/SUBSONIC DYNAMIC STABILITY				X		

*THERMOCOUPLE STACKS ARE INCLUDED

FIGURE 116

ENTRY VEHICLE HEAT SHIELD INSTRUMENTATION

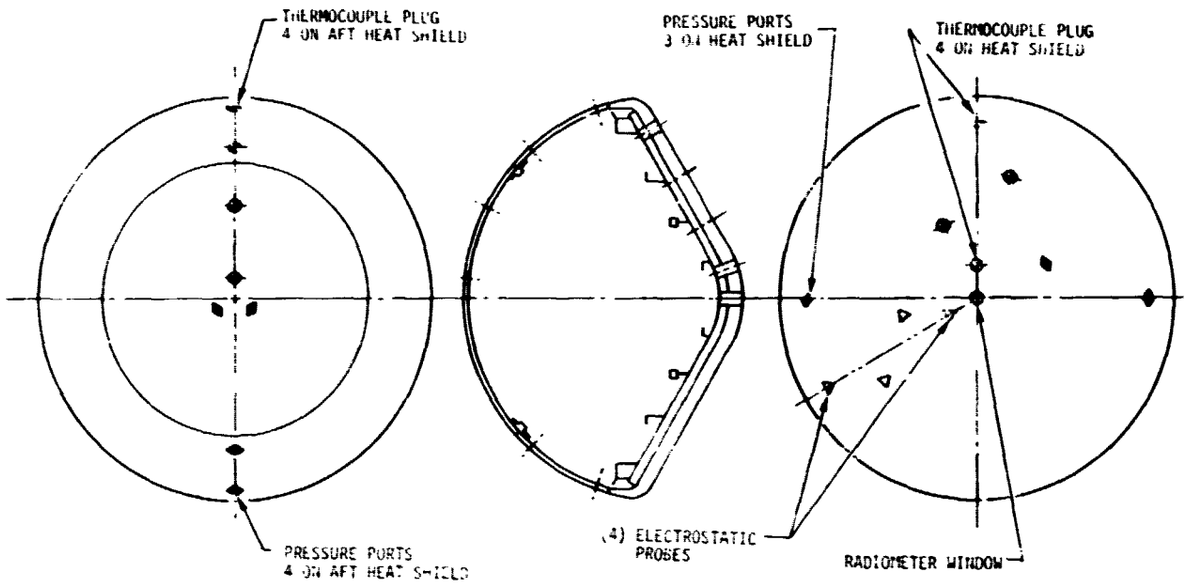

FIGURE 117

EXPECTED RADIAL DISTRIBUTION OF PRESSURE AND RADIATIVE HEATING FOR A 60 HEMISPHERE CONE

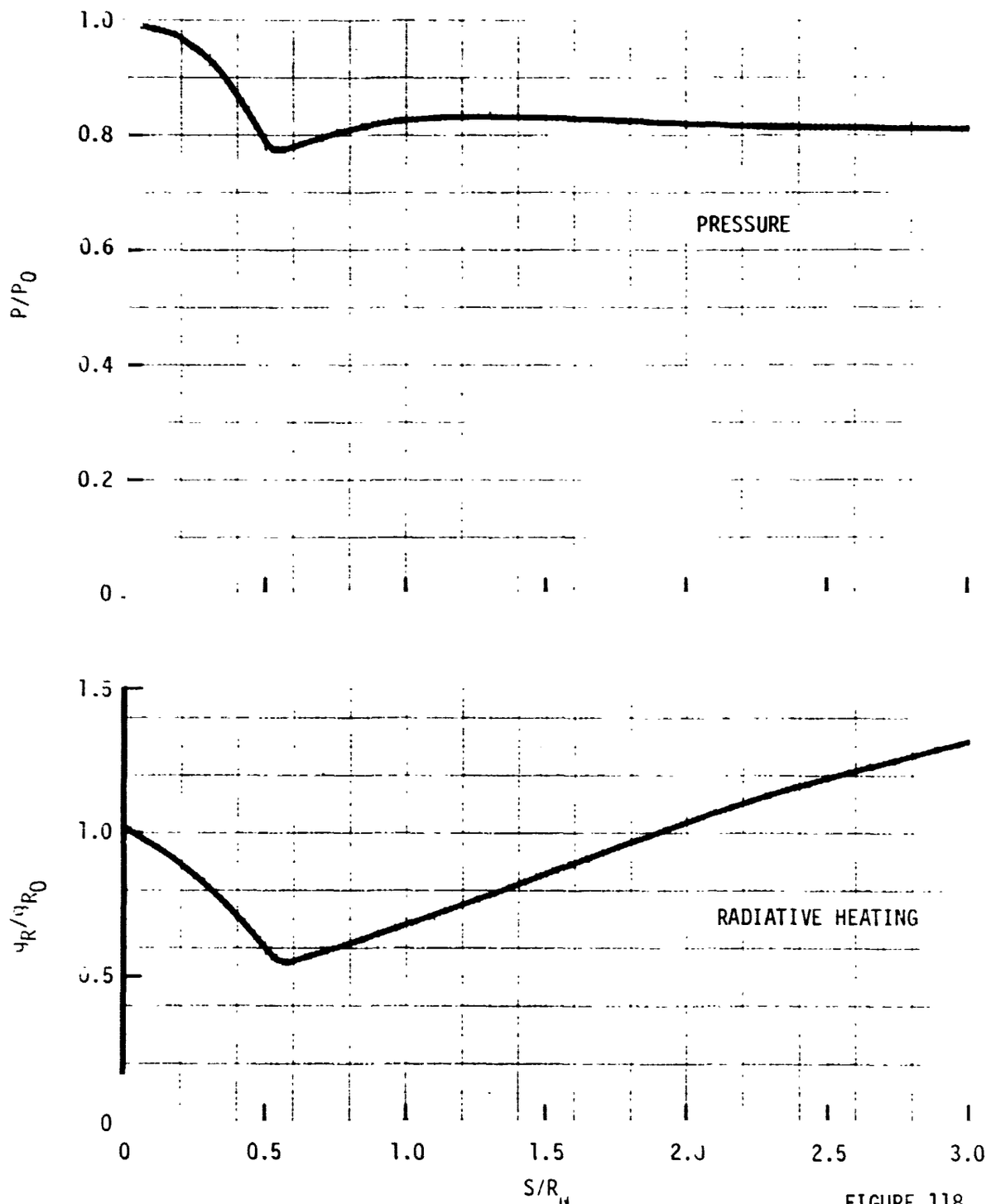

FIGURE 118

SHOCK LAYER ELECTRON CONCENTRATION PROFILE

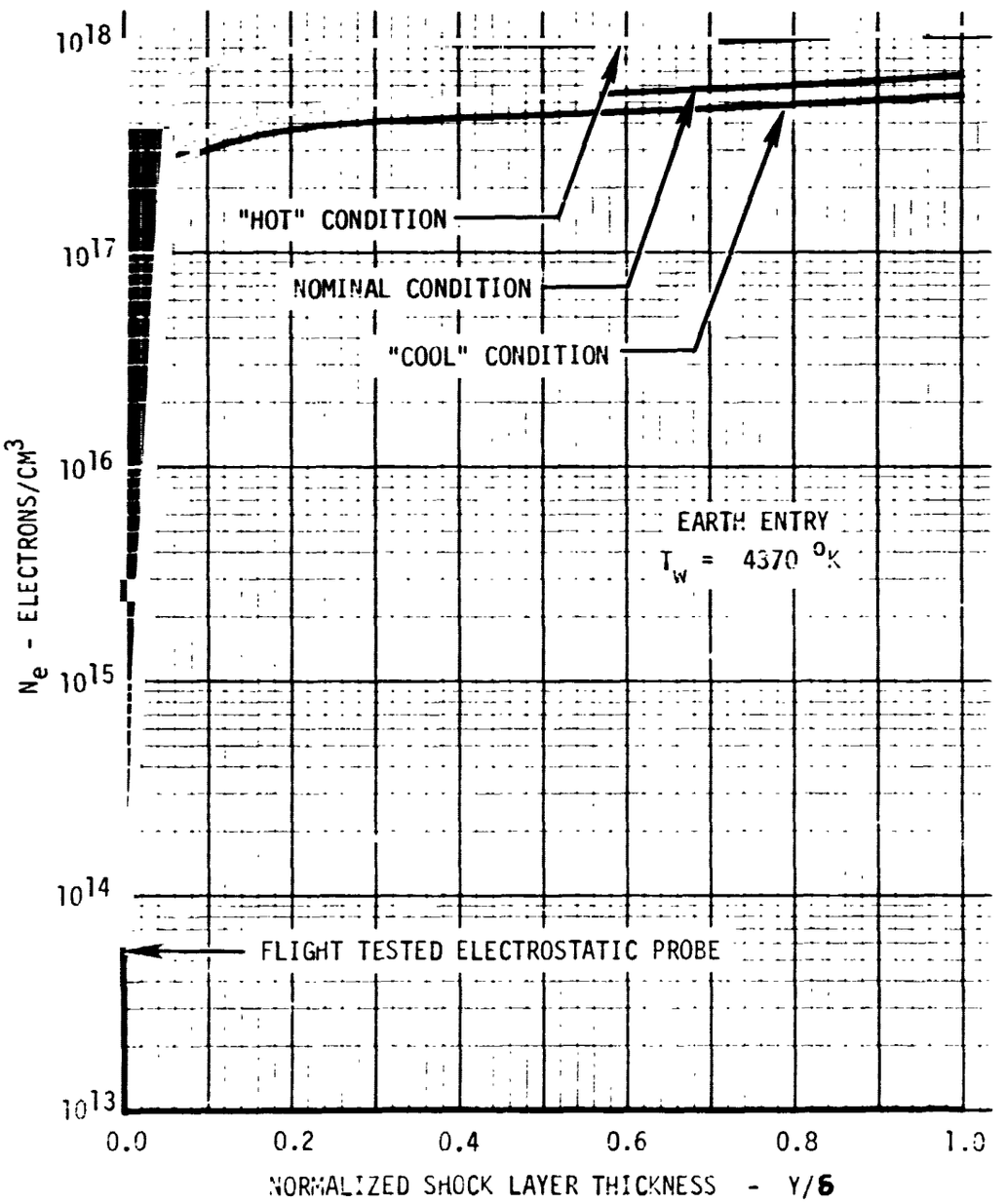

FIGURE 119

SPECTRAL WALL FLUX FOR EARTH ENTRY WITH ABLATING MATERIAL INJECTION

RADICAL/69 COOLED SHOCK LAYER

T_S = 16100°K
T_S^W = 4370°K
P_S = 6.80 ATM
ε = 0.9357 cm

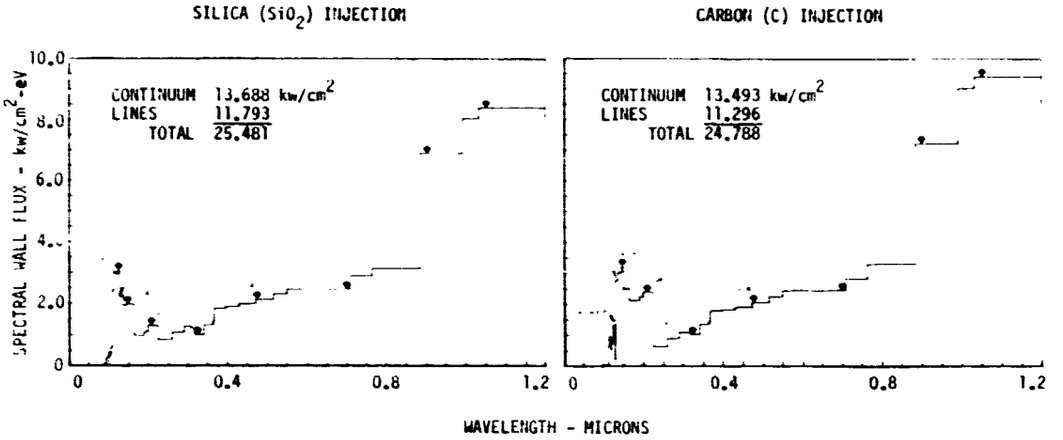

FIGURE 120

SPECTRAL WALL FLUX FOR EARTH ENTRY WITH CLEAN SHOCK LAYER

RADICAL/69 COOLED SHOCK LAYER

CONTINUUM 12.792 kw/cm^2
LINES 9.906
TOTAL 22.698

T_S = 16100°K
T_S^W = 4370°K
P_S^W = 6.80 ATM
ε = 0.9357 cm

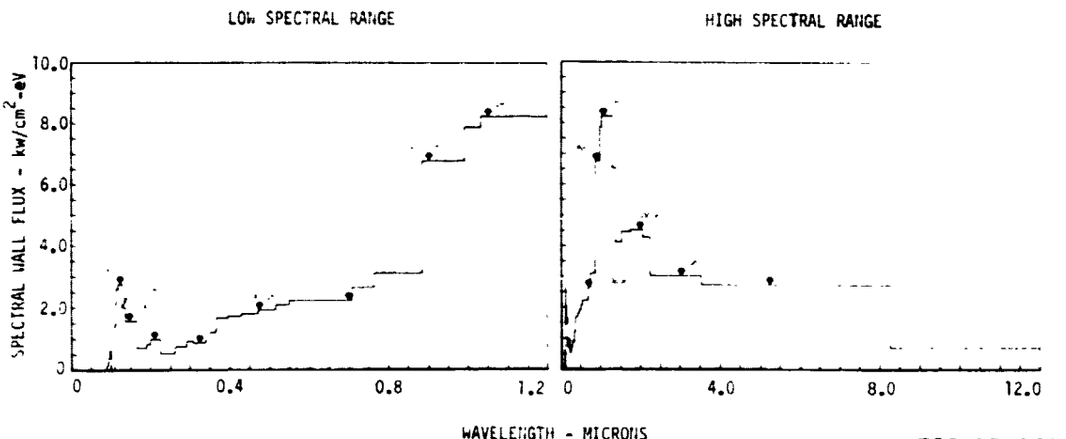

FIGURE 121

SELECTED WAVELENGTHS FOR CHARACTERIZING RADIANT HEATING DURING EARTH ENTRY

0.125 μm
0.133
0.146
0.210
0.325
0.475
0.700
0.900
1.050
2.000
3.050
5.250

FIGURE 122

TEMPERATURE AND INJECTANT PROFILES FOR EARTH SHOCK LAYER

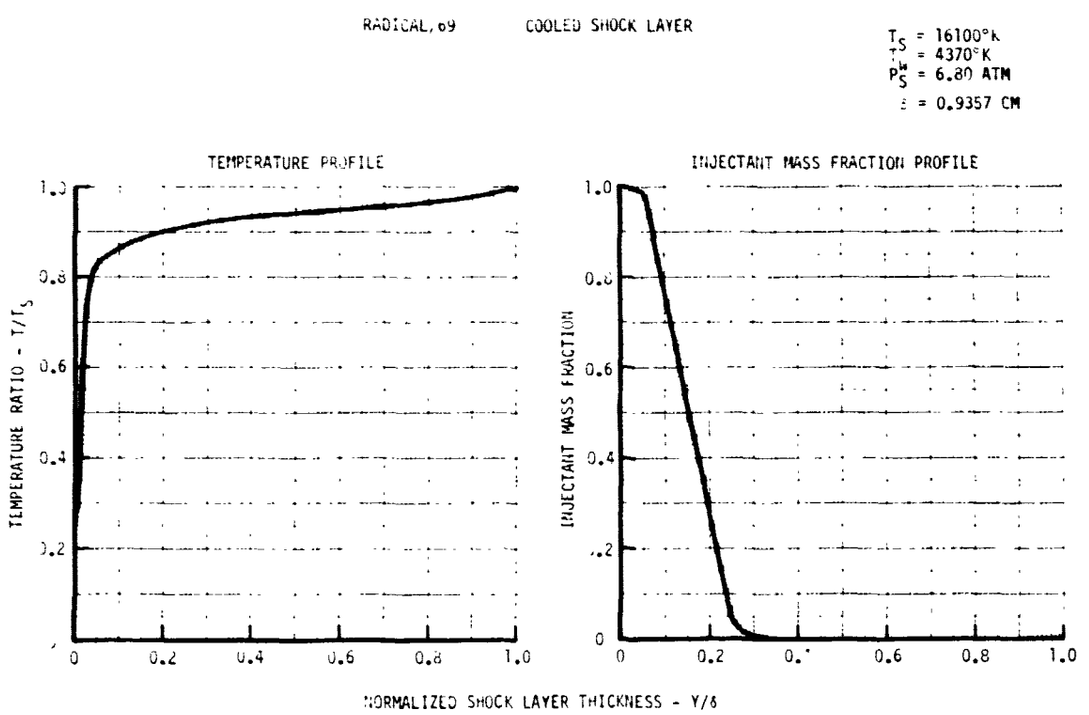

FIGURE 123

8.2 Recommended Measurements - A combined list of measurements identified for the entry vehicle is shown in Figure 124. There are nine (9) types of measurements that will require ninety-four (94) data channels in the telemetry system. The quantity of data channels shown in Figure 124 implies a sensor for each channel except for the radiometer which is a single device with twelve (12) output signals. (The alternate version requires three (3) channels.) Most of the sensors have a high level (HL) 0 to 5 volt output to the telemetry system. The temperature and strain measurements are a low level (LL) 0 to 40 millivolt signal. The data sampling rates, in samples per second (SPS), were chosen to be compatible with the expected rates of temperature rise and other dynamic phenomena encountered during the critical entry period.

The two significant scientific measurements are the electrostatic probes and the radiometer. The electrostatic probes are similar to those successfully used on the MDAC-E designed RVTO-2A vehicle. These probes will measure peak electron density in the vehicle boundary layer. Four probes will be appropriately spaced in the heat shield so that axial variations in electron generation rates can be measured. (See Figure 125).

ENTRY VEHICLE EXPERIMENT MEASUREMENT LIST

Measurand	Range	Data Channels		
		Qty	Type	SPS
Acceleration-Long.	0 to -500g	1	HL	50
	+5 to -25g	1	HL	100
Acceleration-Vert.	$\pm$6g	1	HL	100
Acceleration-Lat.	$\pm$6g	1	HL	100
Electrostatic Probes	10^{-7} to 10^{-3} a/cm^2	4	HL	400
Pressure-heat shield	0 to 150 psia	3	HL	50
Pressure-aft body	0 to 5 psia	4	HL	10
Pressure-internal	0 to 15 psia	1	HL	10
Radiometer-spectral	0 to 40 kW/cm^2	12	HL	100
Rate-Roll	0 to 25 rad/sec	1	HL	50
Rate-Pitch & Yaw	$\pm$8 r d/sec	2	HL	100
Structural deflection	-.10 to +.10 in	3	HL	50
Structural strains	$\pm$0.005 in/in	8	LL	10
Temperature-heat shield	300 to 2400°K	28	LL	25
Temperature-aft body	300 to 1200°K	12	LL	10
Temperature-internal	250 to 500°K	6	LL	10
Voltages-misc	30 V. max	6	HL	10

FIGURE 124

The radiometer will measure spectral energy in the band from 0.100 to 10.00 microns. Two design approaches were investigated. In one approach, energy is measured at twelve discrete wavelengths within the band and in the other, two detectors are used to monitor the output of spherical diffraction gratings. These detectors require rotating mirrors to scan the upper and lower portions of the spectrum. The probes and the radiometer are discussed in more detail in succeeding paragraphs.

Other measurements on the vehicle include accelerometers and rate gyros to measure vehicle motion; temperature and pressure measurements in the heat shield to supplement the environmental data from the radiometer and electrostatic probes; and some structural strains and deflections to assess the environments impact on the vehicle. The total quantity of measurements is constrained by the space available and this precluded the structural deflection measurements which require a relatively large stiff beam as a reference from which deflections can be measured.

8.3 Electrostatic Probes - The probe consists of two flush mounted electrodes separated by a suitable dielectric (insulator) as illustrated in Figure 125. The probe connects to an electronics circuit as shown in Figure 126. A bias voltage is applied so that electrons in the boundary layer plasma are repelled from the negative electrode and attracted to the positive. At some specific bias, the number of electrons reaching the negative electrode approaches zero and the probe current levels off at a value defined as the ion saturation current. This saturation current can be directly related to the ion and electron densities in the boundary layer. By applying a sweeping bias voltage to the probe, the density level at which ion saturation occurs can be accurately determined. At a sampling rate of 400 samples per second and a sweep time of 100 milliseconds, the forty data points obtained will be sufficient to establish the knee of the probe current curve. The repetitive probe bias waveform is shown in Figure 127.

8.4 Radiometers - A major problem in radiometer design is the measurement of vacuum ultraviolet energy, particularly in the range below 0.25 microns. Traditional window materials such as fused quartz are opaque in this region. The only known material which will pass radiation down to 0.12 microns is lithium fluoride. However, this material is thermally and mechanically inferior to quartz and therefore will require environmental protection. The evolved designs, shown in both Figures 128 and 129, consists of an open port through the heat shield and the window located at the entrance to the radiometer. A small tank of helium provides helium flow past

ELECTROSTATIC PROBE

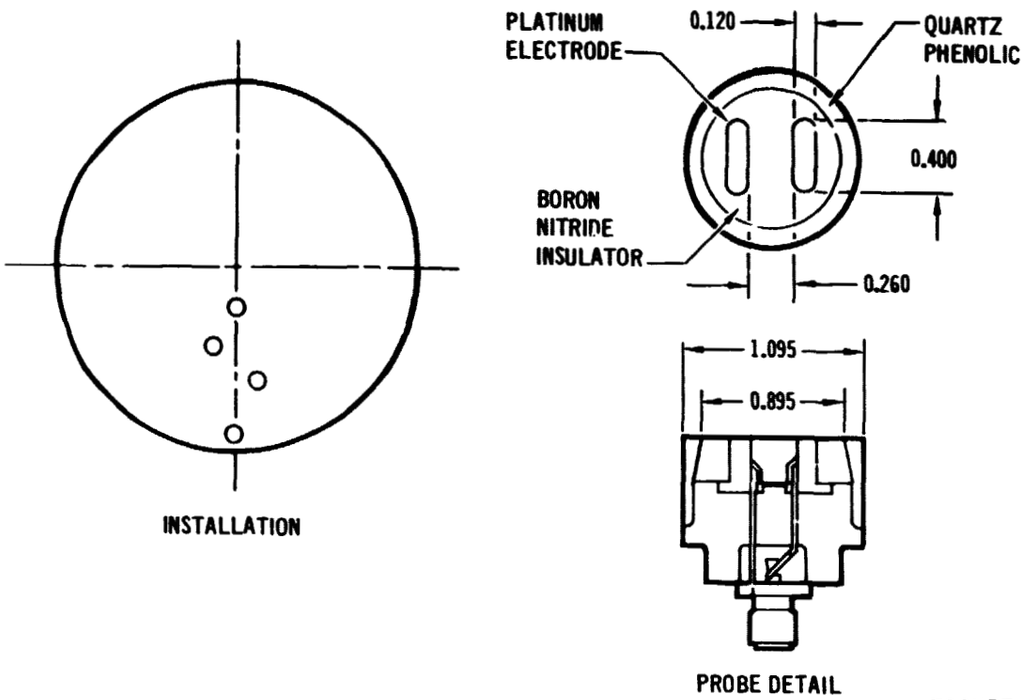

FIGURE 125

ELECTROSTATIC PROBE ELECTRONICS SCHEMATIC

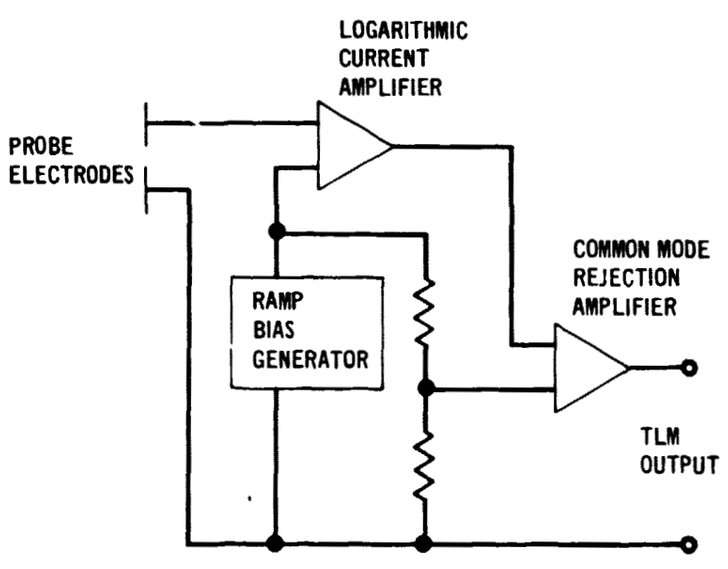

FIGURE 126

ELECTROSTATIC PROBE BIAS WAVEFORM

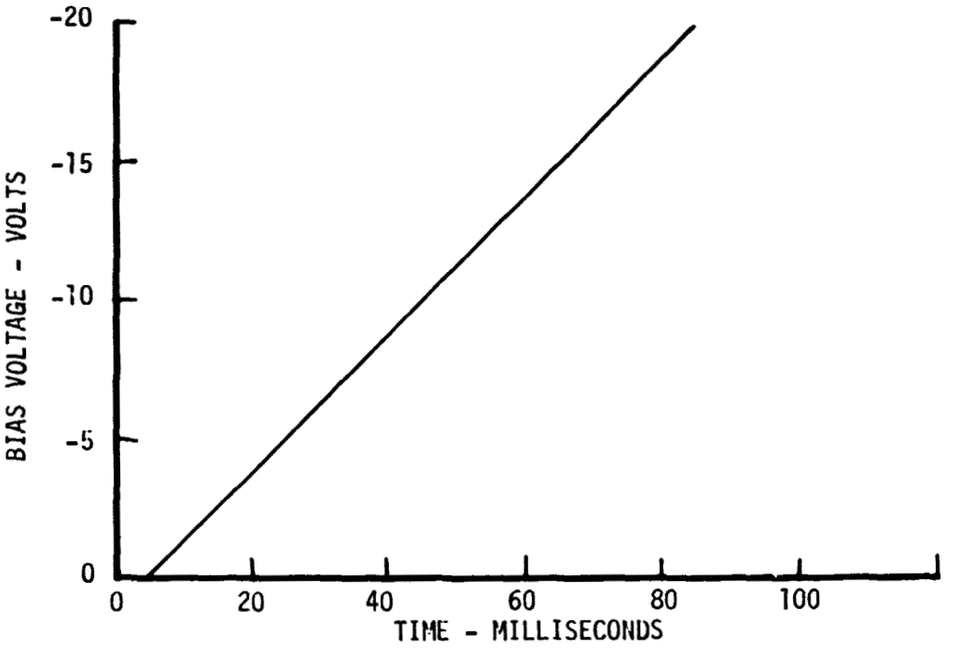

FIGURE 127

the window to cool the window and maintain a positive pressure that reduces the possibility of heat shield fragments obscuring the window by clogging the port. In the design shown in Figure 128, the helium tank is external to the radiometer package. The second design, Figure 129, shows a helium tank and electrically operated shut-off valve inside the package.

8.4.1 Multichannel Radiometer - In the multichannel radiometer design of Figure 128, a 12.7 mm dia collimating lens is located 30 mm from the opening in the housing. This lens is used to collect energy in the band from .1 to .3 μm and project it in parallel rays on the lithium fluoride prism. The prism is a 60 deg prism with a slant height of 15.9 mm and a length of 19.0 mm. The diffracted rays then pass through the 19.0 mm dia focusing lens and the energy focuses on the four detectors, spaced so as to see the four desired wavelengths of .125, .133, .146 and .210 μm. Two folding mirrors are required to accommodate the focal length of 225 mm. This focal length is dictated by the minimum spacing between detectors and the angular difference between two spectral lines. In this design, we have assumed that suitable detectors can be mounted in a standard TO-5 transistor package. Allowing a minimum, 10 mm center-to-center, spacing between detectors, then the angular difference of 2.55 deg between the .133 and .146 μm wavelengths establishes the 225 mm focal length.

Detection of energy at the eight wavelengths above .3 μm is accomplished by intercepting the incoming radiation with sapphire fiber optic "light pipes." These are connected to eight detectors grouped in a ring around the cylindrical housing. The detectors shown in Figure 128 are larger than those shown for the shorter wavelengths because they include an appropriate optical filter and one stage of amplification. Remaining amplification for these detectors and all amplification for the other four detectors is provided in the signal conditioner module.

8.4.2 Spectral Scanning Radiometer - In the spectral scanning radiometer design of Figure 129, diffraction gratings are used instead of the prism and lens arrangement. The beam approaching the prisms is intercepted by a lithium fluoride beam splitter which diverts some of the energy to an unfiltered wide band detector. The grating on the left in Figure 129, is ruled to work in the range from .1 to .3 μm. The ruling density will be 2400 lines per mm and the blaze angle about 8 deg. The grating on the right works in the range from .3 to 10 μm with a ruling density of 1200 lines per mm and a blaze angle of 18 deg. Diffracted energy from the prisms strikes rotating mirrors which, in turn, reflect energy onto the two

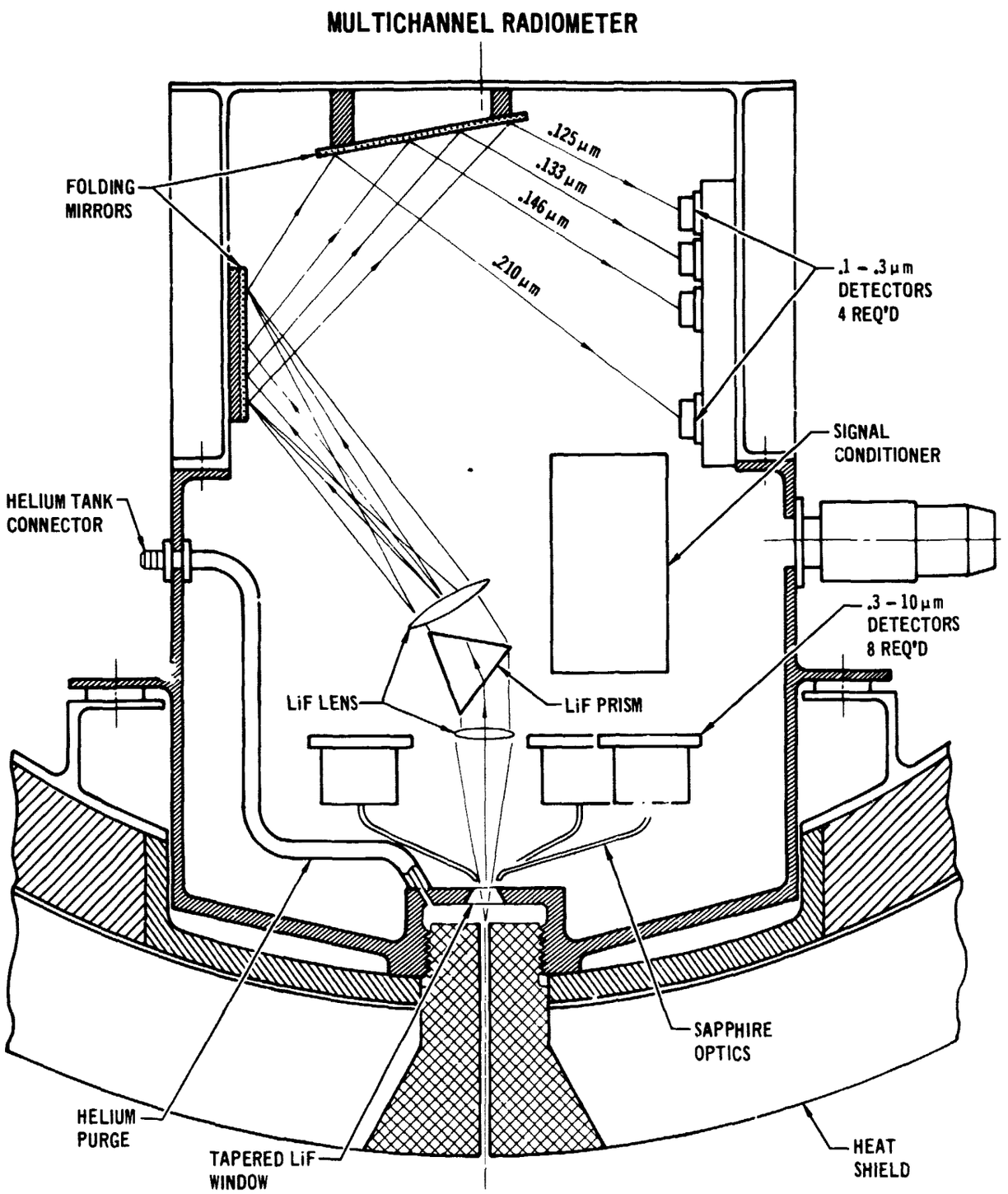
MULTICHANNEL RADIOMETER
.125 μm
.133 μm
.146 μm
.210 μm
FOLDING MIRRORS
.1 – .3 μm DETECTORS 4 REQ'D
SIGNAL CONDITIONER
HELIUM TANK CONNECTOR
.3 – 10 μm DETECTORS 8 REQ'D
LiF LENS
LiF PRISM
SAPPHIRE OPTICS
HELIUM PURGE
TAPERED LiF WINDOW
HEAT SHIELD

FIGURE 128

SPECTRAL SCANNING RADIOMETER

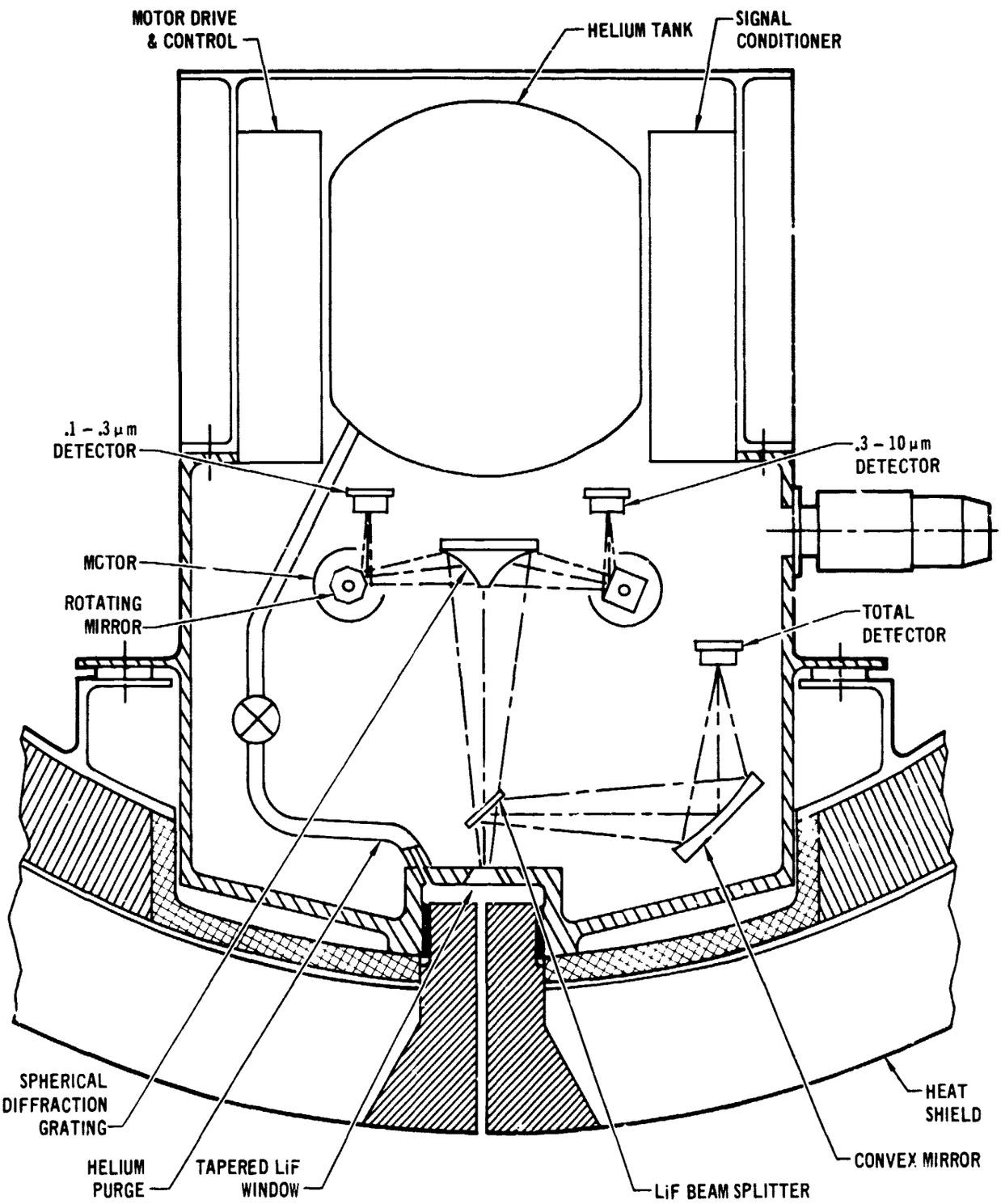

FIGURE 129

detectors. Both motors operate at 600 rpm and the PCM samples each detector at 800 ,. In the .1 to .3 μm band, the eight-sided mirror generates 80 spectral scans per second, giving data output at 10 discrete wavelengths updated 80 times per second. In the .3 to 10 μm band, the four-sided mirror generates 40 spectral scans per second, giving data output at 20 discrete wavelengths, updated 40 times per second.

Comparing the two designs, the multichannel radiometer has the advantage of simplicity, since there are no moving parts and the construction can be sufficiently rigid that the optical characteristics are not affected by the flight environment. The amplitude of the signals seen by the detectors in the twelve channel design are time variant only, within the spectral bandwidth of the filters used; whereas in the spectral scanning design, the signal is both time and wavelength variant as a function of the rotating mirrors which scan the gratings. The use of many discrete channels has the advantage of design simplicity but the number of channels may be insufficient to adequately define the spectral energy distribution. The maximum number of channels is limited by space available in the vehicle for the radiometer package. Use of two scanned channels (one for UV from 0.1 to 0.3 microns and one for visible and IR from 0.3 to 10 microns) provides better spectral coverage but the need for motors to drive the mirrors makes the radiometer design more complex. Calibration and subsequent data processing are also made more difficult since the mirror position must be measured and correlated with the radiometer data to avoid spectral wavelength errors. The motor speed must be constant and unaffected by in-flight environmental conditions. A prism and lens was shown in one design and a diffraction grating in the other. Actually, either diffraction device will work in either design. More detailed design, including cost estimates, will be required to determine the best choice.

8.5 Detectors - Detectors recommended for the spectrometers are silicon photodiodes and pyroelectric devices. Both type devices are available commercially for operation in the visible and infrared wavelengths. Typical photodiodes have good response in the range from .3 to 1.1 μm. Pyroelectric detectors work best in the infrared but are usable at shorter wavelengths. By applying a thin gold film to silicon photodiodes, they are usable at vacuum ultraviolet wavelengths, having a quantum efficiency of three (3) and a sensitivity (electrons per incident photo) of .2 to .35 over the span from .125 to .210 μm. In the multichannel radiometer, gold coated photodiodes are recommended for the .125, .133, .146 and .210 μm detectors shown in the upper right portion of Figure 128. At the eight longer wavelengths,

pyroelectric detectors are recommended. These are physically larger because the first stage of signal conditioning amplification is included in the housing and each detector has a filter window that passes energy at the specified wavelength. These filters are commercially available and have a half-power bandwidth of from 2.5 to 5% of the center wavelength. The detectors in the spectral scanning radiometer are similar except that narrow band-pass filters are not used. Some development effort will be necessary at the short wavelengths to clearly define response characteristics.

9. ENTRY VEHICLE DESIGN

After concluding that it was feasible to launch a high speed earth entry test of a probe-like vehicle, a system and vehicle design was accomplished.

9.1 Entry Vehicle Subsystem Evaluations - As part of the integrated design of the entry vehicle, the components of the entry vehicle were grouped in five subsystems: aeroshell, telemetry and communications, electrical power, recovery and electromechanical interfaces. The facets of each system were evaluated and a balance achieved to arrive at a unified design that married required instrumentation equipment and test objectives.

9.1.1 Aeroshell - The geometry of the entry vehicle was selected to be a symmetrical blunted 60° half angle cone with a 22.2 cm nose radius and a base diameter of 89 cm with a hemispherical aft cover. The main structure is divided into two parts, a conical forebody and a hemispherical shaped afterbody. The forebody structure is the most important since it acts as a decelerator, protects the entry payload during ballistic entry, and provides continuous structure support for the main heat shield. The afterbody structure supports the afterbody heat shield and encloses the entry payload. Alternate structural arrangements were evaluated and the integrally stiffened ribbed structure used by outer probe designers was selected. This structure (Figure 130) permits attaching a variety of heat shield concepts. The structure consists of a honeycomb sandwich conical shell with a fiberglass outer face sheet and an integrally machined aluminum inner face sheet with four integral machined stiffening rings. Loads from the forward heat shield are carried by a honeycomb sandwich to the integrally stiffened structure. This design permits flying either a carbon phenolic or a hyperpure silica heat shield. The aft cover made of light weight ablator is fastened to the structure near the maximum diameter point. It too is supported by a honeycomb sandwich, but a much thinner one because of the lower loads. The afterbody support structure consists of a monocoque honeycomb phenolic fiberglass sandwich shell. In order to deploy the recovery parachutes (see Section 8.2.4), provisions are made in the aft cover for an enclosed cutting charge.

The details of laminant layup for the carbon phenolic heat shield and the casting of the hyperpure silica shield are under development by other investigators and hence was not evaluated in this study. It will suffice to say that these details will be well documented by the time entry flights are authorized. As described in Section 8, several penetrations through the heat shield are necessary: radiometer port, pressure ports, electrostatic probes and thermocouple stacks. In the case of

TYPICAL STRUCTURAL CONFIGURATION LAYOUT

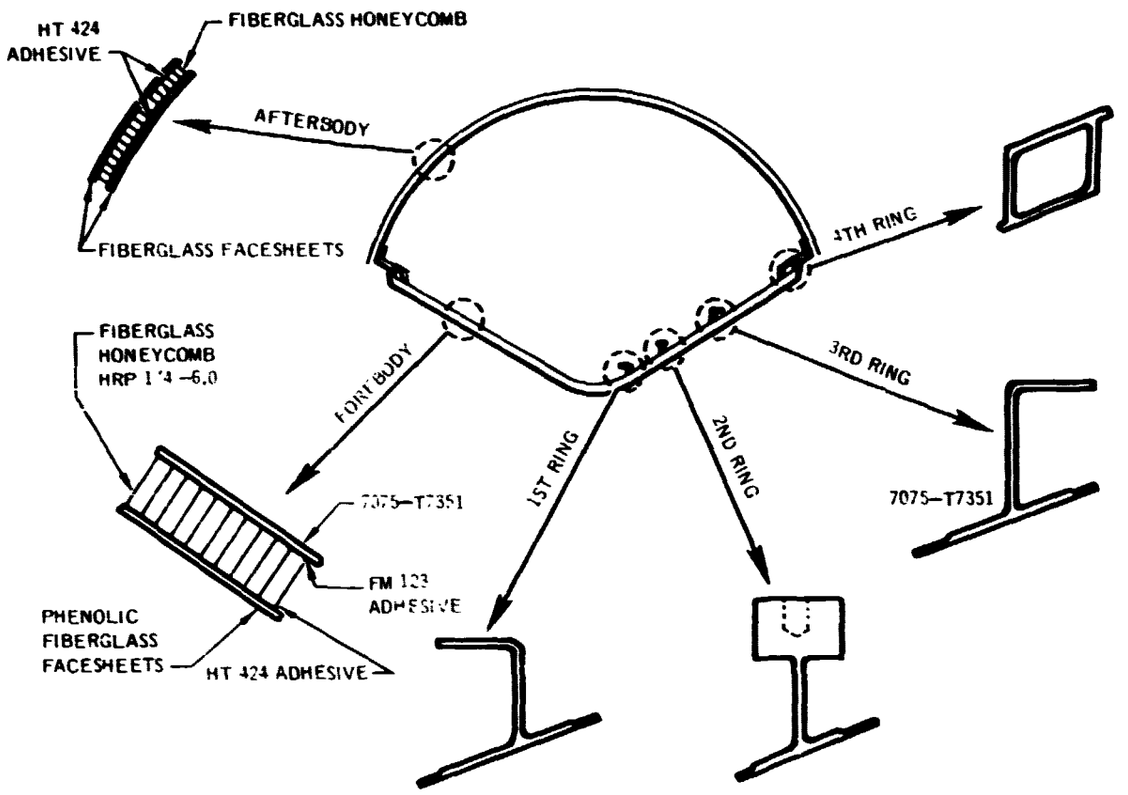

FIGURE 130

the electrostatic probe and the thermocouple stacks, the machined holes are filled with the same material as the heat shield. The difference in the thermal expansion coefficients between the heat shield and the support structure as well as the accommodation of loads may require a Strain Isolation Pad (SIP). This may be particularly true for the silica heat shield. Technology developed for the low density silica heat shield material on Shuttle was evaluated and deemed appropriate. Figure 131 shows the attachment system for the heat shield, heat shield corner attachment and other design features. The heat shield is bonded to a NOMEX SIP which in turn is bonded to the honeycomb structure. The SIP is a good insulator as well as being able to accommodate strains at temperature below the glass transition temperature of adhesives. The SIP is made in eight pie sections to allow for ease of bonding, eliminate wrinkles and provides additional expansion joints. Also shown in the figure is the thermocouple stack installation. Thermocouples are formed by butt welding their leads and then installing in a plug such that the leads lie along isotherms before being routed down the sides of the plug. The entire assembly is then fitted into the heat shield and bonded to the SIP during the attachment of the heat shield. This technique has been successfully used in flight and in many ground tests.

9.1.2 Telemetry and Communications - From the data channels defined in Figure 132, a PCM system was selected to provide an adequate quantity of data channels in a straightforward frame structure, at the correct sampling rates. These specifications are also included in Figure 132.

The use of 8 bit words provides a data resolution an order of magnitude better than average data accuracy. The number of spare channels are included to accommodate changes that can be expected in the design phase. The bit rate of 48 KBPS is sufficiently low to provide good signal margins when used with a 5 watt transmitter, and the flight tape recorder can operate at a standard low speed of 18.4 cm per second. At this speed only 6 meters of tape is required in the recorder to provide thirty (30) seconds of record time. One unique feature of the suggested bit rate is that by adding a switchable "divide-by-four" counter in the PCM timing system, the output bit rate can be reduced to 16 KBPS which is the standard bit rate for Shuttle communication with a separated payload. This makes it compatible with a post-separation checkout of all data channels sampled at one-fourth the normal rate.

UNIQUE FEATURES OF HEAT SHIELD DESIGN

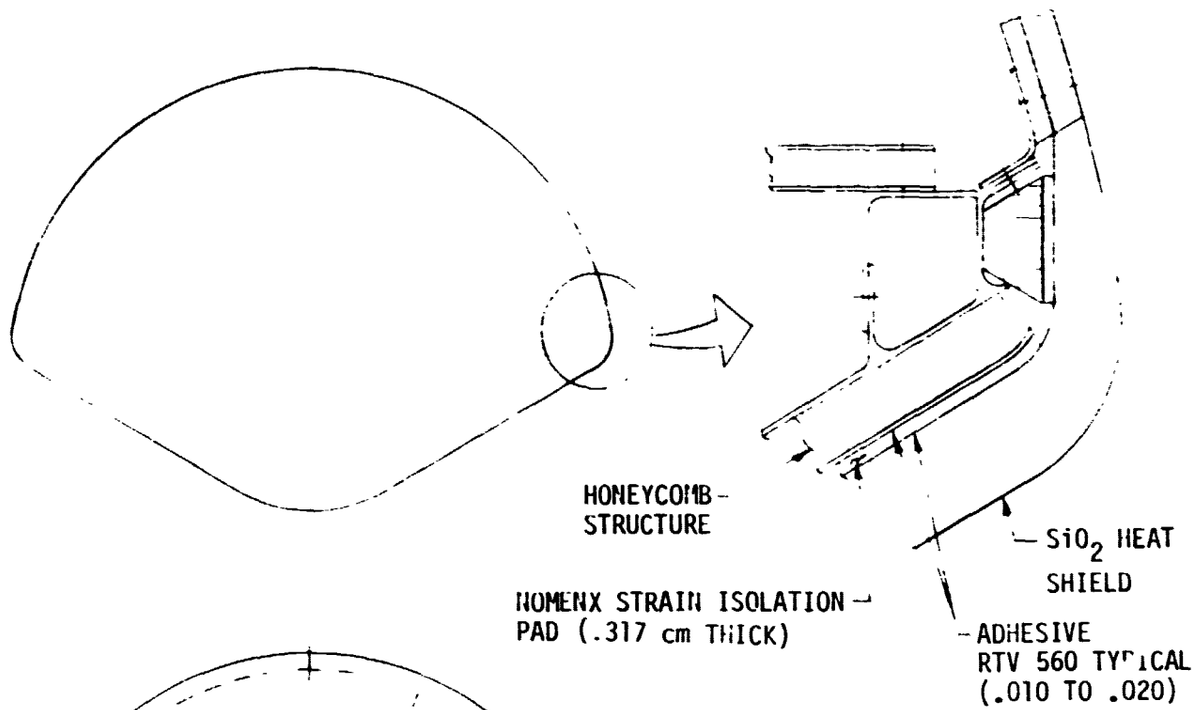

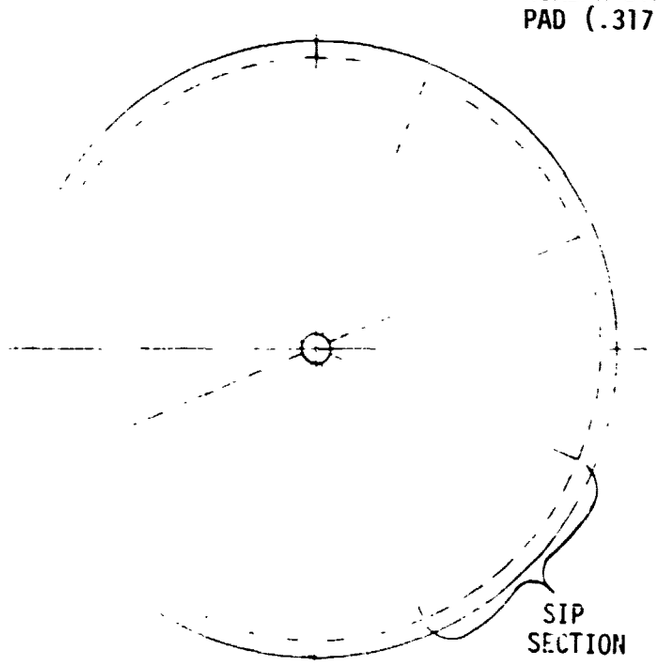

NOTE: SIP IS MADE OF 8 PIE SECTIONS TO ALLOW FOR EASE OF BONDING, ELIMINATE RINKLES AND PROVIDE ADDITIONAL EXPANSION JOINTS.

THERMOCOUPLE STACK INSTALLATION

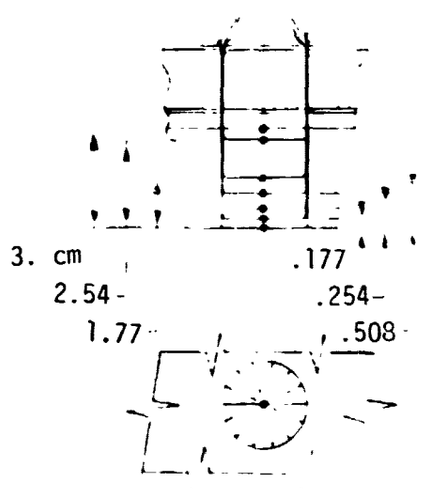

7 T/C PER PLUG
TC = (3 TUNSTEN-RHENIUM)
(4 CHROMEL-ALUMEL)

FIGURE 131

TELEMETRY SYSTEM CHARACTERISTICS

Signal Type	Samples Per Second	Data Channel Qty. Avail.	Need	Margin
HL	400	4	4	0
HL	100	20	17	3
HL	50	16	8	8
HL	10	20	11	9
LL	25	24	20	4
LL	10	40	34	6
		124	94	30

Type: PCM
Bit Rate: 48 KBPS
Word Length: 8 bits
Main Frame: 60 words at 100 sps

FIGURE 132

A block diagram of the complete Instrumentation and Communication system is shown in Figure 133. The PCM system is a single package containing 64 dual input low level channels and 60 single-ended high level channels. The digital output signal is applied to the S-band transmitter and the loop tape recorder. At the end of the blackout period, the record head is disabled and the transmitter switched to the tape recorder. The remaining flight time will be devoted to repetitive playbacks of the data recorded during the blackout period. The signal conditioner package provides resistors to complete the strain gage bridge circuits and to provide bridge balance and sensitivity adjustments. Voltages measured in the vehicle are attenuated by the signal conditioner so as to be compatible with the PCM high level inputs. The vehicle is also equipped with a beacon transponder to aid in radar tracking.

9.1.3 Electrical Power Requirements - The equipment requiring electrical power is listed in Figure 134. The maximum instantaneous power required at any time is less than 200 watts and the total watt-hours required for the mission is 25.59. To meet this requirement, we recommend an auto-activated silver zinc battery with a 40 watt-hour rating. Batteries of this type are being used in current space vehicles; thus development costs would be only those associated with packaging the correct quantity of cells to fit the space available in the entry probe, and to meet the power requirement. Qualification testing will be required to assure that the battery package can withstand the anticipated 700g entry environment. An advantage of the auto-activated battery is that ground support equipment (battery charger and load bank) is not required. The recommended battery is estimated to weigh 2.3 kg and have a volume of 1150 cm^3. The useful wet life is 10 to 24 hours.

Since the battery's useful life is limited after activation, we recommend that the entry vehicle operate from Shuttle power prior to deployment and for the booster where possible. This will permit delays in deployment so that, if the intended orbit is not favorable, a later one can be selected. Battery activation and a final checkout can then be delayed until a launch commitment is firm.

During pre-deployment checkout the transmitters will not be powered, consequently, the power required from Shuttle is only 85 watts which will have minor impact on Shuttle capability. A normal checkout will require about 3 minutes and the heat generated can be dissipated by heat sink, radiation and conduction; active cooling is not required. The Shuttle's capability to support payloads and the Shuttle-payload interfaces are discussed further in Volume IV, Sections 11 and 12.

EARTH ENTRY VEHICLE TELEMETRY AND COMMUNICATION FLOW

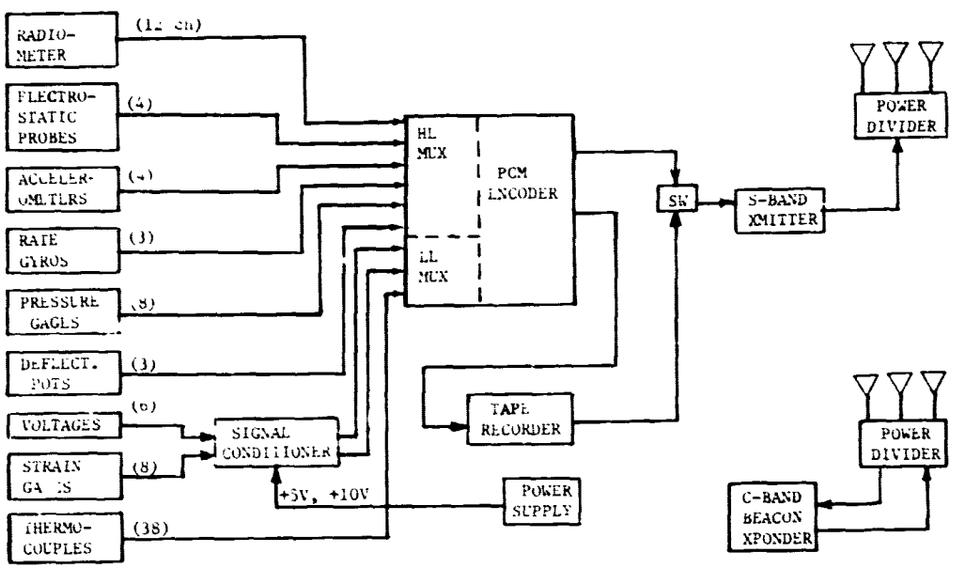

ORIGINAL PAGE IS
OF POOR QUALITY

FIGURE 133

POWER REQUIREMENTS
(EARTH ENTRY VEHICLE)

EQUIPMENT	ENERGY PER MISSION PHASE (WATT-MIN)						TOTAL WATT-MIN
	POWER (WATTS)	ACT & C/O (3-MIN)	1-6 HR	ENTRY (30 SEC)	PRE-RCVY (180 SEC)	RECOVERY (25 MIN)	
PCM Telemetry	10	30.0		5.0	30.0		65.0
Tape Recorder							
Record	20	60.0		10.0			70.0
Playback	20				60.0		60.0
Transmitter (1)	27			13.5	81.0		94.5
Beacon	45			22.5	135.0		157.5
Recovery Transmitter	22					550	550.0
Inst. DC/DC Converter	7	21.0	Dormant Period	3.5	21.0		24.5
Control & Sequencing	5-25	30.0		12.5	75.0	125	242.5
G-Switch	.2	.6		.10	.6		1.3
Press. Transducer (7)	2.1	6.3		1.1	6.3		13.7
Accelerometer (4)	1.2	3.6		.6	3.6		7.8
Rate Gyro (3)	25	75.0		12.5	75.0		162.5
Radiometer	10	30.0		5.0	30.0		65.0
Totals	194.5	256.5		86.3	517.5	675	1535.3

FIGURE 134

9.1.4 Recovery - In order to verify the analytical predictions of the heat shield it is preferable to correlate transmitted surface recession data with the final recession. It is very desirable to examine surface erosion and/or run off patterns on the heat shield after entry. Taking core samples from the heat shield is necessary in macroscopic studies of surface recession and heat shield charring. It is also desirable to recalibrate instruments after the flight to determine their flight qualification for an outer planet mission.

To meet these needs various recovery schemes were considered and an air recoverable system was selected. It circumvents the need for floatation and dye marker subsystems. More important the heat shield and other systems will not be contaminated by immersion in ocean salt water. An air recovery also means that the structure and many other subsystems could be used on subsequent entry flight experiments, thereby reducing cost. Figure 135 shows the recovery sequence.

The recovery system permits air retrieval of the vehicle with a C-130 airplane or CH53 helicopter. The system consists of a main parachute, drogue chute and mortan and a g-switch. The top portion of the afterbody structure is released after entry heating has subsided. The mortar deploys the drogue chute between 21.3 and 18 km. At approximately 15.2 km the drogue chute is released from the vehicle thereby pulling the main chute out. The main chute is sized to provide a descent rate of 7.6 meter per second at 3 km ft. This system allows approximately 25 minutes for the recovery aircraft to spot the vehicle on the chute and retrieve it.

9.1.5 Interfaces - The entry vehicle must be secured to its booster such that the electrical connection and mechanical attachment do not compromise the heat protection, telemetry and experiment complement. Also the loads must be beamed through the attachments. A design very similar to that used on the Delta launch vehicle evolved. Figure 136 shows the design details. The entry vehicle is secured to the final stage with a Ball Lock Separation Bolt at three places. Once the charges in the bolts are fired, cutting the bolts, the compression springs cause the entry vehicle to move away from the support fittings. Note that only three small cut-outs in the entry vehicle aft cover are required. The cutouts are closed off to prevent boundary layer gases from flowing through the entry vehicle. Just prior to separation, the umbilical is cut severing electrical and telemetry lines with the final stage. The final stage and entry vehicle are spun up by the spin table shown in the figure.

RECOVERY SEQUENCE

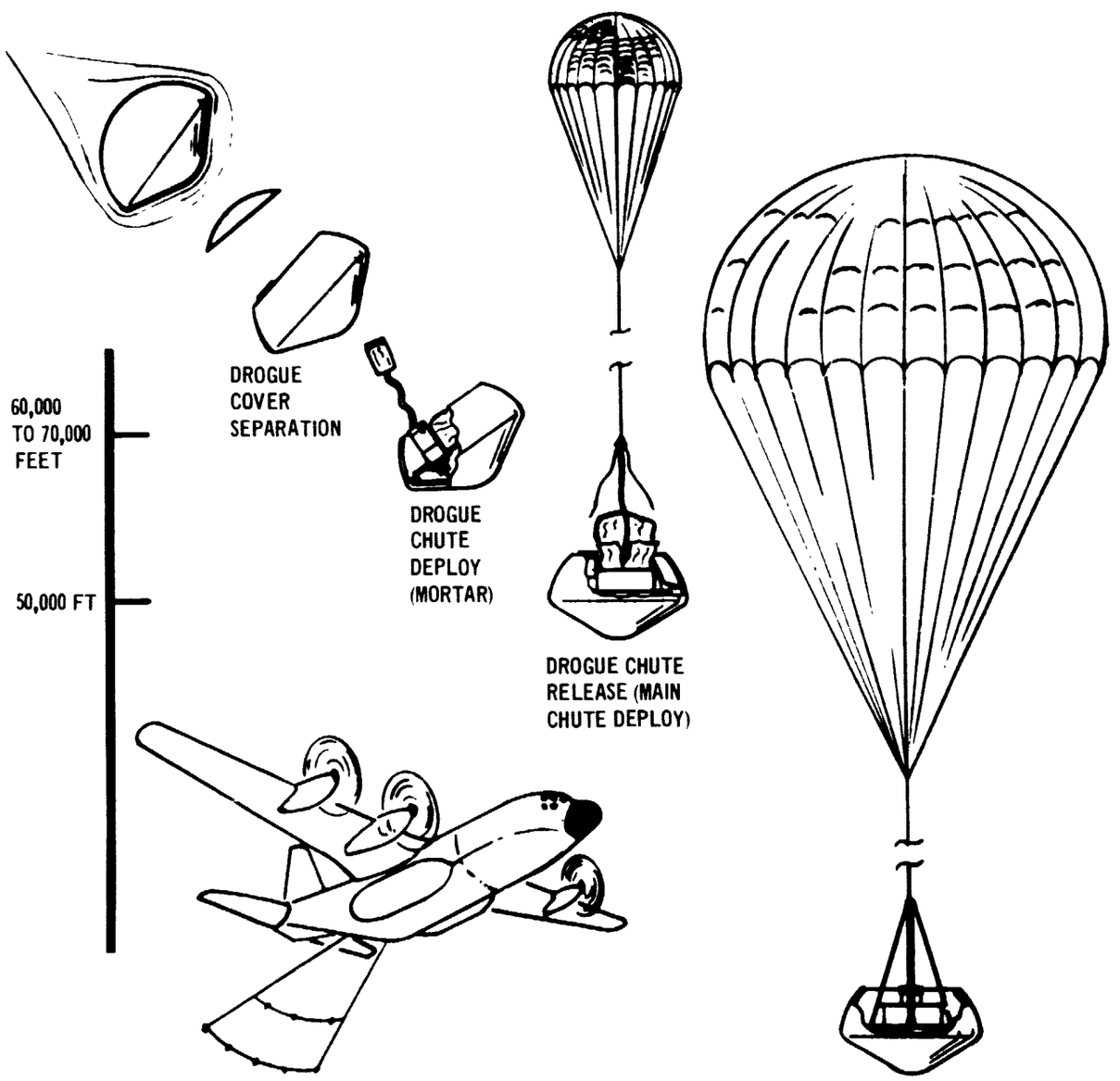

FIGURE 135

ELECTROMECHANICAL INTERFACES

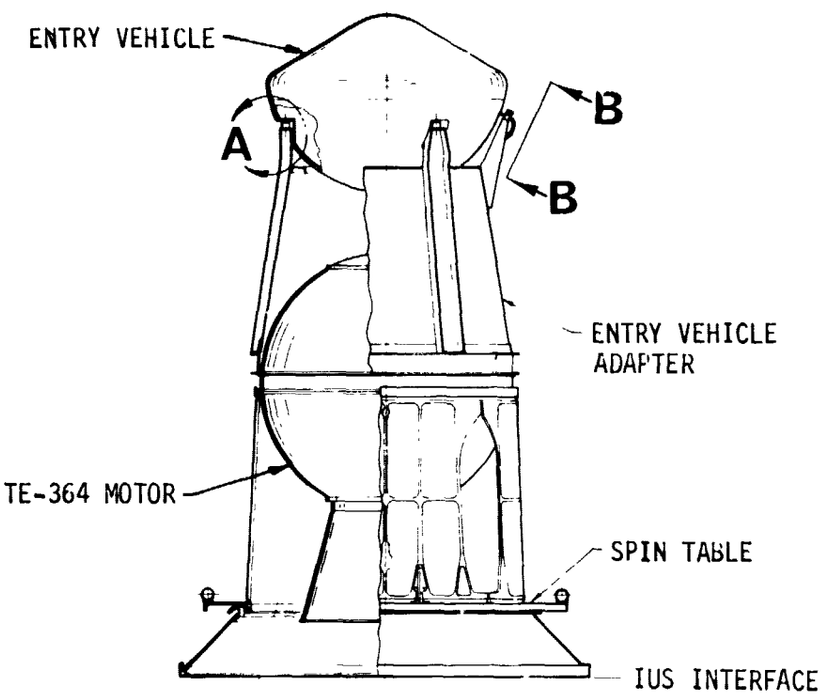

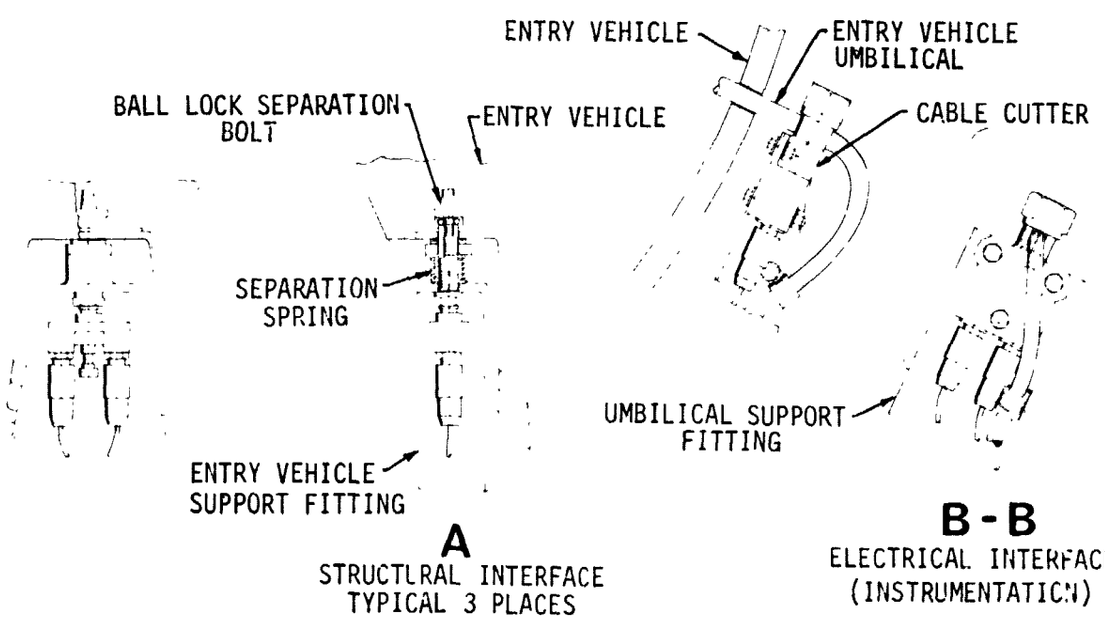

FIGURE 136

Several interfaces with Shuttle were analyzed to determine if there are potential problems. The Shuttle Caution and Warning system can be used to indicate the health of entry vehicle prior to deployment. The payload data interleave can be used as the back-up. The entry vehicle telemetry and power loads are connected through the auxiliary stage to the booster and finally to the Shuttle.

Electrical power interfaces are provided at two locations within the Shuttle payload bay as shown in Figure 137. Two panels are located on the aft bulkhead and provide the average and peak power indicated from the Shuttle bus B and C. Near the front of the payload bay, two more panels exist. One provides power from a payload dedicated fuel cell and the other from the Shuttle main bus. If all four panels were to be used an average power level of 15 kw could be maintained. Power will be required for the booster and the minimal power requirement of the entry vehicle (85 watts) can easily be met by the electrical interfaces.

Figure 138 describes the structural interfaces in the Shuttle payload bay. The retention points are provided for attaching pallets or payload cargo to the payload bay load support points. There are 12 along the bottom centerline beam and 13 on each longeron for a total of 36 attachment points. The stations are indicated in the figure. The entry vehicle/auxiliary stage are secured to the booster which in turn will be attached to the Shuttle payload retention points via pallet or universal structure. This additional structure will be developed as part of the IUS and therefore available.

The coolant interface is shown in Figure 139 and consists of a closed liquid coolant piping system with a payload heat exchanger. A liquid coolant heat exchanger is required for some payload because the bay has no atmosphere and radiation cooling of the payloads is not adequate. The entry vehicle has minimal pre-deployment heat dissipation requirements and consequently will not be connected to this interface.

Another interface of importance is the environmental interface within the payload bay. During Shuttle launch, acoustic levels greater than 135 db are experienced in the Shuttle payload bay. Therefore, the entry vehicle will need to be qualified accordingly and possibly a shroud will be needed over the heat shield ports.

In general, the entry vehicle does not impose severe requirements on Shuttle.

ELECTRICAL POWER INTERFACE

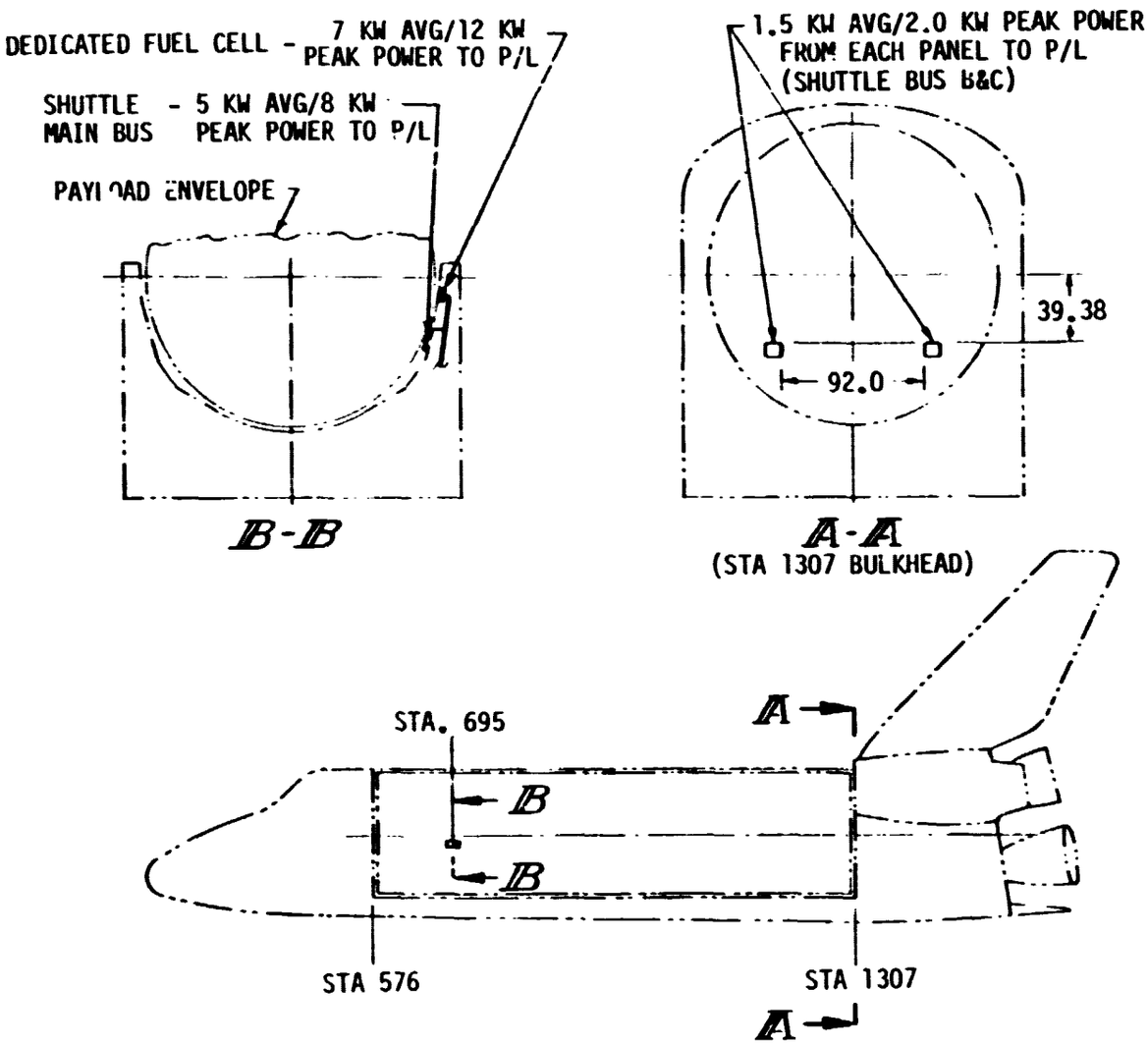

FIGURE 137

SHUTTLE STRUCTURAL INTERFACES

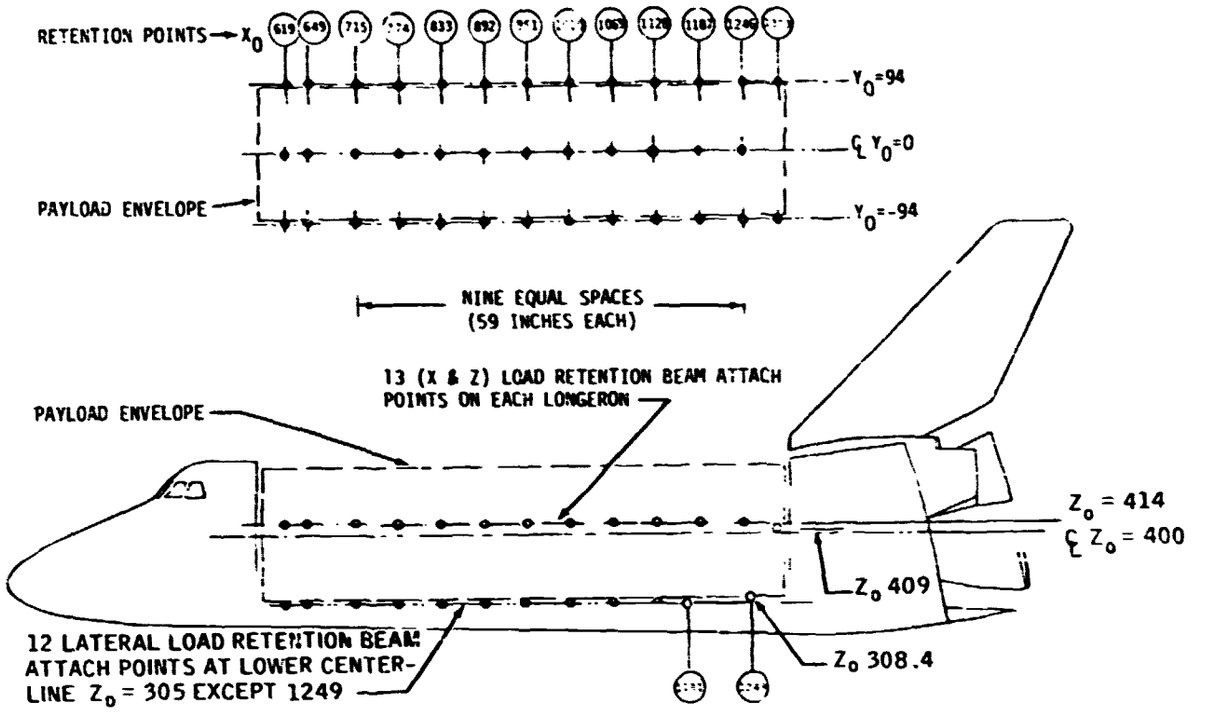

FIGURE 138

SHUTTLE PAYLOAD HEAT EXCHANGER INTERFACE

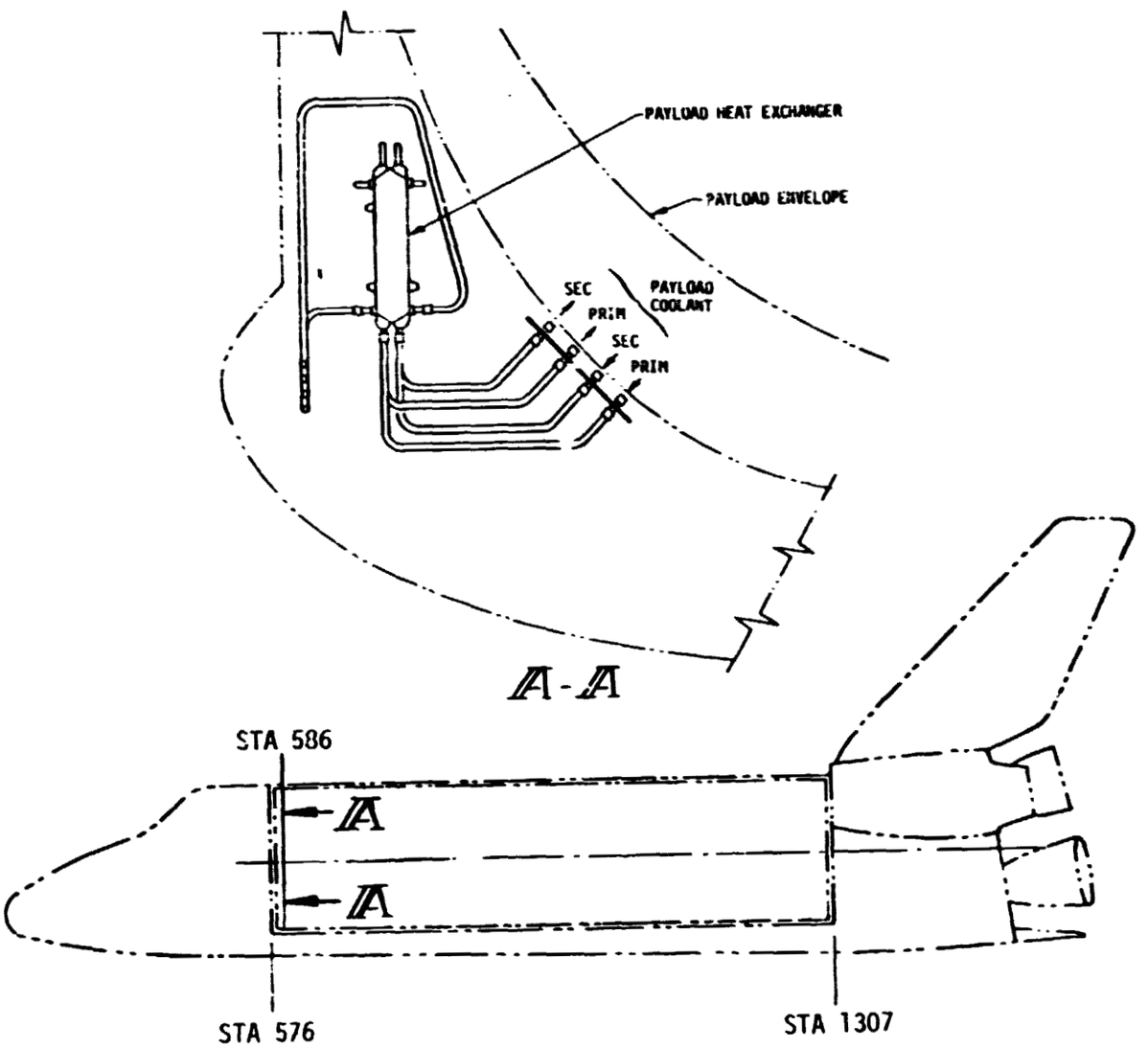

FIGURE 139

9.2 General Arrangement - A significant design, system evaluation and component arranging was performed to arrive at a complete entry vehicle and upper stage design. The information contained herein is of sufficient detail that the next step is to prepare engineering drawings.

9.2.1 Entry Vehicle Design - The baseline vehicle consists of a 60° half angle conic forebody approximately 89 cm in diameter with a hemispherical afterbody. The forebody is made up of a carbon phenolic (1.13 inches thick) or a hyperpure silica heat shield supported by a honeycomb sandwich conical shell with a fiberglass outer face sheet and a machined aluminum inner face sheet with four integral machined stiffening rings. The afterbody structure consists of a monocoque honeycomb phenolic fiberglass sandwich shell covered with an ablator honeycomb filled with a silicone ablation material (S-10). A honeycomb shelf provides a mounting surface for the recovery system.

Figure 140 is an inboard profile of the entry vehicle showing the onboard experiment equipment and supporting subsystem equipment to accomplish the mission. The equipment shown is off-the-shelf equipment where possible, however, some, such as the radiometer, the sequences and the pyro relays are designed and packaged specifically for this mission.

Stability criteria indicate that the center of gravity should be forward of the honeycomb shelf. The equipment modules have been positioned with this in mind and the need for a symmetrical mass distribution during spin up. Also instrumentation leads have been minimized to reduce noise and increased reliability. As can be seen by examining the figure, a compact design was achieved. Equipment modules are secured to the structural rings. The three attach points for the final booster stage are positioned next to a pair of antennas, one a beacon and the other for telemetry. Using antennas spaced at 120 degrees gives good coverage. Also an access door is provided in the aft cover. The confined explosive device for separating the top of the aft cover is shown along with the details of the drogue and main parachute attachment. A "g"-switch is used to initiate the recovery sequence. The mass of each component and the mass properties of the entry vehicle are analyzed in a later section. Balance and ballast masses can be added by replacing selected areas of the honeycomb (behind the forebody heat shield) with heavy metal inserts.

Strain Isolation Pad (SIP) attachment system secures that forebody ablator to the honeycomb support structure. The SIP does what its name implies and because

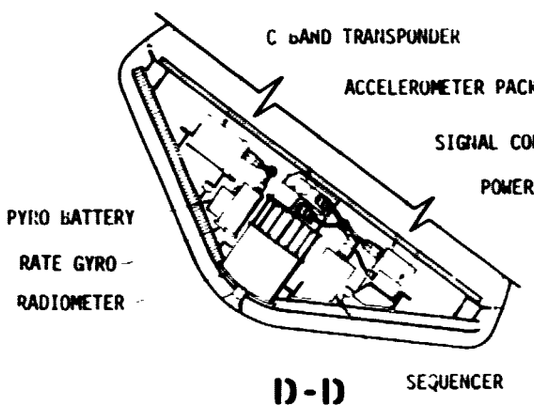

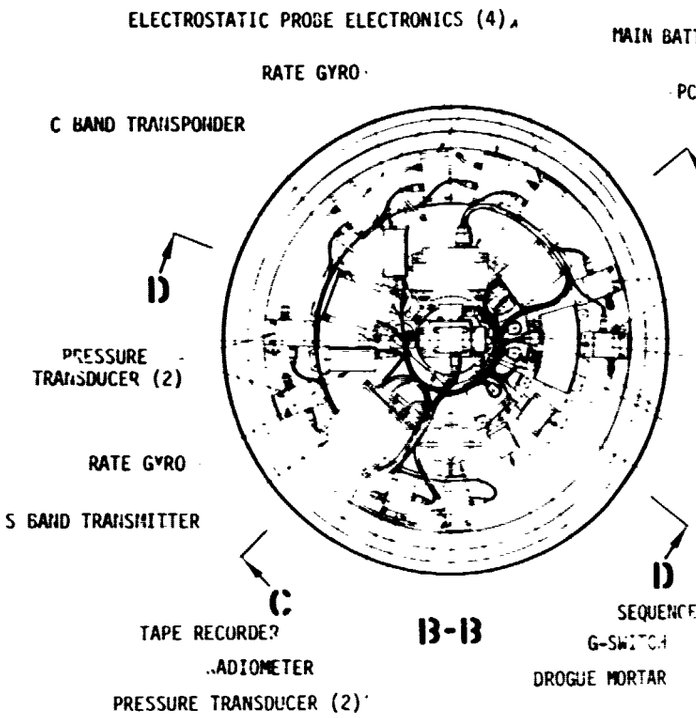

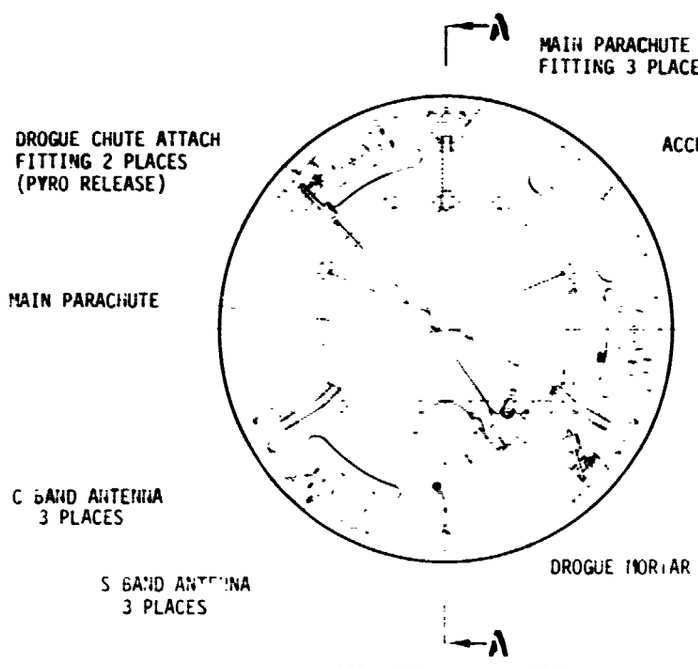

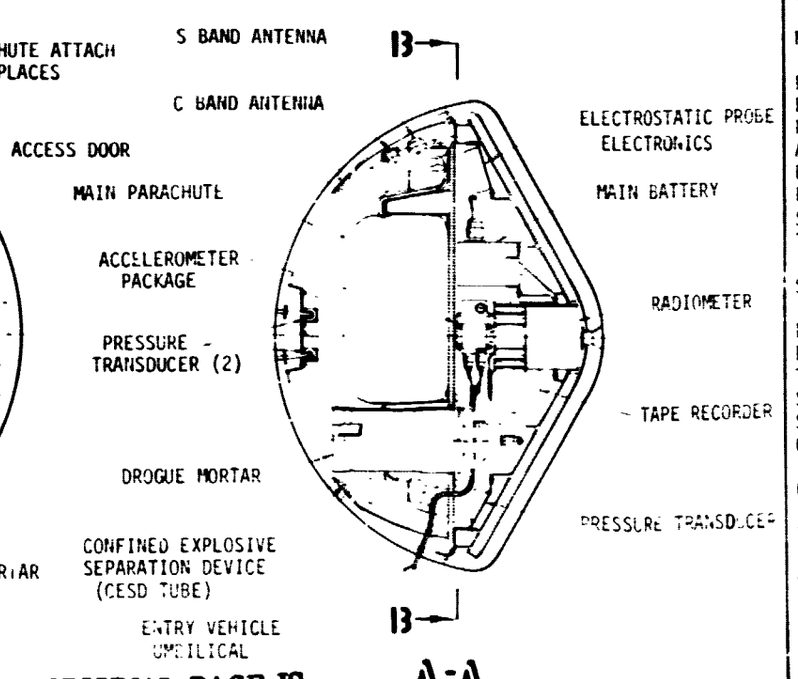

TYPE

SEQUENC.
MAIN BAT
RADIOME
ELECTROS
PROBE EL
ACCELERO
RATE GYR
PRESSURE
STRAIN
THERMOCO
(PLUGS
SIGNAL C
POWER SU
PCM TEL
TAPE REC
S-BAND
S-BAND
C-BAND
TRANSP
C-BAND
PYRO BAT
PYRO REL
CONF. E
DEV.
G-SWITCH
DROGUE
DROGUE
MAIN PA

FOLDOUT FRAME

EARTH ENTRY VEHICLE INBOARD PROFILES

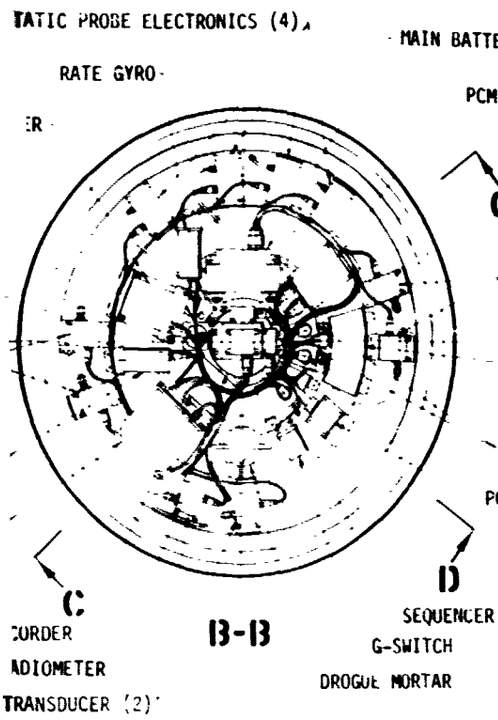

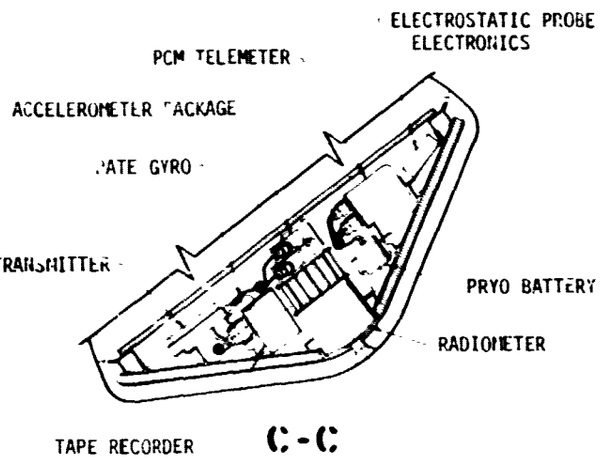

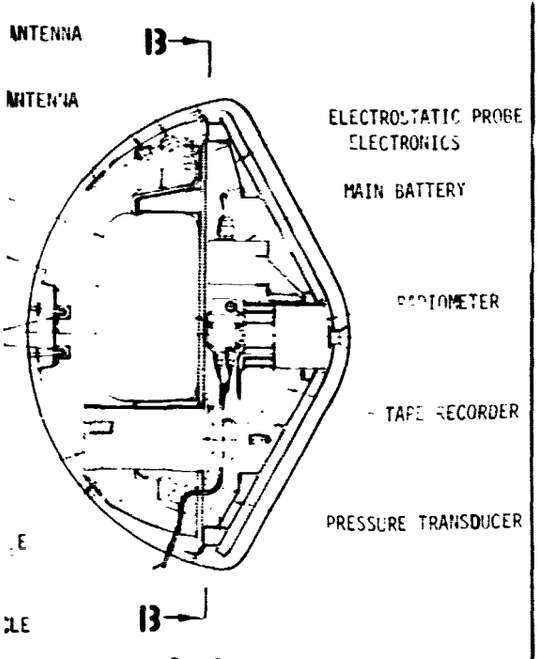

EQUIPMENT LIST

TYPE	FUNCTION	ACTIVE MISSION PHASE				
		PRE-SEP.	PROBE SEP.	PRE-ENTRY	ENTRY	RECOVERY
SEQUENCER	CONTROLS SEPARATION & RECOVERY EVENTS	X	X			X
MAIN BATTERY	ELECTRICAL POWER FOR ALL EQUIP. EXCEPT PYROS		X	X	X	X
RADIOMETER	ATMOSPHERIC DATA			X	X	
ELECTROSTATIC PROBE	ATMOSPHERIC DATA			X	X	
PROBE ELECTRONICS	PROBE POWER & SIGNAL COND.			X	X	
ACCELEROMETER PKG.	3 AXIS VEHICLE MOTION DATA			X	X	
RATE GYROS	3 AXIS VEHICLE MOTION DATA			X	X	
PRESSURE TRANSDUCERS	SURFACE PRESSURE DATA			X	X	
STRAIN GAGES	STRUCTURAL DEFLECTION			X	X	
THERMOCOUPLES (PLUGS)	HEAT SHIELD TEMPERATURE & ABLATION			X	X	
SIGNAL CONDITIONER	DATA SENSOR SIGNAL MODIFICATION			X	X	
POWER SUPPLY	DATA SENSOR POWER			X	X	
PCM TELEMETER	DATA MULTIPLEXER & DIGITIZER			X	X	
TAPE RECORDER	RECORD ENTRY DATA				X	X
S-BAND TRANSMITTER	PCM DATA TRANSMITTER			X	X	X
S-BAND ANTENNAS	RADIATE PCM SIGNAL			X	X	X
C-BAND BEACON TRANSPONDER	RECEIVE & RETRANSMIT TRACKING SIGNAL				X	X
C-BAND ANTENNAS	RECEIVE & RADIATE TRACKING SIGNAL				X	X
PYRO BATTERY	EXPLOSIVE DEVICE POWER					X
PYRO RELAY	TRIGGERS DROGUE MORTAR & CESD					X
CONF. EXPLO. SEP. DEV.	SEPARATES AFT BODY COVER					X
G-SWITCH	INITIATES RECOVERY SEQUENCE					X
DROGUE MORTAR	DEPLOYS DROGUE PARACHUTE					X
DROGUE PARACHUTE	DEPLOYS MAIN PARACHUTE					X
MAIN PARACHUTE	VEHICLE RECOVERY					X

FIGURE 140

FOLDOUT FRAME 2

it is made of a fibrous material it will accommodate strains even at cryogenic temperatures. The details of the STP installation, heat shield corner attachment and thermocouple stack configuration have been described previously.

Also shown on the figure is the scenario of when the various pieces of equipment function during the mission and the function of each piece of equipment.

9.2.2 Launch Configuration - The entry vehicle, upper stage and main booster takes up less than 3/8 of the 18.25 meter Shuttle cargo bay and 43% of its payload capability. A typical launch configuration as shown in Figure 141 weighs 13516 kg and would most likely be positioned more forward in the cargo bay depending on the requirements of other cargo. The upper stage houses a TE-364 solid rocket, contains wire bundles and associated gear, supports the entry vehicle, has a spin table and makes the necessary structural ties to a 3.048 meters diameter adapter ring. This universal adapter ring makes the upper stage compatible with the all boosters considered. The wire bundle-umbilical assembly passes power and telemetry between the entry vehicle and the main booster. The main booster contains all the guidance and control equipment and telemetry equipment necessary to fly the mission and fire the upper stage. This design is very similar to that used on the Delta launch vehicle.

9.3 Entry Vehicle Mass Properties - A detailed mass properties evaluation was conducted for the entry test vehicle configuration described in Figure 140. Two interrelated aspects were of primary interest: (1) the amount of ballast needed to provide a proper entry center of gravity (c.g.) location, (2) the increase in ballistic coefficient (β) attainable by increasing only vehicle mass,and (3) detailed mass property analysis.

9.3.1 Ballast Options - The concern for c.g. location arises from the requirement for a positive static stability margin. Hence the longitudinal c.g. location must be prevented from being appreciably aft of the theoretical cone/hemisphere intersection plane. The location of this aerodynamic reference plane is shown in Figure 142. However, equipment arrangement, particularly the necessarily aft location of the recovery parachute system, indicated the probable need to for ballast in the forward, conical section. Further a significant amount of ballast was anticipated because of the blunt body shape which offers a relatively short ballast moment arm.

Ordinarily, a large ballast mass would be detrimental because it reduces the ΔV available from a given booster. However, the corresponding increase in

ENTRY VEHICLE/UPPER STAGE CONFIGURATION

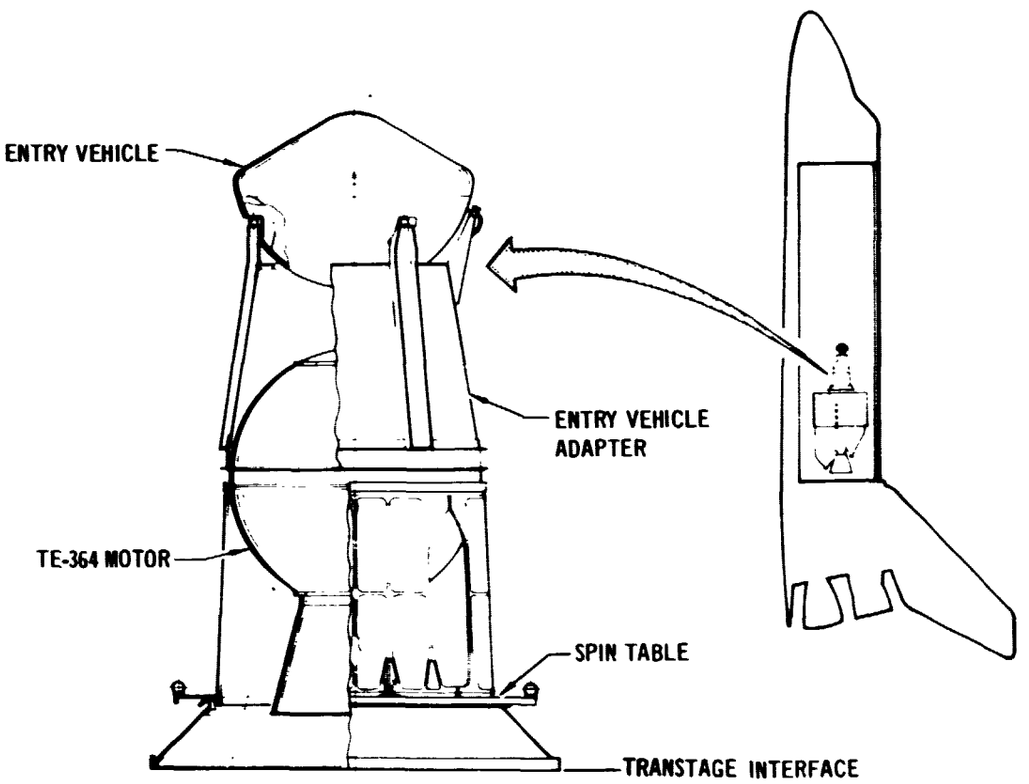

LAUNCH WEIGHT	
ENTRY VEHICLE	160 kg (353 LB)
UPPER STAGE	1121 kg (2472 LB)
TRANSTAGE*	12235 kg (26978 LB)
TOTAL	13516 kg (29803 LB)

*(SIMILAR TO SOLID IUS – 2 SRM AT 12975 kg)

FIGURE 141

BALLAST LOCATION

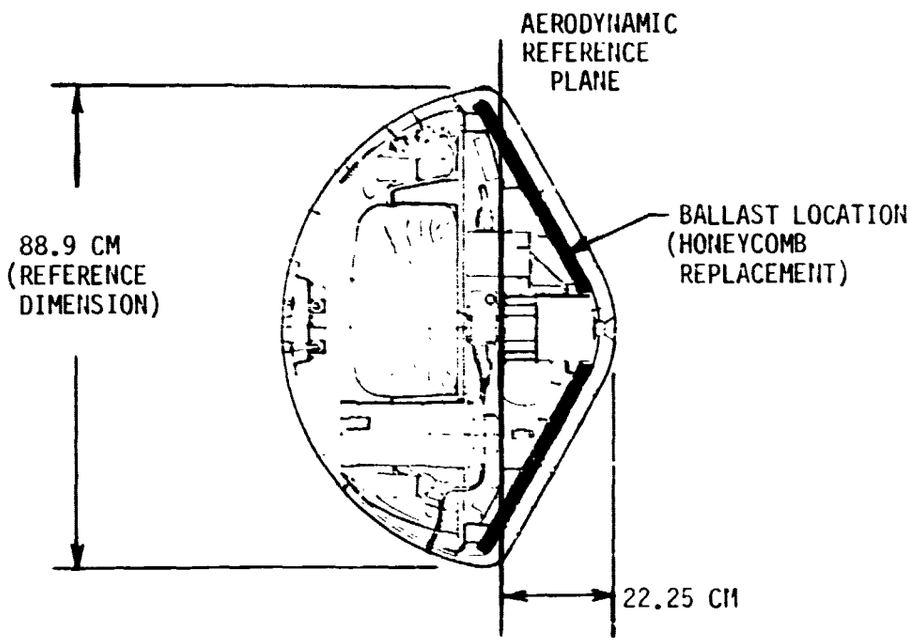

FIGURE 142

LONGITUDIANL BALLAST SUMMARY

	BALLAST CRITERIA		
	NONE	MINIMUM	MAXIMUM
BALLAST MASS (kg)	0	21.90	107.99
VEHICLE C.G. LOCATION FROM NOSE (cm)	24.73	22.25	21.25
FROM REF PLANE (% OF REF DIMENSION)	2.7 (AFT)	0	1.2 (FWD)
TOTAL VEHICLE MASS (kg)	109.42	130.94	215.42
BALLASTIC COEFFICIENT (kg/m^2)	113.92	136.32	224.27

FIGURE 143

ballistic coefficient is a mitigating factor unique to this high radiative flux simulation mission. As noted previously, increasing β decreases the entry velocity and hence the booster ΔV required to simulate a given level of radiative flux. If β is increased only by mass addition (C_DA = constant) the net booster effect is still advantageous. The reduction in booster ΔV required is greater than the reduction in booster ΔV capability.

Entry vehicle mass properties were determined using computer codes developed for the outer planet probe. The effect of ballast mass on total vehicle mass, ballistic coefficient and center of gravity locations was determined. Representative results are tabulated in Figure 143 and are graphically illustrated in Figure 144. Ballast was assumed to be in the form of steel plate segments that replace the honeycomb core of the forward heat shield structure (ref Figure 143). As expected the "no ballast" case resulted in a c.g. location aft of the aerodynamic reference plan. However, it was only displaced by .98 cm (2.7% of reference dimension) relative to the reference plane which was not as far aft as anticipated. While this is marginally acceptable, a c.g. location at or forward of the aerodynamic reference plane was considered necessary at this preliminary design stage to insure an adequate stability margin in the final configuration. Hence a minimum ballast case was investigated in which just enough aluminum honeycomb core was replaced with steel plate to move the c.g. forward to the aerodynamic reference plane. This 21.9 kg of ballast increased total vehicle mass from about 109 kg to 131 kg and β from approximately 114 kg/m^2 to 136 kg/m^2. Although this provided a satisfactory c.g. location it did not represent a maximum ballistic coefficient configuration. A maximum ballast case was therefore evaluated in which all of the aluminum honeycomb core was replaced with steel plate The resulting 108 kg of ballast increased vehicle mass to 215 kg and β to 224 kg/m^2, while moving the c.g. forward of the reference plane by 1.2% of reference dimension. Since this is substantially higher than the 120 kg/m^2 value assumed for the earth entry environment analysis, a net reduction in required booster performance is possible. Further, the maximum ballast case offers a unique vehicle design opportunity. A simple, steel structural shell can be used rather than the more sophisticated honeycomb structure. This would provide a less expensive structural design that also minimizes booster performance requirements and insures a proper c.g. location.

LONGITUDIANL BALLAST EFFECTS

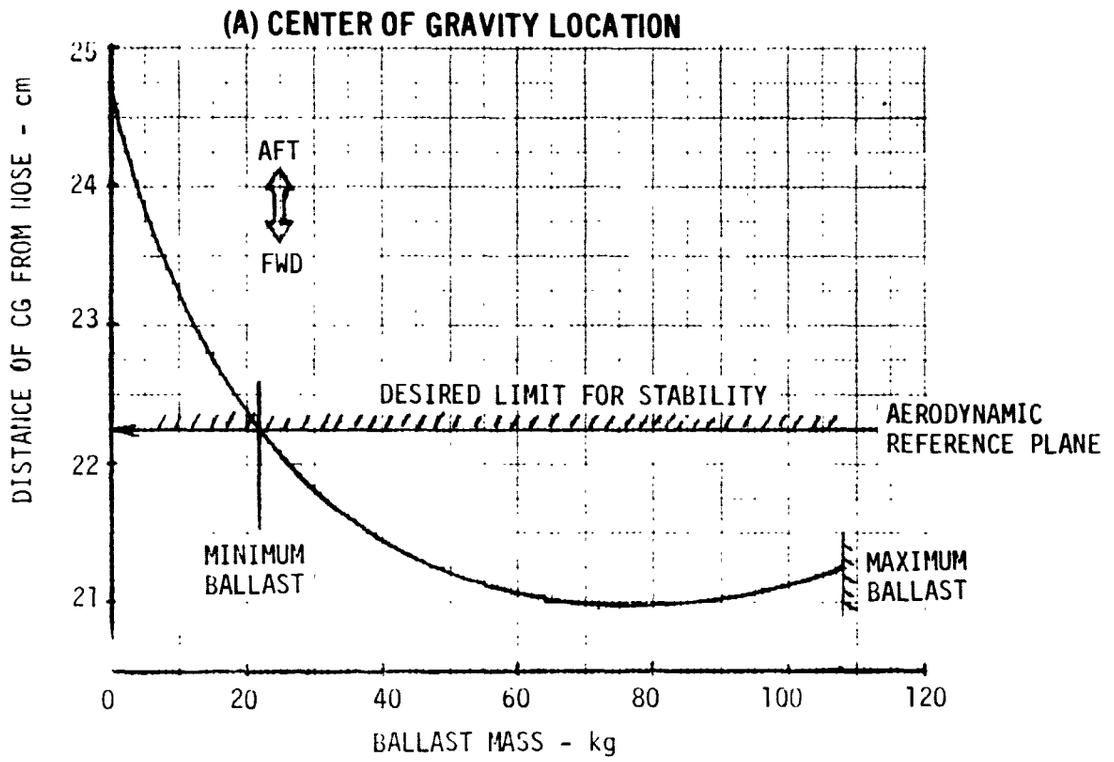

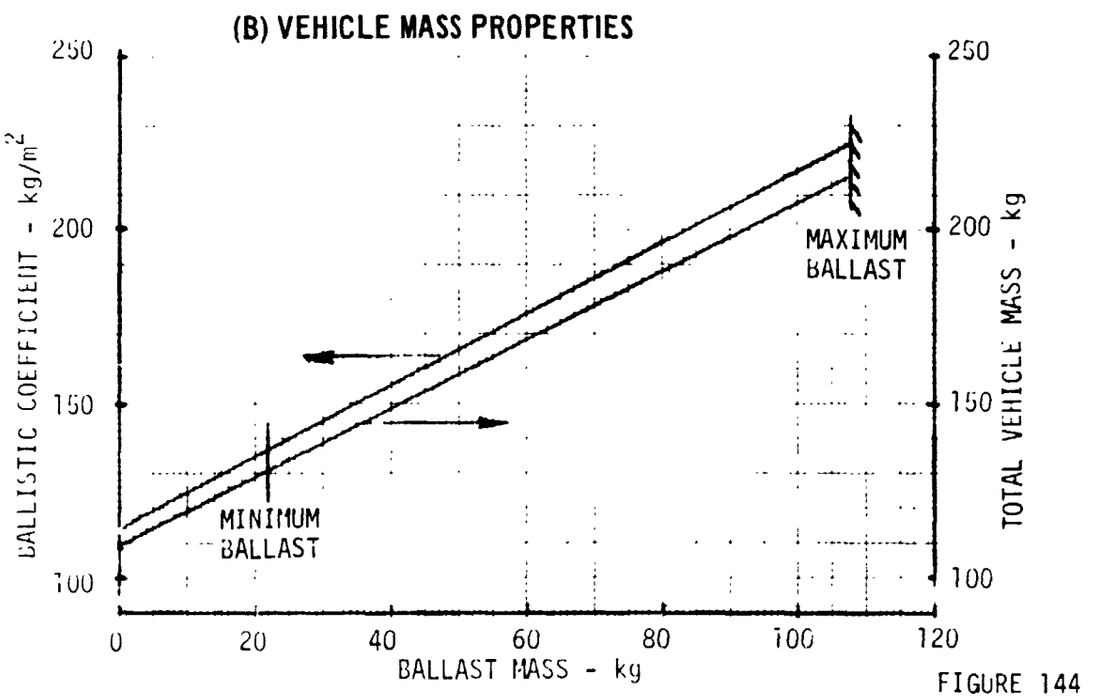

FIGURE 144

9.3.2 Detailed Mass Property Analysis - The mass properties of both the maximum ballast and the minimum ballast mass configuration were analyzed in detail. Component mass/location and structural mass/location were employed to determine overall mass, center of gravity, moment of inertia and associated derivatives.

The entry test vehicle is spin-stabilized during the preentry coast period following booster separation and must be aerodynamically stable during entry and terminal descent. This imposes constraints on the vehicle mass properties which cause the three axis center of gravity (c.g.), the ratio of roll to pitch or yaw inertia and the roll-yaw and roll-pitch products of inertia to be critical.

Much of the engineering equipment is off the shelf and not tailored to provide a forward c.g. location and the recovery system is located in the aft compartment for convenience and minimum cost. The aft c.g. resulting from these design considerations is offset by adding ballast in the form of steel plates in place of the honeycomb core of the forward heat shield backup structure. In addition to the longitudinal ballast a small amount of lateral ballast is added to drive the roll coupled cross products of inertia and the c.g. ecentricities about the roll axis to zero. This ballast can be eliminated in the final design by relocating part of the equipment; however, an allowance is needed for final corrections during actual measurement of the flight vehicle.

The reference axes diagram is presented in Figure 145. The earth entry vehicle mass properties for the maximum and minimum mass are presented in Figures 146 through 148 and Figures 149 through 151 respectively. Figures 146 and 149 summarize the mass perperties of each vehicle while Figures 147 and 150 provide the mission profiles. Figures 148 and 151 present the detail mass, c.g. and radius of gyration data used to compute the vehicle mass properties. In these detail listings the subtotals (and thus the group names) follow the items listed. Note that at all points in the mission profiles of both vehicles the roll inertia is at least 1.3 times the larger of the pitch or yaw inertia thus providing a comfortable margin above the 1.1 ratio required for dynamic stability during the coast phase of the mission.

EARTH ENTRY VEHICLE – REFERENCE AXES DIAGRAM

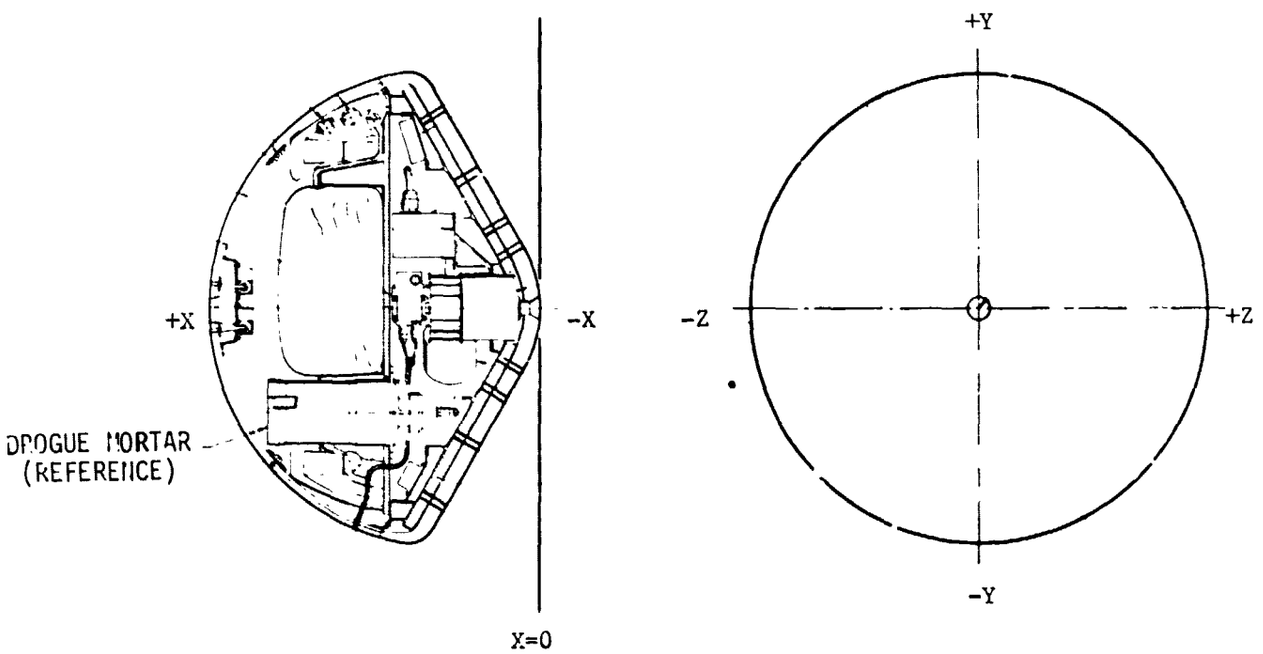

FIGURE 145

MASS PROPERTIES SUMMARY
EARTH ENTRY VEHICLE – MAXIMUM MASS

DESCRIPTION	CURR WEIG (KG)	CENTER OF GRAVITY X (M)	Y	Z
	MOMENT OF INERTIA ROLL	PITCH	YAW	PRODUCT OF INERTIA ROLL-PIT	PIT-YAW	YAW-ROLL
	(KG-METER SQ./I)					
PRI STR FWD	5.754	.202		0.000	.001
.595	.323	.320	0.000	0.000	.001
PRI STR AFT	3.180	.298		-.004	0.000
.244	.122	.122	-.000	0.000	0.000
SEC STRUCT	6.577	.268		.103	.010
.576	.317	.366	-.017	-.034	-.002
STRUCTURE	16.511	.247		.042	.004
1.463	.786	.879	-.003	-.030	-.031
FWD HT SHLD	145.630	.174		0.000	0.000
13.664	9.660	9.660	0.000	0.000	0.000
AFT HT SHLD	5.094	.458		.004	-.005
.638	.397	.394	-.001	-.006	.001
HEAT SHIELDS	150.724	.182		.000	-.000
14.302	10.454	10.452	.004	-.006	-.005
EQUIPMENT	6.391	.245		-.031	.022
.379	.261	.171	.007	-.018	.001
INSTALLATION	1.070	.230		-.031	.022
.064	.044	.028	-.000	-.000	.000
COMMUNICAT	7.466	.243		-.031	.022
.443	.306	.200	.007	-.018	.001
EQUIPMENT	6.822	.220		.036	.021
.320	.236	.222	.004	-.005	-.003
INSTALLATION	1.066	.205		.041	.016
.050	.035	.037	.000	.000	.000
INSTRUMENTAT	7.888	.218		.037	.021
.370	.271	.259	.003	-.00	-.003
EQUIPMENT	8.391	.174		-.024	-.031
.144	.125	.049	.002	.018	.027
INSTALLATION	1.057	.224		-.002	.022
.022	.038	.032	.007	.002	.003
ELECT PWR	9.448	.179		-.022	-.025
.170	.168	.084	.010	.021	.032
PYROTECHNICS	1.588	.265		.062	-.055
.136	.090	.076	.013	.022	.005
DECEL SYS	22.203	.388		-.025	0.000
.697	.447	.635	.055	.033	0.000
PROBE WEIGHT	215.828	.213		.000	.000
17.671	12.394	13.509	.021	.021	.012

FIGURE 146

SEQUENCED MASS PROPERTIES SUMMARY
EARTH ENTRY VEHICLE – MAXIMUM MASS

DESCRIPTION	CURRENT WEIGHT (KG)	CENTER OF GRAVITY X (M)	Y	Z
	MOMENT OF INERTIA ROLL	PITCH	YAW (KG-METER SQ./I)	PRODUCT OF INERTIA ROLL-PIT	PIT-YAW	YAW-ROLL
PROBE WEIGHT	215.828		.213		.000		.000
	17.671	13.394	13.509	.021	.021	.012
I F WIRING	-.408		.453		.265		.159
SEPARATION	215.420		.212		-.000		-.000
	17.623	13.353	13.446	-.000	.000	-.000
EXTERNAL INS	-0.000		0.000		0.000		0.000
BEGIN ENTRY	215.420		.212		-.000		-.000
	17.623	13.353	13.446	-.000	.000	-.000
ABLATED MATL	-8.314		.161		0.000		0.000
POST HEATING	207.106		.215		-.000		-.000
	16.659	12.808	12.901	-.000	.000	-.000
DEPLOY DROG	-3.357		.512		-.081		0.000
ON DROGUE	203.749		.210		.001		-.000
	16.509	12.443	12.481	.061	.000	-.001
DEPLOY MAIN	-14.288		.401		.020		0.000
ON MAIN	189.461		.195		-.000		-.000
	16.308	11.684	11.715	.005	.000	-.001

FIGURE 147

EARTH ENTRY VEHICLE – MAXIMUM MASS

UNITS – GM CM

ITEM	WT	X	Y	Z	KX	KY	KZ
AL SKIN NOSE	131.54	6.48	0.00	0.00	6.35	4.47	4.47
AL SKIN CONE	2604.16	18.87	0.00	0.00	29.69	21.59	21.59
RING 1	185.97	8.59	0.00	0.00	8.13	5.74	5.74
RING 2	1093.16	15.21	0.00	0.00	16.97	11.99	11.99
RING 3	648.64	19.91	0.00	0.00	27.13	19.18	19.18
RING 4	367.41	24.97	0.00	0.00	36.73	25.96	25.96
RING 5	612.35	27.64	0.00	0.00	40.64	28.70	28.70
DIPOLS (3)	240.40	22.20	0.00	0.00	16.97	12.07	12.07
-19 ANGLE	848.22	27.43	0.00	0.00	38.40	27.15	27.15
-33 ANGLE	18.14	27.43	0.00	38.40	1.52	1.02	1.52
PRI STR FWD							
W= 6753.99	X=	20.20	Y=	0.00	Z=	.10	
HC PNL	3179.68	29.82	-.38	0.00	27.69	19.56	19.56
PRI STR AFT							
W= 3179.68	X=	29.82	Y=	-.38	Z=	0.00	
RNGM	653.17	27.43	0.00	0.00	38.10	27.94	27.94
-45 ANGLE	13.61	29.87	0.00	41.28	1.52	.51	1.52
-31 ANGLES	36.29	24.89	17.53	3.30	28.02	25.68	11.18

FIGURE 148
PAGE 1 OF 11

EARTH ENTRY VEHICLE – MAXIMUM MASS

UNITS – GM CM

ITEM	WT	X	Y	Z	KX	KY	KZ
-29 CLIP (2)	18.14	26.57	10.62	-34.75	8.26	2.03	7.62
-27 DOUBLER	117.93	38.10	23.34	-28.83	5.08	5.08	5.08
-25 ANGLE	13.61	23.37	25.40	5.59	1.02	1.52	1.52
-23 SHIM (3)	9.07	20.42	0.00	0.00	16.00	11.30	11.30
-21 ANGLE	467.20	29.87	0.00	0.00	41.28	29.18	29.18
-15 SPACERS	4.54	28.96	0.00	0.00	16.51	11.68	11.68
-13 ANGLES	36.29	26.57	0.00	0.00	36.32	25.68	25.68
-11 ANGLES	45.36	26.57	.05	-.23	36.32	25.68	25.68
INT STG FTG	498.95	38.79	31.24	18.03	4.62	5.26	5.26
INT STG FTG	498.95	38.79	-31.24	18.03	4.62	5.26	5.26
INT STG FTG	498.95	38.79	0.00	-36.07	4.62	5.26	5.26
PAD	104.33	22.20	-30.78	-9.40	2.54	2.54	2.54
INSTL-INTFAC	9.07	38.43	32.11	18.54	.51	.36	.36
INSTL-INTFAC	9.07	38.43	-32.11	18.54	.51	.36	.36
INSTL-INTFAC	9.07	38.43	0.00	-37.08	.51	.36	.36
BALLAST	2367.75	17.15	12.62	11.33	.36	.36	.36
BALLAST	1165.73	28.73	34.42	-13.82	.36	.36	.36

SEC STRUCT

W= 0577.09 X= 26.83 Y= 10.75 Z= .98

STRUCTURE

W= 16510.76 X= 24.69 Y= 4.21 Z= .43

FIGURE 148
PAGE 2 OF 11

EARTH ENTRY VEHICLE – MAXIMUM MASS

UNITS – GM CM

ITEM	WT	X	Y	Z	KX	KY	KZ
CONE-ABL	5633.62	13.82	0.00	0.00	30.43	22.07	22.07
NCAP-ABL	367.41	1.75	0.00	0.00	7.77	5.49	5.49
CNR LWR ABL	1433.35	21.72	0.00	0.00	43.46	30.73	30.73
CNR UPR ABL	879.97	27.33	0.00	0.00	43.87	31.01	31.01
CONE-RET	5633.62	14.94	0.00	0.00	30.43	22.07	22.07
NCAP-RET	349.27	2.36	0.00	0.00	7.59	5.36	5.36
GRVD CONE SY	14533.10	15.49	0.00	0.00	30.43	22.07	22.07
GRVD NCAP S	848.22	3.40	0.00	0.00	7.16	5.05	5.05
GRVD NCAP CI	4.54	3.56	0.00	0.00	1.40	1.40	1.40
GRVD NCAP BC	18.14	4.32	0.00	0.00	6.55	4.62	4.62
CNTR LWR RET	1124.91	21.87	0.00	0.00	42.80	30.25	30.25
CNTR UPR RET	780.18	27.10	0.00	0.00	43.43	30.71	30.71
CNR UPR BACK	1873.34	27.94	0.00	0.00	42.88	30.33	30.33
CNR FIL BACK	158.76	23.44	0.00	0.00	42.24	29.87	29.87
CNR TRI BACK	403.70	24.18	0.00	0.00	42.62	30.15	30.15
CNR RIB BACK	240.40	23.19	0.00	0.00	41.61	29.41	29.41
CNR GRV FELT	762.04	23.19	0.00	0.00	41.61	29.41	29.41
HC CORE CON	105846.69	17.88	0.00	0.00	30.15	26.42	26.42
HC CORE NCAP	2140.96	5.84	0.00	0.00	7.21	5.11	5.11
FG SKIN CONE	1446.96	16.81	0.00	0.00	30.61	26.70	26.70
FG SKIN NCAP	72.57	4.39	0.00	0.00	7.39	5.23	5.23
NPLUG FTG	108.86	3.96	0.00	0.00	4.06	2.87	2.87

FIGURE 148
PAGE 3 OF 11

EARTH ENTRY VEHICLE – MAXIMUM MASS

UNITS – GM CM

ITEM	WT	X	Y	Z	KX	KY	KZ
ADH CONE MF	312.98	16.74	0.00	0.00	30.61	26.70	26.70
ADH CONE FH	312.98	16.89	0.00	0.00	30.61	26.70	26.70
ADH CONE HA	299.37	18.85	0.00	0.00	29.69	26.14	26.14
ADH NCAP MF	18.14	4.32	0.00	0.00	7.44	5.26	5.26
ADH NCAP FH	13.61	4.47	0.00	0.00	7.42	5.23	5.23
ADH NCAP HA	9.07	6.55	0.00	0.00	6.78	4.80	4.80
ADH NPLG FTG	4.54	4.62	0.00	0.00	4.78	3.38	3.38
FWD HT SHLD							
W= 145630.37	X=	17.36	Y=	0.00	Z=	0.00	
INSERTS INCR	95.25	42.75	0.00	0.00	35.97	25.43	25.43
INSERTS INCR	54.43	40.03	25.25	-31.72	10.16	7.62	7.62
INSERTS INCR	131.54	31.85	0.00	0.00	41.81	29.57	29.57
ABLATOR	2072.92	46.30	0.00	0.00	35.23	27.89	27.89
HC CORE	299.37	46.66	0.00	0.00	34.54	27.36	27.36
SKIN2ADH OTR	1367.99	46.91	0.00	0.00	34.77	27.53	27.53
SKIN&ADH INT	925.33	46.38	0.00	0.00	34.32	27.18	27.18
INSTL AFT HS	58.97	31.04	0.00	0.00	42.16	29.82	29.82
INSTL AFT HS	22.68	39.57	24.10	-30.30	38.66	27.38	27.38
INSTL AFT HS	45.36	42.82	0.00	0.00	35.97	25.43	25.43
AFT HT SHLD							
W= 5093.84	X=	45.76	Y=	.38	Z=	-.47	

FIGURE 148
PAGE 4 OF 11

EARTH ENTRY VEHICLE – MAXIMUM MASS

UNITS – GM CM

ITEM	WT	X	Y	Z	KX	KY	KZ	DI
HEAT SHIELDS								
W= 150724.21	X=	18.32	Y=	.01	Z=	-.02		
PCMXMTR	680.39	23.60	12.45	-15.75	3.81	3.81	3.81	
TAPE RECORD	907.18	17.53	-8.38	6.86	3.81	3.81	3.81	
S-BAND XMTR	1270.06	24.00	-17.27	16.51	5.33	3.81	3.81	
C-BAND XPDR	1270.06	23.29	7.11	19.30	3.30	3.30	3.30	
SIG COND	907.18	21.69	-2.03	-21.84	4.57	3.30	5.59	
PWR SUP	226.80	21.18	-14.48	-17.02	1.52	1.52	1.52	
S-BAND PWR D	90.72	21.18	-14.48	-17.02	1.52	1.52	1.52	
C-BAND PWR D	90.72	21.18	-14.48	-17.02	1.52	1.52	1.52	
S-BAND ANT	226.80	36.58	-7.11	-40.13	.51	.51	.51	
S-BAND ANT	226.80	36.58	38.10	13.97	.51	.51	.51	
S-BAND ANT	226.80	36.58	-30.99	26.16	.51	.51	.51	
C-BAND ANT	90.72	41.66	-7.62	-36.83	.51	.51	.51	
C-BAND ANT	90.72	41.66	35.56	12.19	.51	.51	.51	
C-BAND ANT	90.72	41.66	-27.94	24.64	.51	.51	.51	
EQUIPMENT								
W= 6395.65	X=	24.48	Y=	-3.09	Z=	2.22		

FIGURE 148
PAGE 5 OF 11

EARTH ENTRY VEHICLE – MAXIMUM MASS

UNITS - GM CM

ITEM	WT	X	Y	Z	KX	KY	KZ
MTG COMM	616.89	21.95	-3.10	2.24	24.38	20.32	16.26
WIRING COMM	453.59	24.49	-3.10	2.24	24.38	20.32	16.26
INSTALLATION							
W= 1070.48	X=	23.02	Y=	-3.10	Z=	2.24	
COMMUNICAT							
W= 7466.13	X=	24.27	Y=	-3.10	Z=	2.23	
RADIOMETER	1224.70	12.45	0.00	0.00	4.57	5.84	5.84
ACCELEROMET	562.45	25.15	0.00	0.00	3.05	3.05	3.05
RATE GYRO	362.87	21.34	16.76	10.92	3.05	1.52	3.05
RATE GYRO	362.87	21.34	-.36	19.56	3.05	3.05	1.52
RATE GYRO	362.87	16.00	1.02	9.40	1.52	3.05	3.05
PRES XDCR	158.76	24.89	1.27	30.99	.51	.51	.51
PRES XDCR	158.76	24.89	-11.18	28.96	.51	.51	.51
PRES XDCR	158.76	24.89	-29.46	9.65	.51	.51	.51
PRES XDCR	158.76	24.89	-30.99	-1.27	.51	.51	.51
PRES XDCR	158.76	24.89	-1.27	-30.99	.51	.51	.51
PRES XDCR	158.76	24.89	9.65	-28.96	.51	.51	.51

FIGURE 148
PAGE 6 OF 11

EARTH ENTRY VEHICLE – MAXIMUM MASS

UNITS - GM CM

ITEM	WT	X	Y	Z	KX	KY	KZ
PRES XDCR	158.76	44.45	9.40	33.02	.51	.51	.51
PRES XDCR	158.76	44.45	-9.40	-33.02	.51	.51	.51
STRAIN GAGES	362.87	22.10	0.00	0.00	20.32	20.32	20.32
THERMOCPLS	1315.42	22.10	0.00	0.00	20.32	20.32	20.32
ELECTROSTST	249.48	24.49	24.89	18.80	2.79	1.27	2.79
ELECTROSTAT	249.48	24.49	30.99	2.79	2.79	1.27	2.79
ELECTROSTAT	249.48	24.49	30.48	-8.13	2.79	1.27	2.79
ELECTROSTAT	249.48	24.49	25.65	-18.29	2.79	1.27	2.79

EQUIPMENT

W= 6922.03 X= 21.99 Y= 3.58 Z= 2.14

MTG INSTR	612.35	19.46	4.14	1.60	21.59	18.03	18.54
WIRING INSTR	453.59	22.00	4.14	1.60	21.59	18.03	18.54

INSTALLATION

W= 1065.94 X= 20.54 Y= 4.14 Z= 1.60

INSTRUMENTAT

W= 7887.97 X= 21.79 Y= 3.66 Z= 2.07

FIGURE 148
PAGE 7 OF 11

EARTH ENTRY VEHICLE – MAXIMUM MASS

UNITS – GM CM

ITEM	WT	X	Y	Z	KX	KY	KZ
MAIN BATTERY	2267.96	22.56	0.00	13.46	4.57	4.57	4.06
PYRO BATTERY	453.59	15.24	7.62	10.16	1.52	1.52	1.52
PYRO BATTERY	453.59	15.24	7.62	-10.16	1.52	1.52	1.52
PYRO RELAY	1360.78	15.24	2.03	-12.95	1.52	2.79	2.54
PYRO RELAY	1360.78	15.24	-2.79	-12.70	1.52	2.79	2.54
SEQUENCER	2267.96	15.24	-9.65	-8.64	1.52	3.05	3.05
G-SWITCH	226.80	21.18	-19.56	-10.41	1.52	1.52	1.52
EQUIPMENT							
W= 8391.46	X=	17.38	Y=	-2.44	Z=	-3.14	
UMBIL W CCT	127.01	50.80	15.49	10.92	10.16	10.16	10.16
UMBIL C CCT	36.29	71.12	0.00	0.00	.51	.51	.51
MTG PWR	349.27	14.83	-2.44	.99	13.46	12.45	7.62
WIRING PWR	544.31	17.37	-2.44	.99	13.46	12.45	7.62
INSTALLATION							
W= 1056.87	X=	22.40	Y=	-.20	Z=	2.15	
ELECT PWR							
W= 9448.33	X=	17.94	Y=	-2.19	Z=	-2.55	

FIGURE 148
PAGE 8 OF 11

EARTH ENTRY VEHICLE – MAXIMUM MASS

UNITS - GM CM

ITEM	WT	X	Y	Z	KX	KY	KZ
GUILLOTINE	190.51	38.10	36.32	20.96	1.27	1.27	1.27
INIT GUIL	54.43	40.64	35.31	20.32	.51	.51	.51
INIT MSINLET	54.43	13.97	0.00	4.93	1.52	.25	1.52
INIT NEPH DR	54.43	33.27	-18.24	-30.94	.51	.51	.51
INIT TEMP PB	54.43	23.27	-29.77	-9.40	.51	.51	.51
INIT MAIN BT	54.43	17.65	-10.41	6.86	1.52	.76	1.52
CCT SHORT PL	68.04	30.48	1.52	-30.99	.51	.51	.51
CCT SHORT PL	68.04	30.48	14.61	-27.25	.51	.51	.51
CCT W	158.76	21.08	-13.72	1.78	20.32	20.32	7.62
CCT C	18.14	24.77	5.33	27.94	.51	.51	.51
CCT C	18.14	26.67	-2.79	-27.69	.51	.51	.51
CCT W	117.93	21.08	19.81	0.00	19.05	19.05	19.05
CCT C	18.14	26.67	11.18	26.42	.51	.51	.51
CCT C	18.14	24.77	9.40	-26.42	.51	.51	.51
CCT MSPEC W	18.14	21.59	-13.72	-20.57	12.19	7.37	10.92
CCT W	54.43	21.59	-2.54	-31.75	2.54	1.27	2.54
CCT W	27.22	18.80	-10.16	-11.68	14.22	13.97	12.45
CCT MSPEC C	9.07	26.54	-6.86	-16.26	.51	.51	.51
CCT C	9.07	24.13	-6.35	-26.92	.51	.51	.51
CCT C	18.14	17.65	-8.89	5.84	.51	.51	.51
CCT C	36.29	27.94	1.52	-30.99	.51	.51	.51
CCT MSPEC W	22.68	21.59	-5.72	-21.84	12.70	7.62	11.43

FIGURE 148
PAGE 9 OF 11

EARTH ENTRY VEHICLE – MAXIMUM MASS

UNITS – GM CM

ITEM	WT	X	Y	Z	KX	KY	KZ
CCT W	72.57	21.59	15.24	-29.21	4.57	1.27	4.57
CCT W	27.22	18.80	-7.11	-13.21	14.48	14.22	12.70
CCT MSPEC C	9.07	26.54	-17.27	-4.06	.51	.51	.51
CCT C	9.07	24.13	5.46	-26.92	.51	.51	.51
CCT C	18.14	17.65	-11.94	7.62	.51	.51	.51
CCT C	36.29	27.94	14.61	-27.25	.51	.51	.51
CCT W	127.01	27.94	2.54	9.65	30.48	27.94	27.94
CCT W	72.57	30.48	24.13	3.05	15.24	14.99	6.86
CCT C	13.61	23.37	-4.83	-28.70	.51	.51	.51
CCT C	13.61	23.37	7.11	-27.94	.51	.51	.51
WIRE INSTL	22.68	28.45	14.48	-27.31	.51	.51	.51
WIRE INSTL	22.68	28.45	1.52	-30.99	.51	.51	.51
PYROTECHNICS							
W= 1587.57	X=	26.48	Y=	6.24	Z=	-5.49	
DROGUE CHUTE	1360.78	43.18	-20.07	0.00	3.81	4.06	4.06
MORTAR	2721.55	28.96	-20.07	0.00	3.56	10.16	10.16
DROGUE FTG	226.80	32.00	-26.92	-26.92	2.54	2.54	2.54
DROGUE FTG	226.80	32.00	26.92	26.92	2.54	2.54	2.54
MAIN CHUTE	14288.16	40.13	2.03	0.00	11.68	11.68	11.68
MAIN FTG	226.80	32.00	39.62	0.00	2.54	2.54	2.54

FIGURE 148
PAGE 10 OF 11

EARTH ENTRY VEHICLE – MAXIMUM MASS

UNITS – GM CM

ITEM	WT	X	Y	Z	KX	KY	KZ
MAIN TG	226.80	32.00	-19.81	34.29	2.54	2.54	2.54
MAIN PTG	226.80	32.00	-19.81	-34.29	2.54	2.54	2.54
MAIN CONTNR	843.68	36.58	2.54	0.00	20.32	14.22	14.22
MDF COVER	45.36	50.80	0.00	0.00	28.70	20.32	20.32
COVER INIT	235.87	48.26	0.00	0.00	28.70	.25	28.70
COVER INCR	-1732.72	57.40	0.00	0.00	20.32	14.22	14.22
COVER INCR	1732.72	57.40	0.00	0.00	20.32	14.22	14.22
UPR RING DEP	263.08	51.56	0.00	0.00	28.70	20.32	20.32
UPR RING RET	857.29	50.04	0.00	0.00	28.70	20.32	20.32
MTG	226.80	17.78	-20.07	0.00	2.54	2.54	2.54
WIRING DECEL	226.80	38.79	-2.51	0.00	17.78	14.22	17.02

DECEL SYS

W= 22203.35 X= 38.78 Y= -2.52 Z= 0.00

PROBE WEIGHT

W= 215828.32 X= 21.29 Y= .05 Z= .02
RAD OF GYRATIONKROL= 28.61 KPIT= 24.91 KYAW= 25.02
MOM OF INERTIA ROLL=176714688.31 PIT= 133942362.67 YAW=135094951.52
PROD OF INERTIAR-P= 211227.32 P-Y= 205605.53 Y-R= 124011.09

FIGURE 148
PAGE 11 of 11

MASS PROPERTIES SUMMARY

EARTH ENTRY VEHICLE – MINIMUM MASS

11/11/75

DESCRIPTION	CURRENT WEIGHT (KG)	CENTER OF GRAVITY X (M)	Y	Z
	MOMENT OF INERTIA ROLL	PITCH	YAW (KG-METER SQ./1)	PRODUCT OF INERTIA ROLL-PIT	PIT-YAW	YAW-ROLL
PRI STR FWD	6.754	.202		0.000	.001
.596	.323	.320	0.000	0.000	.001
PRI STR AFT	3.180	.298		-.004	0.000
.244	.122	.122	-.000	0.000	0.000
SEC STRUCT	6.659	.267		.108	.013
.578	.317	.369	-.016	-.033	-.033
STRUCTURE	16.592	.247		.043	.006
1.466	.787	.883	-.002	-.027	-.031
FWD HT SHLD	61.072	.141		0.000	0.000
4.648	2.651	2.651	0.000	0.000	0.000
AFT HT SHLD	5.094	.458		.004	-.005
.638	.397	.394	-.001	-.006	.001
HEAT SHIELDS	66.166	.166		.000	-.000
5.336	3.518	3.516	.004	-.006	-.006
EQUIPMENT	6.396	.245		-.031	.022
.379	.261	.171	.007	-.018	.001
INSTALLATION	1.070	.230		-.031	.022
.054	.044	.028	-.000	-.000	.000
COMMUNICAT	7.466	.243		-.031	.022
.443	.306	.200	.007	-.018	.001
EQUIPMENT	6.822	.220		.036	.021
.320	.236	.222	.004	-.005	-.003
INSTALLATION	1.066	.205		.041	.016
.050	.035	.037	.000	.000	.000
INSTRUMENTAT	7.888	.218		.037	.021
.370	.271	.259	.003	-.005	-.003
EQUIPMENT	8.391	.174		-.024	-.031
.144	.125	.049	.002	.018	.027
INSTALLATION	1.057	.224		-.002	.022
.022	.038	.032	.007	.002	.003
ELECT PWR	9.448	.179		-.022	-.025
.170	.168	.084	.010	.021	.032
PYROTECHNICS	1.588	.265		.062	-.055
.136	.090	.076	.013	.022	.005
DECEL SYS	22.203	.388		-.025	0.000
.697	.447	.635	.055	.033	0.000
PROBE WEIGHT	131.351	.223		.001	.001
8.709	6.458	6.577	.020	.024	.012

FIGURE 149

SEQUENCED MASS PROPERTIES SUMMARY

EARTH ENTRY VEHICLE – MINIMUM MASS

11/11/75

DESCRIPTION	CURRENT WEIGHT (KG)	CENTER OF GRAVITY X (M)	Y	Z
	MOMENT OF INERTIA ROLL	PITCH	YAW	PRODUCT OF INERTIA ROLL-PIT	PIT-YAW	YAW-ROLL
		(KG-METER SQ./I)				
PROBE WEIGHT	131.351	.223		.001		.001
	8.709	6.458	6.577	.020	.024	.012
I F WIRING	-.408	.453		.265		.159
SEPARATION	130.943	.223		.000		.000
	8.661	6.419	6.516	.000	.003	-.000
EXTERNAL INS	-0.000	0.000		0.000		0.000
BEGIN ENTRY	130.943	.223		.000		.000
	8.661	6.419	6.516	.000	.003	-.000
ABLATED MATL	-8.314	.161		0.000		0.000
POST HEATING	122.629	.227		.000		.000
	7.697	5.864	5.960	.000	.003	-.000
DEPLOY DROG	-3.357	.512		-.081		0.000
ON DROGUE	119.272	.219		.002		.000
	7.546	5.520	5.560	.059	.003	-.001
DEPLOY MAIN	-14.288	.401		.020		0.000
ON MAIN	104.984	.194		-.000		.000
	7.346	4.783	4.819	.005	.003	-.000

FIGURE 150

EARTH ENTRY VEHICLE – MINIMUM MASS

UNITS – GM CM

ITEM	WT	X	Y	Z	KX	KY	KZ
AL SKIN NOSE	131.54	6.48	0.00	0.00	6.35	4.47	4.47
AL SKIN CONE	2638.16	18.87	0.00	0.00	29.69	21.59	21.59
RING 1	185.97	8.59	0.00	0.00	8.13	5.74	5.74
RING 2	1093.16	15.21	0.00	0.00	16.97	11.99	11.99
RING 3	648.64	19.91	0.00	0.00	27.13	19.18	19.18
RING 4	367.41	24.97	0.00	0.00	36.73	25.96	25.96
RING 5	612.35	27.64	0.00	0.00	40.64	28.70	28.70
RIPODS (3)	240.40	22.20	0.00	0.00	16.97	12.07	12.07
-19 ANGLE	848.22	27.43	0.00	0.00	38.40	27.15	27.15
-33 ANGLE	18.14	27.43	0.00	38.40	1.52	1.02	1.52
PRI STR FWD							
W= 6753.99	X=	20.20	Y=	0.00	Z=	.10	
HC PNL	3179.68	29.82	-.38	0.00	27.69	19.56	19.56
PRI STR AFT							
W= 3179.68	X=	29.82	Y=	-.38	Z=	0.00	
RNRM	653.17	27.43	0.00	0.00	38.10	27.94	27.94
-45 ANGLE	13.61	29.87	0.00	41.28	1.52	.51	1.52
-31 ANGLES	36.29	24.89	17.53	3.30	28.02	25.68	11.18

FIGURE 151
PAGE 1 OF 11

EARTH ENTRY VEHICLE – MINIMUM MASS

UNITS - KG CM

ITEM	WT	X	Y	Z	KX	KY	KZ
-29 CLIP (2)	18.14	26.57	10.62	-34.75	8.26	2.03	7.62
-27 DOUBLER	117.93	38.10	23.34	-28.83	5.08	5.08	5.08
-25 ANGLE	13.61	23.37	25.40	5.59	1.02	1.52	1.52
-23 SHIM (3)	9.07	20.42	0.00	0.00	16.00	11.30	11.30
-21 ANGLE	467.20	29.87	0.00	0.00	41.28	29.18	29.18
-15 SPACERS	4.54	28.96	0.00	0.00	16.51	11.68	11.68
-13 ANGLES	36.29	26.57	0.00	0.00	36.32	25.68	25.68
-11 ANGLES	45.36	26.57	.05	-.23	36.32	25.68	25.68
INT STG FTG	498.95	38.79	31.24	18.03	4.62	5.26	5.26
INT STG FTG	498.95	38.79	-31.24	18.03	4.62	5.26	5.26
INT STG FTG	498.95	38.79	0.00	-36.07	4.62	5.26	5.26
PAD	104.33	22.20	-30.78	-9.40	2.54	2.54	2.54
INSTL-INTFAC	9.07	38.43	32.11	18.54	.51	.36	.36
INSTL-INTFAC	9.07	38.43	-32.11	18.54	.51	.36	.36
INSTL-INTFAC	9.07	38.43	0.00	-37.08	.51	.36	.36
BALLAST	2435.79	17.15	12.37	11.61	.36	.36	.36
BALLAST	1179.34	28.73	34.75	-12.95	.36	.36	.36

SEC STRUCT

W= 6658.74 X= 26.74 Y= 10.79 Z= 1.31

STRUCTURE

W= 16592.41 X= 24.67 Y= 4.26 Z= .57

FIGURE 151
PAGE 2 OF 11

EARTH ENTRY VEHICLE – MINIMUM MASS

UNITS - GM CM

ITEM	WT	X	Y	Z	KX	KY	KZ
CONE-ABL	5633.62	13.82	0.00	0.00	30.43	22.07	22.07
NOSE-ABL	367.41	1.75	0.00	0.00	7.77	5.49	5.49
CNR LWR ABL	1433.35	21.72	0.00	0.00	43.46	30.73	30.73
CNR UPR ABL	879.97	27.33	0.00	0.00	43.87	31.01	31.01
CONE-RET	5633.62	14.94	0.00	0.00	30.43	22.07	22.07
NOSE-RET	349.27	2.36	0.00	0.00	7.59	5.36	5.36
GRVD CONE SY	14533.10	15.49	0.00	0.00	30.43	22.07	22.07
GRVD NOSE S	848.22	3.40	0.00	0.00	7.16	5.05	5.05
GRVD NOSE CI	4.54	3.56	0.00	0.00	1.40	1.40	1.40
GRVD NOSE BC	18.14	4.32	0.00	0.00	6.55	4.62	4.62
CNTR LWR RET	1124.91	21.87	0.00	0.00	42.80	30.25	30.25
CNTR UPR RET	780.18	27.40	0.00	0.00	43.43	30.71	30.71
CNR UPR BACK	1873.34	27.94	0.00	0.00	42.88	30.33	30.33
CNR FIL BACK	158.76	23.44	0.00	0.00	42.24	29.87	29.87
CNR TRI BACK	403.79	24.18	0.00	0.00	42.62	30.15	30.15
CNR RIB BACK	240.40	23.19	0.00	0.00	41.61	29.41	29.41
CNR GRV FELT	762.04	23.19	0.00	0.00	41.61	29.41	29.41
HC CORE CONE	19763.02	10.03	0.00	0.00	15.67	11.23	11.23
HC CORE CONE	1524.07	19.79	0.00	0.00	33.38	23.88	23.88
HC CORE NOSE	2140.96	5.84	0.00	0.00	7.21	5.11	5.11
FG SKIN CONE	1446.96	16.81	0.00	0.00	30.61	26.70	26.70
FG SKIN NOSE	72.57	4.39	0.00	0.00	7.39	5.23	5.23

FIGURE 151
PAGE 3 OF 11

EARTH ENTRY VEHICLE – MINIMUM MASS

UNITS - GM CM

ITEM	WT	X	Y	Z	KX	KY	KZ
APLUG FTG	108.86	3.96	0.00	0.00	4.06	2.87	2.87
ADH CONE HF	312.98	16.74	0.00	0.00	30.61	26.70	26.70
ADH CONE FH	312.98	16.89	0.00	0.00	30.61	26.70	26.70
ADH CONE HA	299.37	18.85	0.00	0.00	29.69	26.14	26.14
ADH NCAP HF	18.14	4.32	0.00	0.00	7.44	5.26	5.26
ADH NCAP FH	13.61	4.47	0.00	0.00	7.42	5.23	5.23
ADH NCAP HA	9.07	6.55	0.00	0.00	6.78	4.80	4.80
ADH NPLG FTG	4.54	4.62	0.00	0.00	4.78	3.38	3.38

FWD HT SHLD

W= 61071.68 X= 14.15 Y= 0.00 Z= 0.00

INSERTS INCR	95.25	42.75	0.00	0.00	35.97	25.43	25.43
INSERTS INCR	54.43	40.03	25.25	-31.72	10.16	7.62	7.62
INSERTS INCR	131.54	31.85	0.00	0.00	41.81	29.57	29.57
ABLATOR	2072.92	46.30	0.00	0.00	35.23	27.89	27.89
HC CORE	299.37	46.66	0.00	0.00	34.54	27.36	27.36
SKIN2ADH OTR	1387.99	46.91	0.00	0.00	34.77	27.53	27.53
SKIN&ADH INT	925.33	46.38	0.00	0.00	34.32	27.18	27.18
INSTL AFT HS	58.97	31.04	0.00	0.00	42.16	29.82	29.82
INSTL AFT HS	22.68	39.57	24.10	-30.30	38.66	27.38	27.38
INSTL AFT HS	45.36	42.82	0.00	0.00	35.97	25.43	25.43

FIGURE 151
PAGE 4 OF 11

EARTH ENTRY VEHICLE – MINIMUM MASS

UNITS - GM CM

ITEM	WT	X	Y	Z	KX	KY	KZ
AFT HT SHLD							
W= 5093.84	X=	45.76	Y=	.38	Z=	-.47	
HEAT SHIELDS							
W= 66165.52	X=	16.58	Y=	.03	Z=	-.04	
PCMXMTR	680.39	23.60	12.45	-15.75	3.81	3.81	3.81
TAPE RECORD	907.19	17.53	-8.38	6.86	3.81	3.81	3.81
S-BAND XMTR	1270.06	24.00	-17.27	16.51	5.33	3.81	3.81
C-BAND XPDR	1270.06	23.29	7.11	19.30	3.30	3.30	3.30
SIG COND	907.18	21.69	-2.03	-21.84	4.57	3.30	5.59
PWR SUP	226.80	21.18	-14.48	-17.02	1.52	1.52	1.52
S-BAND PWR D	90.72	21.18	-14.48	-17.02	1.52	1.52	1.52
C-BAND PWR D	90.72	21.18	-14.48	-17.02	1.52	1.52	1.52
S-BAND ANT	226.80	36.58	-7.11	-40.13	.51	.51	.51
S-BAND ANT	226.80	36.58	38.10	13.97	.51	.51	.51
S-BAND ANT	226.80	36.58	-30.99	26.16	.51	.51	.51
C-BAND ANT	90.72	41.66	-7.62	-36.83	.51	.51	.51
C-BAND ANT	90.72	41.66	35.56	12.19	.51	.51	.51

FIGURE 151

PAGE 5 OF 11

EARTH ENTRY VEHICLE – MINIMUM MASS

UNITS – G i CM

ITEM	WT	X	Y	Z	KX	KY	KZ
C-BAND ANT	90.72	41.66	-27.94	24.64	.51	.51	.51
EQUIPMENT							
W= 6395.65	X=	24.48	Y=	-3.09	Z=	2.22	
MTG COMM	616.89	21.95	-3.10	2.24	24.38	20.32	16.26
WIRING COMM	453.59	24.49	-3.10	2.24	24.38	20.32	16.26
INSTALLATION							
W= 1070.48	X=	23.02	Y=	-3.10	Z=	2.24	
COMMUNICAT							
W= 7466.13	X=	24.27	Y=	-3.10	Z=	2.23	
RADIOMETER	1224.70	12.45	0.00	0.00	4.57	5.84	5.84
ACCELEROMET	562.45	25.15	0.00	0.00	3.05	3.05	3.05
RATE GYRO	362.87	21.34	16.76	10.92	3.05	1.52	3.05
RATE GYRO	362.87	21.34	-.36	19.56	3.05	3.05	1.52
RATE GYRO	362.87	16.00	1.02	9.40	1.52	3.05	3.05
PRES XDCR	158.76	24.89	1.27	30.99	.51	.51	.51

FIGURE 151
PAGE 6 OF 11

EARTH ENTRY VEHICLE – MINIMUM MASS

UNITS - GM CM

ITEM	WT	X	Y	Z	KX	KY	KZ
PRES XDCR	158.76	24.89	-11.18	28.96	.51	.51	.51
PRES XDCR	158.76	24.89	-29.46	9.65	.51	.51	.51
PRES XDCR	158.76	24.89	-30.99	-1.27	.51	.51	.51
PRES XDCR	158.76	24.89	-1.27	-30.99	.51	.51	.51
PRES XDCR	158.76	24.89	9.65	-28.96	.51	.51	.51
PRES XDCR	158.76	44.45	9.40	33.02	.51	.51	.51
PRES XDCR	158.76	44.45	-9.40	-33.02	.51	.51	.51
STRAIN GAGES	362.87	22.10	0.00	0.00	20.32	20.32	20.32
THERMOCPLS	1315.42	22.10	0.00	0.00	20.32	20.32	20.32
ELECTROSTST	249.48	24.49	24.89	18.80	2.79	1.27	2.79
ELECTROSTAT	249.48	24.49	30.99	2.79	2.79	1.27	2.79
ELECTROSTAT	249.48	24.49	30.48	-8.13	2.79	1.27	2.79
ELECTROSTAT	249.48	24.49	25.65	-18.29	2.79	1.27	2.79
EQUIPMENT							
W= 6822.03	X=	21.99	Y=	3.58	Z=	2.14	
MTG INSTR	612.35	19.46	4.14	1.60	21.59	18.03	18.54
WIRING INSTR	453.59	22.00	4.14	1.60	21.59	18.03	18.54
INSTALLATION							
W= 1065.94	X=	20.54	Y=	4.14	Z=	1.60	

FIGURE 151
PAGE 7 OF 11

EARTH ENTRY VEHICLE – MINIMUM MASS

UNITS - GM CM

ITEM	WT	X	Y	Z	KX	KY	KZ
INSTRUMENTAT							
W= 7887.97	X=	21.79	Y=	3.66	Z=		
MAIN BATTERY	2267.96	22.56	0.00	13.46	4.57	4.57	4.06
PYRO BATTERY	453.59	15.24	7.62	10.16	1.52	1.52	1.52
PYRO BATTERY	453.59	15.24	7.62	-10.16	1.52	1.52	1.52
PYRO RELAY	1360.78	15.24	2.03	-12.95	1.52	2.79	2.54
PYRO RELAY	1360.78	15.24	-2.79	-12.70	1.52	2.79	2.54
SEQUENCER	2267.96	15.24	-9.65	-8.64	1.52	3.05	3.05
G-SWITCH	226.80	21.18	-19.56	-10.41	1.52	1.52	1.52
EQUIPMENT							
W= 6391.46	X=	17.38	Y=	-2.44	Z=		-3.14
UMBIL W CCT	127.01	50.80	15.49	10.92	10.16	10.16	10.16
UMBIL C CCT	36.29	71.12	0.00	0.00	.51	.51	.51
MTG PWR	349.27	14.83	-2.44	.99	13.46	12.45	7.62
WIRING PWR	544.31	17.37	-2.44	.99	13.46	12.45	7.62
INSTALLATION							
W= 1056.87	X=	22.40	Y=	-.20	Z=		2.15

FIGURE 151
PAGE 8 OF 11

EARTH ENTRY VEHICLE – MINIMUM MASS

UNITS – GM CM

ITEM	WT	X	Y	Z	KX	KY	KZ
ELECT PWR							
W= 9448.33	X=	17.94	Y=	-2.19	Z=	-2.55	
GUILLOTINE	190.51	38.10	36.32	20.96	1.27	1.27	1.27
INIT GUIL	54.43	40.64	35.31	20.32	.51	.51	.51
INIT MSINLET	54.43	13.97	0.00	4.93	1.52	.25	1.52
INIT NEPH DR	54.43	33.27	-18.24	-30.94	.51	.51	.51
INIT TEMP PB	54.43	23.27	-29.77	-9.40	.51	.51	.51
INIT MAIN BT	54.43	17.65	-10.41	6.86	1.52	.76	1.52
CCT SHORT PL	68.04	30.48	1.52	-30.99	.51	.51	.51
CCT SHORT PL	68.04	30.48	14.61	-27.25	.51	.51	.51
CCT W	158.76	21.08	-13.72	1.78	20.32	20.32	7.62
CCT C	18.14	24.77	5.33	27.94	.51	.51	.51
CCT C	18.14	26.67	-2.79	-27.69	.51	.51	.51
CCT W	117.93	21.08	19.81	0.00	19.05	19.05	19.05
CCT C	18.14	26.67	11.18	26.42	.51	.51	.51
CCT C	18.14	24.77	9.40	-26.42	.51	.51	.51
CCT MSPEC W	18.14	21.59	-13.72	-20.57	12.19	7.37	10.92
CCT W	54.43	21.59	-2.54	-31.75	2.54	1.27	2.54
CCT W	27.22	18.80	-10.16	-11.68	14.22	13.97	12.45

FIGURE 151
PAGE 9 OF 11

EARTH ENTRY VEHICLE – MINIMUM MASS

UNITS – GM CM

ITEM	WT	X	Y	Z	KX	KY	KZ
CCT MSPEC C	9.07	26.54	-6.86	-16.26	.51	.51	.51
CCT C	9.07	24.13	-6.35	-26.92	.51	.51	.51
CCT C	18.14	17.65	-8.89	5.84	.51	.51	.51
CCT C	36.29	27.94	1.52	-30.99	.51	.51	.51
CCT MSPEC W	22.68	21.59	-5.72	-21.84	12.70	7.62	11.43
CCT W	72.57	21.59	15.24	-29.21	4.57	1.27	4.57
CCT W	27.22	18.80	-7.11	-13.21	14.48	14.22	12.70
CCT MSPEC C	9.07	26.54	-17.27	-4.06	.51	.51	.51
CCT C	9.07	24.13	5.46	-26.92	.51	.51	.51
CCT C	18.14	17.65	-11.94	7.62	.51	.51	.51
CCT C	36.29	27.94	14.61	-27.25	.51	.51	.51
CCT W	127.01	27.94	2.54	9.65	30.48	27.94	27.94
CCT W	72.57	30.48	24.13	3.05	15.24	14.99	6.86
CCT C	13.61	23.37	-4.83	-28.70	.51	.51	.51
CCT C	13.61	23.37	7.11	-27.94	.51	.51	.51
WIRE INSTL	22.68	28.45	14.48	-27.31	.51	.51	.51
WIRE INSTL	22.68	28.45	1.52	-30.99	.51	.51	.51
PYROTECHNICS							
W= 1587.57	X=	26.48	Y=	6.24	Z=	-5.49	
DROGUE CHUTE	1360.78	43.18	-20.07	0.00	3.81	4.06	4.06

FIGURE 151
PAGE 10 OF 11

EARTH ENTRY VEHICLE – MINIMUM MASS

UNITS – GM CM

ITEM	WT	X	Y	Z	KX	KY	KZ
MORTAR	2721.55	28.96	-20.07	0.00	3.56	10.16	10.16
DROGUE FTG	226.80	32.00	-26.92	-26.92	2.54	2.54	2.54
DROGUE FTG	226.80	32.00	26.92	26.92	2.54	2.54	2.54
MAIN CHUTE	14288.16	40.13	2.03	0.00	11.68	11.68	11.68
MAIN FTG	226.80	32.00	39.62	0.00	2.54	2.54	2.54
MAIN FTG	226.80	32.00	-19.81	34.29	2.54	2.54	2.54
MAIN FTG	226.80	32.00	-19.81	-34.29	2.54	2.54	2.54
MAIN CONTNR	843.68	36.58	2.54	0.00	20.32	14.22	14.22
MDF COVER	45.36	50.80	0.00	0.00	28.70	20.32	20.32
COVER INIT	235.87	48.26	0.00	0.00	28.70	.25	28.70
COVER INCR	-1732.72	57.40	0.00	0.00	20.32	14.22	14.22
COVER INCR	1732.72	57.40	0.00	0.00	20.32	14.22	14.22
UPR RING DEP	263.08	51.56	0.00	0.00	28.70	20.32	20.32
UPR RING RET	857.29	50.04	0.00	0.00	28.70	20.32	20.32
MTG	226.80	17.78	-20.07	0.00	2.54	2.54	2.54
WIRING DECEL	226.80	38.79	-2.51	0.00	17.78	14.22	17.02

DECEL SYS

W= 22203.35 X= 38.78 Y= -2.52 Z= 0.00

PROBE WEIGHT

W= 131351.28	X= 22.32	Y= .09	Z= .05		
RAD OF GYRATION	KROLL= 25.75	KPIT= 22.17	KYAW= 22.38		
MOM OF INERTIA	ROLL= 87088697.95	PIT= 64581792.39	YAW= 65772903.87		
PROD OF INERTIA	P-P= 204570.72	P-Y= 239885.26	Y-R= 116759.27		

FIGURE 151
PAGE 11 OF 11

9.4 Cost Estimate - The cost of conducting an earth entry flight program could be determined by considering the expenses chargeable for a Shuttle launch, the booster and the entry vehicle. A summary of the total program cost for the entry vehicle is contained in Figure 152. This rough-order-of-magnitude (ROM) estimate is in 1976 dollars and based on actual cost of previous space programs. The effort is divided into six categories: management, system engineering, system test and evaluation, flight hardware design and development, support equipment and flight operations. The following ground rules and assumptions were used:

- o Delivery of a single flight article plus a refurbished proof test model as a flight backup.
- o Program duration of 36 months to delivery with six month post-delivery support.
- o Cost only includes entry vehicle and associated ground support equipment (GSE).
- o Parachute recovery system.
- o Exclusion of post-launch support.
- o Value is at cost level; does not include earnings.
- o Work Breakdown Structure is in accordance with MIL-STD-881.
- o Overall program is considered as a prototype development, and unencumbered by the burden of AF375 series controls, custom reviews and approval of design drawings, specification and testing.

The total recurring cost per flight, including Shuttle, booster and recovery services were also examined with the following results.

Type Launch	Dedicated	Shared
Shuttle	$12.0 M	$7.0 M
Booster	1.0	
Entry Vehicle	3.2	3.2
Recovery	.3	.3
Data Reduction	.5	.5
	$17.0 M	$11.0 M

In the absence of any official Space Transportation System pricing ground rules, certain assumptions were made. A dedicated Shuttle launch cost of $12.0 M (1976 dollars) was obtained by escalating the $10.3 M (1974 dollars) specified in Reference 16. Determining what fraction of a Shuttle launch assigned to this program would depend on the total complement of payloads carried

TOTAL COST FOR EARTH ENTRY VEHICLE

	NON-RECURRING			RECURRING			
	DESIGN & ANALYSIS	EQUIP. & TEST	TOTAL	FLIGHT HARDWARE	MISSION SUPPORT	TOTAL	TOTAL PROGRAM
1.0 MANAGEMENT	$ 479098	$ 111991	$ 591089	$ 136454	$ 7759	$ 144213	$ 735302
2.0 SYSTEMS ENGINEERING	$ 916459	$ 276421	$ 1192880	$ 381785	$ 381785	$ 763570	$ 1956450
3.0 SYSTEM TEST & EVALUATION	$ 0	$ 1779315	$ 1779315	$ 0	$ 0	$ 0	$ 1779315
3.1 HARDWARE	$ 0	$ 1274890	$ 1274890	$ 0	$ 0	$ 0	$ 1274890
3.1.1 ESTU	$ 0	$ 483590	$ 483590	$ 0	$ 0	$ 0	$ 483590
3.1.2 STVU	$ 0	$ 450203	$ 450203	$ 0	$ 0	$ 0	$ 450203
3.1.3 MASS MODEL	$ 0	$ 225108	$ 225108	$ 0	$ 0	$ 0	$ 225108
3.1.4 MOCK-UPS & MISC.	$ 0	$ 115989	$ 115989	$ 0	$ 0	$ 0	$ 115989
3.2 DEVELOPMENT TESTING	$ 0	$ 504425	$ 504425	$ 0	$ 0	$ 0	$ 504425
4.0 FLIGHT HDWE (INCL. PTM)	$ 3296625	$ 4267190	$ 7563815	$ 2300693	$ 0	$ 2300693	$ 9864508
4.1 STRUCTURE	$ 568846	$ 222269	$ 791115	$ 136230	$ 0	$ 136230	$ 927345
4.2 HEAT SHIELD	$ 141476	$ 374737	$ 516213	$ 231594	$ 0	$ 231594	$ 747807
4.3 POWER & DISTRIBUTION	$ 124826	$ 194448	$ 319274	$ 98771	$ 0	$ 98771	$ 418045
4.4 TELECOMMUNICATIONS	$ 523196	$ 1232564	$ 1755760	$ 427036	$ 0	$ 427036	$ 2182796
4.5 RECOVERY	$ 565775	$ 1567893	$ 2133668	$ 193452	$ 0	$ 193452	$ 2327120
4.6 PYROTECHNICS	$ 26[illegible]	$ 43095	$ 70091	$ 45852	$ 0	$ 45852	$ 115943
4.7 ENGR. INSTRUMENTATION	$ 450098	$ 213950	$ 664048	$ 126303	$ 0	$ 126303	$ 790351
4.8 EXPERIMENTS	$ 0	$ 0	$ 0	$ 128735	$ 0	$ 128735	$ 128735
4.9 SYS. INTGR. & ASSY.	$ 617374	$ 0	$ 617374	$ 280237	$ 0	$ 280237	$ 897611
4.10 REFURBISHMENT	$ 0	$ 0	$ 0	$ 144418	$ 0	$ 144418	$ 144418
4.11 SPARES & REPAIR PARTS	$ 0	$ 0	$ 0	$ 488065	$ 0	$ 488065	$ 488065
4.12 TOOLING & TEMPLATES	$ 278038	$ 418234	$ 696272	$ 0	$ 0	$ 0	$ 696272
5.0 SUPPORT EQUIPMENT	$ 349649	$ 0	$ 349649	$ 0	$ 0	$ 0	$ 349649
T O T A L	$ 5041831	$ 6434917	$ 11476748	$ 2818932	$ 389544	$ 3208476	$ 14685224

FIGURE 152

aloft and what satellites were retrieved from space. The length of the payload is important in determining how much room is available for shared payloads. If either Transtage/TE363-4 or the 2 stage SRM IUS/TE364-4 booster were used less than 3/8 of the bay would be used and if the "short length" booster were used only 1/7 would be occupied. For shared payload launches, a linear relationship of cost with payload length was assumed. This reflects the results from past examination of available traffic models which indicated that less than 50% of the Shuttle flights were mass limited whereas almost 90% of the flights were length limited. The booster cost of $1.0 $\overline{M}$ is the current figure being quoted for the solid IUS in the open literature. Costs of the other boosters considered range from $3 $\overline{M}$ to over $6 $\overline{M}$. The shared launch cost of $7.0 $\overline{M}$ for Shuttle and booster reflects either a solid IUS with 50% payload sharing or a short length booster that occupies 1/7 of the payload bay length.

10. CONCLUSIONS

The major conclusion of this study is that the Shuttle and its upper stage can provide high speed earth entry simulation of outer planet environments on a probe shape vehicle. Furthermore, candidate heat shield concepts can be qualified as well as intense environments measured to expand scientific knowledge of entry physics. Even though the entry environments of radiative heating, convective heating, deceleration loads and surface pressures are severe, design provisions enable air recovery so that post flight examination can be made.

From the assimilations and analysis of entry trajectories and environments calculations for entry into the outer planets several conclusions can be drawn. An outer planet probe must withstand a radiant dominant entry heat pulse that is sensitive to the entry path angle, vehicle ballistic coefficient and the atmospheric composition. Jovian entry environments were the most severe conditions and used more extensively to design the earth entry vehicle. Radiative heating is about three times greater than convective. Uncertainties in Jovian entry angle (three degree spread) results in a 58% increase in radiative heating, a 19% increase in convective heating and a 10% increase in shock pressure. Adequate description of shock temperature, temperature distribution across the shock layer, and species concentration are important in determibing radiative heating. Radiative heating is composed of approximately half continuum and half line radiation. Knowledge of the temperature distribution across the shock layer is important to computing radiative heating. Both carbonaceous and hyperpure silica heat shields were analyzed for Jovian entry. Injection of ablation material into the shock further reduced radiative heating to the wall with carbon having the greatest reduction (46%), silica about 18%. However, due to silica's excellent reflectance, it had to accommodate far less heat, only 1.7 kw/cm^2 as compared to 9.1 kw/cm^2 for carbon. Testing of hyperpure and carbonaceous materials under simulated Jovian environments should be performed to substantiate these finds.

It was also concluded that outer planet radiative heating can be simulated during a high speed earth entry. This conclusion is based on analysis of non-blowing, cooled and mass injected shock layers. Maps of attainable environments were prepared to aid the experiment planner. The conclusions for characterizing Jovian entry radiant heating are applicable to earth entry shock layer radiation. Due to the higher molecular weight and lower heat capacity of air as compared to hydrogen-helium, attainment of similar shock layer temperatures, or heating rates, can be

accomplished at much lower entry speed than that of the outer planets. Air shock layers radiate nearly 50 percent of their intensity in the vacuum ultra violet (VUV) whereas most of the radiation in hydrogen-helium mixtures occur in the ultra violet, visible and infrared regimes. However, when mass injection occurs most of the VUV never reaches the surface.

Launching the payload on a Hohmann transfer orbit to an apoapsis between two and 6.5 earth radii followed by deorbit at apoapsis and a kick ΔV just prior entry proved a viable way to achieve the necessary earth entry velocity. Increasing apoapsis radius with a given booster increases radiative heating, stagnation pressure, deceleration loads but decreases total heat. Saturn radiative heating can be simulated using apoapsis radius of two and Jovian heating with an apoapsis radius of 6.5. If need be the radiative heating can be further increased by increasing entry vehicle ballistic coefficient.

Although earth entry conditions can be selected that will result in matching peak radiative flux levels (non-blowing) for entry into Saturn or Jupiter, the precise matching of all other parameters is not possible. The best overall match of incident environments can be obtained for Jupiter at 20 degree entry angle and Saturn at some higher angle (approaching 90 degrees). Mass injection significantly reduces radiative heating. Both the resulting incident and net radiative flux to a carbonaceous heat shield can be simulated but net flux to a silica shield will be higher than required for Jupiter when the incident radiative flux is simulated. This is due to the shift of spectral radiation into the vacuum ultra violet region where silica's reflectance is low. The Transtage/TE363-4 booster is capable of achieving the necessary entry conditions. Analysis indicate that a more powerful solid IUS than was studied will be needed to obtain the desired conditions. Even so, the solid IUS can be used to produce intense radiation dominate environments necessary for planetary technology studies.

The instrumentation needs of the entry vehicle can be met with standard, commercially available equipment. The anticipated high aceeleration may require more rugged packaging than is usually required. The only area of concern is the radiometer which will require some development. In order to keep the package size small, optical focal lengths must be short, which in turn requires that detectors be physically small so that they can be spaced consistent with the small differential diffraction angles. Previous space probes, such as the Skylab ATM experiments, used photomultiplier tubes as detectors. These are too large for this

application, and development of silicon photodiodes in the ultra-violet band is the major requirement for this radiometer. Further analysis will determine whether a prism or a grating is the best diffraction technique. Fabrication methods for lithium fluoride and ruling of gratings to small radii need to be studied.

The telemetry data rate of 48 KBPS should be adequate, but even if a need for additional measurements arises, it can be kept below 64 KBPS which makes pre-deployment checkout, over one Shuttle interface, a simple task.

Mission analyses concluded that booster firing would occur over the Pacific Ocean, deorbit at apoapsis would occur over South America and that radars at Ascension Test Range could track the entry vehicle during the entire descent.

Entry vehicle design study showed that such a vehicle would have sufficient instrumentation and equipment to perform its mission and would be compatible with the Shuttle and its interfaces. Power requirements are minimal and "off the shelf" equipment can be arranged compactly within the vehicle. Even though mid-air recovery system had to be located beneath the aft cover, vehicle c.g. control was maintained. The entry vehicle, upper stage and main booster takes up less than half of Shuttle's cargo bay and 43% of its payload capability. This permits shared Shuttle launches and thereby reducing recurring cost to $11 $\overline{M}$ for entry vehicle, booster, recovery and data analysis.

11.0 RECOMMENDATIONS

Despite the fact that the Shuttle deployed high speed entry vehicle has been shown to be a viable means of simulating outer planet environments and a means to demonstrate heat shield performance, more work remains to be done. In general the additional work centers on doing those things necessary to broaden the technology base by sharpening analytical tools, developing materials, conducting performance tests, critiquing designs, planning missions, etc., all of which lead up to flying the earth entry vehicle. By doing these things the design of the outer planet probes and the scentific data yield will be vastly improved. The recommended work follows.

The understanding of carbon phenolic and hyperpure silica heat shields performance should be expanded by analysis of heat shield integrity and demonstration testing under simulated planetary environments. In the area of heat shield integrity the following is recommended:

- o Study the sensitivity of performance to the shock shape and inviscid flow field modeling.
- o Analyze effects of cooled shock layers on inviscid flow field properties.
- o Improve methods for predicting distributions of environments on the vehicle.
- o Characterize effects of mass injection (moderate and massive blowing) on shock layer radiation.
- o Characterize effects of mass injection on convective heating.
- o Improve modeling of ablators
  - Energy balance at ablator surface
  - Energy transport in material
  - Surface recession
- o Determine thermochemical structural capabilities of the heat shields.

In the area of heat shield demonstration it is recommended to move forward on the design, mission planning analysis, and other activities necessary to fly the entry vehicle evolved in the present study.

o To support the continuing development of an earth entry vehicle and the outer planet probe design, characterization of the candidate heat shield materials is appropriate. This can be accomplished by comparative arc tunnel testing of heat shield specimens and correlation of measured performance with predictions. The results would then feed back into the analytical effort to update calculation techniques.

o Development effort on the radiometer should be pursued. Two design approaches have been suggested in this study, these and other possible designs should be studied

in more detail and a best approach selected. The following areas especially need investigation.

a. Small detectors for the .1 to .3 μm wavelengths.

b. Detector electronics including bias, chopping and amplification.

c. Concave diffraction gratings having small radii and high ruling density.

d. Environmental and optical properties of lithium fluoride.

It is also conceivable that the radiometer could be tested during the arc tunnel testing of the candidate heat shield materials, thereby characterizing the ground test environment by an in-situ measurement and qualifying the hardware.

o As the IUS and upper stages for Shuttle become better defined, integrate their performance into the mission simulation capability analysis. Also conduct a complete mission safety/dispersion analysis.

o Design, fabricate and test an engineering model of the entry vehicle to demonstrate component reliability. Reliability will be very important in order to minimize checkout requirements and delayed Shuttle launches due to payload equipment failure.

o It is also recommended that the earth entry flight experiment be added to the Shuttle traffic model so that the mission can be properly planned and accomplished on an early Shuttle flight in time to aid the planetary probe missions.

o Accomplishment of these activities will greatly expand the technology base for exploration of the solar system.

12.0 REFERENCES

1. Bradley, F. E.; and Cowan, W. D., 1980 Pioneer Jupiter Orbiter Probe Mission, Atmospheric Entry Probe Design Considerations, AIAA Paper 75-1162.
2. Vojvodich, N. S.; Reynolds, R. T.; Grant, T. L.; and Nachtsheim, P. R., Outer Planet Atmospheric Entry Probes - An Overview of Technology Readiness, AIAA Paper 75-1147.
3. Sutton, K., Radiative Heating About Outer Planet Entry Probes, AIAA Paper 75-183.
4. Moss, J. N. and Bolz, C. W., Jr., Viscous-Shock-Layer Solutions with Radiation and Ablation Injection for Jovian Entry, AIAA Paper 75-671.
5. Nicolet, W. E., Aerothermodynamic Environment for Jovian Entry Conditions, AIAA Paper 75-672.
6. The Planet Jupiter (1970), NASA Space Vehicle Design Criteria (Environment), NASA SP-8069, December 1971.
7. The Planet Saturn (1970), Space Vehicle Design Criteria (Environment), NASA SP-8091, June 1972.
8. Myers, H., Models of the Atmosphere of Uranus, McDonnell Douglas Corporation Report E1163, 18 October 1974.
9. Saturn/Uranus Atmospheric Entry Probe, McDonnell Douglas Corporation Report E0870, 18 July 1973.
10. Sutton, K., Stagnation Point Radiative Heat Flux for High Speed Earth Entry, received May 1975 (to be published).
11. McNeilly, W. R. (1975), Advanced Shuttle Payloads Sizing Study, MDC E1189 (NAS1-12436), McDonnell Douglas Astronautics Company-East, St. Louis, Mo.
12. Teeter, R. R. et al (1973), Space Shuttle Expendable Upper Stages, BMI-NLVP-TM-73-4, Battelle Columbus Laboratories, Columbus, Ohio.
13. Vetter, H. C., McNeilly, W. R., Siemers, P. M. III, Nachtsheim, P. R., Shuttle Launched Flight Tests: Supporting Technology for Planetary Entry Missions, AIAA Paper 75-1152.
14. Seiff, A., et al (1973) PAET, An Entry Probe Experiment in the Earth's Atmosphere, ICARUS 18, 525-563.
15. Scallion, W. I. and Lewis, J. H. Jr. (1965), Flight Parameters and Vehicle Performance for Project FIRE Flight 1, Launch of April 14, 1964, NASA TND-2996, Langley Research Center, Hampton, Va.